A Novel Approach to Design an Integrated Antenna-Battery System

by

Michael Anthony Woods

Thesis

Submitted to the University of Kent as part of the

requirement in the subject of Chemistry for the degree

of

Doctor of Philosophy

School of Physical Sciences

and

School of Engineering and Digital Arts

July 2016

Contents

List of Tables

List of Figures

Acknowledgments

First and foremost, I would like to thank my supervisors, Dr. Maria Alfredsson and Dr. John Batchelor for not only providing me with this opportunity, but for all the help and support over these last few years. Their enthusiasm and interest in this work has kept me motivated and determined to keep going, even when things were not going to plan.

I would like to thank the EPSRC and the University of Kent for providing the funding that has allowed this research to be possible.

I would also like to thank the School of Physical Sciences, and School of Engineering and Digital Arts, along with the staff in these departments, for providing the resources and assistance that allowed this work to take place.

I am extremely grateful for the assistance and contribution provided by Dr. David Willock to this work. The help provided by him allowed me to overcome what was possibly the greatest challenge throughout this PhD, allowing me to simulate the polymer systems, and for providing continued support and advice throughout.

I am also indebted to the Linux genius, Tim Kinnear, for helping to solve the seemingly endless computer issues encountered along the way.

Further acknowledgements go to Dr. Dean Sayle, for the assistance provided with regards to analysing some of output files from the simulations.

I am also very grateful for all the support from my friends over the past few years, who have encouraged me to keep going to the end. Despite my almost endless moaning, you have managed to put up with me (something of a miracle), and for that, I am very much appreciative.

Finally, the love and support of my family has always helped me to overcome whatever challenge has come my way, and you will always have my deepest gratitude, including Baxter the cat, whose calming presence definitely helped make the writing up period less stressful.

Declarations

I hereby declare that the work presented in this thesis is entirely that of the author, apart from where due acknowledgment has been made. This work has not been previously submitted, in whole or in part, for any other academic degree.

Candidate: Michael Woods

Publications

- M. Woods and J. Batchelor, "Low-profile Slot Antenna integrated with a thin polymer non-metallic battery", IEEE Loughborough Antenna and Propagation Conference, 2013.
- M. Woods, O. Rakibet, P. Young, R. Luck, M. Alfredsson and J. Batchelor, "Integrated Antenna-Battery for Low-profile Short Range Communications", 8th European Conference on Antennas and Propagation (EuCAP), 2014, 1754-1756.

Abstract

In this study, an integrated antenna-battery was explored. Studying the systems separately allowed information to be obtained relating to the materials' performance and feasibility of an integrated system.

Conducting polymers are promising in modern day lithium ion batteries. With high electrical conductivity as well as good ionic conductivity, they are now becoming more widely used. Here, we present a study of a co-block polymer (PEDOT-PEG) in which a polymer with high electrical conductivity is linked to a polymer with lithium ion conductivity, using a combination of atomistic simulations and experiments.

Simulations showed that the diffusion and ionic conductivity for PEDOT-PEG agreed well with experiments. A trend was identified as a function of lithium salt concentration, in which the ionic conductivity decreased with increasing concentration. This was identified to be down to the significant ion pairing occurring in the system between lithium and the counterion.

Requirements for the antenna were the ability to be mounted easily onto a battery substrate without a significant loss in efficiency and bandwidth. Studies were undertaken in which a slot dipole antenna was modified so as to incorporate properties more closely associated with battery materials i.e. permittivity and dielectric loss. An ultra-thin Mylar prototype was also synthesised and mounted onto a variety of surfaces, to assess how the antenna performed in different environments.

Results for the antenna showed usable bandwidths and efficiencies when the antenna structure was modified to closely resemble a solid state battery. Despite a reduction seen in certain cases, these losses were not significant, and showed promise with regards to designing an integrated system. The Mylar prototype showed a good match between simulation and experiment in free space and when mounted on surfaces such as polymers, indicating that an ultra-thin antenna-battery is feasible.

Chapter 1

Aims

1.1 Background

Batteries and antennas are both widely used components in the electronic and science fields. They both have a long list of applications, some of the most notable being in mobile phones [1, 2, 3] and sensors [4]. These components, namely antennas come in a huge range of different designs dependant upon their target application.

Battery systems are constantly being explored, developed, and improved upon. This is to enable them to cope with the high demand that is set by technological advances. One important quality in order to meet this demand is to ensure that we have an energy supply which is both cheap and sustainable. This is where batteries come into place [5]. Despite a relatively simple concept, the rate of advancement of three-dimensional batteries has been relatively slow. As a matter of fact, batteries are seen as the heaviest, most expensive and least green components of any electronic device.

In its simplest form, a battery can be described as several electrochemical cells connected either in series or parallel in order to provide the required capacity and voltage, respectively [6]. Each cell is made up of a positive and negative electrode, which is separated by an electrolyte solution that enables the transfer of ions between the electrodes. There are many battery systems that have been developed over the years. The earliest batteries contained Zn and MnO_2 as their electrochemical couples [5]. Lead-acid and Ni-Cd were other common materials used in the early days of battery research. More recent batteries systems are the Ni-MH and Li-ion batteries. Lithium tends to be the material of choice at present for portable devices. Lithium ions now are being used in conjunction with nanomaterials. This is because of the advantages offered by nanomaterials such as increased rate of lithium insertion and removal, and enhanced mixed ionic and electronic transport within the particles [7].

Antennas are part of radio communications systems and are devices that either transmit or receive electromagnetic waves [8]. While certain specialised transmit or receive antenna designs exist, in general, antenna designs are not specific to either

a transmit or receive function. The communication system as a whole consists of a transmitter, a transmitting antenna, the propagation medium, a receiving antenna and a receiver [9].

Batteries and antennas are commonly used together in transceivers, with a mobile phone as a key example. Batteries are often required to power the antenna. As separate components, they both can function effectively alongside each other. It is when they are both combined with the intention of creating a reduced size single component where the problems begin to arise. It is a common problem in electronics that antenna performance is degraded in the presence of proximal metal planes. What is meant by performance degradation in this case is antenna mismatch and a reduction in antenna efficiency, properties which will be discussed in Chapter 2. The battery component comprises of metal from both the current collectors, but mainly the hermetic seal, which makes it difficult to combine with antennas. This problem will be discussed in greater detail in Section 1.2. The aim of this investigation is ultimately to solve this problem of degraded antenna performance in combination with a battery.

1.2 Non-metallic battery

Possible future developments in lithium batteries involve using lithium in conjunction with air. In this project, however, the intention is to take a very different approach: to design a battery that contains no metallic components. The reason for this design is to ensure that the battery is then compatible with an integrated antenna system. What we mean by compatibility is that the two components can function side by side without the battery degrading the performance of the antenna. In a standard battery, we have two metallic current collectors situated on either side of the anode/cathode. These current collectors conduct electrons which are involved in the oxidation and reduction processes which occur in the anode and cathode components of the typical lithium ion battery. Figure 1.1 shows the standard setup for the typical lithium ion battery.

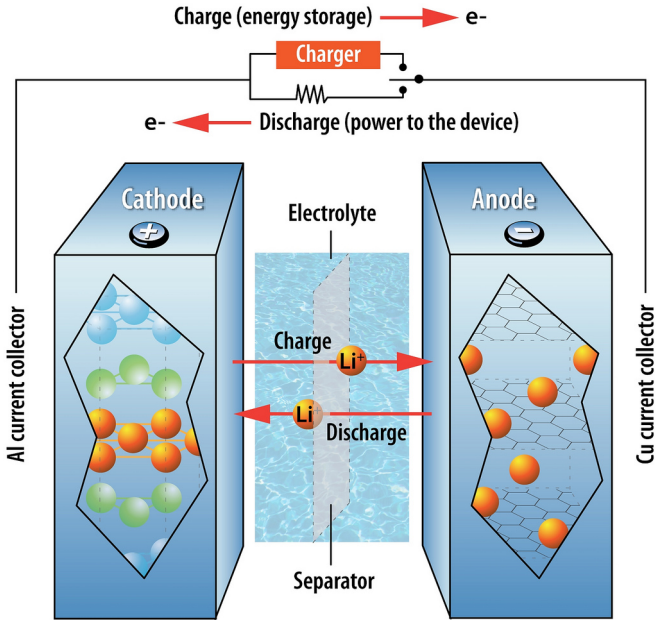

Figure 1.1: Diagram of typical lithium ion battery showing how lithium ions migrate from the anode to the cathode [10]

Conventionally, the battery and antenna have been presented as two stand-alone components. When used in an integrated system, the battery component causes interference with the electromagnetic fields of the antenna component. The interference can be explained in terms of these electromagnetic waves which are transmitted or received by an antenna [8]. As Faraday demonstrated in 1831, electromagnetic induction can occur in the presence of a metallic material [11]. The electromagnetic waves, which are parallel to the metal's surface, are converted into an electric current which is present across the conductor. This causes the signals that are emitted and received by an antenna that is close, and parallel, to a metal surface to suffer a loss in radiated energy.

It has been identified that the mismatch problem is caused by these current collectors from the battery. We are also presented with the problem that both the battery and the antenna are typically two bulky components, which may cause issues such as portability and a difficulty creating compact device envelopes. A prime example of this is with soldiers in the army [11]. Soldiers have a very important need for radio systems, particularly at low frequencies in order for communication. As a result, the antenna needs to be of large dimensions, and this is then combined with large batteries which can be problematic in terms of keeping hidden from enemies and carrying the device around swiftly. The ability to combine smaller, short range antennas with their transceiver batteries could have a significant reduction to the burden on the soldier.

We have therefore been presented with two important questions that need to be addressed:

1. Are we able to design and build a battery containing no metal?

2. Can we integrate the battery and antenna into a design that is both lightweight and easier to transport? That is having one component as opposed to two.

Our design in mind is an integrated system that is easily printable and ultra-thin/compact. A variety of applications have been considered for this combined system including wireless sensors, home monitoring systems and small portable radios for soldiers. Figure 1.2 shows the proposed integrated antenna-battery design for this project.

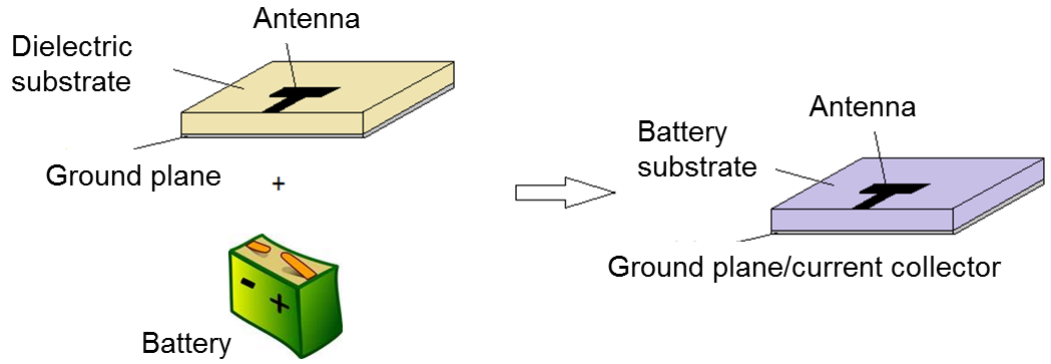

Figure 1.2: Antenna and battery components shown as separate and integrated systems

To begin tackling these issues, we need to have a realistic idea of a way in which these suggested designs can work, while still giving good performance. A crucial aspect necessary for this battery to work is that it must contain a material that is both electrical and ionic conducting. This material therefore must act as a replacement for the metallic current collectors. Without these, the material needs to be able to conduct electrons to compensate. Ionic conductivity is necessary so that lithium ions can be transported from one electrode to the other.

1.3 Polymer Electrolytes

1.3.1 Conducting polymers

One candidate material that fits the criteria required for a non-metallic battery is a polymer electrolyte. Specifically in this case, we are looking at conducting polymers, as opposed to an electrical insulating electrolyte commonly used in typical lithium ion batteries. Electrical conductivity (σ) can be defined as being proportional to the product of the density of charge carriers (n), along with the charge that each carrier holds (e) and also the mobility that each carrier possesses (μ)[12]. Equation (1.1) relates all these terms to each other.

$$\sigma = en\mu \tag{1.1}$$

As mentioned previously, a crucial aspect for a polymer electrolyte to work in this case is mixed electrical/ionic conductivity. Figure 1.3 shows a current setup of a typical lithium ion battery, followed by a proposed design replacing the current collectors with conducting polymers.

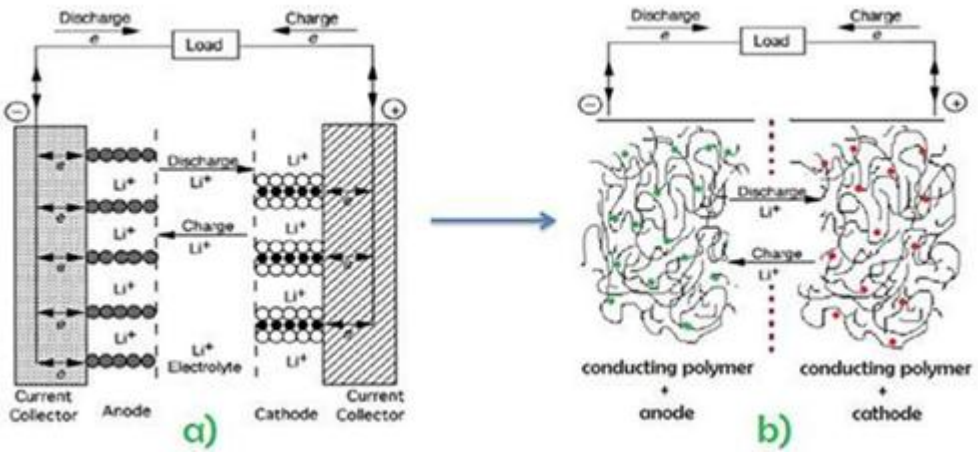

Figure 1.3: a) A typical lithium ion battery setup and b) Proposed non-metallic battery with conducting polymers acting as the electrodes, replacing the current collectors [11]

Obviously, to have any chance of the proposed design being successful, we need a polymer electrolyte that is suitable. A conducting polymer would be able to transport electrical energy converted from chemical energy through it, negating the requirement for a current collector [11]. However, for this to be successful, the conducting polymer is also required to be both chemically and thermally stable, along with good conductivity at room temperature. With these in place, it is hoped that the electrolyte would be cyclable in a lithium ion battery.

With regards to the setup of the new proposed battery, the negative electrode consists of the polymer matrix mixed together with the anode material, while the positive electrode consists of the polymer matrix mixed with the cathode material. Acting as the separator would be an electrically insulating membrane such as PEO, which would enable lithium migration and ensure that short-circuits are avoided. It is well known that many different polymer electrolytes offer good ionic conductivity, giving them a good ability to transfer ions from the anode to the cathode and vice versa.

So how do we know that replacing the metallic current collectors with polymer electrolytes will work? Well in terms of electrical conductivity, polymers have been investigated as current collectors previously. A prime example of this is in the application of electrochromic windows [13], where the copolymer poly(3,4-ethylenedioxythiophene) polystyrene sulphonate (PEDOT:PSS), was used for both electrodes, separated by a polyelectrolyte, with the colour contrast in the electrochromic display observed throughout the experiment.

Polymer electrolytes are now commonly used in batteries, but often for other purposes, such as binders in electrode materials. For example, polypyrrole has been used in silicon anodes [14] to form a composite which reduces the initial irreversible capacity loss, producing good reversibility, greater cycle life and higher coulombic efficiency than the pure silicon anode. They are also often used as separators, such as the polyvinylidene difluoride/polydimethylsiloxane (PVDF/PDMS) membrane [15], where blending PDMS into the PVDF membrane lead to decreased crystallinity, as well as increased stability of entrapped liquid electrolyte and ionic conductivity. Another polymer that has shown to improve the PVDF membrane properties in lithium ion batteries is poly(methyl methacrylate) (PMMA) [16]. Using a relatively new technique known as electrospinning to fabricate the fibrous polymer membrane, PMMA has a plasticisation effect on the PVDF polymer, leading to a decreased crystallinity, and thus a higher ionic conductivity. The increased conductivity of this composite is a result of increased electrolyte uptake, a three-dimensional network structure, and a higher porosity.

As mentioned throughout, it is simply not enough to have either electrical or ionic conductivity for our polymer electrolyte to be able to be used in the proposed battery design. The polymer must be a mixed conductor having both of these properties in order to be suitable. However, this does not necessarily mean that a polymer containing just one of these properties should automatically be discounted. In many cases, a polymer can be doped, which may lead to an increase in electronic conductivity. Composite polymers can also be synthesised which may greatly enhance its properties and allow it to be used in a wider array of applications. It is worth looking at specific polymers individually to begin with, so as to allow us to assess the options available to us. What is perhaps the most important property to begin investigating is electrical conductivity. We are hoping to use polymer electrolytes with the highest electrical conductivity values possible, giving them greater ability to conduct electrons. Figure 1.4 shows the electrical conductivity values of various polymer electrolytes along with some other materials that include transition metals.

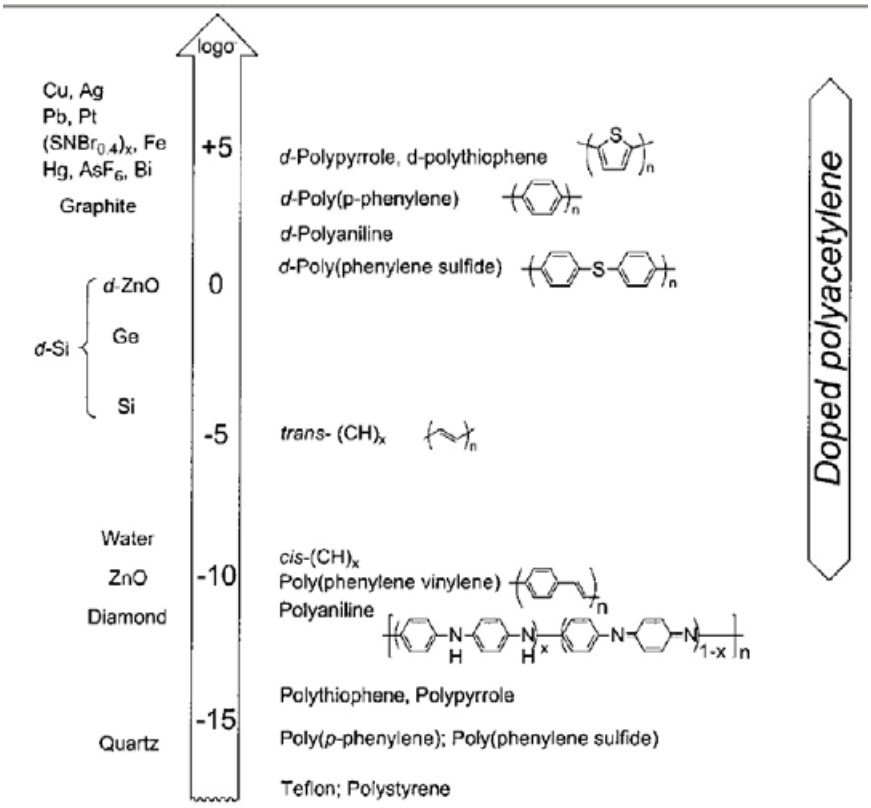

Figure 1.4: A diagram showing the electrical conductivities of various polymers and materials. Note that the polymers are on the right side of the diagram [17]

Here, we can immediately see which polymers have the greatest conductivity. What is instantly noticeable is the vast difference in conductivity between the pure polymers, and their doped counterparts (shown on the diagram by *d*-). This suggests that with doping, the conductivity values on these polymers can reach levels close to transition metals. This means that in terms of electrical conductivity, polymer electrolytes are very much a valid replacement if we are trying to create non-metallic batteries.

When we consider conducting polymers suitable for a battery, there are several key parameters that need to be observed. The charge density is an important factor, and values greater than 200mAh/g are preferable [18]. The charge density is determined by the polymer mass or volume that is required per exchangeable unit charge. Specific charge, often used to express the charge of a battery as well, can often be quoted as capacity instead and this is in reference to both the electrodes and the entire battery. It should be noted that in any battery, the capacity tends to be limited by the electrode with the overall lowest capacity.

Further important features of a good conducting polymer are a voltage difference relative to the counter electrode which is greater than 2V. A high coulombic efficiency is sought after, with a value closer to 100% seen as a preference. A suitable polymer should also feature a voltage efficiency greater than 80%. The main other prerequisites are to do with the overall lifetime of the material. A cycle life greater

than 500 cycles is ideal, while self-discharge due to reactions with the electrolyte for example should occur at less than 1% per day to ensure that the polymer has a good chemical stability. The final point is that the electrolyte should have a shelf life of more than a year, in the charged or discharged state.

The next step here is to briefly investigate the model polymer electrolytes that have been tested in many battery systems previously. In this case, some of the most studied polymers include polyacetylene, polyaniline, polypyrrole, polythiophene and poly(p-phenylene).

1.3.2 Ionic conductivity

Ionically-conducting polymers behave differently to those that specifically conduct electrons. These types of polymers act as hosts, forming complexes with alkali metal salts [19]. The process can be described by Equation (1.2)

$$mMX + (-RY-)_n \rightarrow (MX)_m \cdot (-RY-)_n \tag{1.2}$$

Here, (-RY-) is the polymer repeat unit. For a reaction such as this to be successful, several requirements must be fulfilled. Firstly, the system will need to be thermodynamically favourable, which is achieved when the Gibbs energy of solvation of the salt by the polymer is substantial enough to overcome the salt's lattice energy. A simpler way to describe this is the relationship between the ability of the salt to form a homogenous complex and the ability of the monomer to dissolve this salt. Further requirements are that the polar groups present on the polymer chain need to be of a high concentration in order to effectively solvate the salt. The cohesive energy that a polymer contains must not be too high. The polymer must also be quite flexible, allowing reorientation of the local coordination geometry to be achieved allowing for effective solvation.

In order to conduct ions, polymers require specific features, in this case, known as coordination centres. These coordination centres are often particular atoms/groups situated on a polymer, which allow ions to be coordinated to them. We are specifically looking at Li^+ ions in this case, with the bigger picture being which polymers favour the migration of Li^+ ions in their polymer matrix.

So what is meant exactly by a coordination centre? Take poly(ethylene oxide) or PEO for example. PEO is one of the most commonly known polymer electrolytes and possesses oxygen atoms in its structure, as shown in Figure 1.5.

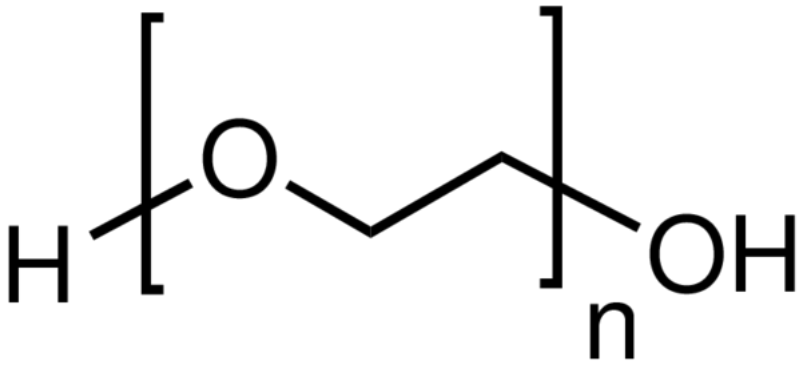

Figure 1.5: Chemical structure of poly(ethylene oxide)

These oxygen atoms are electronegative and contain two lone pairs of electrons. The oxygen atoms are an attractive site for lithium, and with chains of PEO, enable Li^+ ions to essentially travel from one oxygen to another. Therefore, we see a migration of lithium across the structure of PEO, meaning it possesses ionic conductivity. The oxygen atoms in this case are referred to as coordination centres.

As well as polymers containing oxygen such as poly(propylene oxide) and polysiloxanes, we are also interested in any that contain nitrogen and sulphur atoms. This includes polymers such as polypyrrole and polythiophene.

1.3.3 Polyacetylene

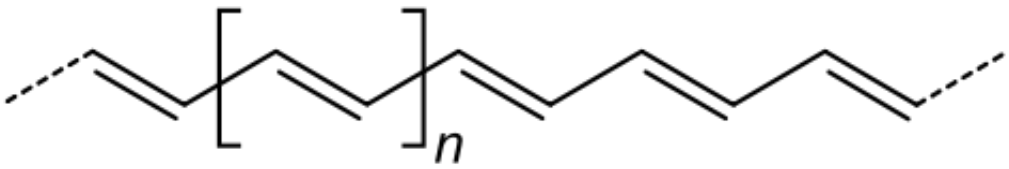

Figure 1.6: Chemical structure of polyacetylene

When looking for a suitable polymer to incorporate into the battery, it is a good idea to start from the beginning. The first known electrical conducting polymer is polyacetylene, shown in Figure 1.6. It was discovered that polyacetylene could be reversibly oxidised and reduced, which essentially meant that it could reversibly switch from the insulating state to either a semiconducting or conducting state [20]. After this discovery, attempts were made using the redox reactions of polyacetylene to store charge [18]. Among many of the conducting polymers, polyacetylene tends to be regarded as a model material, which is in some way due to its bivalence property (which means it acts as a host for both positive and negative charge). There is also a large amount of theoretical data on polyacetylene that has been acquired by physicists.

During the redox reactions that occur in conducting polymers, the polymer electrolyte needs to either give off or take up ions in order to ensure that the material remains charge neutral. This process is often referred to as doping, which is an ion insertion process. An example of a dopant used in conjunction with a conducting polymer is Titanium Disulfide [21]. Doping essentially increases the redox state and thus the electrical conductivity of the polymer [18]. These charge-compensating ions are free to move within the polymer meaning that doped conducting polymers are in fact, both electrical and ionic conducting.

One of the key features of polyacetylene that gives rise to its high conductivity is the fact that it is a conjugated polymer. Conjugated polymers are charged conducting macromolecules that contain a large number of ionisable/ionic groups [22]. It is the alternating carbon-carbon double bonds present in the main polymer chain which give rise to its conductivity. Due to polyacetylene's extensive conjugation, as well as the ionic groups that it possesses upon doping, polyacetylenes are viewed as an attractive prospect for energy storage devices. As a matter of fact, in freshly prepared doped polyacetylene, several conductivity values of the order of 10^5 S/cm have even been reported [23].

One important feature of the polyacetylene molecule is that there are two possible isomers, the *cis*-isomer [24] and the *trans*-isomer [25]. These isomers are known as stereoisomers and describe the ways in which the atoms or functional groups position themselves relative to a reference plane [26]. In *cis*-isomerism, the atoms are situated on the same side, whereas in *trans*-isomerism, the atoms are on different sides.

Past research has very much been focused on polyacetylene films, which are prepared by the polymerisation of acetylene in the gaseous state, situated on a layer of concentrated Ziegler-Natta catalyst solution [27]. The resulting material is insoluble, inhomogenenous and poorly characterised. This had made it difficult for scientists to understand the main electrical properties of both pristine, and doped polyacetylene. In order to understand these properties, it is necessary to separate the single chain effects (or intramolecular forces) from the chain-chain interactions (or intermolecular forces) [28]. Previous attempts to solve this problem, which often involve modification of the monomer have tended to yield poor results. More successful polyacetylene materials have been created by incorporating polyacetylene into a graft co-block polymer.

Results show that either graft or co-block polymerisation of acetylene in conjunction with a suitable carrier polymer can lead to a soluble polyacetylene [28]. This then allows investigation of the single-chain characteristics of the polymer. Interestingly, these results obtained by Bates and Baker indicate the presence of amorphous polyacetylene trapped inside microdomains. In fact, it would seem that the likelihood of these polyacetylene microphases existing in a crystalline state is low due to their size and spatial constraints that are associated with graft function placement

at the domain interface [29].

Polyacetylene has been studied for use in organic batteries previously. For example, Nagatomo fabricated a rechargeable all-plastic battery using polyacetylene film for both electrodes, along with a PVDF·$LiClO_4$· PC (propylene carbonate) polymeric solid electrolyte film in between [30]. A gold film was placed on top of the positive electrode, while a sheet of aluminium foil was placed underneath the negative electrode. The design is shown in Figure 1.7.

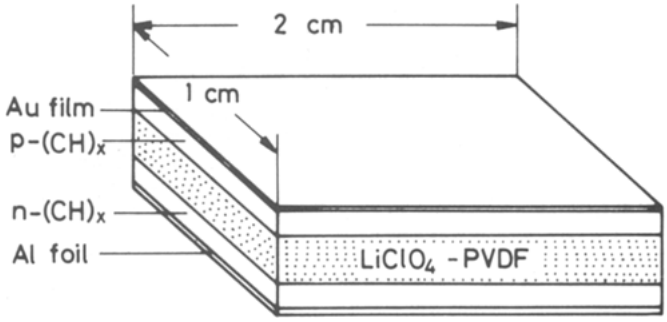

Figure 1.7: Diagram showing the layout of a rechargeable polyacetylene battery with a polymer solid film of PVDF·$LiClO_4$·PC acting as the electrolyte [30]

In this case, the ionic conductivity of the polymeric solid electrolyte increased as the mole percentage of $LiClO_4$ in PVDF increased. Average values ranged from 4×10^{-6} to 5×10^{-3} S/cm. The battery was found to be suitable for usage in low current electronic devices. However, it suffered from several problems, such as the ionic conductivity of the electrolyte being insufficient, the degradation of the battery performance and the adhesion between the polyacetylene film and the polymeric solid electrolyte.

1.3.4 Polyaniline

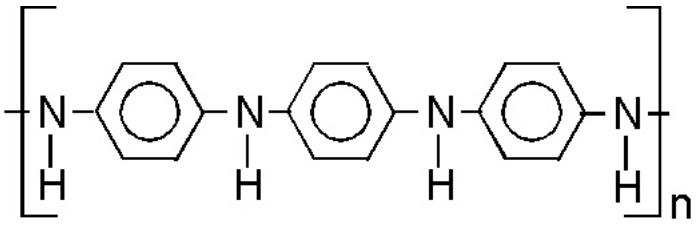

Figure 1.8: Chemical structure of polyaniline

Polyaniline, shown in Figure 1.8, is one of the most investigated conducting polymers and it fulfils the requirements of an electrode material for usage in a light-weight battery [18]. Polyaniline tends to be produced from either anodic and chemical oxidation of an aniline monomer. Perhaps one of polyaniline's most desirable features is that it is a conjugated polymer [31]. With an ease of synthesis, and good commercial availability of both the monomer and polymer, it happens to be one of the most commonly used conducting polymers in battery application.

As with polyacetylene, one of the reasons for the high conductivity of polyaniline is due to its extensive conjugativity. Further explanation of conjugativity can be described by the overlap of adjacent π-orbitals which give rise to the electronic and optical properties of the polymer. In fact, the combination of molecular orbitals across a backbone of a conjugated polymer result in band structures which are comparable to those witnessed in inorganic semiconductors [20, 32]. However, conjugated polymers are associated with a maximum conjugation length, defined as the point where further addition of monomer units will no longer have any bearing of the electronic properties of the material [33, 34, 35].

The performance characteristics of polyaniline [36] are an operating voltage vs Li/Li^+ of between 3 and 4V. A theoretical capacity of 294mAh/g has been deduced while experimentally, the capacity can range from 100 to 147mAh/g. It demonstrates an energy density of 300mWh/g along with a power density of 100mW/g. Other properties that make polyaniline desirable for a battery are its high coloumbic efficiency of 90-100%, a good cyclability of over 500 cycles along with a good chemical stability, tunable properties and a low cost [12, 18]. Of particular interest is the conductivity of polyaniline. In pellet form, values of up to 58 S/cm have been quoted when synthesised with H_3PO_4, while stretched polyaniline films have shown electrical conductivity of up to 500 S/cm in the stretching direction [37].

Polyaniline/lithium batteries are actually among the few to have been commercially successful [31]. Researchers are continuously looking for ways on which to improve the performance of polyaniline in batteries as a result of its favourable properties such as oxidative stability, theoretical capacity and electrochemical reversibility [38]. Despite the benefits offered by polyaniline, it does suffer some drawbacks, with the most notable being insolubility and intractability. However, these issues have been addressed in other studies that involved dispersion of the polymer via multiple steps designed to remove aggregates, resulting in a stable suspension [39]. In more recent years, other methods have allowed an easier form of solution suspension in polyaniline, such as template synthesis with polyanions [40].

1.3.5 PEDOT

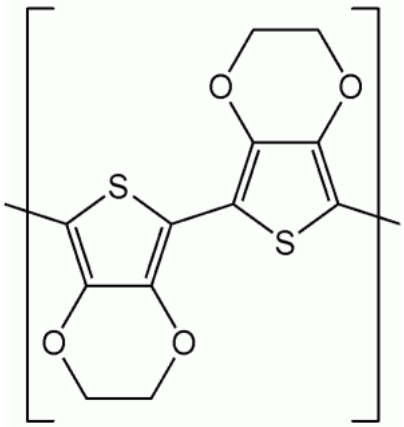

Figure 1.9: Chemical structure of PEDOT

Poly(3,4-ethylenedioxythiophene) or PEDOT, shown in Figure 1.9, is a polymer that has perhaps not been so widely studied compared to polyacetylene and polyaniline. Like the previously mentioned polymers, PEDOT is a conjugated polymer that functions as an electronic conductor [41]. PEDOT has demonstrated interesting electrochemical properties such as an operating voltage (V vs Li/Li^+) of between 2.7-4.2V [31]. Other key properties include a theoretical capacity of 191mAh/g, and an experimental capacity of between 30-70mAh/g. Energy densities of between 1-4mWh/g have been quoted while power density values can range from 35-2500mW/g.

What is perhaps one of the most interesting features of PEDOT is its electrical stability, which is why it has been attracting more and more attention [41]. PEDOT also has a good cycle life, greater than 500 cycles, the amount usually required for lithium ion batteries. PEDOT has also been used as a composite with carbon, showing impressive cycling stability of 25mAh/g over 220 cycles [42]. No fading of capacity was shown over these tested cycles, and a coulombic efficiency of over 99% was observed.

PEDOT has previously been studied in a variety of applications such as a conducting surface layer for electrodeposition of copper [43] along with biosensor applications [44]. It has been shown to demonstrate enhanced electrochromatic switching properties, along with high electronic conductivity [45]. PEDOT is able to be processed from solution, and has demonstrated conductivity values of as high as 300 S/cm [43]. Due to its conductivity, PEDOT is commonly incorporated as an electronically conducting phase in many material systems [13].

1.3.6 Poly(ethylene oxide)/Poly(ethylene glycol)

Poly(ethylene oxide) or PEO, which can also be known as Poly(ethylene glycol) or PEG depending on chain length, has attracted attention because of its Li-ion conductivity. It has the ability to solvate ions, therefore allowing it to act as a solid

polymer electrolyte that makes it suitable for many electrochemical applications, such as batteries with high energy density [46]. Unlike the previous examples of conjugated polymers which we are looking at, the main attribute of PEO is its function as an ionically-conducting polymer. As mentioned in Section 1.3.2, PEO contains oxygen atoms which allow it to solvate lithium ions, allowing them to migrate across the polymer chains.

PEO is in fact the most studied host for cations out of the polymer electrolytes [47]. It contains a simple monomer unit (CH_2-CH_2-O) along with a high chemical stability. Due to a flexible chain, it is able to adopt several low energy conformations. PEO is suited to forming multidentate polymer-ion bonds, which is due to the distance between the ether oxygens in the chain. As mentioned previously, the chain lengths, or molecular weight will determine the designation of the polymer, along with the structure. For low molecular weights, the polymer is referred to as PEG and is in the form of an amorphous, viscous liquid. For higher molecular weights, the polymer is referred to as PEO and is semicrystalline, possessing both amorphous and crystalline regions. As a result, PEO takes on a helical structure [48]. As the molecular weight of PEO is increased, the crystallinity will decrease due to entanglements in the system.

In this study, we are interested in the behaviour of PEO/PEG systems as a polymer electrolyte, and thus the conduction mechanisms of lithium ions. It is expected that the ionic conductivity will increase as a function of increasing salt concentration. However, though this is true in most cases, the $LiClO_4$-PEO system shows an initial increase before reaching a peak at an intermediate concentration [49]. At higher concentrations, the conductivity starts to decrease. This can be explained in terms of ion pairing, whereby aggregates are formed at high salt concentrations [50]. When a polymer-salt system becomes more concentrated, the distances between the ions become shorter and form clusters [47]. This results in a lower mobility of the ions due to the increased size of the clusters. Furthermore, the polymer backbone will become more rigid with increasing salt concentration which leads to a reduction in the number of available coordination sites. The clusters also affect the charge, since the uncharged ion pairs will become monovalent ions, and thus have no contribution to the ionic conductivity.

Materials such as PEO are of great interest in all-solid-state batteries [51]. The ionic conductivity of PEO-based electrolytes is temperature dependant. At ambient temperature, relatively low values are observed, of the order of 10^{-8} S/cm [52] which can be partially a result of high localised crystallinity. Li-ion conductivity can increase up to around 10^{-5} S/cm at about 100°C. It is found that ionic conductivity is more prominent in the amorphous regions of PEO [53]. Therefore, approaches have been made to try and reduce the crystallinity including the addition of plasticisers [47]. Water is one such example of this and has been known to increase the ionic

conductivity for polymer electrolytes by several orders of magnitude [54]. As well as improving ionic conductivity and mobility of the polymer chains, water absorption also decreases the amount of crystalline phase present in the material.

For our proposed design, PEG/PEO remains a good potential prospect for our system, and could become useful in combination with other polymers, leading to mixed conducting polymers, such as the co-block PEDOT-PEG discussed in Section 1.3.7.

1.3.7 PEDOT-PEG

In terms of conduction mechanism, PEDOT is mostly known to provide electrical conductivity while PEG is a provider of ionic conductivity. By creating a co-polymer from these two structures, we aim to create a co-polymer demonstrating mixed conductivity, meaning it possesses the properties of both an electrical conductor and an ionic conductor. This opens up many possibilities in the field of chemistry and electronics. In terms of the battery component, having a mixed conducting polymer would essentially act as a replacement for the anode/cathode components as well as the current collectors. It would allow us to use the conducting polymer to initiate transport of electrons across the battery, and allow lithium to be stored and transported from the anode to the cathode.

Little work has been done to assess the possibility of using PEDOT-PEG as an electrode in a battery, and this work would be focused on seeing how well this co-polymer could function as an anode/cathode and a current collector. One such application that has been discussed is the use of PEDOT-PEG in organic light emitting diodes (OLED) [55]. In this case, PEDOT-PEG has been doped with both perchlorate and *para*-toluenesulphonate. PEDOT-PEG is another example of an intrinsically conducting polymer consisting of extended π-conjugation along the polymer chain. Therefore, when this co-polymer is doped, its conductivity increases by several orders of magnitude. The PEG component in PEDOT-PEG serves to stabilise the colloidal dispersion of the PEDOT component, which allows non-acidic dopants and aprotic solvents to be used.

PEDOT-PEG is a neutral material and in the use of Polymer Light Emitting Diodes (PLEDs), it exhibits conductivity values of between 0.1-2 S/cm [56]. The role of the dopants can be relatively significant in terms of conductivity. For example, in the study conducted by Sapp, PEDOT-PEG showed a conductivity of 0.4 S/cm when doped with perchlorate (PC), while the PTS-doped polymer showed much lower conductivities of around 10^{-3} S/cm [55].

In terms of battery applications, PEDOT-PEG has been used as a protective layer on lithium electrodes, in order to improve cycling stability [57]. The co-polymer showed strong adhesion to the lithium electrode which suppressed corrosion of the lithium metal as well as stabilising the interface of the electrode which was in contact

with the organic electrolyte. Furthermore, the polymer coating improved capacity retention of the $Li/LiCoO_2$ cell with an increase from 9.3% to 87.3% after 200 cycles.

1.3.8 PEDOT:PSS

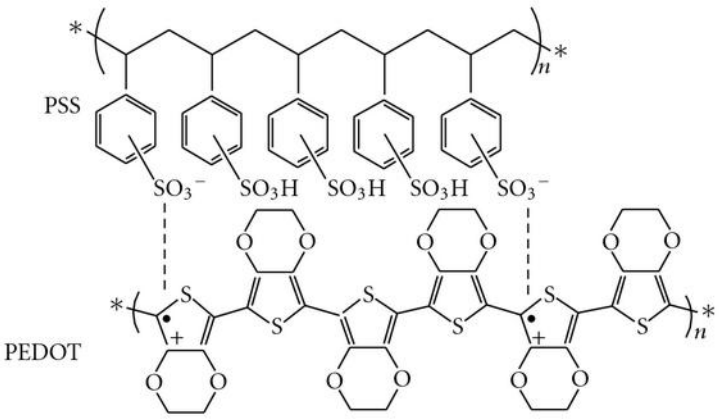

Figure 1.10: Chemical structure of PEDOT:PSS [58]

PEDOT:PSS, shown by Figure 1.10, is another copolymer that shows promise with regards to application in a non-metallic battery. In this case, the polystyrene sulphonate (PSS) component is expected to coordinate cations, much like the PEG phase in PEDOT-PEG. The SO_3^- group can attract positive lithium ions, allowing for energy storage and ionic conductivity. PSS is a polyanion, which when used as a dopant for PEDOT, it gives rise to desirable properties such as good compatibility with polar group polymers, and in turn allows good device performance when used with aqueous electrolytes [59]. In the PEDOT:PSS dispersion, the PSS chain acts as the charge-compensating counterion in excess that stabilises the positively charged PEDOT chain [60].

PEDOT:PSS, like PEDOT-PEG, has also been used in PLEDs, and is in fact one of the most widely used materials for the hole transport layer, preventing the oxidation of the light emitting materials as they interface with the emitting layer [56]. However, as polystyrene sulphonate is a strong acidic functional group, it corrodes the indium tin oxide (ITO) present in the PLED, causing a diffusion of indium into the emitting layer. This problem can somewhat be resolved by synthesising multi-layered PLEDs, using materials such a PEDOT-PEG to prevent corrosion.

In terms of conductivity values, one study in particular demonstrated a significant enhancement from 0.3 to 3065 S/cm for PEDOT:PSS films when doped with H_2SO_4 [61]. Other notable values of 1325 S/cm [62] and 1418 S/cm [63] have been quoted. These values for doped PEDOT:PSS show a significant improvement over the original conductivity, which is something to consider in terms of battery performance.

PEDOT:PSS has been used in batteries, for example as a binder and conducting additive for a carbon black free $LiFePO_4$ composite electrode [64]. It was found that composite cathodes containing 8% PEDOT:PSS showed a comparable electrode capacity along with a better cyclic stability than a conventional composite cathode. PEDOT:PSS has also been used in order to coat sulphur-activated porous graphene composite cathodes in lithium-sulphur batteries [65]. Here, the conductive PEDOT:PSS layer facilitated charge transportation and prevented dissolution of polysulfides. This composite cathode showed an improved specific discharge capacity of 1198mAh/g at a current rate of 0.1 C for the first cycle along with good cycling stability by retaining a reversible capacity of 845mAh/g after 200 cycles.

1.4 Antenna background

The antenna properties and performance of the short range systems considered here come under the topic of Microwave engineering, and it is to these Microwave systems that the antenna will be applied [66]. Microwave engineering tends to cover alternating current signal behaviour in the frequency range of 3 MHz to 300GHz. The corresponding electrical wavelength, λ, is between 10cm and 1mm respectively, when $\lambda = c/f$, where c is the speed of light and f is the frequency.

Insignificant voltage phase variation over electronic component dimensions is seen at large (sub-microwave) wavelengths. Microwave components are often described as *distributed* elements due to the fact that the voltage or current phase will progress significantly over the physical extent of the device. This is due to the dimensions of the device being in the order of the electrical wavelength.

The theory of Microwave engineering in terms of electromagnetics is described by Maxwell's equations. Maxwell's equations are complex due to their vector differential or integral operations on vector field quantities, and it is these fields which are functions of spatial coordinates. Due to this complexity, they are beyond the scope of this work. While a field theory solution will give a complete description of the electromagnetic field at each point in space, device terminal quantities such as power and impedance are more tangible and are very useful in terms of antenna performance.

A propagating electromagnetic field is best described as a flow of energy travelling through a medium and is in the form of both an electric field, E, and a magnetic field, H. The electromagnetic wave can be either vertically or horizontally polarised [8]. With vertical polarisation, the E vector is vertical. This means that a vertical polarised antenna is required to launch it. In the horizontal case, the E vector is horizontal, therefore requiring a horizontal antenna in order to launch it. It is also possible that circular polarisation may be used. This is the combination of both vertical and horizontal polarisation where a 90° phase difference between

the E vectors causes the wave front polarisation to rotate 360° in orientation for every wavelength propagated. In many cases, electromagnetic waves are vertically polarised as this enhances wave propagation over the earth's surface.

Microwave wireless transmission is popular owing to the ability of the signals to travel by line of sight, meaning they avoid being bent by the ionosphere, or ground conduction, as occurs for signals of lower frequency [66]. Various molecular, atomic and nuclear resonances occur at Microwave frequencies which affect propagation and have application in basic science and medicine. The vast majority of applications are in wireless networks and communication systems, wireless security systems, environmental remote sensors and medical systems.

When designing a suitable antenna which could be successfully integrated with a battery, an important parameter is efficiency, which is the ratio of power output to supplied input power for an antenna [66]. A good operating bandwidth is also desirable, and this is defined as the range of frequencies over which the antenna functions according to a specified criteria, which is often the quality of the input impedance match. Signal bandwidth is expressed as a fraction of the centre, or carrier frequency. Therefore, high frequency microwave signals have the advantage of offering large bandwidths. The specific antenna properties under investigation will be explained in greater detail in Chapter 2.

What needs to be determined in this study is the type and design of the antenna. For this antenna to be useful, it must be able to offer a good bandwidth, meaning it can be used over a range of frequencies, along with usable efficiency for certain applications. There is no specific application for the prototype integrated system at this stage. However, a wider bandwidth will allow a wider range of applications to be possible. Antenna efficiency is important to ensure that significant power loss is not occurring in the system. Different antenna types offer different properties affecting their suitability for battery integration and microwave transmission. Various candidates will be considered in Section 1.4.1 and Section 1.4.2.

1.4.1 Microstrip patch antennas

A microstrip patch antenna is one in which a conductor of a certain resonant length is printed onto a thin, dielectric substrate containing a ground plane. With advances in wireless communication systems in terms of compact device size and broadband operations, microstrip patch antennas are of increasing interest [67]. These types of antenna are low-profile, lightweight, compact, able to be mass produced and easy to integrate with an electronic system [68, 69, 70]. Furthermore, these antennas can be designed with the characteristics of other types of antenna, namely, circularly polarised radiation and multiband operations i.e. the frequency bands at which antennas operate [68]. An example of a microstrip patch antenna is shown in Figure 1.11.

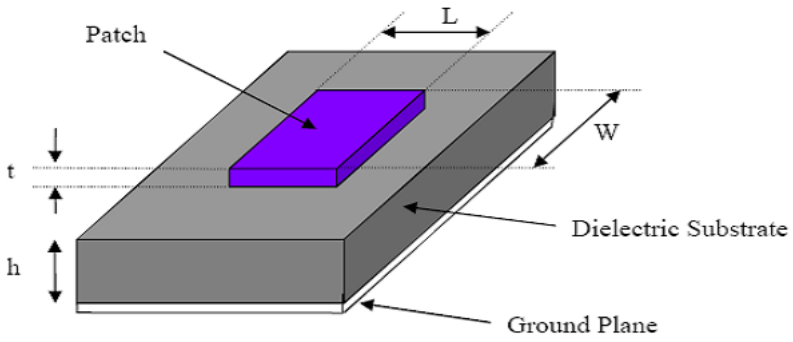

Figure 1.11: Typical microstrip patch antenna [71]

In their most basic form, these antennas consist of a flat plate over a ground plane [72]. The antenna itself is usually built from printed circuit board material, with the antenna substrate acting as the dielectric. The bandwidth for patch antennas can be determined by the distance between the patch and ground plane, therefore being controlled by the height of the substrate and its dielectric constant. In many cases, the patches are rectangular or square in shape, although sometimes, they can be other shapes such as circular.

Studies on microstrip antennas have recently focused on improving bandwidth as well as designing to operate at multiple bands with one study in particular achieving a fractional bandwidth of 95% in terms of voltage standing wave ratio (VSWR)[73]. VSWR is the measure of the mismatch of a transmission line. Other studies demonstrate dual-band operations for antennas of this type [74].

Microstrip patches radiate due to having parallel and co-phased horizontal E-fields present at each edge. On the contrary, the vertical fields will not radiate since they are in the opposite direction and sum to zero in the radiated field. Figure 1.12 shows how the fields lead to radiation in the microstrip patch.

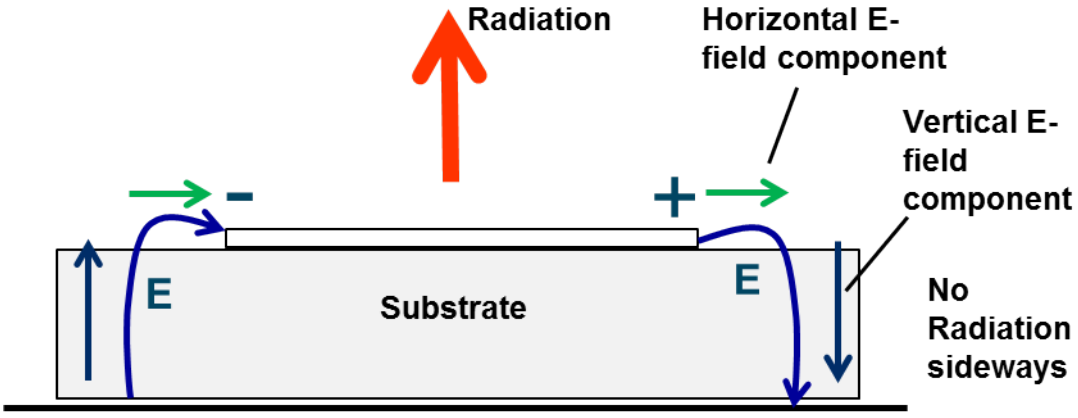

Figure 1.12: Process of radiation due to E-fields in microstrip patch antenna

Due to their low-profile structure and ease of installation in electronic systems, microstrip patch antennas provide one possibility for the proposed antenna-battery

design. Referring back to Figure 1.2, a microstrip patch could in theory rest on top of a battery substrate, with a ground plane underneath. However, it is known that patch antennas are at their most efficient on a thick dielectric that has a low relative permittivity value. We are looking at an ultra-thin integrated system which maintains usable efficiencies. Furthermore, it is likely that the battery substrate may have a greater permittivity than that which would ensure optimal performance for a microstrip patch.

Due to the limitations caused by the dielectric substrate mentioned previously, single layer microstrip patch antennas will generally have narrow bandwidths, with enhancement being necessary for many applications [67]. In the case of [73], though a bandwidth of 95% could be achieved, the patch was suspended over the ground plane and supported with a non-conductive pin. This configuration would be impractical for an ultra-thin low-profile integrated system such as the one proposed. Also, the electrical losses associated with the battery electrolyte material would mean it would be an inefficient substrate for a microstrip patch.

1.4.2 Slot antennas

In the case where an ultra-thin antenna is desired, and particularly where the intention might be to mount on a structure which has a very high permittivity, a slot antenna becomes a viable option. Slot antennas often are in the form of a slot dipole, which is the complement of a normal dipole. A dipole in this case is a centre-fed linear antenna that has a length, L [9]. One of the most common types of dipole antennas is the *halfwave dipole*, defined with length, $L = \lambda/2$, shown in Figure 1.13.

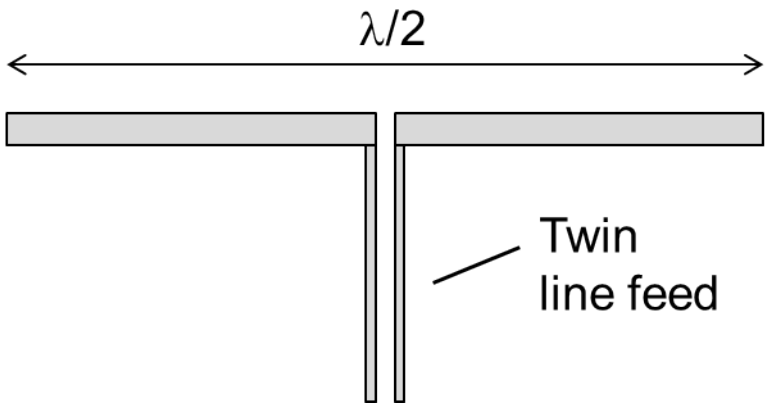

Figure 1.13: An example of a halfwave dipole

In the case of a slot antenna, it is an opening cut in a sheet of conductor such as copper [9]. It comes under the general term of aperture antennas. The antenna is energised, for example, via a waveguide. A typical slot dipole may be half a wavelength long, such as that shown in Figure 1.14

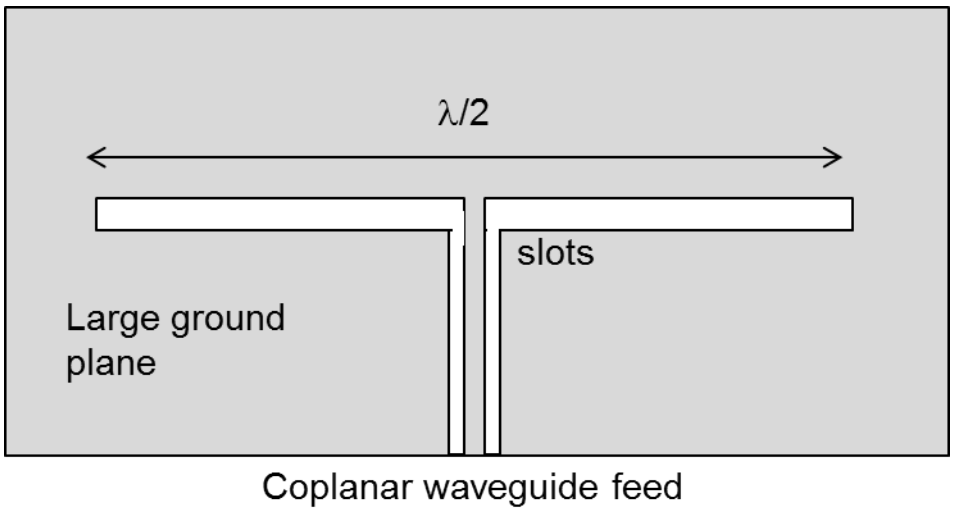

Figure 1.14: An example of a halfwave slot dipole

In terms of radiation, a horizontal slot will produce vertical polarisation in the direction that is normal to the slot, while a vertical slot will produce horizontal polarisation. Radiation can occur from both faces of the conducting sheet. Figure 1.15 shows a simplified depiction of the E and H fields around the slot. These fields give rise to the radiated fields.

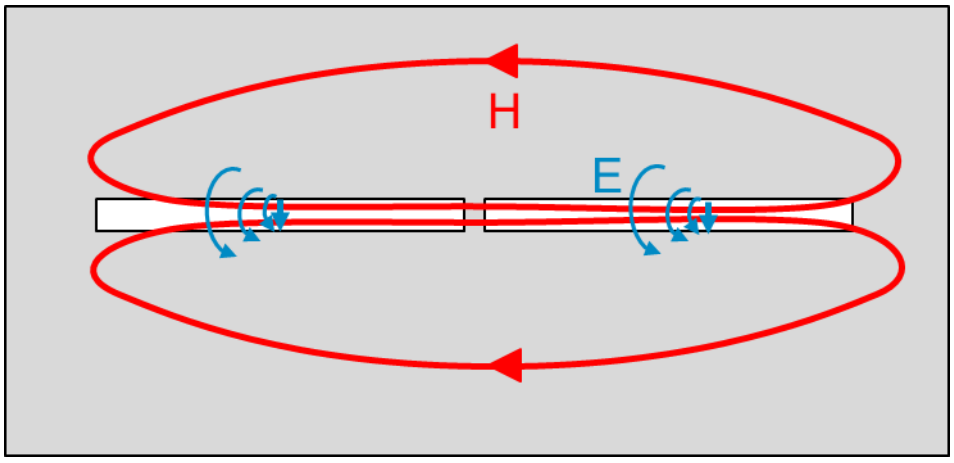

Figure 1.15: H and E fields in a slot dipole

In order for radiation to occur, an electric field stimulus should be placed across the slot aperture [75]. This then allows the magnetic field to be partially aligned along the slot edge. If the width of the slot is significantly less than a wavelength, then the long edges of the slot will carry equal and opposite current meaning that only the E-fields across the slot width will exist. At half a wavelength, the currents at the short edges of the slot are in phase, however, they do not radiate efficiently as they are immediately adjacent to the conductor. At a certain distance from the narrow slot edges, the vertical components of the E field will reinforce, which results in far-field radiation. The ground plane ideally should be at least one wavelength larger than the slot.

Slot antennas offer the advantage over microstrip patch antennas of having wide bandwidth, and good impedance matching is possible with appropriate techniques [76]. Research has demonstrated that in one case, several slot antennas consisting of a slot dipole, a coplanar patch-slot (CPA) and bow-tie design were able to attain bandwidth values of 17-40% [77]. A coplanar patch-slot is where the antenna consists of a rectangular patch surrounded by a non-uniform width slot. Another study shows how the bandwidth of a Coplanar Waveguide (CPW) slot antenna can be improved by altering the slot dimensions, with an asymmetric configuration yielding the biggest improvement [78]. This was for the purpose of designing an antenna suitable for use in Wireless Local Area Network (WLAN) applications. A coplanar waveguide is the feeding in which the side-plane conductor is ground and the centre strip carries the signal. Figure 1.16 shows the typical geometry for a coplanar patch-slot, bow-tie slot and coplanar waveguide antenna.

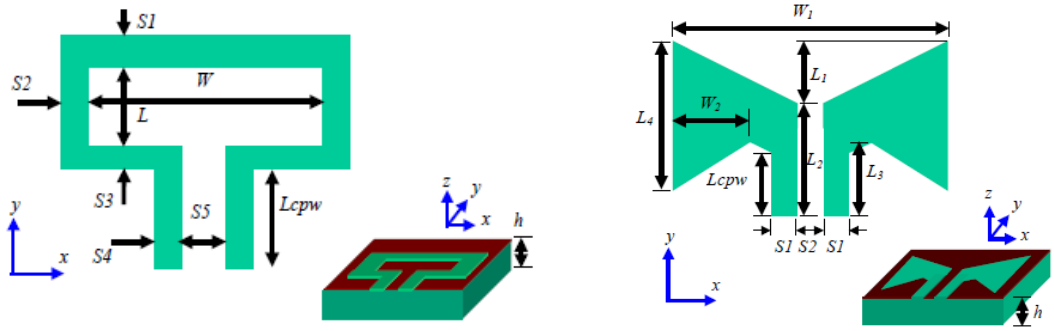

(a) (b)

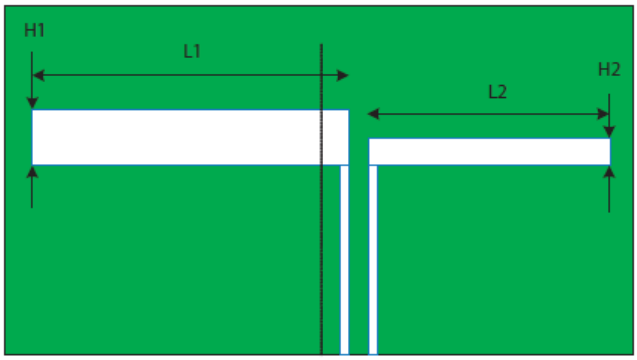

(c)

Figure 1.16: (a) Coplanar patch slot (CPA) [77], (b) bow-tie slot [77] and (c) coplanar waveguide (CPW) slot antenna [78]. For (a) and (b), the slots are represented in green, while for (c), the slots are shown in white

1.4.3 Electrical impedance

In typical electrical circuits, charges will be stored on a capacitor, which will consist of a pair of conductors [79]. The energy stored by a capacitor can be expressed as

capacitance, C, and is dependant upon the geometry of the conductors. One of the simplest examples is the parallel plate capacitor. Here, two plates of an area, A, are separated by a distance, d, which represents the insulating dielectric material. Figure 1.17 gives a visual representation of the standard parallel plate capacitor.

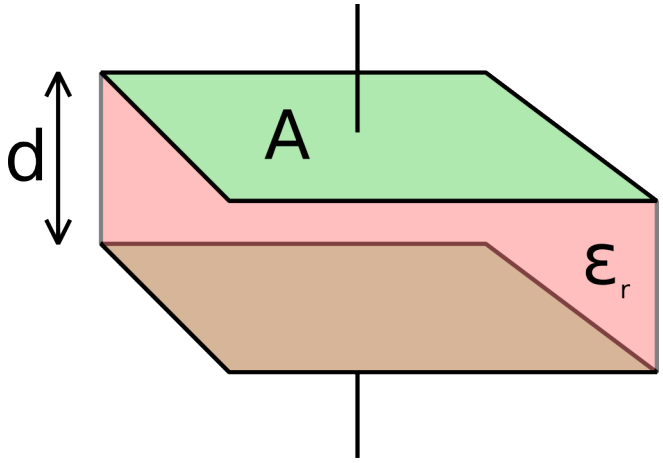

Figure 1.17: The parallel plate capacitor

In a quantitive sense, the capacitance can be expressed by Equation (1.3).

$$C = \varepsilon_r \varepsilon_0 \frac{A}{d} \tag{1.3}$$

Here, ε_r represents the relative permittivity of the dielectric material between the plates (also known as the dielectric constant), while ε_0 is the electric constant (8.85×10^{-12}F/m). Capacitance is typically quoted in units of Farads, F. It is directly proportional to the area of the conducting plates, and inversely proportional to the height of the dielectric. Therefore, the closer the two plates are together, the greater the capacitance.

In terms of A.C. circuits, the idea of impedance becomes important. Impedance in itself is used to describe the complex ratio of voltage to current in A.C. circuits [66]. The impedance of the capacitor, Z_C, can be related to both capacitance and frequency, by Equation (1.4) [79].

$$Z_C = \frac{1}{\omega j C} = \frac{1}{2\pi f j C} \tag{1.4}$$

j is the imaginary unit, where $j^2 = -1$. At low frequencies, the impedance value for a capacitor will be large. Meanwhile, for high frequencies, Z_C becomes small, and therefore the capacitors will exhibit a low impedance to the alternating current flow.

1.5 Summary

For the rest of this study, PEDOT-PEG will be used as the model system. PEDOT is known to be a good electrical conductor, while PEG is seen as the model system for ionic conductors. Therefore, it will be of interest to assess the properties of this co-block polymer in terms of mixed electrical/ionic conductivity. With PEG having been studied extensively in terms of ionic conductivity, it will be of interest to observe how the co-polymer PEDOT-PEG compares to previous research, both experimentally and computationally.

In terms of the antenna, the decision has been made to investigate the slot antenna for our proposed integrated design. This is due to the advantages it holds over microstrip patches in terms of bandwidth and impedance matching. Furthermore, slot antennas are more suitable for thinner designs such as the one proposed. In addition, with slot antennas being more suited for mounting onto materials of potential high dielectric constants, this makes it a better option overall than the microstrip patch. Therefore, if we refer back to Figure 1.2, our design is expected to be a solid state battery, with a slot dipole on top. Research will be conducted in order to design a slot antenna of suitable dimensions which shows reasonable bandwidth and efficiency for short range communications.

Chapter 2

Methodology

2.1 Introduction to atomistic simulations

So why are we looking towards computer modelling? Scientists look to computer simulations due to the financial and time constraints associated with laboratory trials. Theoretical chemistry can provide fundamental insights as well as allowing studies on materials that are either difficult or dangerous to capture in situ, for example, radiation damage due to long time scales and elevated pressures as they are difficult to achieve and interpret experimentally.

Computer simulations can be performed at a multitude of different scales. This refers to the broad space-time scale of interest, which can span several orders of magnitude [80]. The scales can range from nm (atomic scale) to mm, and ps to minutes, respectively. When considering computer simulations, one must select the scale that is most appropriate for the system and properties of interest. The most suitable scale is selected based on what best fits the order of magnitude in the space-time scale of interest. The accuracy and the time it takes to perform the calculations depend on the chosen scale. Atomistic simulations based on solving the Schrödinger equation are the most accurate, but computationally are more expensive than for example, interatomic potential simulations. The least accurate are finite element methods which are applied to large space and time scales. Figure 2.1 shows how these different simulation methods link together.

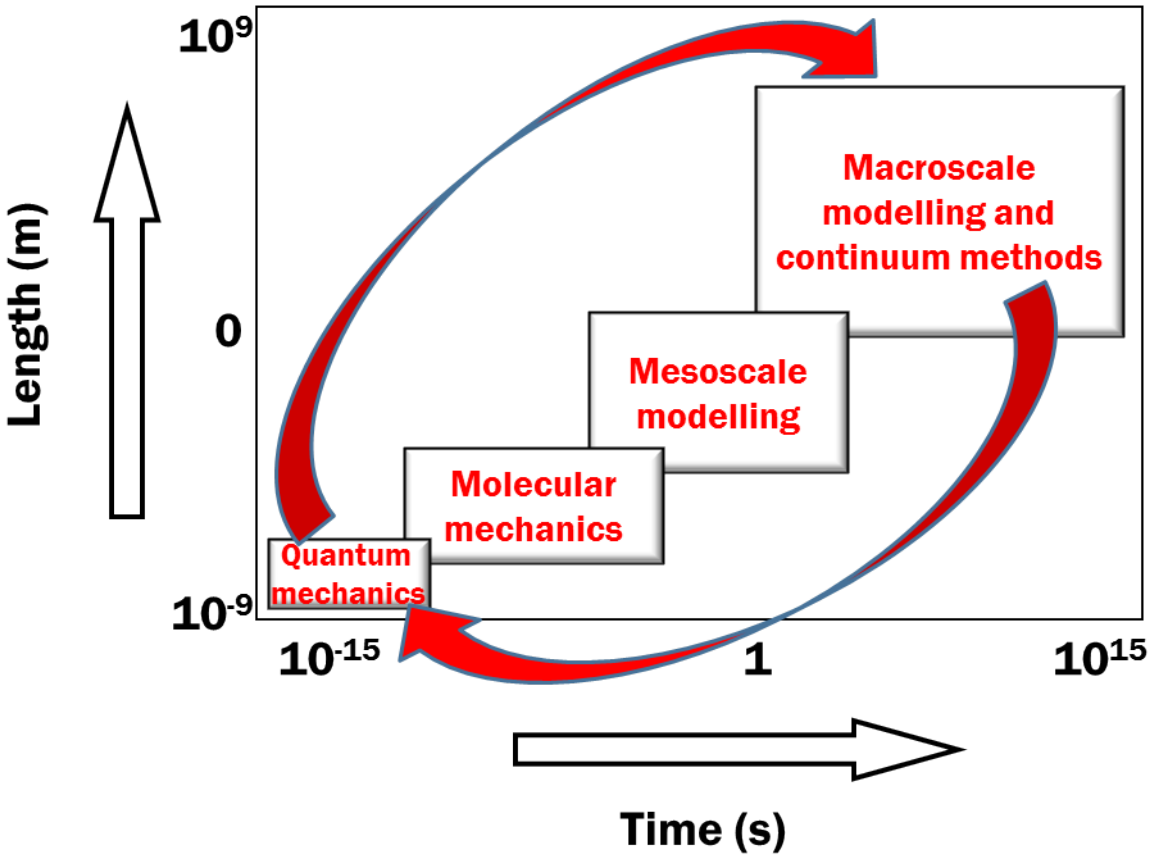

Figure 2.1: Different areas of computational modelling compared with time frame and simulation size

As we go down the scale, the system sizes become smaller along with the timescale for which the simulations take place in. For each scale, different laws and methods apply. At the macroscale, macroscopic conservation laws are important [81]. The mesoscale employs methods such as mean field methods, and the Lattice-Boltzmann method. Interatomic based Molecular dynamics (MD) tend to be used at the molecular scale. For quantum mechanical methods (atomic scale), density-functional theory (DFT) and/or Hartree-Fock (HF) methods are commonly used.

In relation to this project, the quantum mechanical methods link in with the macroscale simulations. In order to simulate and investigate the performance of polymer electrolytes, computational modelling is useful [81]. In this project, modelling has been employed to polymer electrolytes in order to screen potential materials for battery applications. The calculations for the polymer electrolyte can be performed using atomistic and molecular calculations, while simulations for the antenna are performed at the macroscale. Information obtained using quantum mechanics, in particular, the data about the substrate permittivity and conductivity, can then be fed into the antenna simulations. This can help maximise the properties of polymer electrolytes functioning in the presence of antennas and vice versa. In turn, using macroscale simulations, information about the most appropriate parameters to use for the substrate can be obtained, and if necessary, fed back to the

polymer electrolyte simulations that employ quantum mechanical methods.

2.2 Quantum Mechanical simulations

The usefulness and importance of computational simulations is somewhat restrained by the computing power available to us. However, as recent years have seen vast improvements in computer power, computational methods have greatly benefited as a result. It has been claimed that since the beginning of the 50s, the power of computers has in fact doubled every 2 years, and nowadays doubles every year [80]. This has lead to a big increase in the number of programs available to us, and the number of applications that are being pursued. Nowadays, simulations provide a vital tool in applying scientific theory to chemical and physical systems. Simulators are also allowing us to design electronic structures and assess their performance based on specific parameters. Computational chemistry will essentially provide a prediction of specific properties, which can be very useful as either a starting point to a study, or as a complementary technique alongside experiments.

One such program that is of strong focus to this study is the CRYSTAL09 code. CRYSTAL is a general-purpose program that is mainly utilised for studying the solid state [82]. The program calculates the electronic structure of periodic systems that are within either Hartree Fock, density functional or hybrid approximations. Therefore, this makes it a Quantum Mechanical tool in terms of the space-time scale. Using CRYSTAL, many physical and chemical properties can be studied for molecules, polymers, surfaces and crystalline solids (up to three dimensions). These properties include structural features, vibrational properties and dielectric properties amongst other information.

CRYSTAL uses ab initio calculations in order to investigate ground state energy, energy gradient, electronic wave function and properties of the systems. Ab initio calculations are a form of electronic structure methods, which are based on the laws of quantum mechanics as opposed to classical physics [83]. The laws of quantum mechanics state that specific properties of a molecule, in particular the energy, can be obtained by solving the Schrödinger equation. The time-independent, non-relativistic equation is defined by Equation (2.1).

$$\hat{\mathrm{H}}\Psi(\mathbf{R},\mathbf{r}) = \mathrm{E}\Psi(\mathbf{R},\mathbf{r}) \tag{2.1}$$

In this equation, $\hat{\mathrm{H}}$ is the Hamiltonian operator for a many particle system. Ψ is the wave function and contains all the information that can be derived from the quantum system described. E is the numerical value of the energy of the state that is being described by the wave function [84].

Electronic structure methods generally use mathematical approximations [83]. Ab initio methods in particular, do not use any experimental parameters for their

calculations, instead, basing them entirely upon the laws of quantum mechanics. They compute solutions to the Schrödinger equation via a series of mathematical approximations, as described below. As a result, ab initio methods can provide quantitive predictions that are considered to be of high quality, for a range of different systems.

With the CRYSTAL09 package, you are given a choice of using either the Hartree-Fock or Kohn-Sham Hamiltonians [82]. The Kohn-Sham Hamiltonian adopts an Exchange-Correlation potential that follows the postulates of Density-Functional theory.

2.2.1 The Schrödinger equation - a brief overview of quantum chemistry

For the majority of quantum chemical approaches, the ultimate aim is the approximate solution of the Schrödinger equation [84]. $\hat{\mathrm{H}}$, the Hamiltonian operator for a many particle system, will consist of M nuclei and N electrons that are in the absence of either magnetic or electric fields. $\hat{\mathrm{H}}$ is representative of the total energy. This equation cannot be solved exactly but approximations are introduced.

The simplest way to look at the equation is to observe the differences between the masses of nuclei and electrons in atoms. In the most basic case of hydrogen, ^{1}H, the proton still weighs around 1800 times more than an electron. This ratio is further increased for larger atoms. The obvious deduction from all of this is that the nuclei will move considerably slower than the electrons. This lends itself to the well-known *Born-Oppenheimer approximation*. The main considerations of this approximation are that the electrons are perceived to be moving in a field of fixed nuclei.

This approximation means that the wave function, $\Psi(\mathbf{R}, \mathbf{r})$, can be factorised into two independent terms: a) A nuclear term, $\Phi(\mathbf{R})$, and b) an electronic term, $\varphi_R(\mathbf{r})$, where nuclei are fixed at their equilibrium positions and electrons move freely [80]. Based on this approximation, the Schrödinger equation can be expressed by Equation (2.2).

$$\Psi(\mathbf{R}, \mathbf{r}) = \Phi(\mathbf{R})\varphi_R(\mathbf{r}) \tag{2.2}$$

For a set of electrons that are moving in the field of a nuclei set, it is intended to find the lowest energy configuration of the electrons [85]. This lowest energy state is the ground state of the electrons. By having M nuclei situated at positions $\mathbf{R}_1, ..., \mathbf{R}_M$, it is possible to express the ground-state energy, E, as a function of the positions of these nuclei, $E(\mathbf{R}_1, ..., \mathbf{R}_M)$. This function is known as the *adiabatic potential energy surface* of the atoms.

With the Schrödinger equation, the Hamiltonian is defined based upon the phys-

ical system that the equation is describing. Perhaps the most famous examples are the particle in a box and the harmonic oscillator, in which the Hamiltonian is simple, allowing for the equation to solved exactly. For a system containing more than two particles, the Schrödinger equation cannot be solved exactly. We are interested in multiple electrons that are interacting with multiple nuclei. This leads to a far more complete description of the Schrödinger equation which is shown in Equation (2.3).

$$\left[-\frac{h^2}{2m}\sum_{i=1}^{N}\nabla_i^2+\sum_{i=1}^{N}V(\mathbf{r}_i)+\sum_{i=1}^{N}\sum_{j<i}U(\mathbf{r}_i,\mathbf{r}_j)\right]\Psi=E\Psi \tag{2.3}$$

In this case, m represents the mass of the electrons. The three terms present in the brackets represent the kinetic energy of the system, the interaction energy between each electron along with the collection of atomic nuclei, and the interaction energy between two separate electrons, all in order. In this case, Ψ is the electronic wave function, which is representative of the spatial coordinates for every one of the N electrons. This means that $\Psi = \Psi(\mathbf{r}_1, ..., \mathbf{r}_N)$, while E is the time-independent ground state energy. However, it is also feasible to approximate Ψ as a product of individual wave functions, so that $\Psi = \Psi_1(\mathbf{r})\Psi_2(\mathbf{r}), ..., \Psi_N(\mathbf{r})$. It is desirable to approximate the full wave function in this manner for certain reasons, in particular, due to the number of electrons far outweighing the number of nuclei as the computational time increases exponentially with the number of particles. The full wave functions would lead to a large number of dimensions in for example, single molecules, which is why it becomes practical to take the individual one-electron wave function approach.

The Schrödinger equation is considered to be a many-body problem. This is due to the fact that in order to find the individual electron wave function defined above, the individual electron wave functions associated with each of the other electrons must all be considered simultaneously. This is essential for defining the term in the Hamiltonian that considers electron-electron interactions, which in turn makes it vital for solving the equation. Despite the Schrödinger equation being at the forefront of quantum mechanics, it is important to realise that the wave function for a certain set of coordinates is not something that can be observed directly. The measured quantity in this case is in fact the probability that the electrons being considered will be present at a particular location defined by coordinates, $\mathbf{r}_1, ..., \mathbf{r}_N$. This can be expressed as $\Psi^*(\mathbf{r}_1, ..., \mathbf{r}_N)\Psi(\mathbf{r}_1, ..., \mathbf{r}_N)$. The asterisk here represents a complex conjugate.

As the many-body problem cannot be solved exactly, approximations need to be introduced. The areas discussed below are the Hartree-Fock (HF) and density functional theory (DFT) approximations.

2.2.2 Hartree-Fock approximation

The first of these mathematical approximations to be looked at is the Hartree-Fock method. The Hartree-Fock (HF) approximation is considered to be the corner stone of most conventional wave function based quantum methods and is considered of great importance conceptually [84]. The HF scheme employs the simplest approximation to the many-electron wave function described above. The basic principle is that it approximates the N-electron wave function via an antisymmetrised product of N one-electron wave functions. The product in this case is commonly known as the *Slater determinant* (Φ_{SD}). The basic principle of an antisymmetrised product is that it treats electrons as indistinguishable, while a simple product as a wave function for fermions assigns a specific one electron function to a specific electron, violating the fact they are indistinguishable.

The Hartree-Fock approximation is based on the assumption that the N-electron wave function can actually be replaced by a single Slater determinant. Therefore, it is in the best interests to derive the best Slater determinant, using what is known as the Variational Principle. This principle involves systematically approaching the wave function of the ground state, Ψ_0, which is a state delivering the lowest energy, E_0. This approach is known as the Self-Consistent Field procedure. The drawback for a Slater determinant, however, is that flexibility is only provided by spin orbitals. The spin orbitals in this case are varied under the constraint in which they are orthonormal, meaning that the energy for the corresponding Slater determinant is minimal.

The self-consistent field is based on the variational principles and applied to both HF and DFT methods. The basis of the SCF procedure is that it begins with an approximated set of atomic orbital coefficients whereby the HF equations are solved. The new set of atomic orbitals generated from this are fed into the next iteration and this process continues until the energy or calculated density differs by less than a certain threshold that is predetermined. In many cases, particularly with the CRYSTAL09 code, a finite basis set is introduced in order to expand the molecular orbitals.

It should noted that in the Hartree-Fock approximation, the electron will interact with the average potential which is created by all of the other electrons in the system [86]. This means that HF methods will give the exact exchange term, since we can find the exact one-electron Hamiltonian of the system. However, despite this, the HF energy will not be exact from this approximation since the instantaneous correlation in the electronic motions is underestimated. This is due to a missing contribution known as the electron correlation. The fundamental theory behind electron exchange and correlation will be discussed in more detail in Section 2.2.4.

2.2.3 Density Functional Theory

Kohn-Sham density functional theory is regarded as one of the most well-known and used methods in electronic structure calculations for condensed matter physics and quantum chemistry [87, 88]. While there are similarities between both Hartree-Fock and DFT approximations, there are differences which separate them and the way in which they perform calculations. Both techniques consider single-electron functions. However, while HF theory calculates the full N-electron wave function, DFT only calculates the total electronic energy, based on the overall distribution of the electron density [89]. DFT in fact draws on basic elements from the Thomas-Fermi model, which was developed in the late 1920s. The foundation was established thanks to a study from Hohenberg and Kohn in 1964 [90] demonstrating that the ground state energy along with other properties were defined uniquely by the electron density, $\rho(\mathbf{r})$. To express this, the energy, E, was described as a unique functional of $\rho(\mathbf{r})$. A functional, which is usually written using square brackets, allows a function to be mapped to a number. The energy functional itself can be written as a sum of two terms shown in Equation (2.4).

$$E[\rho(\mathbf{r})] = \int V_{ext}(\mathbf{r})\rho(\mathbf{r})d\mathbf{r} + F[\rho(\mathbf{r})] \tag{2.4}$$

Here, the first term is due to the interaction of an external potential, $V_{ext}(\mathbf{r})$, with the electrons, while $F[\rho(\mathbf{r})]$ is the sum of both the contribution of interelectronic interactions and the kinetic energy of the electrons. The minimum energy is corresponding to the ground-state of the electron density, allowing a variational approach to be used. The electron density itself is constrained by the number of electrons which is in turn fixed. The DFT equivalent of the Schrödinger equation is defined in Equation (2.5).

$$\left(\frac{\delta E[\rho(\mathbf{r})]}{\delta\rho(\mathbf{r})}\right)_{V_{ext}} = \mu \tag{2.5}$$

Where the subscript, V_{ext}, shows that fixed nuclear positions are enforced. The Lagrange multiplier, μ, relates to the chemical potential of an electron cloud for its nuclei, which can then be related to the electronegativity. The next breakthrough in DFT was made by Kohn and Sham [87], who suggested that the function, $F[\rho(\mathbf{r})]$, defined in Equation (2.6) can be approximated as the sum of three terms.

$$F[\rho(\mathbf{r})] = E_{KE}[\rho(\mathbf{r})] + E_H[\rho(\mathbf{r})] + E_{XC}[\rho(\mathbf{r})] \tag{2.6}$$

Here, E_{KE} is the kinetic energy, E_H is the electron-electron Coulombic energy while E_{XC} is the contribution from both exchange and correlation (as discussed in Section 2.2.4). E_{KE} specifically refers to the kinetic energy of a particular system of non-interacting electrons that possess the same density, $\rho(\mathbf{r})$, as the real system

under analysis. E_H is also referred to as the Hartree electrostatic energy. In this instance for the Hartree approach, the electrostatic energy arises from the interaction between two charge densities. All of these terms can be combined and expanded to form the Kohn-Sham scheme. In order for the Kohn-Sham equations to be solved, a self-consistent method is used. This can be summarised by feeding in a density value, from which a set of DFT orbitals can be derived. In turn, an improved value for the density is obtained. This new value is used in the second iteration and the process is repeated until the system is converged.

2.2.4 DFT: The Exchange Correlation Functional

One of the most important features when it comes to the success of DFT, is the exchange-correlation functional [89]. This is particularly true as HF is missing the correlation term. It is highly desirable for many reasons, for example, simple approximations to this functional can still yield improved results compared to HF. The simplest form of utilising this contribution is to use the *local density approximation* (LDA). This is based upon a model known as the uniform electron gas, whereby the electron density is constant throughout all space. By integrating over all space, the total exchange-correlation energy, E_{XC}, can be obtained, as shown in Equation (2.7).

$$E_{XC}[\rho(\mathbf{r})] = \int \rho(\mathbf{r})\varepsilon_{XC}(\rho(\mathbf{r}))d\mathbf{r} \tag{2.7}$$

In this case, $\varepsilon_{XC}(\rho(\mathbf{r}))$ describes the exchange-correlation energy per electron as a function of density, in the uniform electron gas. The LDA method gained special success in metals but failed to describe anisotropic systems satisfactorily.

It is common to consider exchange and correlation contributions separately when an analytical approach is used. For example, in LDA, Equation (2.8) [91] is used for the exchange-only energy.

$$E_X[\rho_\alpha(\mathbf{r}), \rho_\beta(\mathbf{r})] = -\frac{3}{2}\left(\frac{3}{4\pi}\right)^{1/3} \int (\rho_\alpha^{4/3}(\mathbf{r}) + \rho_\beta^{4/3}(\mathbf{r}))d\mathbf{r} \tag{2.8}$$

Here, α and β are representative of the up and down spins in the system. While this is considered a relatively simple expression, more focus has been paid to the correlation contribution due to the fact that it does not have a simple functional form. Perdew and Zunger [92] came up with a parametric relationship for the correlation contribution, as shown by Equation (2.9).

$$\varepsilon_C(\rho(\mathbf{r})) = \begin{cases} -0.1423/(1 + 1.9529{r_s}^{1/2} + 0.3334r_s) & r_s \geq 1 \\ -0.0480 + 0.0311\ln r_s - 0.0116r_s + 0.0020r_s\ln r_s & r_s < 1 \end{cases} \tag{2.9}$$

Here, r_s is the parameter for the density [93]. Specifically, it is the Wigner-sphere radius given in units of Bohr radii. This equation is applicable in the case where both the number of up spins and down spins are equal, therefore, meaning it does not apply to any system with an odd number of electrons. The correlation energy functional was also described by Vosko, Wilk and Nusair [94], who came up with the following solution in Equation (2.10).

$$\begin{aligned} \varepsilon_C(\rho(\mathbf{r})) = \frac{A}{2}\left\{\ln\frac{x^2}{X(x)} + \frac{2b}{Q}\tan^{-1}\frac{Q}{2x+b} - \frac{bx_0}{X(x_0)}\left[\ln\frac{(x-x_0)^2}{X(x)} + \frac{2(b+2x_0)}{Q}\tan^{-1}\frac{Q}{2x+b}\right]\right\} \\ x = {r_s}^{1/2}, \quad X(x) = x^2 + bx + c, \quad Q = (4c - b^2)^{1/2}; \\ A = 0.0621814, \quad x_0 = -0.409286, \quad b = 13.0720, \quad c = 42.7198 \end{aligned} \tag{2.10}$$

LDA is not the only functional that is employed in DFT calculations. LDA enables us to completely define the Kohn-Sham equations, although the results obtained from the equations do not solve the true Schrödinger equation [85]. This is because the exchange-correlation functional being used is not considered to be the true functional. One of the most well known functionals after LDA is the approach in which information is used about the local electron density and local gradient within the electron density - the generalised gradient approximation (GGA). The E_{XC} energy term can be improved by adding terms which depend on the gradient of the density, as shown in Equation (2.11) [86].

$$E_{XC} = E_{XC}[\rho, \nabla\rho] \tag{2.11}$$

There are a variety of distinct GGA functionals since there are a multitude of ways in which information from the gradient of electron density can be included. Prime examples for solids are the Perdew-Wang (PWGGA) [95, 96, 97, 98], Perdew-Burke-Ernzerhof (PBE) [99], and BLYP [100, 101] functionals. The latter one being employed to acetylene in this thesis. Also, the hybrid functional (see Section 2.2.5), B3LYP [102], is a GGA based functional.

2.2.5 Hybrid Methods: Hartree-Fock/DFT

As discussed previously, both Hartree-Fock and density functional theory employ different approaches to computational systems. DFT methods will incorporate correlation effects at the start, something not offered by Hartree-Fock [89]. However, Hartree-Fock will give an exact means of describing the exchange contribution, obtained from the Slater determinant of the Kohn-Sham orbitals. The idea of adding a correlation energy that is derived from DFT to the Hartree-Fock energy was earlier discussed by Becke. In this case, the correlation component derived from DFT (e.g. the local density approximation) is added to the exact exchange term from

Hartree-Fock. This approach, however, had shortfalls despite much promise.

Becke came up with a strategy that had a lot more promise [102, 103]. He suggested that the exchange-correlation energy be written in the form shown in Equation (2.12).

$$E_{XC} = \int_0^1 U_{XC}^{\lambda} d\lambda \tag{2.12}$$

λ is a coupling parameter with values ranging from 0 to 1. In the case where λ is zero, there is no coulomb repulsion (U_{XC}) between the electrons. Coulomb repulsion can be increased up until $\lambda = 1$, at which point this describes the 'real' system where full interactions are occurring. In each case, the electron density will equal the density of the real system. Through linear interpolation (performed as it is unpractical for integration analytically), we have the following expression shown by Equation (2.13).

$$E_{XC} = \frac{1}{2}(U_{XC}^0 + U_{XC}^1) \tag{2.13}$$

In this case, U_{XC}^0 refers to the exchange-correlation potential energy of the non-interacting reference system. When $\lambda = 0$ and there are no electronic interactions in the system, the correlation term disappears, therefore U_{XC}^0 is the pure exchange energy of the Kohn-Sham determinant. This allows it to be determined exactly. U_{XC}^1 describes the exchange-correlation potential energy of the full-interacting real system. Becke suggested this term to be calculated via the local spin-density approximation, meaning it can be expressed by Equation (2.14).

$$U_{XC}^1 \approx U_{XC}^{LSDA} = \int u_{XC}[\rho_\alpha(\mathbf{r}), \rho_\beta(\mathbf{r})] d\mathbf{r} \tag{2.14}$$

u_{XC} describes the exchange-correlation potential energy of the density for an electron gas. Despite appearing to be a much better method than previous ideas of mixing exchange and correlation energies, Becke realised that his own approach also had a shortfall, when $\lambda = 0$. The electron gas model was not suitable near the described exchange-only limit when it came to bonds between molecules. To combat this, Becke eliminated the U_{XC}^0 term, and wrote the exchange-correlation energy as shown in Equation (2.15).

$$E_{XC} = E_{XC}^{LSDA} + a_0(E_X^{exact} - E_X^{LSDA}) + a_X \Delta E_X^{GC} + a_c \Delta E_C^{GC} \tag{2.15}$$

Here, E_X^{exact} describes the exact exchange energy (which is obtained from the Slater determinant of the Kohn-sham orbitals), E_X^{LSDA} refers to the exchange energy under the local spin density approximation, ΔE_X^{GC} and ΔE_C^{GC} are the gradient correction terms for the exchange and correlation respectively. a_0, a_X and a_C are empirical coefficients that are obtained by least-squares fitting to the experimental

data consisting of a total of 56 atomisation energies, 42 ionisation potentials, 8 proton affinities and the total atomic energies for the ten first row elements. Becke's initial study on hybrid methods featured his own gradient correction for the exchange term, along with Perdew and Wang's gradient correction for correlation. Becke came up with the idea of using the Lee-Yang-Parr (LYP) [101] correlation functional, as well as the local correlation functional suggested by Vosko, Wilk and Nusair (VWN) [94]. Becke named this the B3LYP density functional [102], which is now commonly used in the field of ab initio simulations. The functional is expressed by Equation (2.16).

$$E_{XC}^{B3LYP} = (1-a_0)E_X^{LSDA} + a_0 E_X^{HF} + a_X \Delta E_X^{B88} + a_C E_C^{LYP} + (1-a_c)E_C^{VWN} \quad (2.16)$$

Based on Becke's fitting to experimental data, he proposed a mixing of 20% HF with 80% Becke (DFT) exchange, which is applied in the B3LYP functional.

2.2.6 Basis Sets

The approach in the CRYSTAL code is based on the use of basis sets comprised of a series of atomic Gaussian functions. Basis functions in solid state codes such as CRYSTAL are ultimately Bloch functions, which have been modulated over the infinite lattice [82]. Basis sets can often be the most common source of approximation with regards to quantum mechanical simulations. Generally, the larger the basis set, the more accurate the calculation. On the other hand, many crystalline systems are densely packed, which can give rise to a large overlap between basis functions. As a result, a quasi-linear dependance may occur, often down to numerical limitations, forcing the size of the basis set to be reduced. Then again, the large overlap of orbitals in the solid state do allow a reduction of the basis set, but the choice of basis set will have a significant bearing on the results and needs thorough testing on suitable model systems.

Slater-type-orbitals (STO) would have been considered a good choice to begin with, but they are not easily implemented in molecular orbital calculations [89]. This is due to some of the integrals being either difficult or impossible to evaluate when atomic orbitals are centred on different nuclei. Therefore, in many ab initio calculations, the Slater orbitals are replaced by functions which are based upon Gaussians. In many approaches, the basis set is chosen to consist of *Gaussian-type-orbitals*, GTOs, that take the general form shown in Equation (2.17) [84].

$$\eta^{\mathrm{GTO}} = \mathrm{N}\, \mathrm{x}^{\mathrm{l}} \mathrm{y}^{\mathrm{m}} \mathrm{z}^{\mathrm{n}} \exp[-\alpha \mathrm{r}^2] \quad (2.17)$$

N is a normalisation factor, α represents the orbital exponent determining whether the resulting function is compact or diffuse. A small α value means the function is

diffuse, while a large α value refers to a compact function. The term L = l + m + n allows the GTO to be classified as an s-function (L=0), a p-function (L=1), a d-function (L=2) and so forth.

A general rule of thumb is that in order to achieve a certain accuracy, three times as many GTO than STO functions are required. The advantage of GTO functions are that the product of two Gaussians can be expressed as one Gaussian [89]. Despite its advantages, Gaussian functions do have their shortcomings, which can be seen when comparing them to Slater functions. STOs show the correct cusp behaviour at the origin and have a desirable rate of exponential decay in the tail regions. Figure 2.2 shows the distribution of STOs in this case compared with Gaussian expansions.

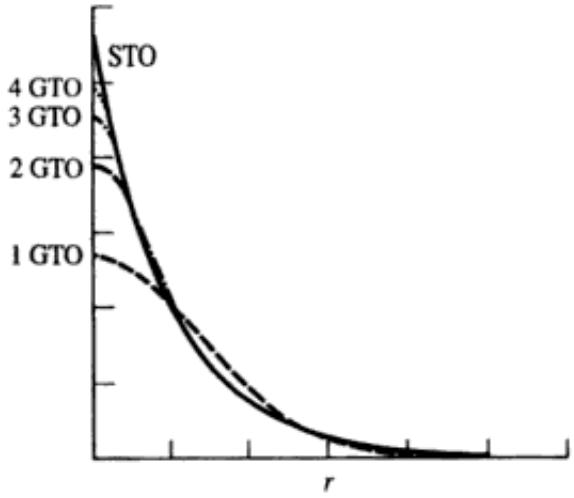

Figure 2.2: Plot showing 1s Slater type orbital in comparison with Gaussian expansions up to 4 terms [89]

On the contrary, GTOs do not have a cusp at the origin and decay towards zero at a much quicker rate. This means that replacing a STO with a single Gaussian function simply is not an option. However, it is possible to represent each atomic orbital as a linear combination of Gaussian functions. For each linear combination, it will have the form given by Equation (2.18).

$$\phi_\mu = \sum_{i=1}^{L} d_{i\mu}\phi_i(\alpha_{i\mu}) \tag{2.18}$$

Here, $d_{i\mu}$ is the coefficient of the primitive Gaussian function, ϕ_i, with an exponent of $\alpha_{i\mu}$. L represents the number of functions in the expansion. As the number of Gaussian functions in the linear combination increases, the fit with the STO is improved. Despite this, the Gaussian functions are still unable to give an accurate description of the exponential tail in the true function as well as the cusp at the nucleus. This leads to an underestimation of the long-range overlap between atoms, as well as the charge and spin density at the nucleus. The key parameters of a Gaussian

expansion are the coefficient and exponent. In an uncontracted Gaussian function, these parameters are allowed to vary during the calculation. In a contracted function, these values remain constant throughout the calculation. Calculations using uncontracted Gaussians are expensive computationally, hence, contracted functions are more commonly used.

The simplest of basis sets are known as *minimal basis sets* [84][89]. A minimal basis set is a representation containing only the amount of functions required in order to accommodate all of the occupied orbitals in each individual atom. These basis sets tend to include all of the atomic orbitals in the shell. A particular example is the STO-3G basis set. In this instance, three primitive GTO functions are combined into one contracted Gaussian function. In the case of hydrogen, only a single s-type function would be required, while five functions for carbon are needed, with one each for the 1s and 2s orbitals and the other three for the 2p shell ($2p_x$, $2p_y$ and $2p_z$). It is of no surprise that as these basis sets only use the bare minimum number of functions to describe the occupied orbitals, ignoring unoccupied ones, they have some severe drawbacks. For example, as they only contain one contraction per atomic orbital [89], the functions cannot expand or contract in accordance with the molecular environment during the calculation. With atoms at the end of a period such as fluorine, they are described as having the same amount of basis functions as atoms at the beginning of the period, even though they contain more electrons. Minimal basis sets also are unable to describe non-spherical aspects of the electronic distribution, for example, certain functions are restricted in terms of incorporating anisotropy.

One approach to address these issues is to use a *double zeta* basis set, in which the number of functions in the minimal basis set is doubled. In particular, double zeta basis sets solve the issue of anisotropy. The SCF process during the calculations will determine whether a particular orbital requires a more contracted or diffuse approach. It is then possible to have different combinations of orbitals such as p_x, p_y and p_z, allowing anisotropy to be introduced.

If it is taken into account that the valence space is where changes in the electronic wave function will occur, the doubled set of functions can be limited to just the valence orbitals [84]. Meanwhile, the most chemically inert core electrons are treated in a minimal set. The feasibility of this approach is that the core orbitals do not have much effect on chemical properties, and will only vary slightly from molecule to molecule. These basis sets are known as *split valence* basis sets. Examples include the 3-21G, 4-31G and 6-31G Gaussian basis sets. In the case of 3-21G, three Gaussian functions are used in order to describe the core orbitals [89]. Three Gaussians are also used to represent the valence electrons, with two Gaussians used to describe a contracted function and one Gaussian describing the diffuse function.

Despite improving anisotropy in a given system, split valence basis sets do not

solve the problem completely, and increasing the number of basis functions does not help in this case. The issue tends to arise from electron distribution within a molecule, with electrons being attracted from one atom to another nuclei i.e. polarisation. In terms of the orbitals, it can be said that a p-orbital can mix into an s-orbital of an isolated atom, to form an sp-hybrid. Unoccupied d-orbitals can also cause asymmetry with p-orbitals. In order to solve this issue, *polarisation functions* are introduced into the basis set. These functions have higher angular momentum than those that would be occupied in the atom, for example, introducing p-functions for hydrogen or d-functions for any of the first-row elements. These functions have more angular nodal planes than occupied atomic orbitals allowing the orbitals to distort from their original symmetry and to adapt better to the molecular environment. An asterisk is used to indicate a polarised basis function. Using 6-31G* as an example, this refers to a 6-31G basis set in which polarisation functions are introduced solely on the heavy atoms (non-hydrogen). When two asterisks are used i.e. 6-31G**, this indicates that polarisation functions are used on hydrogen and helium, as well as the heavy atoms. These can also be represented as 6-31G(d) and 6-31G(d,p). Partial polarisation basis sets are also in use. One particular example is the 3-21G$^{(*)}$ basis set. This has the same set of Gaussians as the 3-21G basis set, but this time, six d-type Gaussians are incorporated to account for the second row elements, therefore accounting for d-orbital effects in molecules that contain second-row elements.

All of the above basis sets so far have one thing in common: they have an inability to deal with charged species such as cations and anions, and molecules containing lone pairs. The amplitudes of the Gaussian basis functions are low and far from the nuclei which results in this failure. Highly diffuse functions are therefore required to solve this problem and added to the basis set. To identify these functions, a '+' is used. The 3-21+G basis set has a single set of diffuse s- and p-type Gaussian functions added. '++' is used when the diffuse functions are also included for hydrogen as well as heavy atoms.

Several larger basis sets exist and are commonly used in calculations. The number of functions can be increased in various categories, leading to types such as triple- and quadrupole-zeta basis sets [84]. Such examples are the cc-pVQZ (correlation-consistent polarised valence quadruple zeta) and cc-pV5Z (where the 5 is used for quintuple). Studies have shown that in fact, these correlation-consistent basis sets work very well in combination with the hybrid B3LYP functional.

2.2.7 Basis Set Superposition Error

In terms of bimolecular complexes or greater, calculating the energy of formation becomes more of a challenge, particularly for systems such as a hydrogen-bonded water dimer. The typical way to calculate the energy of formation would be to

first calculate the energy of a single water molecule, and the dimer separately. The energy of the isolated water molecules (reactants) would then be subtracted from the energy of the dimer (products). The issue with this calculation is that it represents an overestimation of the true value. The discrepancy in this case is what's known as *basis set superposition error*, or BSSE [89].

This error arises because as two water molecules approach each other, the energy of the system decreases for two reasons: 1) Favourable intermolecular interactions, and perhaps more importantly, 2) basis functions associated with each molecule actually provide a better description of the electronic structure around the other molecule. The BSSE is relative to the size of the basis set, with smaller basis sets (which do not provide a detailed representation of the electron distribution further out from the nuclei) tending to give the largest BSSE.

In order to account for this in ab initio methods, Boys and Bernardi [104] proposed a counterpoise correction, where the whole basis set was included for all calculations. The general expression for the counterpoise correction is shown in Equation (2.19).

$$\mathrm{A} + \mathrm{B} \rightarrow \mathrm{AB} \tag{2.19a}$$

$$\Delta E = E(\mathrm{AB}) - [E(\mathrm{A} + E\mathrm{B}) + E(E\mathrm{A} + \mathrm{B})] \tag{2.19b}$$

Using this equation, the energy of the individual species, A, is calculated in the presence of 'ghost' orbitals of B. A ghost orbital in this case refers to an orbital without the nuclei or electrons of B. Similarly, the energy of the species, B, is then calculated using the ghost orbitals on A. Figure 2.3 gives a graphical representation of how the counterpoise method is applied to a system.

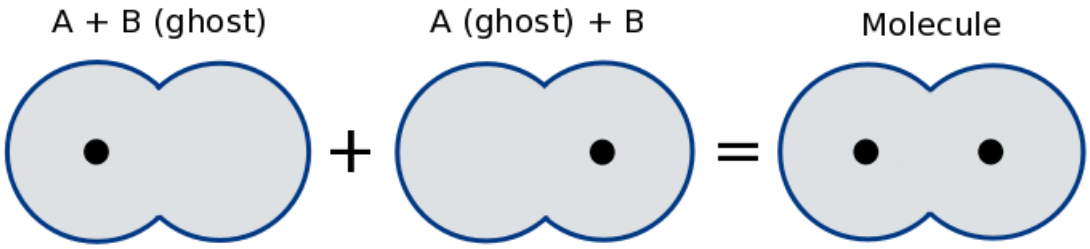

Figure 2.3: Visual representation of the counterpoise correction for BSSE

2.2.8 CRYSTAL09

The quantum mechanics simulation package used in this study is the CRYSTAL09 code. As mentioned earlier, the program can be used to calculate the electronic structure of periodic systems within Hartree Fock, Density Functional or hybrid approximations [82]. In order to successfully run a CRYSTAL calculation, an input file is required. This input file requires three different pieces of information. The

geometry of the system, a Gaussian-type of basis functions for each atom type, and finally, the choice of Hamiltonian, along with the number of k-point in periodic systems. With all this information, the required data about the properties of the system can be obtained.

The CRYSTAL code makes full use of the symmetry specified by the space group. This implies that only the coordinates for the primitive cell are required to reproduce the infinite crystalline structure. For a non-periodic molecular system, a point group is selected, which defines the symmetry of the system. In terms of defining the molecule, the number of atoms is stated and only atomic number and coordinates are used.

Once the geometry of the system has been fully described, the basis set must be chosen for each atom type. CRYSTAL allows the following types of shells to be employed: s, sp, p, d and f. The basis set set definition is considered to be the most important step for ab initio calculations of periodic systems that use Gaussian-type orbitals and to ensure proper use of the BSSE correction.

The final input section in CRYSTAL09 is used to define specific computational settings, such as the choice of Hamiltonian, the truncation criteria of Coulomb and exchange infinite sums, as well as the number of k-points. Other options may be necessary in order to allow a particular system to converge or to allow corrections to be added e.g. GRIMME allows for the correction of van der Waals forces. CRYSTAL will consider open-shell calculations as well as closed-shell simulations.

For DFT calculations, both an exchange and correlation functional can be defined. The functionals that can be employed for DFT include local density approximations (LDA), gradient-corrected (GGA) and hybrid methods. Some of the exchange functionals available in CRYSTAL include LDA (Dirac and Slater [105]), BECKE (Becke 1988 [100]) and PBE (Perdew, Burke and Ernzerhof 1996 [99]). All of these functionals are considered either in terms of total density (closed shell) or spin density. Some correlation functionals available to use include VWN (Vosko, Wilk and Nusair 1980 [94]) and LYP (Lee, Yang and Parr 1988 [101]). For the hybrid functionals, the user can define exactly the amount of Hartree-Fock exchange to incorporate ranging between 0-100%. Control over the relative weight of both the local and non-local part of the exchange and correlation potentials with respect to the standard definition of the GGA potentials is also built into the code. Examples of pre-defined hybrid functionals include B3LYP (Becke's 3 parameter functional) [102] and B3PW [102, 95, 96, 97, 98].

The tolerances for coulomb and exchange sums via a series of truncation criteria for the bielectronic integrals needs to be converged for each system. Five parameters are used in order to control the accuracy of the calculation: 1) The overlap threshold for Coulomb integrals, 2) The penetration threshold for Coulomb integrals, 3) The overlap threshold for Hartree-Fock exchange integrals and 4) and 5) being pseudo-

overlap for the Hartree-Fock exchange series. The SCF convergence threshold on the total energy of the system is also optimised.

One mandatory piece of information that a calculation requires are the shrinking factors. There are two factors that can be defined, with the first generating a grid of **k** points in reciprocal space (known as a brillouin zone), via the Pack-Monkhorst method [106]. This factor works by computing a Hamiltonian matrix in direct space, $\mathbf{H_f}$, performing a Fourier transform for each value of **k**. After this, the value is diagonalised in order to give the eigenvectors and eigenvalues shown by Equations (2.20) and (2.21).

$$H_k = \sum_g H_g e^{i\mathbf{gk}} \tag{2.20}$$

$$H_k A_k = S k A_k E_k \tag{2.21}$$

In the case of 3D crystals, the sampling points belong to a lattice referred to as the Pack-Monkhorst net, and possess basis vectors: $\mathbf{b}_1/is_1, \mathbf{b}_2/is_2, \mathbf{b}_3/is_3$, where $\mathbf{b}_1$, $\mathbf{b}_2$ and $\mathbf{b}_3$ represent the reciprocal lattice vectors while is_1, is_2 and is_3 are integers of the shrinking factors. In the CRYSTAL code, a second shrinking factor is also specified and this defines the sampling of k points, within the "Gilat net" [107][108]. The latter is used for calculating the density matrix and determining the Fermi energy in the case of conductors.

The Gilat net is built in the same way as the Pack-Monkhorst grid using shrinking factors. For a metallic system, the shrinking factor is twice the value of the Pack-Monkhorst grid. The value of the shrinking factor needs to be optimised and is dependant upon the size of the cell and the electronic structure. The greater the size of the cell in direct space, the smaller the size of the first brillouin zone, and, therefore, the lower the value of the shrinking factor. In the case where the cell is very large in direct space, only a single k-point can be adopted. To compute the Fermi energy for conducting systems, a large number of k-points are required than for an insulating one.

2.3 Molecular Dynamics

Molecular dynamics is a technique in which many successive configurations of a particular system are generated with the integration of Newton's laws of motion [89]. The end result that is obtained is a trajectory that shows how velocities and positions of the particles in a chemical system vary over a given time. Reminding ourselves of Newton's laws:

1. A body will continue to move in a straight line at constant velocity unless it has a force acting on it.

2. Force is equal to the rate of change of momentum (F = ma).

3. Every action has an equal and opposite reaction.

In order to obtain a molecular dynamics trajectory, the differential equations to Newton's second law must be solved as shown in Equation (2.22).

$$\frac{d^2x_i}{dt^2} = \frac{F_{x_i}}{m_i} \tag{2.22}$$

The motion of a particle that has a mass, m_i, is described along one coordinate (x_i). F_{x_i} is the force that acts on this particle in that direction at the time, t.

Newton's laws of motion can essentially be applied to three different types of problem, the simplest of which is the case where no force is acting on any of the particles between collisions. After each collision, the particle's position changes by $\mathbf{v}_i\delta t$ with $\mathbf{v}_i$ being the constant velocity and δt representing the time between each collision. The second problem is when a particle experiences a constant force between each collision such as a charged particle that moves in a uniform electric field. The third problem involves the force on a particle being dependant on its position relative to the other particles in the system.

2.3.1 The first molecular dynamics simulation

The very first molecular dynamics or MD simulation of a condensed phase system, was conducted by Alder and Wainwright in 1957 [109]. A hard-sphere model was tested in this case, where spheres were able to move at a constant velocity in a straight line between each separate collision. Each collision was perfectly elastic (total kinetic energy before the collision is equal to the total kinetic energy after the collision) and occurred when the separation between the sphere's centre equalled the sphere's diameter. In order to perform the molecular dynamics calculation of the hard-sphere, several steps had to be considered:

1. The next pair of spheres to collide had to be calculated, along with the time at which the collision will occur.

2. The position of every sphere at the time of the collision needed to be ascertained.

3. For the two spheres undergoing collision, their new velocities had to be obtained.

The conservation of linear momentum is applied to the model in order to calculate the new velocities of the spheres after a collision. Early models such as these were useful in gaining an insight into the nature of fluids. The earliest investigations involving MD simulations involved analysing differences between solid and fluid phases.

2.3.2 Continuous Potentials: Finite difference methods

The early studies of molecular dynamics had many drawbacks and did not provide the most realistic study of molecular systems. More realistic models took into account that the force on each particle changes with its position or the position of other particles with which it interacts with. These methods required continuous potentials, with the very first simulation of this kind being performed on argon by Rahman in 1964 [110], who subsequently went on to simulate water in 1971 with Stillinger [111]. Using continuous potentials, the particles' motions are coupled together leading to a many-body problem with which the equations of motion are integrated by means of a *finite difference method*.

Finite difference techniques are widely used for MD simulations. They work by generating a trajectory with a continuous potential model, assumed to be pairwise additive in this case. Here, the integration process is broken down into small steps, with each being separated by a fixed time, δt. In order to calculate the total force on each particle at a time, t, the vector sum of the interaction with other particles is calculated. Using force and the known mass of the particles, acceleration can be calculated. This is combined with the particles' positions and velocities at a time, t, allowing positions and velocities to be calculated at a time, $t + \delta t$. During the timestep of the simulation, it is expected that the force will remain constant. As the particles move to new positions, the resulting forces are determined, which in turn leads to new positions and velocities at a time, $t + \delta t$. This process is then repeated.

For performing the integration steps in finite difference methods, there are many available algorithms, each of which approximate the positions and properties of the particles as a Taylor Series expansion shown by Equation (2.23).

$$\mathbf{r}(t+\delta t) = \mathbf{r}(t) + \delta t\mathbf{v}(t) + \frac{1}{2}\delta t^2\mathbf{a}(t) + \frac{1}{6}\delta t^3\mathbf{b}(t) + \frac{1}{24}\delta t^4\mathbf{c}(t) + ... \tag{2.23a}$$

$$\mathbf{v}(t+\delta t) = \mathbf{v}(t) + \delta t\mathbf{a}(t) + \frac{1}{2}\delta t^2\mathbf{b}(t) + \frac{1}{6}\delta t^3\mathbf{c}(t) + ... \tag{2.23b}$$

$$\mathbf{a}(t+\delta t) = \mathbf{a}(t) + \delta t\mathbf{b}(t) + \frac{1}{2}\delta t^2\mathbf{c}(t)... \tag{2.23c}$$

$$\mathbf{b}(t+\delta t) = \mathbf{b}(t) + \delta t\mathbf{c}(t) + ... \tag{2.23d}$$

Here, $\mathbf{r}$ refers to the positions of the particles, $\mathbf{v}$ is the velocity obtained from the first derivative of the particles' positions, with respect to time. $\mathbf{a}$ is acceleration, also known as the second derivative with respect to the integration. $\mathbf{b}$ is the third derivative and so on.

One of the most commonly used and well known algorithms used in molecular dynamics is the *Verlet algorithm* [112]. It works by using the positions of the particles and accelerations at a time, t, along with positions from the previous integration step, $\mathbf{r}(t-\delta t)$, in order to calculate new positions at $t+\delta t$, $\mathbf{r}(t+\delta t)$. These quantities and velocities at time, t, can be related via Equation (2.24).

$$\mathbf{r}(t+\delta t) = \mathbf{r}(t) + \delta t\mathbf{v}(t) + \frac{1}{2}\delta t^2\mathbf{a}(t) + ... \tag{2.24a}$$

$$\mathbf{r}(t-\delta t) = \mathbf{r}(t) - \delta t\mathbf{v}(t) + \frac{1}{2}\delta t^2\mathbf{a}(t) - ... \tag{2.24b}$$

Which can be combined to give Equation (2.25).

$$\mathbf{r}(t+\delta t) = \mathbf{2}r(t) - \mathbf{r}(t-\delta t) + \delta t^2\mathbf{a}(t) \tag{2.25}$$

The velocities for the particles can be obtained by dividing the difference in positions at times, $t+\delta t$ and $t-\delta t$, by $2\delta t$ shown by Equation (2.26).

$$\mathbf{v}(t) = [\mathbf{r}(t+\delta t) - \mathbf{r}(t-\delta t)]/2\delta t \tag{2.26}$$

The velocities may also be calculated by estimation at the half step, $t + \frac{1}{2}\delta t$, shown in Equation (2.27).

$$\mathbf{v}(t+\frac{1}{2}\delta t) = [\mathbf{r}(t+\delta t) - \mathbf{r}(t)]/\delta t \tag{2.27}$$

While the Verlet algorithm is relatively simple to implement, it does suffer from some drawbacks. Obtaining the velocities can be particularly difficult and remain unavailable until the positions have been obtained from the next step of the calculation. A loss of precision can occur since the positions are obtained by addition of a small term, $(\delta t^2\mathbf{a}(t))$, to the difference of two larger terms in $2\mathbf{r}(t)$ and $\mathbf{r}(t-\delta t)$. The algorithm also suffers in the sense that it is not self-starting, meaning that the new positions of the particles have to be obtained from the current positions, $\mathbf{r}$(t), as well the positions from the previous time step, $\mathbf{r}(t-\delta t)$. This means that when $t = 0$, only one set of positions exists, and the calculation needs to be initiated in some way so that the positions at $(t-\delta t)$ can be obtained. Truncating the Taylor series (Equation (2.23)) after the first term is one such way of achieving this.

To overcome some of the problems, variations of the Verlet algorithm have been created, such as the *leap-frog* algorithm by Hockney in 1970 [113]. The leap-frog algorithm is shown in Equation (2.28).

$$\mathbf{r}(t+\delta t) = \mathbf{r}(t) + \delta t\mathbf{v}(t+\frac{1}{2}\delta t) \tag{2.28a}$$

$$\mathbf{v}(t+\frac{1}{2}\delta t) = \mathbf{v}(t-\frac{1}{2}\delta t) + \delta t\mathbf{a}(t) \tag{2.28b}$$

In order to implement this algorithm, the velocities $\mathbf{v}(t+\frac{1}{2}\delta t)$ are calculated from the velocities at time, $t-\frac{1}{2}\delta t$, and accelerations at time, t. The positions of the particles, $\mathbf{r}(t+\delta t)$, can be worked out using the velocities that have just been calculated along with the positions at time, t, $\mathbf{r}(t)$, in Equation (2.28a). In order to calculate the velocities at time, t, Equation (2.29) is used.

$$\mathbf{v}(t) = \frac{1}{2}[\mathbf{v}(t+\frac{1}{2}\delta t) + \mathbf{v}(t-\frac{1}{2}\delta t)] \tag{2.29}$$

The algorithm gets the name 'leap-frog' due to the fact that the velocities will leap over the positions to obtain their values at $t+\frac{1}{2}\delta t$. In turn, the positions will leap over the velocities, to give their values at $t+\delta t$. Once again, the velocities will leap-frog over the positions obtaining values at $t+\frac{3}{2}\delta t$, and the process continues.

The leap-frog algorithm specifically includes the velocity unlike the standard Verlet algorithm. It is not necessary to calculate the difference of large numbers in the algorithm, giving it an advantage over the Verlet method. The leap-frog method does, however, suffer from a lack of synchronicity with the positions and velocities, and the kinetic energy is not calculated at the same time as the definition of the positions, meaning the potential energy cannot be defined in this way.

To overcome the drawbacks of the previous two methods, an algorithm needs to be able to give positions, velocities, and accelerations all at the same time, without losing precision. The *velocity Verlet* [114] method was developed for this purpose, shown by Equation (2.30).

$$\mathbf{r}(t+\delta t) = \mathbf{r}(t) + \delta t\mathbf{v}(t) + \frac{1}{2}\delta t^2\mathbf{a}(t) \tag{2.30a}$$

$$\mathbf{v}(t+\delta t) = \mathbf{v}(t) + \frac{1}{2}\delta t[\mathbf{a}(t) + \mathbf{a}(t+\delta t)] \tag{2.30b}$$

The velocity Verlet method is dependant on the new velocities requiring the accelerations at t and δt in order to be calculated. The process begins by calculating the positions at $t+\delta t$ (Equation (2.30a)), using the velocities and accelerations at time, t. The new velocities at time, $t+\frac{1}{2}\delta t$, can be calculated by using Equation (2.31).

$$\mathbf{v}(t+\frac{1}{2}\delta t) = \mathbf{v}(t) + \frac{1}{2}\delta t\mathbf{a}(t) \tag{2.31}$$

Using the current positions, new forces can be calculated, therefore allowing accelerations to be determined giving $\mathbf{a}(t+\delta t)$. Finally, the velocities at time, $t+\delta t$ are calculated via Equation (2.32).

$$\mathbf{v}(t+\delta t) = \mathbf{v}(t+\frac{1}{2}\delta t) + \frac{1}{2}\delta t\mathbf{a}(t+\delta t) \tag{2.32}$$

The velocity Verlet method is known as a three-stage procedure.

These are just a selection of the integration methods that are available in molecular dynamics. In terms of ideality, a method should be rapid, with minimal memory requirements and easy in terms of programming. The most significant demand in a molecular dynamics simulation is to calculate the force on each particle in the system. A good algorithm should conserve energy and momentum, as well as being time-reversible. It should also allow a long time step, δt, to be utilised. The time step is particularly important in terms of computational demands. When a long time step is used, fewer iterations of the algorithm will be required in order to cover a given amount of phase space. While a calculated trajectory obtained from a simulation will differ from the exact trajectory of a system, it is desirable for the calculation to give results as close as possible to the exact analytical trajectory.

2.3.3 Force fields

Calculating the electronic energy (E_e) of a system for a given nuclear configuration is both time and computer demanding [115]. In order to get around this issue, *Force Field* (FF), methods can be used. Here, the potential energy is written as a parametric function of the nuclear coordinates. The parameters which are fitted either to experimental data or high level computational data are input into the function. The basis for molecules is that they are modelled as atoms connected via "bonds" (depending upon the force field used). Atoms will be of varying size and "softness", while bonds are expressed in terms of rigidity or stiffness, which lends itself to molecules being described as a "ball and spring" model [116].

In force field simulations, the quantum aspects of electronic motion are bypassed, allowing the dynamics of the atoms to be treated using classical mechanics, described by Newton's second law [115]. For time-independent cases, the issue can be reduced further to calculating the energy at a given geometry. It is of interest to locate geometries of energetically stable molecules/conformations, by finding energy minima on the potential energy surface. They allow calculation of relative energies as well as barriers for interconversion of different conformations. These calculations will be referred to as molecular mechanics simulations.

One observation used when constructing force fields is that molecules are composed of units. These units are comparable on a structural level in different molecules. A rough example is the C-H bond, in which the bond lengths and stretch vibrations are similar in all molecules. As a result, different molecules can be pictured as being composed of functional groups.

The force field energy (E_{FF}) can be expressed as a summation of individual energy terms. Each term describes the energy that is necessary to distort the molecule in a particular way. The energy is expressed in Equation (2.33).

$$E_{FF} = E_{str} + E_{bend} + E_{tors} + E_{vdw} + E_{el} + E_{cross} \tag{2.33}$$

E_{str} describes the energy required for stretching a bond between two atoms. E_{bend} is representative of the energy necessary for bending an angle. E_{tors} is the energy change for rotation around a bond. E_{vdw} and E_{el} are both non-bonded atom-atom interaction energy terms for van der Waals interactions and electrostatic interactions, respectively. Finally, E_{cross} is used to provide a description of coupling between the first three energy terms. With an energy function such as this, geometries and relative energies of a system can be calculated.

As mentioned above, E_{str} is an energy function for stretching a bond between two different atoms labelled A and B. It can be simplified in the form of a Taylor expansion with an equilibrium bond length, R_0, and written in Equation (2.34).

$$E_{str}(R^{AB} - R_0^{AB}) = k^{AB}(R^{AB} - R_0^{AB})^2 = k^{AB}(\Delta R^{AB})^2 \tag{2.34}$$

One thing to note is that the R_0 value is not the experimental equilibrium bond distance. Instead, it is the geometry optimised value when zero-point energy is neglected, corresponding to the bond distance at the minimum of the potential energy well. R_0 represents the equilibrium bond length in a diatomic molecule, but for all other situations, experimental equilibrium bond lengths are slightly greater than R_0.

In Equation (2.34), k^{AB} acts as the force constant for the A-B bond, in the form of a harmonic oscillator. This is because the harmonic form is the simplest, while still being sufficient to determine the majority of equilibrium geometries. However, in some cases, such as strained or crowded systems, the calculated results may differ significantly from the experimental results. One of the ways to get around this is to add more terms to the Taylor expansion for the E_{str} term. However, caution needs to be used in this approach, as polynomial expansions of the stretch energy do not provide the correct limiting behaviour, meaning that the energy will go towards either $-\infty$ or $+\infty$ at long bond distances depending on the order of termination of the function. The correct limiting behaviour for bonds that are stretched to infinity is for the energy to converge towards the dissociation energy. One such function which adheres to this is the Morse potential [117], shown by Equation (2.35).

$$E_{Morse}(\Delta R) = D[1 - e^{\alpha \Delta R}]^2 \tag{2.35}$$

In this case, D represents the dissociation energy, while α is related to the force constant. The potential agrees quite well with the experimental behaviour for a wide range of bond distances. It does come with a few drawbacks, for example, at long bond lengths, the restoring force can be quite small. As a result, any structures that become distorted during a simulation will have a slow convergence towards the equilibrium bond length. One of the ways to get around this issue is to ensure that the n^{th} order derivative at R_0 matches the corresponding derivative obtained from the Morse potential. This can be achieved with a fourth-order expansion shown in

Equation (2.36).

$$E_{str}(\Delta R^{AB}) = k^{AB}(\Delta R^{AB})^2[1 - \alpha(\Delta R^{AB}) + \frac{7}{12}\alpha^2(\Delta R^{AB})^2] \tag{2.36}$$

For every type of bond, the two parameters that must always be determined are k^{AB} and R_0^{AB}, while for higher order expansions and the Morse potential, α or D must be determined, respectively.

The E_{bend} term specifically describes the energy necessary for bending an angle that is formed by three atoms labelled A-B-C, whereby there is an interaction between A and B, as well as B and C. It is also expanded via a Taylor series, around a natural bond angle, and giving a harmonic approximation after being terminated at second order, shown in Equation (2.37).

$$E_{bend}(\theta^{ABC} - \theta_0^{ABC}) = k^{ABC}(\theta^{ABC} - \theta_0^{ABC})^2 \tag{2.37}$$

Similar to the E_{str} term, the harmonic expression will be more than suitable for the majority of applications, but a higher degree of accuracy may sometimes be necessary. Adding a third-order term gives a good description over a large range of angles. Higher-order force constants can be taken as a fixed fraction of the harmonic constant, however, any constants above third-order cannot be assigned with a high degree of confidence, due to lack of experimental data. When the central atom is di- or trivalent, this can present a problem. However, by considering the bending function to be identified for all types of atom, this can be bypassed. For all of the combinations of the three atom types, A, B and C, the two mandatory bending parameters to be determined are k^{ABC} and θ_0^{ABC}.

E_{tors} corresponds to a four atom sequence A-B-C-D and is the change in energy required for rotation around a B-C bond. The torsional angle, ω, is defined as the angle that is created by the A-B and C-D bonds and can either be taken in the range [0°, 360°] or [−180°, 180°]. The function for E_{tors} is periodic in the angle, ω. Also, the energy required to distort the molecule by rotation is usually low, which can give rise to large deviations from the minimum energy structure. As a result, a Taylor expansion is not recommended, and instead a Fourier series is used, which takes into consideration the periodicity as shown by Equation (2.38).

$$E_{tors}(\omega) = \sum_{n=1} V_n cos(n\omega) \tag{2.38}$$

n=1 corresponds to a rotation which is periodic by 360°. n=2 is periodic by 180°, n=3 is periodic by 120° and so on. The V_n constants in the series represent the size of the energy barrier that needs to be overcome in order for rotation around the B-C bond, which can be zero for n-values in some cases, i.e. ethane. In this particular example, hydrogens staggered relative to each other form the most stable conformation. On the other hand, the eclipsed conformation represents a maximum

energy. Since ethane has three identical hydrogen atoms at each end, there are a total of three energetically equivalent staggered, and eclipsed conformations. The rotational profile therefore has three minima and three maxima. Only terms such as n=3, 6, 9 and so on will have V_n constants that differ from zero.

In some cases, new terms may need to be added to the series such as when different conformations in a system (e.g butane) possess different energies. A term corresponding to n=1 can be used to account for this. Another key example is in the case of ethene. It is important to consider the greater energy cost for rotation around a C=C double bond. The rotation must be periodic by 180°, and only the terms n=2, 4 and so on can be used. The increased energy cost will be reflected in the larger value of V_2. For the four atom types considered, A, B, C and D, three torsional parameters are usually considered, V_1^{ABCD}, V_2^{ABCD} and V_3^{ABCD}. The torsional angle is represented visually in Figure 2.4.

Figure 2.4: Definition of the torsional angle. Image obtained from [115]

E_{vdw} represents the van der Waals energy contributions, describing either the repulsion or attraction between non-bonded atoms. The van der Waals energy tends towards zero as the interatomic distance increases. At small distances, repulsion is greater, due to overlap between fictional "electron clouds" and repulsive interactions between negative electrons. A small attraction occurs at intermediate distances. This is due to dipole-dipole interactions. This can occur even if the molecule possesses no permanent dipole moment, due to an uneven distribution of the "electron cloud", giving rise to instantaneous dipole moments, and inducing this in neighbouring molecules, resulting in an attraction. Theoretically, the attraction is varied as a result of the inverse sixth power of distance between the two molecules, referred to as R^{-6}. These interactions are known as London dispersion forces [118], occurring in non-polar molecules as the main force of attraction. E_{vdw} can be expressed as in Equation (2.39).

$$E_{vdw}(R^{AB}) = E_{repulsive}(R^{AB}) - \frac{C^{AB}}{(R^{AB})^6} \tag{2.39}$$

As R goes toward infinity, the function will tend toward zero. One of the most well-known potentials based on these requirements is the *Lennard-Jones* (LJ) [119] potential, in which repulsion is given by R^{-12}, shown in Equation (2.40).

$$E_{LJ}(R) = \frac{C_1}{R^{12}} - \frac{C_2}{R^6} \tag{2.40}$$

C_1 and C_2 in this case are constants. Another form of the Lennard-Jones potential is written in Equation (2.41).

$$E_{LJ}(R) = \varepsilon \left[\left(\frac{R_0}{R} \right)^{12} - 2 \left(\frac{R_0}{R} \right)^{6} \right] \tag{2.41}$$

Here, R_0 represents the minimum energy distances, and ε describes the depth of the energy potential well.

Repulsion occurs due to overlap of electronic wave functions for real systems in electronic structure theory, so naturally, the electron density will decrease, in this instance, exponentially, as a function of the distance from the nucleus. Therefore, this means that the repulsive part can be modelled as an exponential functional. In its most general form, the exponential R^{-6} E_{vdw} function can be expressed by Equation (2.42).

$$E_{vdw}(R) = Ae^{-BR} - \frac{C}{R^6} \tag{2.42}$$

This is known as a "*Buckingham*" or "*Hill*" potential [120]. A, B and C represent constants. This potential does have its shortfalls, mainly at short interatomic distances. As the R value decreases toward zero, the exponential becomes a constant, A, and the R^{-6} term goes toward -∞. Therefore, at very short interatomic distances, minimising the energy can result in nuclear fusion.

In addition to Lennard-Jones and Buckingham potentials, the aforementioned Morse potential can be used for van der Waals forces. Like the Buckingham potential, the Morse potential is also exponentially dependant. It does not possess the R^{-6} dependence for long ranges, but this is not a huge issue due to the presence of R^{-8} and R^{-10} terms, which in reality are related to induced quadrupole-dipole and quadrupole-quadrupole interactions. There will be differences of course in the values of the Morse potential for the E_{vdw} term compared with the E_{str} term. D and α will be much smaller for E_{vdw} while R_0 will be longer. The Morse function is particularly suitable for small systems, performing slightly better than the Buckingham potential, which in turn performs noticeably better than the Lennard-Jones potential.

What distinguishes each of the three functions is the way in which the repulsive part is described at short interatomic distances. Both the Lennard-Jones and Buckingham potentials tend to overestimate this repulsion. However, the attraction part in intermolecular interactions behaves similarly in all three functions. The Morse and Buckingham potentials have a slightly better description potentially as a result of having three parameters, as opposed to the two used in the Lennard-Jones potential. Despite this, the Lennard-Jones function is still widely used in theoreti-

cal methods. It is less demanding computationally than the exponential potentials. Furthermore the repulsive part of E_{vdw} is not often considered to be very important, and therefore the Lennard-Jones potential has been shown to give accurate results, while being more efficient on a computational basis. In this study, the Lennard-Jones potential has been employed for all MD simulations to describe the force field.

Van der Waals forces form one part of the non-bonded interactions necessary for calculating the force field energy. The other part is the electrostatic energy, E_{el}, which is the internal distribution of electrons, which lead to positive and negative sections of a molecule. An example is a carbonyl group, in which the oxygen is negatively charged, leading to a positively charged carbon. At the most basic level, electrostatic energy can be simply modelled by assigning a formal charge to each atom. In other cases, the bond between the atoms may be assigned a dipole moment. These two approaches will often yield slight differences in terms of results, and only in the case of the long-distance limit of interaction will the results be identical. For point charges, the interaction can be modelled by the well known Coulomb potential described by Equation (2.43).

$$E_{el}(R^{AB}) = \frac{Q^A Q^B}{\varepsilon R^{AB}} \tag{2.43}$$

Here, ε is the dielectric constant and Q represents the quantity of charge on each atom. The most common technique is to assign the atomic charges on the basis of fitting to the electrostatic potential, which is calculated by means of electronic structure methods.

For bond dipole moments, the electrostatic interaction can be modelled by Equation (2.44).

$$E_{el}(R^{AB}) = \frac{\mu^A \mu^B}{\varepsilon (R^{AB})^3}(cos\chi - 3cos\alpha_A cos\alpha_B) \tag{2.44}$$

χ and α in this case represents angles, shown in Figure 2.5.

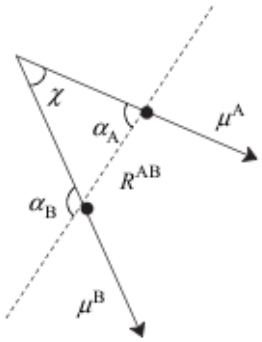

Figure 2.5: Variable definition for a dipole-dipole interaction [115]

The easiest way to parametrize this model is to fit it to an electronic wave function based on first principles simulation. The importance of the "effective"

dielectric constant, ε, is to model the effect of the solvent molecules that may be present along with any interactions between distant sites that may be part of the same molecule. When ε is 1, this represents a vacuum. As ε increases, long range charge-charge interactions become less important.

Both of the non-bonded energy terms only consider two-body contributions. This leads to limitations when it comes to polarisation effects. The three-body contribution is often quite significant for polar species [121], as the interaction between two atomic charges can be altered due to the polarisation effect from a third atom. While improvements can be made to account for this, they significantly increase the computational time, and hence are not often used. However, the average polarisation is implicitly included, as atomic charges are frequently selected to result in a dipole moment that is greater than the value that would be observed in an isolated molecule.

Finally, the E_{cross} term covers coupling between the aforementioned first three terms. The reason that this term may be required are in the cases where the first three energy terms in the force field energy do not accurately model the system and disregard any coupling that may occur. An example of this is H_2O, in which the hydrogens can come closer together when the bond angle is reduced. In turn, repulsion between the hydrogens is increased, and thus to compensate, the bonds increase in length. This coupling between angle and bond length cannot be modelled by the first three energy terms alone, and therefore a term that is dependant on both angle and bond length is required. E_{cross} can include a series of terms incorporating two or more bonded terms.

The E_{cross} term takes the form of a Taylor-like expansion in the individual coordinates. The most well-known example is the stretch/bend term for an A-B-C sequence written as in Equation (2.45).

$$E_{str/bend} = k^{ABC}(\theta^{ABC} - \theta_0^{ABC})[(R^{AB} - R_0^{AB}) + (R^{BC} - R_0^{BC})] \tag{2.45}$$

Other useful examples include Equations (2.46) and (2.47).

$$E_{str/tors} = k^{ABCD}(R^{AB} - R_0^{AB})cos(n\omega^{ABCD}) \tag{2.46}$$

$$E_{bend/tors/bend} = k^{ABCD}(\theta^{ABC} - \theta_0^{ABC})(\theta^{BCD} - \theta_0^{BCD})cos(n\omega^{ABCD}) \tag{2.47}$$

Another useful correction relating to cross terms is where parameters are modified for atoms that are not strictly involved in the interaction being described by the parameter. A common example is in the case of carbon-carbon bond lengths, which are reduced in the presence of electronegative atoms present at each end.

A correction term can be added to the natural bond length, R_0^{AB} [122], to give Equation (2.48).

$$R_0^{AB-C} = R_0^{AB} + \Delta R_0^C \tag{2.48}$$

Nowadays, many different force fields are in use, examples of these being COMPASS, the polymer consistent force field (PCFF) and AMBER. Each of these force fields will differ in the way in which they describe the interactions in molecular systems.

2.3.4 Polymer Consistent Force Field (PCFF)

Many well-parametrized force fields are available including CHARMM [123], AMBER [124, 125], CFF93 [126, 127, 128, 129] and MMFF94 [130, 131, 132, 133, 134], with the latter used in MarvinSketch (See Section 2.6). All of these were designed with biologically interesting molecules in mind [135]. Interest in materials science has led to a requirement to develop force fields designed specifically for organic materials and polymers. As a starting point, the protein CFF91 force field was chosen, later being developed into CFF93. From this, a dozen functional groups from the most common organic and inorganic polymers were parametrized, with the force field named the polymer consistent force field (PCFF).

As with the CFF93 force field, the parameters in PCFF were derived from ab initio calculations using a least-squares-fit technique developed by Hagler et al. [136]. PCFF uses atomic partial charges and Lennard-Jones 9-6 parameters in its description of the non-bonding parameters, with many of these taken from the CFF91 force field [135]. The latter parameters were derived by fitting to molecular crystal data by using energy minimization calculations [137, 138, 139, 140, 141, 142].

2.3.5 COMPASS Force Field

PCFF has been shown to perform well in many cases, however, for some applications, shortfalls are present [135]. For these specific situations, systematic errors were found in the pressure-volume-temperature (PVT) relation in MD simulations for liquids and polymers, with discrepancies in the calculated and experimental densities. Therefore, a force field suitable for condensed phase applications was constructed, by modification of the non-bonding parameters and valence parameters, between which coupling can occur. The new approach, based on the PCFF force field, utilised both ab initio and empirical methods. Several new molecular classes were parametrized, while the non-bonding parameters were all re-parametrized. The resulting force field was called COMPASS, which stands for condensed-phase optimised molecular potentials for atomistic simulation studies.

The three categories of parameters to be derived were the charge, valence and

van der Waals terms. The charge parameters were derived by means of a constrained ab initio electrostatic potential energies (ESP) fit [143, 144], while the valence parameters were obtained using ab intio data [126, 127, 128, 129, 145, 146, 147, 148, 149, 150, 151]. Initially, the van der Waals parameters were transferred from the PCFF force field and fixed. The final step involved optimising the van der Waals parameters via MD simulations of molecular liquids. The overall process was iterated to ensure consistency. Generic atom types were introduced with extensive transfer of parameters in order to maximise coverage and minimise the number of parameters present.

2.3.6 DL_POLY

In this study, the molecular dynamics simulation package DL_POLY is used. It is a general purpose classical molecular dynamics (MD) simulation software, and was developed at Daresbury Laboratory initially by W. Smith and T.R. Forester [152]. More recent versions of the code have been developed by W. Smith and I.T. Todorov [153]. The package consists of subroutines, programs and data files designed to simulate polymers, macromolecules, ionic systems and solutions, on a distributed memory parallel computer. The version of DL_POLY that will be utilised is DL_POLY 4. This version uses a Domain Decompostion (DD) strategy [154, 155]. It is most suitable for large scale calculations that often range from 10^3 to 10^9 atoms on large processor counts. The DL_POLY program contains a number of different potentials required for a wide range of systems, as described by Equation (2.49). These include van der Waals, hydrogen bond, chemical bond, valence angle, dihedral angle and tether potentials among many others. The parameters that describe these potentials can be obtained from force fields such as AMBER or Dreiding [156] and can be easily adapted to run in DL_POLY 4.

DL_POLY can accommodate isolated molecules or apply boundary conditions to a system. These involve cubic, orthorhombic and parallelepid boundaries. The system can also be run as a slab. Simulations can be run either on a single processor or in parallel. In terms of the Molecular Dynamics algorithms, the default choices are based on the Velocity Verlet method, due to its simplicity and being time-reversible. As well as Velocity Verlet, DL_POLY also allows the user to use algorithms based on the Leapfrog Verlet (LFV) scheme. Despite being simpler and faster numerically, it does not offer the time reversibility of the Velocity Verlet scheme, nor the numerical stability. All kinetic related properties also have approximate estimators, which is due to being half a step out of phase between velocity and position.

The trajectories are generated in the microcanonical NVE ensemble. Here, N stands for the number of particles, V stands for the volume of the system and E represents the total energy in the system. In this case, the total energy is conserved. Other ensembles that can be generated in DL_POLY include NVT, NPT and $N\underline{\underline{\sigma}}T$.

A selection of thermostats and barostats can also be implemented. In the case of thermostats, a system is coupled to a heat bath ensuring that the average temperature is kept close to the specified temperature. By introducing a thermostat, the standard equations of motion become modified and therefore the system no longer samples the NVE ensemble. Instead, trajectories are generated for example, in the canonical NVT ensemble. In order to solve bond constraints in the Velocity Verlet and Leapfrog Verlet algorithms, RATTLE and SHAKE algorithms can be employed. In order to dynamically adjust the size and shape of a simulation cell, the system may be coupled to a barostat. This will allow the user to obtain a desired average pressure (P_{ext}) and/or an isotropic stress tensor (σ).

In DL_POLY, the total energy of a molecular system can be expressed by Equation (2.49).

$$
\begin{aligned}
U(\underline{r}_1, \underline{r}_2, ..., \underline{r}_N) = & \sum_{i_{shel}=1}^{N_{shel}} U_{shel}(i_{shel}, \underline{r}_{core}, \underline{r}_{shell}) \\
& + \sum_{i_{teth}=1}^{N_{teth}} U_{teth}(i_{teth}, \underline{r}_i^{\mathbf{t}=t}, \underline{r}_i^{\mathbf{t}=0}) \\
& + \sum_{i_{bond}=1}^{N_{bond}} U_{bond}(i_{bond}, \underline{r}_a, \underline{r}_b) \\
& + \sum_{i_{angl}=1}^{N_{angl}} U_{angl}(i_{angl}, \underline{r}_a, \underline{r}_b, \underline{r}_c) \\
& + \sum_{i_{dihd}=1}^{N_{dihd}} U_{dihd}(i_{dihd}, \underline{r}_a, \underline{r}_b, \underline{r}_c, \underline{r}_d) \\
& + \sum_{i_{inv}=1}^{N_{inv}} U_{inv}(i_{inv}, \underline{r}_a, \underline{r}_b, \underline{r}_c, \underline{r}_d) \\
& + \sum_{i=1}^{N-1} \sum_{j>i}^{N} U_{2-body}^{(metal,vdw,electrostatics)}(i, j, \mid \underline{r}_i - \underline{r}_j \mid) \\
& + \sum_{i=1}^{N} \sum_{j\neq i}^{N} \sum_{k\neq j}^{N} U_{tersoff}(i, j, k, \underline{r}_i, \underline{r}_j, \underline{r}_k) \\
& + \sum_{i=1}^{N-2} \sum_{j>i}^{N-1} \sum_{k>j}^{N} U_{3-body}(i, j, k, \underline{r}_i, \underline{r}_j, \underline{r}_k) \\
& + \sum_{i=1}^{N-3} \sum_{j>i}^{N-2} \sum_{k>j}^{N-1} \sum_{n>k}^{N} U_{4-body}(i, j, k, n, \underline{r}_i, \underline{r}_j, \underline{r}_k, \underline{r}_n) \\
& + \sum_{i=1}^{N} U_{extn}(i, \underline{r}_i, \underline{v}_i)
\end{aligned}
\tag{2.49}
$$

Here, $U_{shel}, U_{teth}, U_{bond}, U_{angl}, U_{dihd}, U_{inv}, U_{2-body}, U_{tersoff}, U_{3-body}$ and U_{4-body} are all empirical interaction functions. They describe ion core-shell polarisation, tethered particles, chemical bonds, valence angles, dihedral angles, inversion angles, two-body, Tersoff, three-body and four-body forces respectively. The first six functions in the configuration energy are all intramolecular interactions, while the next four functions are intermolecular interactions. The final function describes the external field potential. $\underline{r}_a, \underline{r}_b, \underline{r}_c$ and $\underline{r}_d$ are position vectors and refer to the atomic positions involved in a particular interaction. In each case, N represents the total number of each interaction in the simulated system, while i represents the indices of an individual interaction of each type. It should be noted that all intramolecular interactions must be individually cited in DL_POLY 4. In the case of intermolecular interactions, the indices must be specified globally according to atom types due to the larger number of atoms usually involved.

Otherwise referred to as position restraining, tethering forces allow atomic sites to be tethered to a fixed point in space, taken as their position at the start of a simulation. Bond potentials are used to describe the chemical bonds between certain atoms. Valence angle potentials describe the bending terms of a bond between specified atoms. Dihedral angle potentials on the other hand describe the interaction which results from torsion in the molecule. Inversion angle potentials refer to the interaction that results from a certain geometry of three atoms surrounding a central atom. The trigonal pyramid structure of ammonia is a good example of this, where the hydrogen atoms can invert to produce an identical structure, albeit with a change in chirality. The inversion potentials can be used to restrict the molecule in question to one structure.

Two-body potentials describe the short ranged van der Waals pair forces. Metal potentials can also be used to describe the bonding of a metal atom in terms of its local electronic density, making them suitable for determining the properties of metals and alloys. The Tersoff [157] potential is a pair potential, in which for real systems, the strength of each bond is dependant on the local environment. It essentially couples two-body and higher many-body correlations into just a single model. Three-body potentials are mainly used to describe valence angle forms, and are aimed at amorphous materials such as silicate glasses. Finally, four-body potentials deal with inversion angle forms, also with the intention of simulating amorphous materials.

External force fields can be used in addition to the molecular force field. Examples include an electric field, a gravitational field and a magnetic field. In cases where external force fields are applied, they are often accompanied by a thermostat.

With the DL_POLY force field designed to be adaptable, it allows other force field parameters to be used. This means that a user can choose the most appropriate force field for the system. All calculations using DL_POLY 4 have been done with

the PCFF force field.

2.4 Zebedde

To create the polymer structure for DL_POLY, the Zebedde code is used. Zebedde is an automated construction method that can be used to build polymer chains of arbitrary molecular mass, using a Monte Carlo approach [158]. Zebedde stands for Zeolites By Evolutionary De-novo Design of templates, as it was written originally for the de novo design of zeolite templating agents [159]. Recent developments of the code have adapted it to join monomer units via a step-growth process, allowing it to construct polymers. During the construction process, the chain conformation is continually adjusted to give the best representation of the system sterically.

The code functions by randomly selecting either a build or twist action. In the case of build, a new monomer unit is added to a seed molecule. The twist action selects a non-aromatic C-C bond situated in the up to date polymer chain at random, and alters the dihedral by a random amount falling within the range of $\pm 3^{\circ}$. Using the Metropolis Monte Carlo criterion, the new configuration is either accepted or changed, depending upon a given energy criteria. In order for the build action to work, in the building blocks, certain hydrogen atoms are labelled either H_A or H_B. These atoms are the ones which are randomly selected by the code, and following this, a complementary H atom on a new fragment to be added to the monomer unit is chosen. This H atom is added by antialigning the C-H_A or C-H_B bonds so as to allow the H atom to be easily removed in order to form the new C-C bond. The intention here is to ensure that only carbon atoms that were connected to a H_A or H_B atom could form a bond.

The purpose behind having a twist option is that if a build step is unsuccessful, the polymer could be orientated so that any new fragments which may have initially given poor calculated energies could be positioned in a way that was more preferably sterically.

2.5 Forcite

An alternative program to DL_POLY 4 is the Forcite module available in Materials Studio [160]. This module was only used on a parallel workstation hence, the size of the computations were limited to smaller systems. This module was used to confirm the results with DL_POLY 4 that were obtained, including the use of the COMPASS force field.

Forcite plus is an advanced classical mechanics tool [161]. It permits the user to perform energy calculations, geometry optimisations and molecular dynamics simulations on a wide variety of different structures. This can range from simple

molecules to 3D periodic structures. It has a good range of analysis tools allowing the user to obtain information, such as radial distribution functions and diffusion coefficients. Structures that can be modelled well with Forcite plus include polymers, crystals, catalysts and zeolites. In the case of polymers, properties such as density, diffusion, mechanical properties and solubility can be calculated. Diffusivity of atoms or small molecules in polymer matrices is a key speciality of the program, meaning it can be used to measure the diffusion of lithium ions in polymers.

Forcite offers the user a variety of forcefields including the Universal force field (UFF) [162], CVFF [163], PCFF, COMPASS and Dreiding. As with DL_POLY, thermostats and barostats can be used if required. Ensembles which are available include NVE, NVT, NPT and NPH. The NVE ensemble was used for all calculations with Forcite.

To create the polymers for Forcite, the Materials Studio polymer builder is used. Models can be created and edited in the Materials Studio projects. For example, a monomer unit can be built by hand by adding the required atoms and optimising the bond lengths. A polymer can be built from this by defining the repeat unit and multiplying it to give a polymer chain. From here, any of the tools can be applied to perform a variety of simulations. A periodic boundary can also be applied to the model, with the user being able to define the cell parameters by hand.

2.6 MarvinSketch

Using a graphical user interface, MarvinSketch allows the user to draw chemical structures [164]. Atoms and bonds can be defined by hand allowing a large multitude of different structures and types of molecules to be drawn. In this study, a series of monomer units such as ethylene glycol were drawn in MarvinSketch. A variety of simulations can be performed on the defined structure, including molecular mechanics simulations. The MMFF94 force field was used for all structures.

After each monomer unit was optimised, the resulting output structure could be exported, and then opened again in MarvinSketch. The structures can be viewed in both 2D and 3D.

2.7 Antenna simulations

2.7.1 Introduction to antenna methodology

In addition to atomistic simulations, both simulations and measurements were required for the research into the antenna design. The intention was to design an antenna, which could also act on a battery substrate, by means of an integrated design. Chapter 1 discusses the proposed design in greater detail, showing a slot dipole antenna cut into an upper plane of metal, with a battery underneath. The

metal in this case will act as both the current collectors for the battery, as well as containing the antenna. The battery substrate itself will contain no metal, to avoid causing antenna performance degradation in terms of efficiency.

Therefore, a starting point needs to be ascertained for the size and design of the antenna required for this integrated design. The full details of the procedures and results obtained for this are discussed in greater detail in Chapter 6 and Chapter 7, outlining the initial design chosen, along with all modifications, simulations and measurements carried out. The purpose of this section is to provide an overview of the antenna simulation method, as well as the experimental procedures undertaken to perform all of the measurements.

2.7.2 CST Microwave Studio

All simulations for the antenna were performed using the package CST Microwave Studio®. Using the tools available in this package, the size, shape and material could be specified in terms of building blocks and built on a three-dimensional working plane as shown in Figure 2.6.

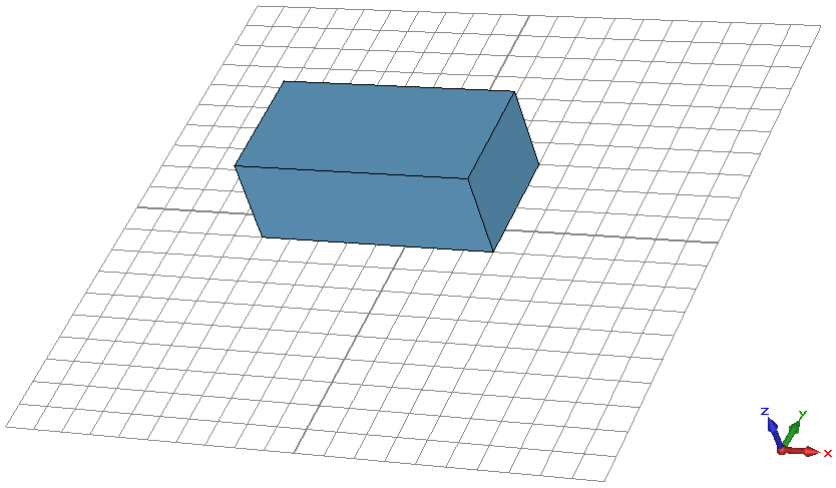

Figure 2.6: The CST three-dimensional working plane allows the user freedom to construct a vast variety of shapes

A frequency range for the simulation could be defined. For all simulations, a range of 1-6GHz was selected to cover the 2.4GHz design frequency later chosen for this project. Once the antenna structure was constructed with all geometric specifications chosen, a port was required. In this case, a waveguide port was added to the structure.

A waveguide port simulates an infinitely long waveguide which excites the antenna [165]. These type of ports are used in order to feed the calculation domain with power, and absorb any power reflected. In an excited waveguide port, the input signal is normalised to 1 sqrt(Watt). In a coplanar waveguide antenna such as the ones used in this study, the waveguide port is placed across the feed of the

antenna with a width of 2-3 times the width of the inner conductor, including the width of the two gaps in the feed. Figure 2.7 shows the recommended dimensions of a coplanar waveguide port.

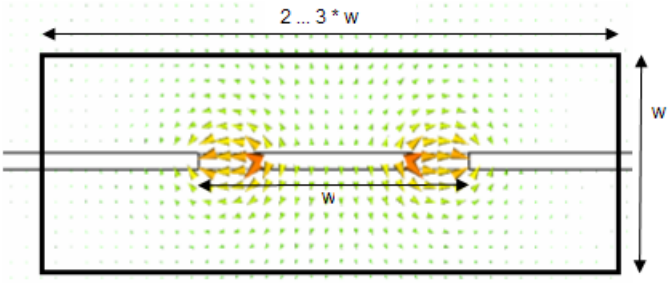

Figure 2.7: Recommended dimensions for a CPW port. Image obtained from CST Online Help [165]

The port should also be enlarged by half of the inner conductor width on each side. In the case of grounded coplanar antennas, the port should be a size sufficient enough to touch the metal ground plane. It is important for the right size port to be defined, since an overly large port will cause higher order modes to propagate resulting in slow energy decays in transient simulations. A port which is too small will not launch the transmission line mode efficiently and will result in degradation of the S-parameter accuracy, possibly causing the transient solver to become unstable.

With the port constructed, a variety of simulations could be performed. For the purposes of this work, the S_{11} parameters and farfield radiation patterns were required. In order for general purpose simulation methods to be applied, the calculation domain is divided up into small cells, known as the mesh. It is in these small cells that Maxwell's equations are solved. To achieve this, the Transient Solver was chosen for this work. The Transient Solver is one of several different types of solver methods used by CST, with the Frequency Domain Solver and Eigenmode Solver being some of the alternatives. The Frequency Domain Solver is particularly useful for electrically small structures, while the Eigenmode Solver is primarily for simulation of closed resonant structures.

The Transient Solver is a time domain solver which can calculate the development of fields through time at discrete locations and time samples. It permits the user to calculate the transmission of energy between various ports along with other sources of excitation or even open space of the structure of interest. The solver is efficient for many high frequency applications including antennas and transmission lines. It can also obtain the whole broadband frequency behaviour of a device from just a single calculation run. This makes the Transient Solver the most suitable for our aims.

The Transient Solver uses a Finite Integration Technique to apply advanced numerical techniques, in particular the Perfect Boundary Approximation (PBA)®, which is used for the spatial discretization of the structure. This is often used in

combination with the Thin Sheet Technology™ (TST). TST is useful particularly for Perfect Electrical Conductor (PEC) structures where details are lower than the method's resolution, as it enables two non-PEC regions within a single cell (See Figure 2.8). However, if more than two non-PEC areas are present in a cell, it must be filled completely with PEC material. Using a hexahedral mesh, complex structures and curved surfaces can be simulated, within the cubic mesh cells without extreme refinement of the mesh. Both of these techniques are very useful in avoiding extremely small mesh steps which has a positive effect on the simulation time.

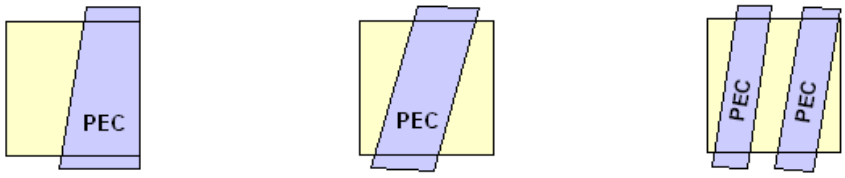

(a) 1 non-PEC area (b) 2 non-PEC areas (c) Many non-PEC areas

Figure 2.8: (a) A normal PBA mesh cell with one non-PEC area (b) TST allowing two non-PEC areas (c) A critical cell (multiple non-PEC areas), therefore must be filled completely with PEC material. Images obtained from CST Online Help [165]

Each field in the transient simulation is calculated by means of a step by step "Leap Frog" time progression scheme. The mesh has influence over the accuracy of the simulation as well as the speed. Owing to the electrically thin layers, for the simulations in this study, the minimum number of mesh lines per wavelength was set to 40, as this gave a good simulation accuracy without slowing down the calculation noticeably. Once the simulation was performed in each case, a variety of post-processing tools were available with which to analyse the results in further detail. The tools used in this project were for the analysis of S-parameters and radiation patterns.

2.7.3 S_{11} parameters

When working at microwave frequencies, there is an issue when attempting to measure voltages and currents [66]. This is because direct measurements may involve the magnitude and phase of a wave travelling in a given direction, or also of a standing wave. Therefore, equivalent voltages and currents along with related impedance and admittance networks become an issue in high-frequency networks, being considered more of an abstraction. In order to give a representation more in line with direct measurements, the scattering matrix is introduced. This takes into account incident, reflected and transmitted waves.

The scattering matrix gives a complete description of the network, which can be seen at the N-ports. An N-port network is an arbitrary network whereby the ports may be for any type of transmission line or equivalent for a single propagation

waveguide mode. If a single network port is a waveguide that supports multiple propagating modes, additional ports can be added to account for these extra modes. A terminal plane, t_n, along with equivalent voltages and currents for incident (V_n^+, I_n^+) and reflected (V_n^-, I_n^-) waves, is defined at a specific point on the nth port of the network. At the nth terminal plane, the total voltage and current are shown by Equations (2.50) and (2.51).

$$V_n = V_n^+ + V_n^- \tag{2.50}$$

$$I_n = I_n^+ + I_n^- \tag{2.51}$$

Referring back to the scattering matrix, we know that for an N-port network, V_n^+ is the amplitude of the incident voltage wave at the nth port, while V_n^- is the amplitude of the reflected voltage wave at the nth port. These incident and reflected voltage waves can be related to the scattering matrix, or $[S]$ matrix as shown below:

$$\begin{bmatrix} V_1^- \\ V_2^- \\ \vdots \\ V_N^- \end{bmatrix} = \begin{bmatrix} S_{11} & S_{12} & \cdots & S_{1N} \\ S_{21} & & & \vdots \\ S_{N1} & \cdots & & S_{NN} \\ \vdots & & & \end{bmatrix} \begin{bmatrix} V_1^+ \\ V_2^+ \\ \vdots \\ V_N^+ \end{bmatrix}$$

The scattering matrix can also be represented by Equation (2.52).

$$[V^-] = [S][V^+] \tag{2.52}$$

When it comes to obtaining S-parameters from the simulated antenna, we are looking at a specific element of the scattering matrix. In order to determine a specific element, Equation (2.53) is used.

$$S_{ij} = \left. \frac{V_i^-}{V_j^+} \right|_{V_k^+ = 0 \text{ for } k \neq j} \tag{2.53}$$

This equation in simple terms shows that S_{ij} can be identified by exciting port j with an incident wave of voltage, V_j^+, and then measuring the amplitude of the reflected wave, V_i^-, that comes out of port i. All ports other than the jth port are terminated (meaning the incident wave is set to zero) in matched loads. This is done to avoid reflections. This means that S_{ij} can be defined as the transmission coefficient from port j to i. Meanwhile, S_{ii} is also known as the reflection coefficient, when looking into port i. In both cases, all other ports are terminated in matched loads.

For each antenna simulated in this study, only one waveguide port is present. This means that only the S_{11} parameters, or the reflection coefficient can be analysed.

Therefore, S_{11} is shown by Equation (2.54).

$$S_{11} = \left.\frac{V_1^-}{V_1^+}\right|_{V_2^+=0} \tag{2.54}$$

From the S_{11} parameters, properties such as the fractional bandwidth can be calculated. It is also useful in comparison to measurements to ensure that they match at the resonant frequency. Figure 2.9 shows an example of a S_{11} plot obtained from CST.

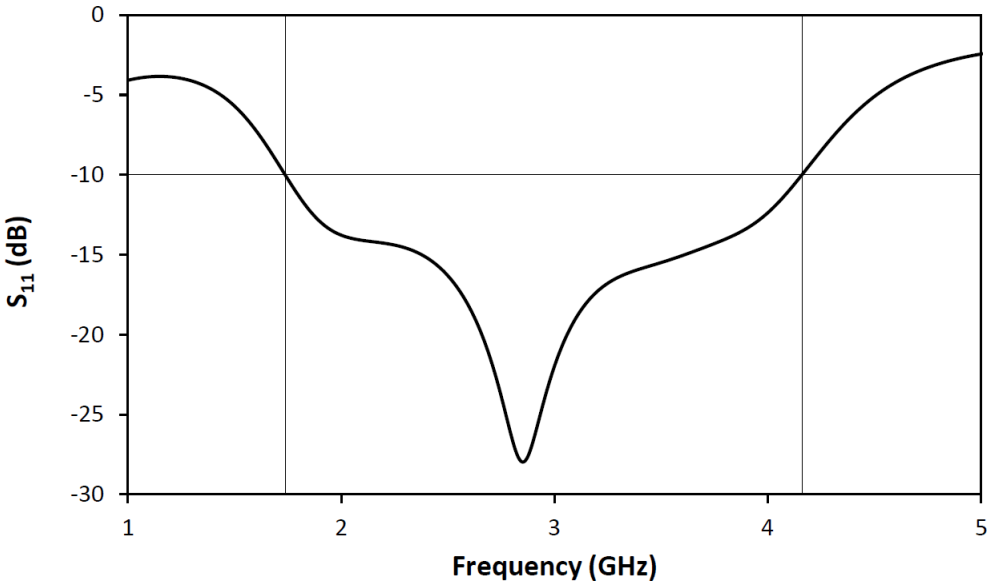

Figure 2.9: Example S_{11} plot for slot antenna

In this particular example, the peak observed here is the resonant frequency, or reflection coefficient. The depth and sharpness of the peak can indicate how well matched it is. The lines in the example indicate the matched operating band, which in this case is below -10dB. From the operating frequency, which is seen at the null of the peak, we can calculate the fractional bandwidth of the antenna. This is done by subtracting the lower frequency limit of the operating band (the lowest frequency at -10dB) from the upper frequency limit of the operating band (the highest frequency at -10dB). This value is then divided by the operating frequency (usually the frequency of the null), and multiplied by 100 to obtain a percentage. This is summarised in Equation (2.55).

$$\%bandwidth = \frac{Freq.^{upper} - Freq.^{lower}}{Freq.^{null}} \times 100 \tag{2.55}$$

S_{11} parameters can also give us other useful information such as showing how lossy an antenna is. They are also useful for showing how a simulated antenna compares with measurements, with a match at the resonant frequency showing good comparison between the two. Antenna input impedance match can also be observed from the S_{11}. This is defined as the ratio of voltage to current at its input [8]. In our

study, the feed line for the antenna is normalised to match at an input impedance of 50Ω. This value is chosen as it provides a good compromise between power handling and attenuation.

The input impedance for the antenna is measured in CST by using a curve marker on the S_{11} plot, and placing it at the null of the resonant frequency. An impedance Smith Chart can then be viewed, which shows the input match, with the real and imaginary numbers shown at the bottom of the screen. An example impedance Smith Chart is shown in Figure 2.10.

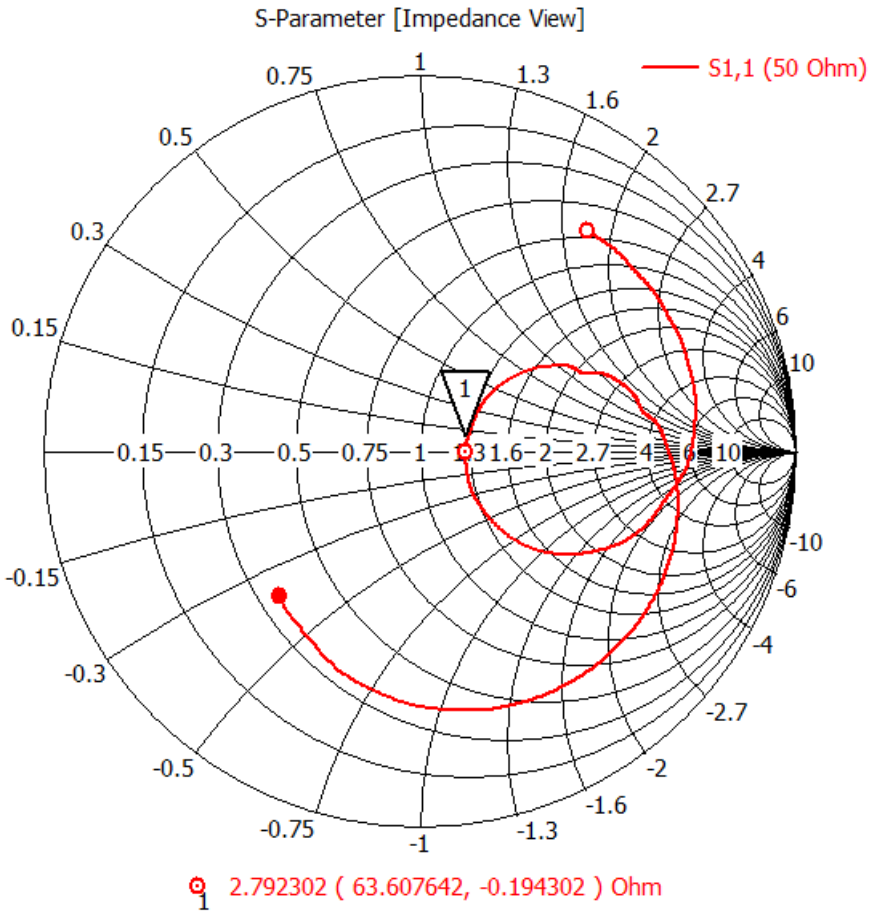

Figure 2.10: A Smith Chart example showing the input impedance match

Underneath the Smith Chart in red, displayed in brackets, are the real and imaginary parts of the impedance, i.e. the resistance and reactance at the resonant frequency. Since the above example is normalized to 50Ω, the closer the real number is to 50Ω (and the closer the imaginary number is to 0), the better the antenna input impedance match.

2.7.4 Radiation patterns

Radiation patterns (or polar diagrams) are one of the most important properties of an antenna [8]. For a transmitting antenna, this is a plot of the power/field strength transmitted by the antenna in a variety of different angular directions.

Polar diagrams can be obtained for both the vertical and horizontal planes. The same patterns will apply regardless of whether the antenna radiates or receives due to the principle of reciprocity. The power that an antenna radiates can be concentrated in a certain direction. This value of directivity can be expressed in terms of its power gain, G. This is defined in a particular direction by Equation (2.56).

$$G = \frac{\text{Power radiated by an antenna}}{\text{Power radiated by the reference antenna}} \tag{2.56}$$

In other words, antenna gain is the ratio of maximum radiation intensity from the antenna specified, to the maximum radiation intensity given from a loss-free isotrope [9]. Losses due to resistance in metallic and dielectric materials are common, and lead to differences between power delivered to the antenna input and the power that an antenna radiates [66]. Radiation efficiency for an antenna is defined as the ratio of desired output power to the input power that is supplied. This is shown in Equation (2.57).

$$\eta_{rad} = \frac{P_{rad}}{P_{in}} = \frac{P_{in} - P_{loss}}{P_{in}} = 1 - \frac{P_{loss}}{P_{in}} \tag{2.57}$$

Here, P_{rad} is the power radiated by the antenna, while P_{in} is the power which is supplied to the antenna input. P_{loss} is the power which is lost in the antenna. Other factors may play a part in the effective loss of transmit power, i.e. impedance mismatch at the antenna input, or polarisation mismatch with the receiving antenna. These losses, however, are not normally attributed to the antenna itself, since they can be negated by the use of matching networks or positioning of the receiver antenna.

Referring back to the directivity of the antenna, we know that it is a function of the shape of the radiation pattern, or polar diagram, meaning any losses in the antenna itself have no bearing. It is a known fact that the radiation efficiency of less than unity means that the antenna will not radiate the entirety of the input power it receives. Therefore, the antenna gain, G, can also be represented as a product of its directivity and radiation efficiency, shown in Equation (2.58).

$$G = \eta_{rad} D \tag{2.58}$$

What we can establish from this is that the gain will always be either equal to or less than the directivity. Antenna gain is often expressed in units of dBi meaning decibels referred to an isotropic antenna. Figure 2.11 shows an example radiation pattern obtained from a slot antenna in CST, both in three-dimensions, along with the two-dimensional polar diagram.

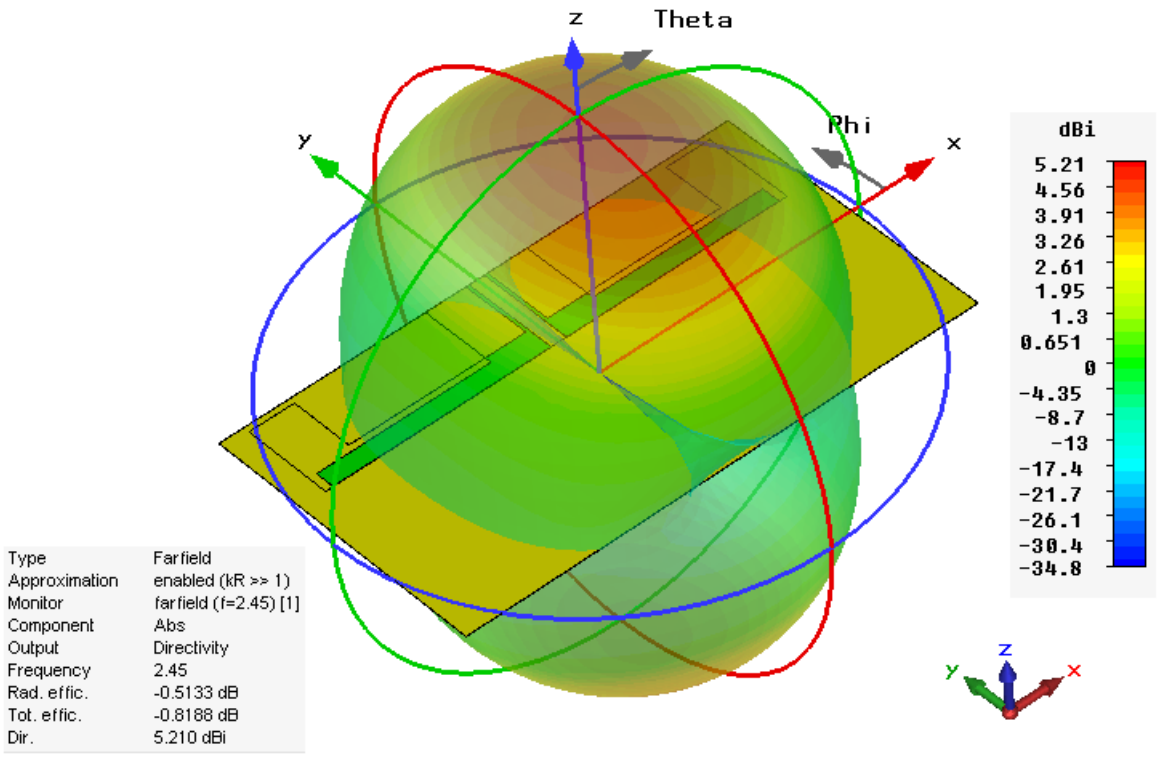

Figure 2.11: (a) Simulated 3D radiation pattern for antenna

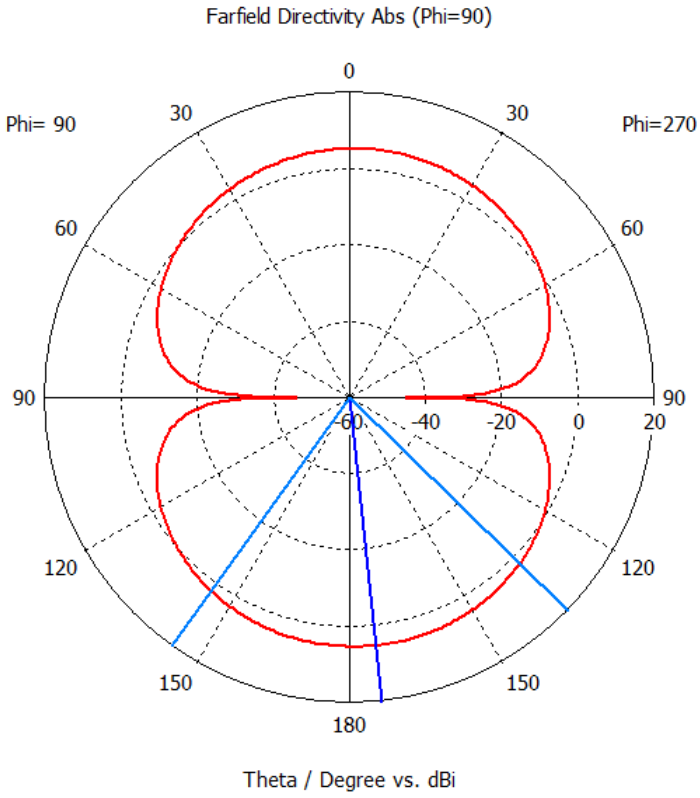

Figure 2.11: (b) Simulated polar diagram for antenna

A radiation pattern is obtained in CST by means of a field monitor. Here, the frequency at which the radiation pattern is desired (often the resonant frequency) is

specified. In the above example, the three-dimensional radiation pattern shows the underlying antenna structure. From this, we can assess how the power is radiated in relation to the position of the antenna. Other key details from this include the directivity value, along with the total efficiency, from which the antenna gain can be calculated. In a polar diagram, the lobe with the maximum magnitude of far-zone field strength with relation to elevation angle, θ, is classed as the main beam [66]. Any additional lobes that may be present at lower levels are referred to as sidelobes.

Another property of importance to the radiating antenna is its radiation resistance [8]. This is associated with the transmitted power from the antenna. The radiated power can be expressed as I^2R_r watts, where I is the r.m.s antenna current and R_r is the radiation resistance, which acts like a circuit resistance dissipating heat. The larger the radiation resistance, the greater the power radiated by the antenna. On the other hand, for receiving antennas, the input impedance is key. In most cases, it equals the radiation resistance. For example, a centre-fed half wavelength dipole has an input impedance of 75Ω, which is equal to a radiation resistance, also of 75Ω.

2.8 Antenna synthesis

In order to compare with the simulated results, several antenna measurements were also performed. In order to achieve this, the antenna was synthesised via an etching procedure, and measured to obtain the S_{11} parameters and radiation patterns. Since it was important to ensure that all dimensions for the fabricated antenna were identical to the simulation, a mask was created, using the antenna patterns for the simulated design of choice. To create this, the antenna slot pattern in CST was exported as a Gerber layer, and this was opened in a package known as ViewMate [166]. The antenna pattern could then be printed as a negative to create the mask.

A copper film was used with a Mylar substrate, a polyester film made from Polyethylene Terephthalate (PET). To begin with, the film was cleaned with IPA (isopropyl alcohol). The antenna mask was laminated onto the copper layer using a UV-sensitive etch-resist film. The negative slot dipole pattern was then exposed under UV light, before being developed with potassium carbonate to wash all areas that had not been struck by the UV light. Iron (III) chloride was used to etch the antenna pattern, after which the antenna was washed with water to remove the acid. The UV-sensitive film was removed using a photo-resist stripper (sodium metasilicate), and washed with water, before drying in air. A port was then attached to the antenna feed line by use of a soldering method.

2.9 Antenna measurements

2.9.1 S_{11} measurements

The fabricated antenna was measured using a Vector Network Analyser (VNA), in order to view the S_{11} patterns. Before a measurement took place, the cable used to attach the antenna port to the VNA was effectively removed from the measurement by calibration using a set of known value terminations. After this, the antenna was fixed securely to the cable, and the S_{11} could be measured. The S-parameters could be exported from the VNA, from which the data could be obtained. Figure 2.12 shows the VNA used in this study.

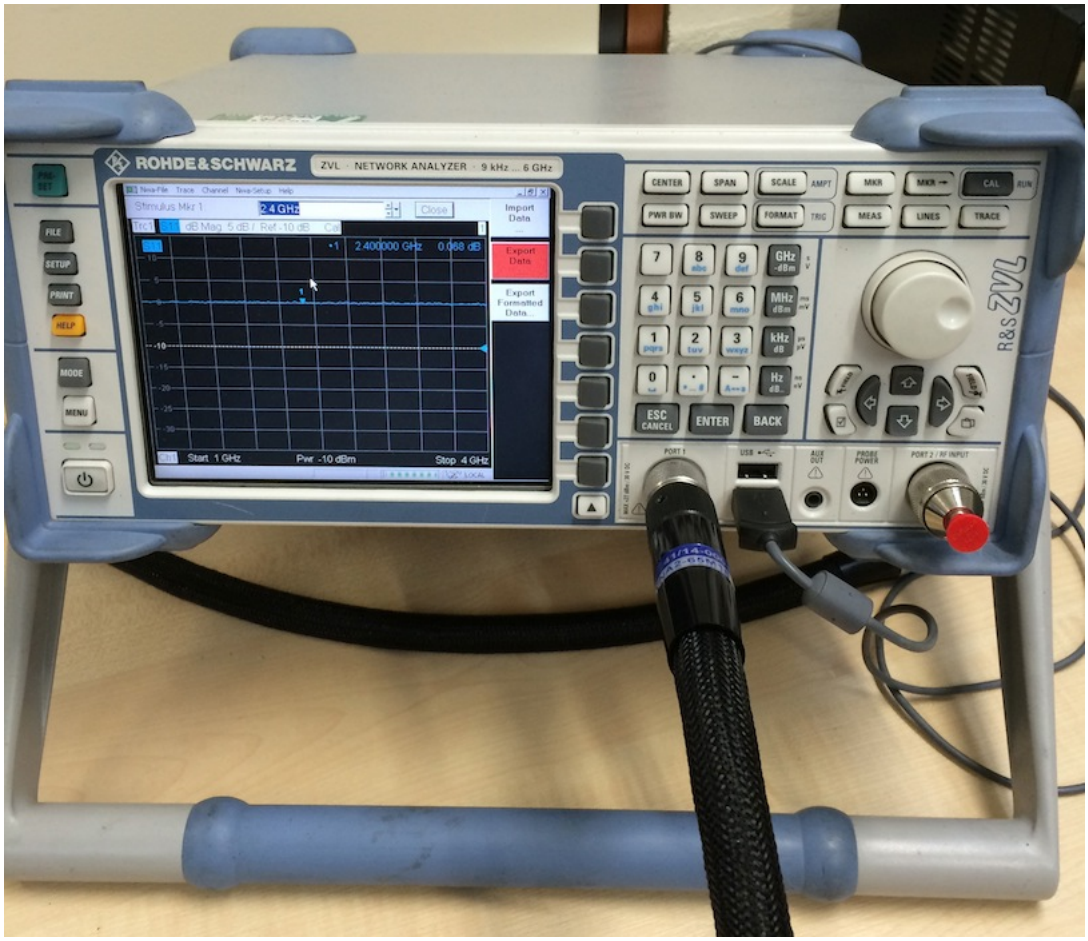

Figure 2.12: VNA used for S_{11} measurements

2.9.2 Radiation pattern measurements

Radiation pattern measurements could also be obtained. Here, a two-port VNA was used for measuring the S_{21} parameters. A transmit and receiver antenna were set up in an anechoic chamber. A general purpose wide-band transmit antenna was used for our purposes. A 360° scan was performed with sweeps measured as the transmit antenna rotated. For the first set of measurements, a total of four polarisations took place with the transmit antenna, whereas the second set required the use of a

pedestal in order to mount the antenna, meaning at least two different polarisations were possible. Figure 2.13 shows an example of a transmit antenna in the anechoic chamber along with the receiver antenna.

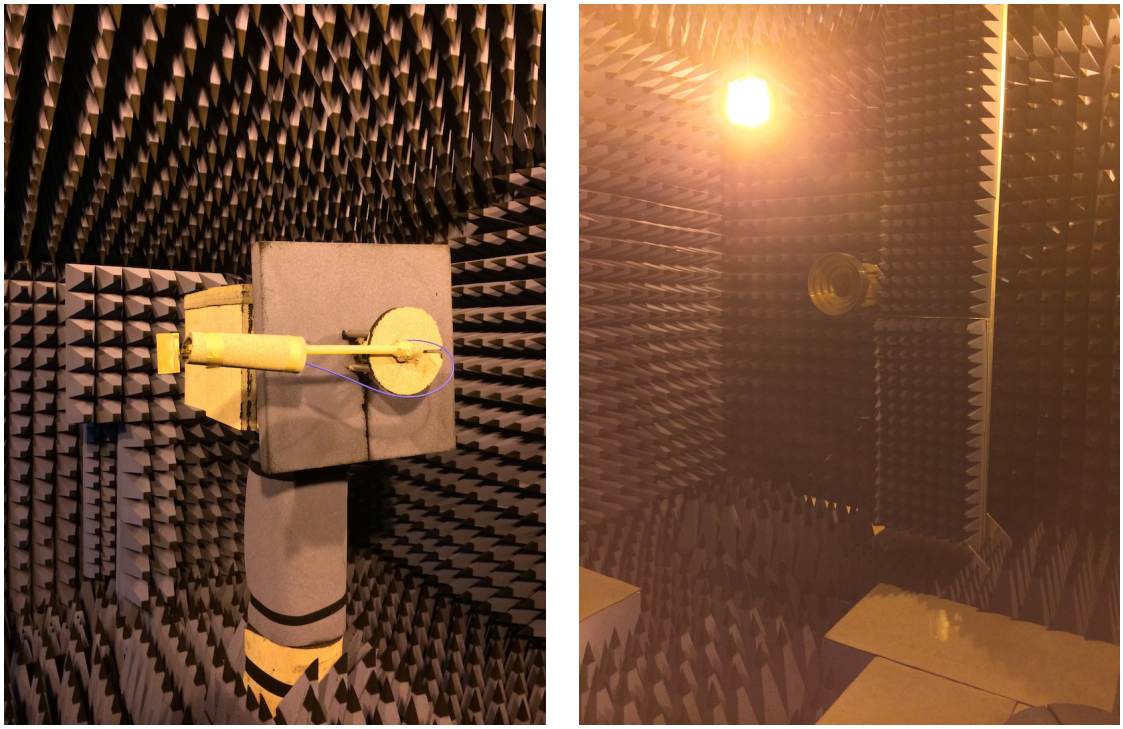

(a) (b)

Figure 2.13: Set-up of (a) transmit and (b) receiver antenna in the anechoic chamber

2.9.3 Permittivity measurements

Permittivity and dielectric loss measurements were performed on a sample of the co-polymer PEDOT:PSS [167]. Aliquots (∼30ml) of conductive grade PEDOT-PSS (3% weight dispersion in water) were pipetted into five separate sample dishes. The samples were dried for 48 hours at 55°C under atmospheric pressure. The precipitate was collected from each sample and processed within a ball-mill (800rpm, 40mins). A fine powdered sample was produced and subsequently pressed into a pellet by use of a 25mm pellet-press. The pellet had dimensions of a width of 25mm with a thickness of 3mm.

The permittivity measurements of the sample were achieved by etching a 24mm long CPW line onto a Mylar sheet which was then placed directly on top of the sample. The gap between the signal and ground lines was set to 1.5mm to ensure good penetration of the field into the material at the frequency range of measurement. An Anritsu 37397C network analyser with on-wafer calibration was used to measure the S-parameters up to 20GHz. The line proved to be well matched to 50Ω allowing the phase constant and effective permittivity of the line to be calculated directly from the S_{21} measurement. The phase difference between two lengths of CPW lines placed on top of the PEDOT:PSS pellet was calculated using Equation (2.59).

$$\phi = \beta \times (L1 - L2) \tag{2.59}$$

Here, ϕ is the phase delay, while β is the propagation constant, and *L1* and *L2* are the two transmission line lengths. β is equal to $2\pi/\lambda$. From this, the effective permittivity can be found using Equation (2.60).

$$\epsilon_{eff} = \frac{\beta^2}{k_0^2} \tag{2.60}$$

Here, $k_0 = \omega/\mathrm{c}$, where ω is the frequency and c is the speed of light in free space. The relative permittivity, ϵ_r can be solved using Equation (2.61).

$$\epsilon_{eff} = \frac{(\epsilon_r + 1)}{2} \tag{2.61}$$

This technique is similar to the Thru-Reflect-Line method which can also be used to calculate ϵ_{eff} [66]. However, in this case, it was simplified due to the assumption that the S_{11} in this case was small. This assumption was made due to the expected high dielectric loss in the sample and was shown to be the case.

Chapter 3

Acetylene

With polyacetylene being regarded as a big discovery and a breakthrough with regards to conducting polymers, it is of interest as a non-metallic battery material. Due to its simple structure, it can be used as a model system when developing novel, more complex computational theories. For this purpose, a detailed investigation has been undertaken on the monomer unit, acetylene. Simulations of acetylene can provide us with a useful insight into its electrical properties, with future work leading up to a potential analysis of three-dimensional polyacetylene, such as that performed by Zicovich-Wilson [168]. Figure 3.1 shows the chemical structure of the acetylene molecule.

Figure 3.1: Structure of acetylene

Acetylene (C_2H_2) is the simplest molecule amongst those that possess the carbon-carbon triple bond [169]. It is a linear molecule crystallising in two known polymorphs, dependant upon the temperature and pressure of the system. Acetylene crystallises in both a low temperature and a high temperature structure [170]. These crystal structures can be defined experimentally by use of techniques such as neutron diffraction [170, 171]. The low temperature structure is defined by an orthorhombic crystallographic cell, with the *Acam* (*Cmca*) space group. Here, the acetylene molecules in the cell are found to be almost perpendicular to each other [172] (See Figure 3.2a). The high temperature structure takes the form of a cubic crystallographic cell. This phase was determined by Sugawara and Kanda [169] at 156K, using single-crystal X-ray diffraction. Here, the space group *Pa3* was used to describe the cell with a lattice parameter at 156K of a = 6.14Å with acetylene monomers in a T-shaped configuration (See Figure 3.2b).

The transition temperature between the two phases was reported to be 133K for C_2H_2 [169] and 149K for C_2D_2 [173]. Further refinements were made for the

cubic structure with the single-crystal X-ray data measured at 141K by van Nes and van Bolhuis in 1979 [174]. For C_2D_2, the structural parameters were obtained using neutron powder diffraction at 4.2K for the orthorhombic *Acam* space group [175]. These measurements were further refined at 77K [176] and 109K [177]. A refinement for orthorhombic C_2D_2 was also made against neutron diffraction data at 15K by McMullan [170] and it is this particular structure of acetylene that is of interest to our study using ab initio calculations. This is because the D-positions can be seen in this refinement, while the H-positions cannot been seen in Neutron or X-Ray Diffraction.

A problem that is present in the modelling of acetylene within the DFT framework is the description of van der Waals forces between molecules in the crystal structure for density functional theory. Kohn-Sham density functional theory is now seen as one of the most well-known and used methods for electronic structure calculations in the areas of condensed matter physics and quantum chemistry [87, 88]. With the thermochemistry of molecules considered, the first major step in that direction was to introduce generalised gradient approximations (GGAs) to provide a correction for local density approximation (LDA). LDAs did not appear to yield an improvement in results compared to Hartree-Fock (HF). However, one of the most significant drawbacks in GGA functionals was the poor description of long-range electron correlations, which are responsible for van der Waals forces [178, 179, 180]. It is apparent that van der Waals interactions present a major challenge for DFT approximations. The issue with LDA functionals are that they to tend to overbind [180, 181, 182, 183]. GGA and hybrid functionals are more sensitive to the choice of approximation [179], with the Becke 1988 exchange [100] showing a repulsive interaction in many cases [178, 180, 181, 183, 184, 185] while functionals based on PW91 and PBE show binding but with a lack of accuracy [182, 183, 184, 185, 186].

Conventional exchange-correlation functionals have been utilised for a range of different systems, in particular, dimers such as N_2 [187], C_6H_6 [178, 184, 186, 188], as well as C_2H_2 [186, 189]. In the case of N_2, ab initio MP2 and MP4 methods were compared to DFT [187]. The study confirmed that B3LYP was unable to correctly model the van der Waals forces in the N_2 systems, as opposed to the exchange-correlation functional PW91-PW91, which agreed well with the MP results. The benzene study also compared DFT methods to MP2 calculations along with experiments [188]. Here, LDA, LDA+B and LDA+B+LYP functionals were tested. In this case, B represents the Becke gradient correction. With the dispersion-corrected results, LDA overestimated the binding energy of the dimer, and underestimated the dimer separation significantly, while LDA+B and LDA+B+LYP showed better agreement with the MP2 calculations. For the acetylene dimers, it was established that the BLYP, BPW91 and B3LYP functionals do not correctly model the dispersion interaction [189]. They also showed poor agreement with the HF methods

employed, which suggested that the functionals also did not correctly model the repulsion interaction.

In order to address these issues regarding dispersion, empirical long-range corrections e.g. damped $C_6 \cdot R^{-6}$ terms are among the most promising [190] with the most widely applied and tested method being DFT-D, proposed by Grimme [191]. This method uses damped interatomic potentials to describe the dispersive energy. Combined with the BLYP and PBE functionals, Grimme's correction gave desirable accuracy for a range of applications including dimers and trimers of pyridine [192], and azulene [193]. A few problems were, however, identified with the original DFT-D method [191]. Firstly, consistent atomic parameters (C_6) were only available for a small number of elements, being H, and C-Ne. Any calculations involving third-row elements gave errors. The correction also showed inconsistencies for normal thermochemistry properties such as atomisation energies. Grimme [191] initially defined a general set of atomic parameters with which he then improved by addressing the above issues [190]. The new DFT-D approach was less empirical and required less parameters than other methods. Furthermore, a set of s_6 scaling parameters were derived, which were functional-dependant, in order to adjust the dispersion correction.

Despite these improvements, a few problems still remained. Civalleri's study [194], showed that the hybrid B3LYP-D method gave poor agreement with the experimental structures in the case of NH_3, CO_2 and cubic C_2H_2 as lattice parameters were underestimated. The B3LYP-D dispersion parameters were modified slightly to try and show an improvement in agreement. Several aspects were considered when explaining the underestimation. For molecular complexes, the empirical term was calibrated, while for molecular crystals, the intermolecular contacts are shorter leading to a larger overlap between charge density distributions. The damping function controls this feature and is likely considered too short-range for most crystalline systems. The s_6 scaling factor increases the whole contribution for B3LYP by a factor of 1.05. The end result was an estimation of the dispersion contribution which was unbalanced, leading to overestimation in cohesive energy and underestimation of lattice parameters.

Civalleri *et al.* modified the dispersion correction by following a method initially suggested by Jurečka *et al.* [195]. The atomic van der Waals radii in the form of the damping function were rescaled, which allowed for more activity in the long-range region. This lead to a decrease in the dispersion contribution which was only included in the regions for which B3LYP does not contribute to the intermolecular interactions. Along with the scaling factor of the correction, the van der Waals radius of hydrogen was also identified as a key contribution. This value has a determination upon the penetration of the damping function in terms of balancing the dispersion contribution for both dispersion bonded and hydrogen bonded crystalline

systems. Therefore, to improve the dispersion correction term, the original s_6 scaling factor was modified to a value of 1.00. The scaling factor for the atomic van der Waals radius of hydrogen was altered. Furthermore, the van der Waals radii of all heavy atoms (all atoms other than hydrogen) were rescaled from their original values assigned by Grimme. All numbers for heavy atoms were scaled by a factor of 1.05. In order to derive these modifications, the atomic van der Waals radii were increased progressively to determine the best fit between simulation and experiment. This augmented correction term is known as B3LYP-D*.

In some cases, however, using B3LYP causes issues. For example, when lithium metal is used, B3LYP results in a semi-conducting/insulating system due to a band gap, as opposed to the desired conducting system, necessary for situations such as measuring lithium conductivity. For this reason, hybrids such as B3LYP are not always suitable, particularly for mixed conducting systems such as polymer electrolytes. Therefore, it is proposed to use the non-hybrid BLYP functional as an alternative for these systems. Due to the advantages that B3LYP offers as a whole, it is desirable to take an approach similar to B3LYP, but removing the Hartree-Fock exchange which is causing mixed conducting systems to become insulating. Therefore, BLYP provides an adequate solution to this issue, making it more desirable over a different functional such as PBE.

The aim of this study is to show a detailed investigation into what effect the dispersion correction is having on the systems of cubic and orthorhombic acetylene, and to gain a greater understanding of the electrostatic properties. For this study, a new model (BLYP-DS) was derived and compared with Grimme's traditional model (BLYP-D). What makes this newly derived model unique is that it is primarily for solids, and similar to Civalleri's B3LYP-D* method. Several hydrogen-bonded systems are used to derive the BLYP-DS approach, which is then applied to the two polymorphs of acetylene to see how it compares with the other functionals.

3.1 Methodology

All calculations in this study were undertaken with the CRYSTAL09 [82] software employing both pure (BLYP) [100, 101] and hybrid (B3LYP) [102] density functional theory (DFT). In the CRYSTAL09 code, the atomic orbitals are expanded as Gaussian basis functions. For all atoms, a 6-31G(d,p) [196] basis set was employed. Other larger basis sets such as aug-cc-pVTZ failed to optimise due to being too diffuse, while basis sets such as 6-311G** lead to conducting systems. The structure was also optimised with the TZVP basis set at the BLYP level, but the experimental structure was poorly modelled, so the decision was made to employ the 6-31G(d,p) basis set for all functionals used in this study. A Pack-Monkhorst grid of 8×8×8 was employed while the Columb and exchange integrals were trun-

cated at $10^{-7}, 10^{-7}, 10^{-7}, 10^{-7}$ and 10^{-14}. All calculations were performed self-consistently. Geometry optimisations were performed using the Broyden-Fletcher-Goldfarb-Shanno (BFGS) [197, 198, 199, 200, 201] algorithm and converged to an energy value of 10^{-7} Hartree while the gradient and root mean square (rms) displacement were 6×10^{-5} and 1.2×10^{-4} Hartree/bohr, respectively.

As the crystal structure is being modelled, the experimental crystal structure is required from the literature. Table 3.1 shows all of the necessary crystal data required to replicate the cubic and orthorhombic structures of acetylene.

Table 3.1: Experimental crystal structure data for orthorhombic and cubic acetylene [170]

Parameter		Orthorhombic	Cubic
Temperature		15K	131K
Space group		*Acam*	*Pa3*
Lattice parameters	a	6.198	6.094
	b	6.023	
	c	5.578	
Cell volume (Å^3)		208.2	226.3
Fractional coordinates		C_x: 0.0621	C_x: 0.0562
		C_y: 0.0756	C_y: 0.0562
		C_z: 0.0000	C_z: 0.0562
		D_x: 0.1709	H_x: 0.1524
		D_y: 0.2135	H_y: 0.1524
		D_z: 0.0000	H_z: 0.1524

Dispersion forces were treated with the method originally proposed by Grimme [190] and added to the BLYP functional given by Equation (3.1)

$$E_{\mathrm{BLYP-D}} = E_{\mathrm{BLYP}} + E_{\mathrm{Disp}} \tag{3.1}$$

E_{Disp}, the empirical term is described by Equation (3.2).

$$E_{\mathrm{Disp}} = -s_6 \sum_{\mathbf{g}} \sum_{ij}{}' f_{\mathrm{dmp}}\left(R_{ij,\mathbf{g}}\right) \frac{C_6^{ij}}{R_{ij,\mathbf{g}}^6} \tag{3.2}$$

Grimme proposed a defined set of parameters with an optimised scaling factor (s_6), which is functional dependant. Grimme derived the s_6 value to be equal to 1.2 for BLYP. To include long range dispersion contributions, pair-wise damping factors were introduced for each atom referred to as C_6 and R_{vdw} in Equation (3.2), corresponding to the dispersion coefficient and van der Waals radius, respectively (see Table 3.2).

A series of parameters were required for the GRIMME keyword in CRYSTAL09 [82], i.e. the scaling factor (s_6), steepness of the damping function (d=20) and cutoff radius for the direct lattice summation ($\mathbf{g}$) in Equation (3.2). The number of atomic species were then defined, and for each individual atom, the following information was needed: The atomic number of the species, the dispersion coefficient, and the van der Waals radius. Table 3.2 gives the parameters used throughout this study compared with those used by Grimme [190].

Table 3.2: A summary of van der Waals dispersion parameters derived by Grimme (D) [190], and current work (DS). An s_6 parameter of 1.20 was applied to BLYP-DS

Element	C_6	R_{vdw} (D)	R_{vdw} (DS)
H	0.14	1.001	1.300
C	1.75	1.452	1.452
N	1.23	1.397	1.397
Cl	5.07	1.639	1.639
F	0.75	1.287	1.287

For the newly-derived BLYP-DS, the van der Waals radius for hydrogen was modified from 1.001 to 1.30, while keeping Grimme's parameters for the heavy atoms unchanged. The van der Waals radius of hydrogen was considered to be the main contribution to the dispersion, and it was intended to change as few parameters as possible. Fewer parameter changes increases the likelihood of being able to transfer this correction to other functionals such as PBE. The newly derived s_6 value was 1.20. The BLYP-DS method has been applied to urea, ammonia, hydrogen cyanide (HCN), hydrogen chloride (HCl) and hydrogen fluoride (HF) in addition to acetylene. Table 3.3 shows the results for the optimised lattice parameters and lattice energies used in each of these hydrogen-bonded systems.

Table 3.3: Optimised lattice parameters and counterpoise-corrected energies for HCN [202], HCl [203, 204], HF [205, 206], urea [82, 207] and ammonia [208]

Molecule/Functional		Exp. (Å)	Calc. (Å)	Error (%)	$\Delta E_{latt}^{exp.}$ (kJ/mol)	$\Delta E_{latt}^{calc.}$ (kJ/mol)	Error (%)
HCN - BLYP	a	4.13	4.58	9.6	-38.5	-20.6	-46.5
	b	4.85	5.16	6.5			
	c	4.34	4.17	-1.5			
HCN - BLYP-D	a	4.13	3.96	-5.3	-38.5	-39.6	2.8
	b	4.85	4.47	-7.8			
	c	4.34	4.19	-3.4			
HCN - BLYP-DS	a	4.13	3.94	-6.0	-38.5	-38.6	0.1
	b	4.85	4.46	-8.0			
	c	4.34	4.22	-3.0			
HCl - BLYP	a	5.84	7.81	33.8	-25.9	-10.7	-58.8
	b	5.06	7.40	46.3			
	c	5.38	5.88	9.4			
HCl - BLYP-D	a	5.84	6.03	3.4	-25.9	-20.4	-21.2
	b	5.06	5.36	5.9			
	c	5.38	5.50	2.3			
HCl - BLYP-DS	a	5.84	6.06	3.9	-25.9	-19.8	-23.4
	b	5.06	5.38	6.3			
	c	5.38	5.50	2.2			
HF - BLYP	a	3.31	3.83	15.7	-54.0	-45.4	-16.0
	b	5.22	5.34	2.4			
	c	4.26	4.28	0.6			
HF - BLYP-D	a	3.31	3.37	1.9	-54.0	-59.2	9.6
	b	5.22	5.32	2.0			
	c	4.26	4.25	-0.2			
HF - BLYP-DS	a	3.31	3.37	1.9	-54.0	-57.4	6.3
	b	5.22	5.33	2.0			
	c	4.26	4.28	0.6			
Urea - BLYP	a	5.57	5.73	3.0	-103.6	-73.2	-29.4
	c	4.68	4.70	0.3			
Urea - BLYP-D	a	5.57	5.31	-4.6	-103.6	-129.1	24.6
	c	4.68	4.66	-0.6			
Urea - BLYP-DS	a	5.57	5.43	-2.5	-103.6	-121.5	17.3
	c	4.68	4.66	-0.6			
NH_3 - BLYP	a	5.05	5.29	4.8	-36.0	-29.0	-19.5
NH_3 - BLYP-D	a	5.05	4.77	-5.5	-36.0	-53.7	49.1
NH_3 - BLYP-DS	a	5.05	4.96	-1.8	-36.0	-46.5	29.1

For all systems, BLYP-DS is making a noticeable improvement in lattice energy while for lattice parameters, the trend is less straightforward. It should be noted that the differences between BLYP-D and BLYP-DS in HCN, HCl and HF are small when comparing their error in lattice parameters, although it does give slightly better lattice energies for HCN and HF.

For urea and NH_3, we see the great benefit of the BLYP-DS method. In both cases, BLYP-DS shows a clear improvement in both lattice parameters and energies with values closer to the experiment. In this situation, it does appear that the newly derived DS correction is making a significant difference, and needs to be considered for hydrogen-bonded systems such as these. BLYP-D is underestimating the lattice parameters and energies for urea and NH_3, but by augmenting the correction term, we can make reasonable improvements in these values with much smaller percentage errors. To summarise, the BLYP-DS approach is improving the overall results for the solid state.

When deriving the s_6 scaling factor for BLYP-DS, it is important to consider how the results are affected for multiple s_6 values to determine the best fit. In this instance, it is important to ensure that the derived correction is consistent across multiple molecular solids. It is no use in modifying the scaling factor in a way which shows improved results for some molecular solids while losing accuracy for others. To test this, three different scaling factors for BLYP-DS were tested (1.1, 1.2 and 1.3) for HCN, HCl, HF, Urea, NH_3, and both the cubic and orthorhombic structures of acetylene. As the scaling factor made a minimal difference upon the lattice parameters, the lattice energies will be observed. Table 3.4 shows the lattice energies in each case.

Table 3.4: Lattice energies for HCN [202], HCl [204], HF [206], urea [207] and ammonia [208] using the BLYP-DS functional at different scaling factors

Molecule	Scaling factor (s_6)	$\Delta E_{latt}^{calc.}(kJ/mol)$	$\Delta E_{latt}^{exp.}(kJ/mol)$
HCN	1.1	-36.3	-38.5
	1.2	-38.6	
	1.3	-40.9	
HCl	1.1	-18.7	-25.9
	1.2	-19.8	
	1.3	-21.1	
HF	1.1	-56.3	-54.0
	1.2	-57.4	
	1.3	-58.6	
Urea	1.1	-117.0	-103.6
	1.2	-121.5	
	1.3	-126.1	
NH_3	1.1	-44.8	-36.0
	1.2	-46.5	
	1.3	-48.2	
C_2H_2 - cubic	1.1	-21.2	-21.8
	1.2	-23.5	
	1.3	-25.9	
C_2H_2 - orthorhombic	1.1	-21.0	-23.5
	1.2	-23.0	
	1.3	-25.0	

As can be seen from Table 3.4, the results for the s_6 scaling factors that have been changed from the original BLYP-D scaling factor of 1.2 to 1.1 or 1.3 are inconclusive. While one molecular solid may show an improvement in terms of lattice energy when the scaling factor is decreased, another may show better agreement with the experimental value when the scaling factor is increased. HCN and orthorhombic acetylene in particular show very good agreement when the original scaling factor of 1.2 for BLYP-D is used. It is, therefore, apparent that a scaling factor of 1.2 for BLYP-DS gives us the best fit overall, giving consistent results across all molecular solids. Therefore, employing an s_6 value of 1.2 allows us to have results which allow consistency across all molecular solids.

3.2 Results and Discussion

3.2.1 Lattice Parameters

Full geometry optimisations were performed on both acetylene polymorphs, with the intention of comparing the B3LYP and BLYP functionals along with the different dispersion corrections in combination with the BLYP functionals.

The lattice parameters were investigated for the fully optimised crystal structures of acetylene. Table 3.5 shows all of the geometry optimisation results in the cubic structure.

Table 3.5: Optimised lattice parameters in cubic acetylene (Expt. a = 6.094Å [170])

Functional		Calculated (Å)	Percentage Error (%)
B3LYP	a	6.17	1.3
BLYP	a	6.23	2.3
BLYP-D	a	5.59	-8.3
BLYP-DS	a	5.76	-5.4

Considering the cubic polymorph (Table 3.5), we observed that the optimised lattice parameters are in best agreement for the uncorrected functionals B3LYP and BLYP, showing small percentage errors of 1.3% and 2.3%, respectively. B3LYP used 20% HF exchange, known to localise the electronic structure and, therefore, gives rise to slightly higher electrostatic interaction than pure DFT, which gives a solution that is more dispersed. When the original GRIMME correction (D) is used, a noticeable change in the calculated lattice parameter for BLYP is observed. The lattice parameter is underestimated with a percentage error of 8.3% for BLYP-D. The modified BLYP-DS method does show a slight improvement in terms of the optimised lattice parameter. However, the lattice parameter is still underestimated by 5.4%.

Referring back to the conclusions by Civalleri *et. al.* [194], regarding B3LYP-D and their augmented B3LYP-D* method, it is apparent that despite the improvement shown by B3LYP-D*, the dispersion correction is strongly influenced by the basis set. Civalleri used the basis sets 6-31G(d,p) and TZP, yielding calculated lattice parameters of 5.82Å and 5.96Å respectively. The percentage error for 6-31G(d,p) was 4.5%. On the other hand, the percentage error produced from the TZP basis set was 2.2%.

Table 3.6 displays the optimised lattice parameters for orthorhombic acetylene. Using B3LYP, BLYP and BLYP-D, the orthorhombic structure shows a tetragonal cell, suggesting that all of these approaches are failing to reproduce the orthorhombic structure.

Table 3.6: Optimised lattice parameters in orthorhombic acetylene (Expt. a = 5.578Å, b = 6.198Å, c = 6.023Å [170])

Functional		Calculated (Å)	Percentage Error (%)	Tetra./Ortho.
B3LYP	a	6.04	8.4	Tetragonal
	b	6.21	0.2	
	c	6.07	0.8	
BLYP	a	6.28	12.5	Tetragonal
	b	6.05	-2.3	
	c	6.28	4.2	
BLYP-D	a	5.79	3.9	Tetragonal
	b	6.21	0.1	
	c	5.78	-4.1	
BLYP-DS	a	5.70	2.1	Orthorhombic
	b	6.26	1.0	
	c	6.04	0.2	

For the B3LYP and BLYP methods, lattice parameter 'a' gives relatively poor agreement with the experiment, giving percentage errors of 8.4% for B3LYP and 12.5% for BLYP. Lattice parameters 'b' and 'c' give good experimental agreement for B3LYP, but not for BLYP. It appears that overall, B3LYP gives a better agreement than BLYP with the experimental data, showing that the HF exchange is having positive impact on the results. However, it is not the agreement with the experimental values which is the main issue here. As mentioned above, B3LYP, BLYP and BLYP-D are giving a tetragonal cell.

This issue is resolved with the BLYP-DS method which results in an orthorhombic structure. In addition, a noticeable improvement in the lattice parameters are reputed for BLYP-DS. For lattice parameters 'a' and 'b', overestimation values in BLYP-DS are given as 2.1% and 1.0% respectively. Lattice parameters 'a' and 'c' are showing a greater agreement with the experiment than any of the other approaches shown. Most significantly, the system now retains its orthorhombic structure with the lattice parameters noticeably different from one another. This provides further clarification that the newly derived DS approach can be applied to functionals such as BLYP in order to successfully model the van der Waals interactions in molecular systems such as acetylene.

3.2.2 Lattice Energies

The lattice energies were calculated with the counterpoise method correcting for the Basis Set Superposition Error (BSSE) method applied in each case. Table 3.7 shows

the lattice energies for both cubic and orthorhombic acetylene with the functionals of interest, along with the dispersion corrected results for BLYP. In addition to the presented results and methods thus far, an additional test was conducted using BLYP-D*, which used Civalleri's derived method, originally for B3LYP. The exact same procedure was applied to the BLYP functional with the intention of seeing how it compared with the BLYP-DS method derived for this study.

Table 3.7: Optimised lattice energies in cubic (Expt. -21.8kJ/mol [209]) and orthorhombic acetylene (Expt. -23.5kJ/mol [210]), where BSSE refers to the counterpoise corrected energies

Cubic		
Method	$\Delta E_{latt.}$ (kJ/mol)	$\Delta E_{latt.}^{BSSE}$(kJ/mol)
B3LYP	-16.10	-4.98
BLYP	-14.15	-2.18
BLYP-D	-44.06	-26.09
BLYP-DS	-39.87	-23.52
BLYP-D*	-38.56	-22.63
Orthorhombic		
B3LYP	-17.57	-5.68
BLYP	-15.08	-2.95
BLYP-D	-41.38	-26.28
BLYP-DS	-37.58	-23.00
BLYP-D*	-36.69	-22.15

Without a correction for the dispersion forces in the crystal structure, the counterpoise-corrected (See Section 2.2.7) cohesive energies for each functional are greatly overestimated. BLYP-DS underestimates the lattice energy for the cubic structure but still gives an improvement over the BLYP and BLYP-D functionals, and in particular, gives good agreement for the orthorhombic structure.

BLYP-D* appears to show slight variation in terms of lattice energies in comparison with BLYP-DS. As discussed in Chapter 3, Civalleri's approach for deriving B3LYP-D* involved scaling the van der Waals radii of the heavy atoms as well as hydrogen, whereas only the hydrogen van der Waals radius was scaled in BLYP-DS. BLYP-D* results in a lattice energy which is in slightly better agreement with the cubic experimental value. However, BLYP-DS gives a better agreement with the orthorhombic lattice energy. Since BLYP-DS has demonstrated good overall agreement in terms of modelling the orthorhombic structure, the decision was made to continue with the BLYP-DS functional.

From Table 3.7, it is on the other hand, apparent that there is an issue with regards to the ordering of lattice energies. Experimentally, it is known that the

orthorhombic structure, which is a low temperature phase will be the most stable structure and, therefore, will have a lower lattice energy. This is not what we observe with regards to some of the calculations. With B3LYP and BLYP, the energies are in the correct order, with the same being said for BLYP-D when BSSE is applied. It is in the case of the solid state corrections (BLYP-DS and BLYP-D*), where the low temperature orthorhombic phase is less energetically favourable than the cubic phase. While these corrections are improving the lattice energies in terms of comparison with the experimental values, they are also resulting in the incorrect order with regards to the different polymorphs.

From other published material, it appears that this problem is not just limited to ab initio methods. A study from Shuler and Dykstra [211] shows that with molecular mechanics simulations on acetylene dimers, the same problem of the energies of the two phases is encountered, with the cubic phase producing lower lattice energies. Another ab initio study by Nyburg [212], using Hartree-Fock calculations on the two phases of acetylene also shows the same issue for energies without BSSE correction.

We have identified two possible reasons for the discrepancy. The first could be related to the choice of the basis set employed. While the 6-31G(d,p) basis set gave reasonable lattice parameters, particularly for the orthorhombic structure, instead for the cubic structure, the lattice energies are underestimated with regards to the experimental value. Another reason could be down to the internal geometry of the cubic structure.

An analysis of the intra- and intermolecular bond distances in the two crystalline polymorphs were compared with experimental values. It is known that solid acetylene prefers to be arranged in a T-shaped configuration [170]. Therefore, the intermolecular distance measured will be between the carbon atoms and a hydrogen atom from a neighbouring acetylene molecule. What was discovered from this approach is that for both structures, the intramolecular distances are modelled correctly. Table 3.8 shows a summary of the intramolecular distances in acetylene.

Table 3.8: Intramolecular distances in cubic and orthorhombic acetylene (Exp. cubic C-C = 1.177Å, C-H = 1.024Å, exp. orthorhombic C-C = 1.193Å, C-H = 1.070Å [170])

Cubic		
Functional	C-C calc. (Å)	C-H calc. (Å)
B3LYP	1.19	1.02
BLYP	1.19	1.02
BLYP-D	1.19	1.02
BLYP-DS	1.19	1.02
Orthorhombic		
B3LYP	1.19	1.07
BLYP	1.19	1.07
BLYP-D	1.19	1.07
BLYP-DS	1.19	1.07

Looking at the intramolecular bond distances between the atoms in acetylene, we see good agreement between the simulation and experiment for both polymorphs. Therefore, it can be ruled out that the internal geometry of the system is causing the problem with regards to the ordering of the lattice energies. Table 3.9 and Figure 3.2 shows the intermolecular distances for both polymorphs of acetylene.

Table 3.9: Intermolecular distances in cubic and orthorhombic acetylene (Exp. cubic C–H (1) = 3.091Å, C–H (2) = 3.290Å, exp. orthorhombic C–H (1) = 2.737Å, C–H (2) = 2.738Å [170])

Cubic		
Functional	C–H (1) calc. (Å)	C–H (2) calc. (Å)
B3LYP	3.09	3.29
BLYP	3.09	3.29
BLYP-D	3.09	3.29
BLYP-DS	3.09	3.29
Orthorhombic		
B3LYP	2.74	2.74
BLYP	2.74	2.74
BLYP-D	2.74	2.74
BLYP-DS	2.74	2.74

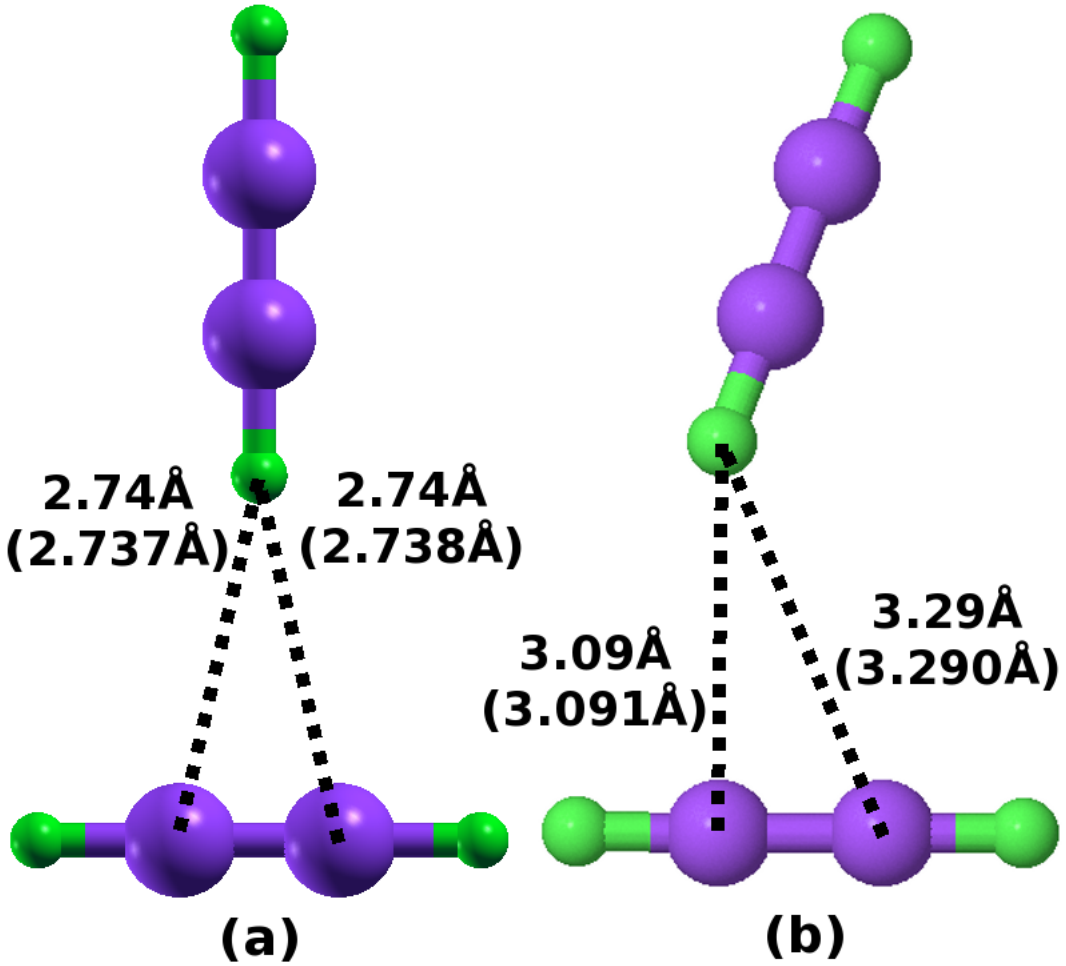

Figure 3.2: Configuration for (a) Orthorhombic and (b) Cubic acetylene, showing optimised C- - - H intermolecular bond distances. Experimental values are given in brackets [170]

For the orthorhombic structure, both of the C-H intermolecular distances are identical, which is expected for a T-shaped configuration. On the other hand, in the cubic structure, the acetylene molecules are not aligning themselves in a symmetric T-shaped configuration. This is in agreement with the experiment as the experimental structure has been used as the starting geometry. This suggests that the error in lattice energy order is not related to the internal energy.

To ensure that this alignment for the cubic phase is the most energetically favourable, an alternative method of optimising the crystal structure was employed. This could allow us to observe whether the lattice energies could be corrected to give the correct order with respect to phase. To do this, the crystal cell is firstly optimised individually followed by a separate optimisation of the atomic coordinates. This method is repeated several times until convergence is reached. Convergence is determined by plotting the respective total energies of the system against the lattice parameter until an energy minimum is found. An example of this is shown by Figure 3.3 for B3LYP.

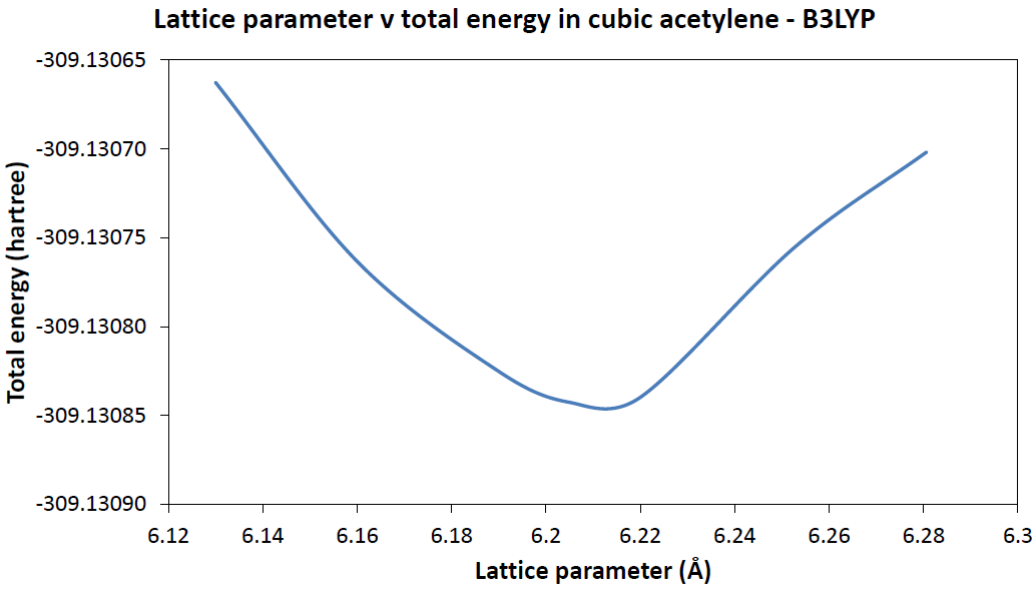

Figure 3.3: Graph showing total energy of cubic acetylene when the cell and coordinates are optimised individually, plotted against the change in lattice parameter

The intention of this procedure was to ensure that we are in the correct global energy minimum with regards to the optimised structure. By plotting out the energies in this manner, we can check where the global minimum for the optimised lattice parameter lies, and ensure that CRYSTAL is in this minimum when it comes to the full geometry optimisation procedure. While local minima may exist, it is essential to ensure that the global minimum is what is calculated by CRYSTAL when the cubic structure of acetylene is simulated. It is expected that by simulating the cubic structure while optimising the cell and atomic coordinates separately, we should achieve lattice energies very similar to those previously calculated (Table 3.7).

The minimum energy is then used to calculate the new lattice energy, with the minimum energy lattice parameter used to calculate the BSSE. Since this was an test to see if we were in the global minimum, the minimum energy in this case was taken as the lowest point of the curve as shown by the values plotted. Table 3.10 shows the new lattice energies obtained from performing a cell optimisation followed by a coordinate optimisation of the cubic structure of acetylene.

Table 3.10: Lattice energies obtained from optimising cell and coordinates separately in cubic acetylene (Exp. -21.8kJ/mol [209])

	Cubic	
Method	$\Delta E_{latt.}$ (kJ/mol)	$\Delta E_{latt.}^{BSSE}$ (kJ/mol)
B3LYP	-16.16	-5.30
BLYP	-14.31	-2.49
BLYP-D	-42.57	-25.61
BLYP-DS	-39.29	-23.28

If we refer back to Table 3.7, we see that the new cubic lattice energies are similar to the ones calculated previously. This shows that we are in the correct global minimum with regards to the optimisation process. Once again, we see the same issue as previously with regards to the ordering of lattice energies. B3LYP, BLYP and BLYP-D show the correct order with regards to phase stabilisation. However, the BLYP-DS correction is still resulting in a slightly lower lattice energy for the cubic structure, which opposes the experimental values. It is apparent that optimising the cubic structure of acetylene in this way does not solve the issue with regards to the lattice energies for the two different phases.

Instead, we propose that the origin to the lattice energy ordering is related to the fact that lattice parameters for the cubic structure are underestimated using a dispersion correction, resulting in lattice energies that are underestimated with regards to the experimental value. As the energy difference between the two polymorphs is small, the failure of correctly representing the cubic structure may result in the observed lattice energy ordering. This is further enhanced as the BSSE correction will be underestimated owing to the small error in lattice parameters.

3.2.3 Electronic Structure

By calculating atomic charges and bond population analysis, it is possible to judge the electron localisation of the system. The higher the charges and electron population, the more localised the system. Figure 3.4 and Tables 3.11 to 3.12 show the results of the atomic charges and bond population analysis for both polymorphs of acetylene.

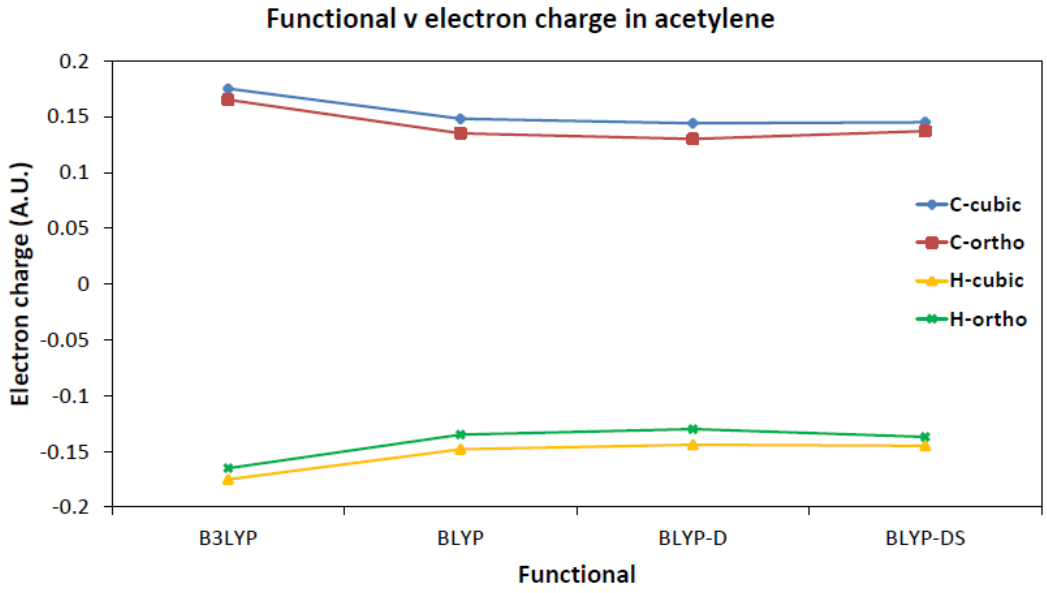

Figure 3.4: Functional v Mulliken charges per atom for (a) cubic and (b) orthorhombic acetylene

Table 3.11: Mulliken charges per atom for cubic and orthorhombic acetylene. Electron charge (q) given in (e)

Functional	q(C)	q(H)
Cubic		
B3LYP	0.175	-0.175
BLYP	0.148	-0.148
BLYP-D	0.144	-0.144
BLYP-DS	0.145	-0.145
Orthorhombic		
B3LYP	0.165	-0.165
BLYP	0.135	-0.135
BLYP-D	0.130	-0.130
BLYP-DS	0.137	-0.137

Table 3.12: Mulliken bond population analysis reported in units (e) for the optimised structures of cubic and orthorhombic acetylene

	Bond population			
Bond	B3LYP	BLYP	BLYP-D	BLYP-DS
Cubic				
C—H (intra.)	0.351	0.350	0.350	0.349
C≡C (intra.)	0.968	0.914	0.884	0.899
C- - -H (inter.)	-0.036	-0.044	-0.046	-0.044
Orthorhombic				
C—H (intra.)	0.341	0.339	0.336	0.340
C≡C (intra.)	0.951	0.896	0.882	0.894
C- - -H (inter.)	-0.038	-0.048	-0.049	-0.047

From Figure 3.4 and Tables 3.11 to 3.12, it is seen that the original Grimme correction results in a more delocalised solution than the pure DFT functional. However, the dispersion correction derived for solids in this study compensates for the delocalisation and results in a slightly more localised solution, but still less localised than the pure DFT functional. It is worth noting that the hybrid functional is still more localised than the Grimme-corrected BLYP method. These findings were supported by the electron charge difference maps between pure BLYP and the two dispersion-corrected BLYP functionals shown in Figure 3.5.

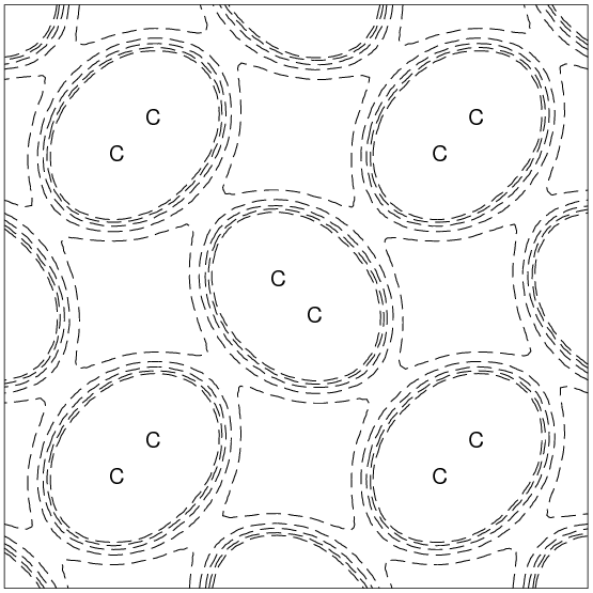

(a)

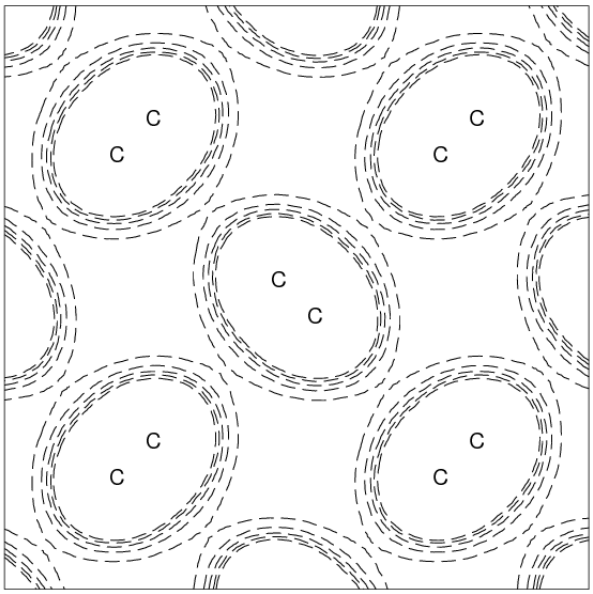

(b)

Figure 3.5: Electron density difference maps for (a) BLYP vs BLYP-D and (b) BLYP vs BLYP-DS in cubic acetylene within the experimental structure. Dashed line represents electron deficiency in the pure DFT functional. $\Delta\rho$(r)=0.135 e/Å^3

For each of these maps, the dashed lines represent electron deficiency in the pure DFT functionals. Hence, the BLYP functional shows a higher electron localisation than the dispersion-corrected solutions as they are indicating electron deficiency between the molecules. Again, the dispersion correction derived for solids in this study shows less features i.e. less electron deficiency than the original Grimme correction, indicating DFT-DS being more localised than DFT-D. The results from the electron charge difference maps support the findings in the Mulliken population analysis (Tables 3.11 and 3.12) and both show the same results in terms of electron localisation and delocalisation.

3.2.4 Electron Field Gradients and Quadrupole Coupling Constants

The Electron Field Gradients and Quadrupole Coupling Constants (QCC) are known to be sensitive to the local structure and its electronic description. Here, a range of functionals including Hartree-Fock and LDA were used along with a basis set dependance study for the B3LYP functional. Initially, a study was undertaken on the acetylene molecule to determine the effect regarding the choice of basis sets and functionals. Furthermore, experimental data was available for the acetylene molecule, therefore, providing a comparison. Secondly, a study into the effect of forming a solid was undertaken by studying the QCC shift compared to the molecule. The latter is also a measure of the effect of the dispersion correction.

Using Equation (3.3), the QCC values for each atom were calculated.

$$\mathrm{QCC} = (\mathrm{qQV_{33}})/\mathrm{h} \tag{3.3}$$

Here, q represents the electronic charge of a single atom, V_{33} is the largest value for the gradient tensor (Table 3.13), Q represents the quadrupole moment for the atom and h is Planck's constant. All quadrupole gradient tensors (V_{33}, V_{22} and V_{11}) for each atom in the acetylene molecule are shown in Table 3.13.

Table 3.13: Quadrupole tensors for acetylene given in (a.u.)

Functional	Atom	$\lvert V_{33}\rvert$	$\lvert V_{22}\rvert$	$\lvert V_{11}\rvert$
B3LYP	C	0.990	0.495	0.495
	H	0.168	0.084	0.084
BLYP	C	0.733	0.367	0.367
	H	0.180	0.090	0.090
BLYP-D	C	0.737	0.368	0.368
	H	0.179	0.090	0.090
BLYP-DS	C	0.734	0.367	0.367
	H	0.180	0.090	0.090

With quadrupole moment values of $6\times10^{-30}\mathrm{m}^2$ and $2.86\times10^{-31}\mathrm{m}^2$ used for carbon and hydrogen respectively, Figures 3.6 and 3.7 show the QCCs for each of the functionals and basis sets. From the results, it is apparent that in the case of BLYP, the QCC values are not greatly affected by the dispersion correction.

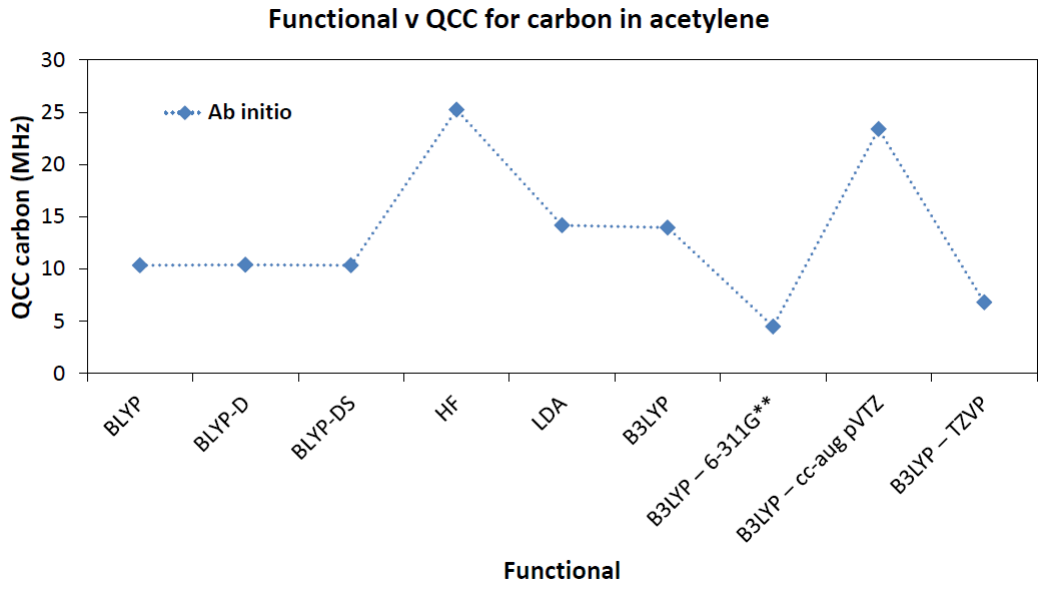

Figure 3.6: QCC values for carbon in the acetylene molecule calculated from Equation (3.3)

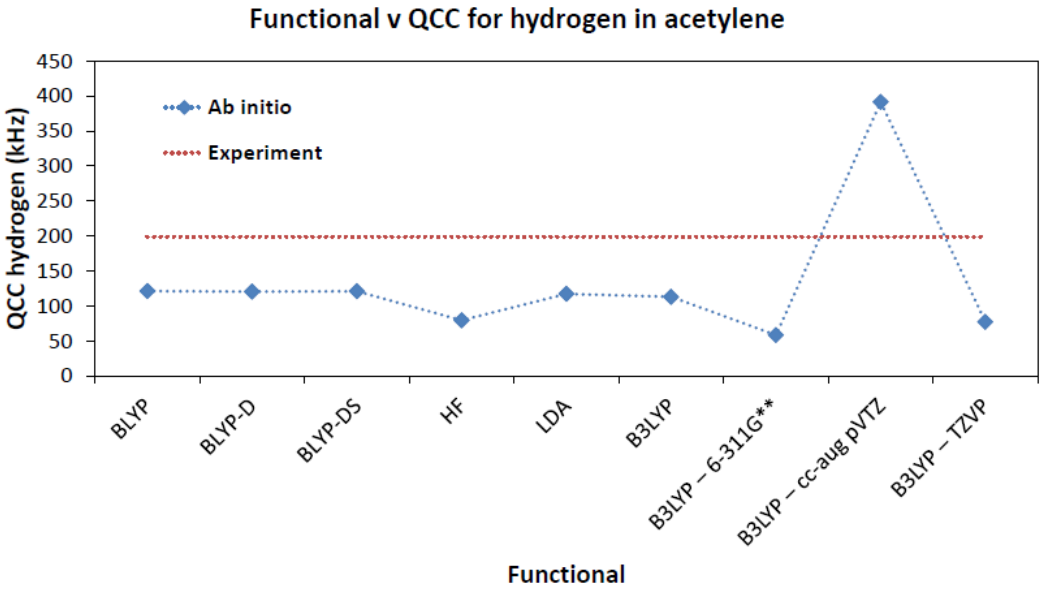

Figure 3.7: QCC values for hydrogen in the acetylene molecule calculated from Equation (3.3). Experimental value = 198.6kHz for the gas molecule [213]

For carbon, the QCC increases very slightly with BLYP-D. BLYP-DS gives a value smaller than BLYP-D but greater than BLYP. For hydrogen, the opposite pattern occurs. This time, the QCC value decreases very slightly with BLYP-D and BLYP-DS, with BLYP-D having a greater effect. Despite these small changes, as mentioned above, it is clear that the dispersion correction is not having a significant effect on the quadrupole coupling constant. The hydrogen isotope (Deuterium) has a known nuclear quadrupole coupling constant in the acetylene gas molecule with a value of 198.6kHz [213], which shows that the calculated values are underestimated compared to experiments.

For this purpose, the LDA functional, as well as a Hartree-Fock approach were compared alongside the DFT methods. The LDA functional gave a QCC value similar to Becke's functionals, while Hartree-Fock underestimated the hydrogen value more than the DFT functionals (See Figure 3.7). The QCC value for carbon using HF is instead twice the value of the DFT methods (Figure 3.6).

Up till now, all calculations were run with the 6-31G(d,p) basis set. For comparison using the B3LYP functional, the 6-311G**, cc-aug pVTZ and TZVP basis sets were included in the study. For 6-311G** and TZVP, the QCC was significantly underestimated in both atoms as compared with 6-31G(d,p). On the contrary, cc-aug pVTZ significantly overestimated the QCC for both carbon and hydrogen. With such a variation in results between the different basis sets, we can deduce that the quadrupole coupling constant in acetylene is likely to be basis-set dependant for DFT functionals.

The QCC shift was calculated by subtracting the QCC value of the isolated optimised molecule from the QCC of the crystal structure. Figures 3.8 and 3.9 show the QCC shifts of the geometry optimised crystal structures for carbon and hydrogen. As for the other electronic properties, the new solid state correction gives shifts in between the pure DFT and the original Grimme-corrected method. It is noted that the shifts for the B3LYP and BLYP-based Hamiltonians are similar suggesting that the Hartree-Fock exchange correction is less important when calculating ΔQCC values.

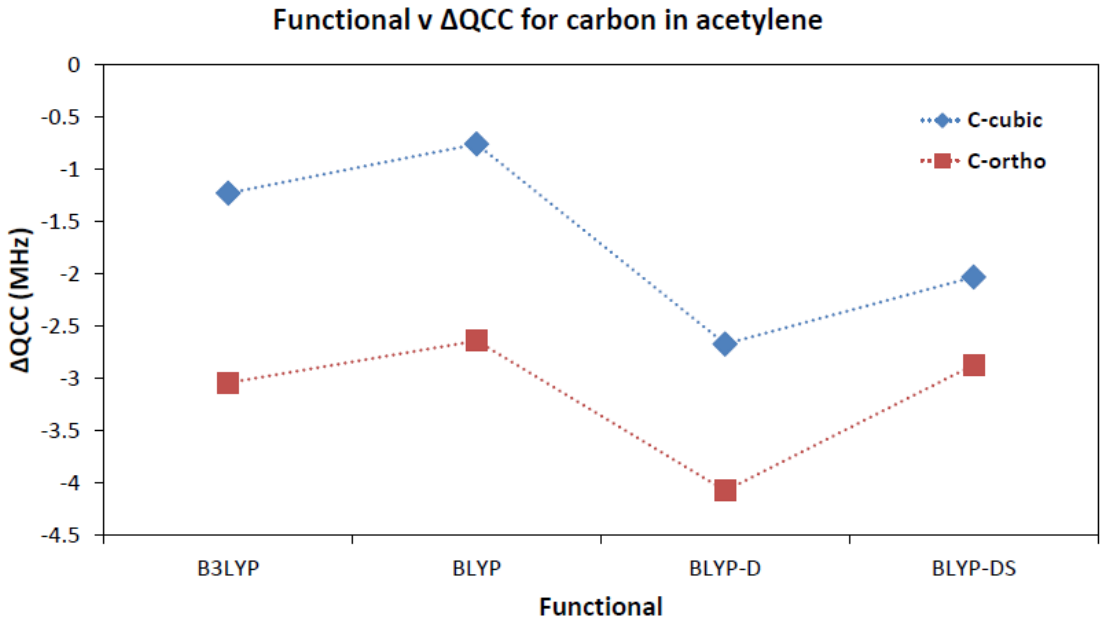

Figure 3.8: ΔQCC for carbon in cubic and orthorhombic acetylene, calculated as the difference between the solid and the optimised molecule

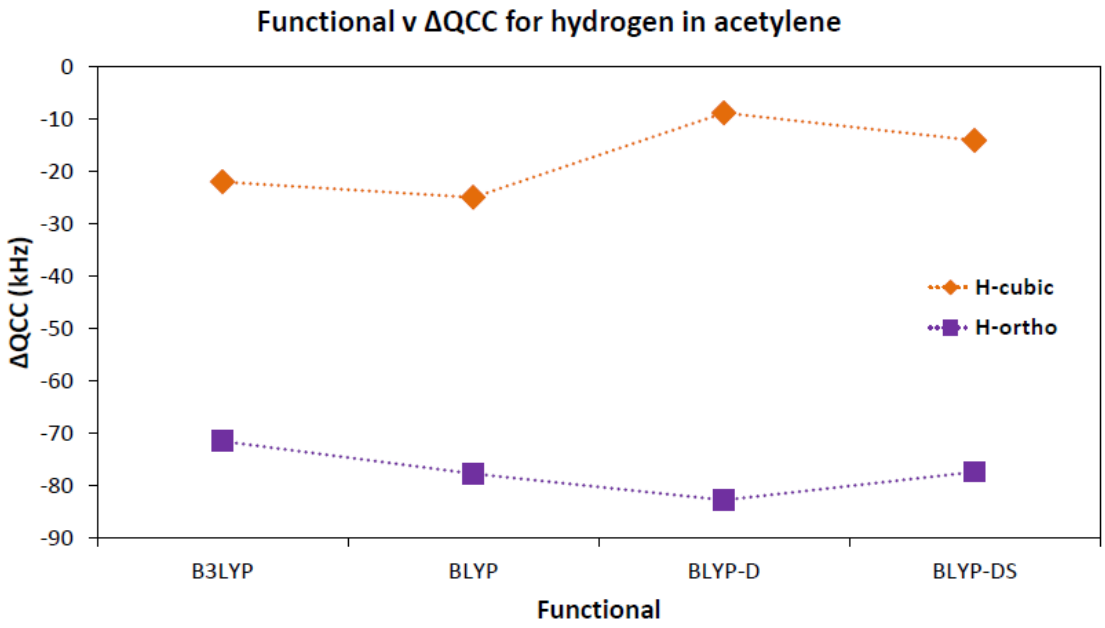

Figure 3.9: ΔQCC for hydrogen in cubic and orthorhombic acetylene, calculated as the difference between the solid and the optimised molecule

With regards to the cubic structure of acetylene, there is a pattern in the QCC shift for carbon using BLYP. For carbon, BLYP-D gives a greater shift than both BLYP and BLYP-DS, with BLYP-DS giving a slightly greater shift than BLYP. The opposite is seen with regards to hydrogen in the cubic structure.

The QCC shift for the orthorhombic structure shows a less straightforward pattern. The ΔQCC values are noticeably greater for both carbon and hydrogen compared with the corresponding cubic values. This could be explained possibly due to a much higher degree of asymmetry in the orthorhombic polymorph, compared to the symmetrical cubic structure. For carbon, the same pattern is observed as for the cubic shifts, with BLYP-D giving the greatest shifts. However, for hydrogen, BLYP-D is giving the most significant ΔQCC, opposite from the cubic structure. Interestingly, in this case, BLYP-DS actually showed the smallest ΔQCC.

3.3 Conclusions

The effect of the Grimme correction, derived for molecules results in an over-delocalisation of the electronic density compared to pure DFT. This was shown by studying both Mulliken population analysis and electron density distributions. The dispersion correction derived for solids in this study improves on the electron delocalisation. As a result, the orthorhombic acetylene structure predicted by BLYP-DS demonstrates lattice energies and parameters in good agreement with experimental values. Also, for the cubic structure, the calculated lattice energies are improved with the solid state corrected BLYP Hamiltonian compared to experiments.

However, the cubic structure is better represented by the pure DFT and hybrid

functionals. It was deduced that this approach was also basis set dependant, as shown by Civalleri *et. al.*, who achieved a good agreement with the experimental result using the TZP basis set for cubic acetylene with their B3LYP-D* method.

Electric field gradients are known to be sensitive to the local structure and the electron density, and indeed, it is found that the QCC is method dependent, as shown by Hartree-Fock and LDA functionals. While the LDA functional gave a QCC value close to Becke's functionals in hydrogen, Hartree-Fock underestimated the value more than DFT functionals. It was discovered that the dispersion corrections had little impact on the QCC values for BLYP. However, it appears that the QCC values are highly basis set dependent. The calculations with the original DFT basis set (6-31G(d,p)) result in a QCC value for hydrogen close to 100kHz, which should be compared to an experimental value of about 200kHz. Increasing the size of the basis set to an augmented method, instead results in a QCC value close to 400kHz for hydrogen.

The quadrupole shifts for carbon and hydrogen are found to depend on the localisation of the electron distribution, resulting in larger shifts for the dispersion-corrected values than pure DFT for most cases, excluding hydrogen in the cubic polymorph, which shows the opposite trend. On the other hand, the Hartree-Fock exchange has only minor influence on the QCC shifts as B3LYP and BLYP both give similar results.

To summarise, the newly derived solid state dispersion correction improves most properties calculated in this study and suggests that it is important to correct for the solid when employing van der Waals corrections. By studying the transferability of the BLYP-DS functional to other hydrogen-bonded systems, it is shown that it performs as well if not better than the pure BLYP or BLYP-D functionals.

Chapter 4

Molecular Dynamics Analysis of Pure Polymers

4.1 Determining the most suitable geometry for PEDOT-PEG

In the case of PEDOT-PEG, it is known that it exists in multiple geometrical arrangements, including the multi-block form and the tri-block form shown in Figure 4.1 [214]. PEDOT-PEG, also known as Aedotron^{TM} has a significant range of bulk conductivities, depending upon the structural geometry of the co-block polymer. Research has shown that the tri-block PEDOT-PEG has the highest conductivity, ranging from about 1 to 60 S/cm. Instead, the multi-block structure has a lower range, for example, with perchlorate as the dopant and dispersed in propylene carbonate, between 0.1 to 3 S/cm.

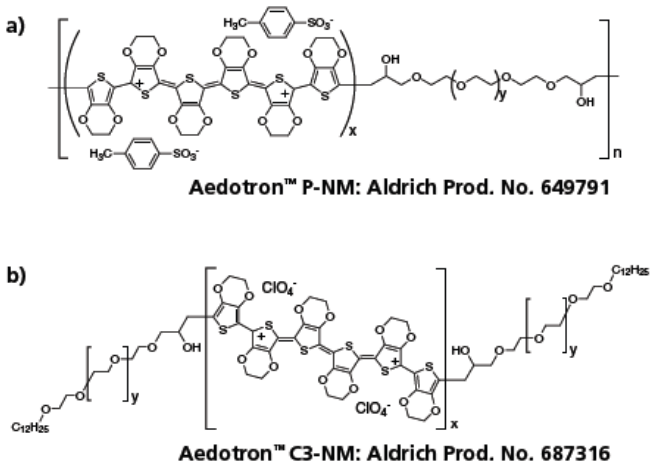

Figure 4.1: (a) Multi-block structure and (b) Tri-block structure of PEDOT-PEG [214]

Experimentally, the multi-block polymer was used in our studies. Issues such as stability are important to consider. Using the MMFF94 force field [130, 131,

132, 133, 134], a geometry optimisation was performed in MarvinSketch [164]. Both the multi-block and tri-block geometries were compared to determine which is the energetically most stable one. For this purpose, two 18-unit blocks of PEDOT-PEG were created, where A represents PEDOT and B represents PEG. A multi-block configuration of AAAAAABBBBBBBBBBBB was designed, and compared to a tri-block configuration of BBBBBBAAAAAABBBBBB. Figure 4.2 shows the two optimised geometries, with Table 4.1 listing their total energies in kJ/mol.

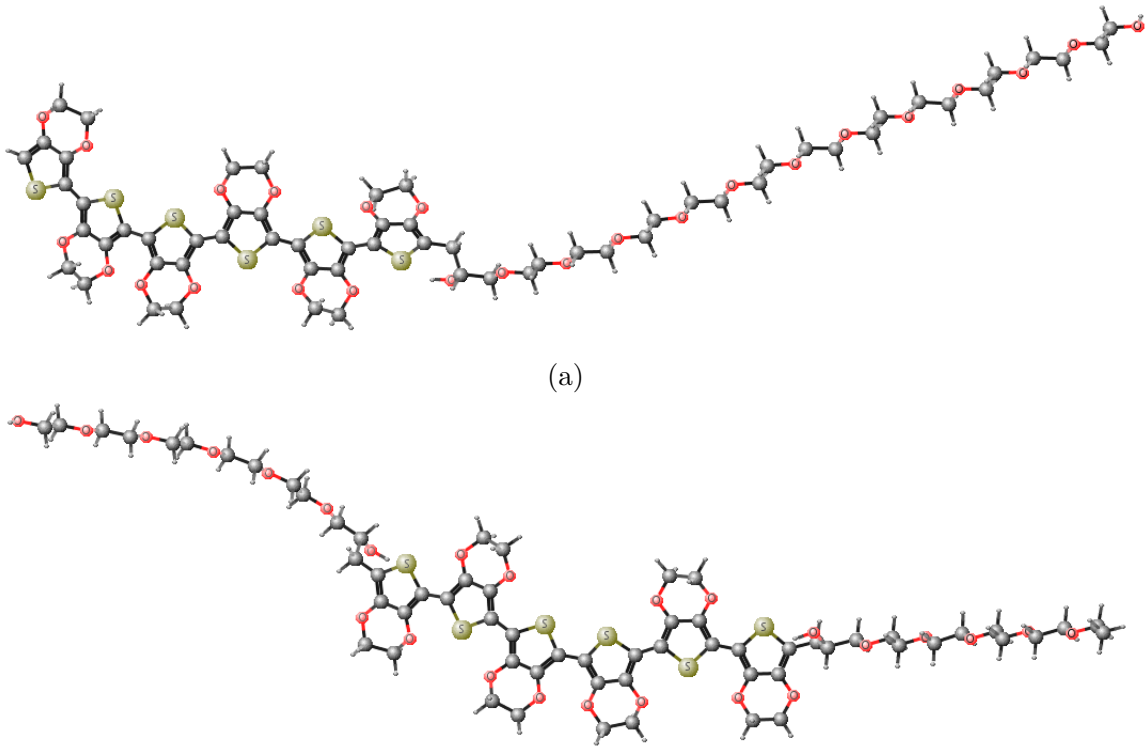

(a)

(b)

Figure 4.2: (a) Optimised Multi-block and (b) Tri-block structures of PEDOT-PEG tested in MarvinSketch

Table 4.1: Geometry configuration of PEDOT-PEG along with the optimised total energy given by the MMFF94 optimisation algorithm in MarvinSketch

Geometry	Total energy (kJ/mol)
Multi-block	-1980.3
Tri-block	-1937.0

Here, the MMFF94 force field optimisation procedure results in the multi-block PEDOT-PEG having a lower total energy than the tri-block geometry. This suggests that the multi-block structure is energetically more stable with a difference of less than 50 kJ/mol compared to the tri-block configuration. Based on this investigation, and because the experiments performed in this overall study were using the multi-block structure of PEDOT-PEG, doped with perchlorate dispersed in propylene

carbonate, the decision has been made to study only the multi-block structure from this point onwards. This is so that we can obtain a more reliable comparison between the simulations and experiments. Future work may be performed on the tri-block structure for comparison purposes.

4.2 Method

Molecular dynamics simulations were performed on the co-block polymer PEDOT-PEG as well as the individual polymers PEDOT and PEG as reference systems. The aim by studying the pure polymer systems separately was to gain a greater insight into how their behaviour changes when forming the co-block polymer, but also to justify the computational settings. Particularly, PEG was studied for the latter purpose as many experimental as well as theoretical studies are published previously.

Two different force fields were used for comparison, namely PCFF [135] and COMPASS27 [135]. In addition, two different softwares were compared: DL_POLY 4 [153] and the Forcite module available within Materials Studio 6.1 [160]. It was of interest to see whether the two different force fields produced similar and consistent results for the systems of interest.

4.2.1 Isolated Polymers

The Zebedde code [158] was used in order to construct the polymer chains for use with the DL_POLY package using the PCFF force field. For the Zebedde input, a seed molecule was chosen (See Figure 4.3). The seed is then replicated using a step-growth process in which monomer units are joined together. Figure 4.3 shows the labelled seed molecules of PEDOT and PEG, which were used in the Zebedde input. The polymers are constructed using a Metropolis Monte Carlo criterion. Chain conformation is adjusted throughout in order to ensure that the system is well represented sterically. A more detailed description of Zebedde can be found in Section 2.4.

The periodic boundary varied from 100×100×100Å to 200×200×200Å depending on the length of the polymer. A cubic cell was used in each case. The polymer was modelled as an isolated chain, rather than in a dense amorphous cell.

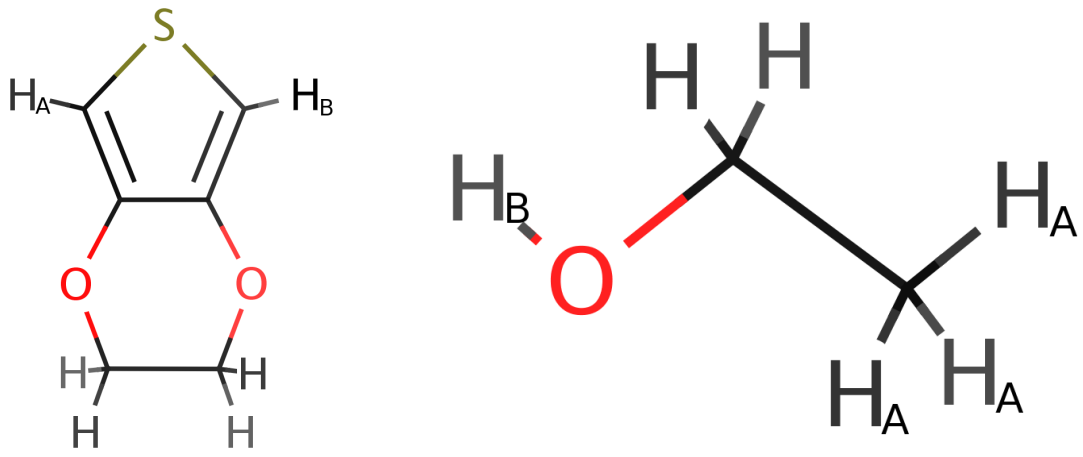

(a) (b)

Figure 4.3: (a) PEDOT and (b) PEG seeds

In the case of building PEDOT-PEG, a successful run of the PEDOT polymer was completed. The chain length of the PEDOT polymer was chosen and became the new seed molecule. By selecting which end of the polymer to keep a point of attachment active, the point from which the PEG was grown could be controlled. To do this, either the H_A or H_B atom was modified to a standard H atom, while keeping the other end unaltered, depending on which was preferable in steric terms. PEG was selected as the library fragment and grown from the PEDOT chain to create PEDOT-PEG.

The DL_POLY simulations in this study using the PCFF force field were all ran for a total simulation time of 5000ps, with a timestep of 0.001ps. The default system temperature for the simulations in this study was 300K. Before each MD simulation, the starting structures were minimised in DL_POLY using the zero-temperature minimisation algorithm, with the target system reset to 10K. The system was equilibrated for 100ps. The local density variation was permitted with a value of 100% in the system. The system temperature was rescaled every step during the equilibration procedure. The NVE ensemble was used for the simulations, with the Velocity Verlet algorithm employed. The long-ranged and short-ranged van der Waals (vdW) interactions cutoff was set to 12Å. Electrostatic forces were calculated using an Ewald summation with an automatic parameter optimisation. A value of 1×10^{-6} was used for this purpose.

The same approach to modelling the polymers with the COMPASS27 force field was undertaken in Materials Studio 6.1, using the Forcite [161] module. Each of the polymer systems modelled in DL_POLY were replicated and built using the Materials Studio polymer builder. This approach resulted initially in a straight-chain configuration as opposed to the random distribution of the chains in Zebedde. The structures were relaxed using the Forcite geometry optimisation. For this procedure, the convergence tolerance for the energy was set to 4.184×10^{-3}kJ/mol. The optimised structures were then selected and a Molecular Dynamics simulation was

performed. Once again, all simulations in the study were ran for 5000ps with a timestep of 0.001ps. The system was equilibrated for 100ps, with an Ewald sum used for calculating electrostatic forces. The system temperature was again set to 300K, and the NVE ensemble was chosen. A vdW cutoff distance of 12.5Å was used in this case. Table 4.2 summarises the sizes of the polymers studied.

Table 4.2: Polymer chain lengths investigated in this study, including the number of units for each, along with the total number of atoms, and cell volume

Polymer	$(PEDOT)_m$	$(PEG)_n$	$m + n$	No. atoms	Cell volume (Å)
PEDOT	20	N/A	20	262	1×10^6
PEDOT	120	N/A	120	1562	8×10^6
PEG	N/A	20	20	142	1×10^6
PEG	N/A	120	120	842	1×10^6
PEDOT-PEG	20	20	40	402	1×10^6
PEDOT-PEG	80	80	160	1602	8×10^6

It was found that with a straight-chain structure as given by the Materials Studio polymer builder, for the 120 unit chain of PEDOT and the 160 unit chain of PEDOT-PEG, the simulation failed in Forcite for the COMPASS force field. This was found to be down to the straight-chain starting configuration for the system, with the chain perhaps being too long to achieve stability in terms of steric arrangement. Therefore, these two systems were then run using the same starting configuration built by Zebedde, but this time, applying the COMPASS force field in Forcite. This allowed the simulation to be run successfully.

4.2.2 Amorphous Polymers

The systems currently investigated have been isolated chains, in a large cell. While this has allowed us to analyse how the polymer chains behave under different force fields at ambient temperature, we are unable to observe properties such as diffusion. This is due to the very low density of the systems. A much smaller cell is required for this purpose, with multiple polymer chains.

To create an amorphous cell with fixed density, the Amorphous Cell module [215] was used in Materials Studio. It simply requires an input structure, which in this case was an isolated polymer chain consisting of 20 units (or 40 for the co-block PEDOT-PEG polymer - see Figure 4.4c). The number of polymer chains to be constructed can be specified. With the density fixed, the size of the cell varies to accommodate the number of chains created. The end result is an amorphous polymer matrix in a dense periodic cell. Figure 4.4 shows the three amorphous pure polymer matrices created for PEDOT, PEG and PEDOT-PEG.

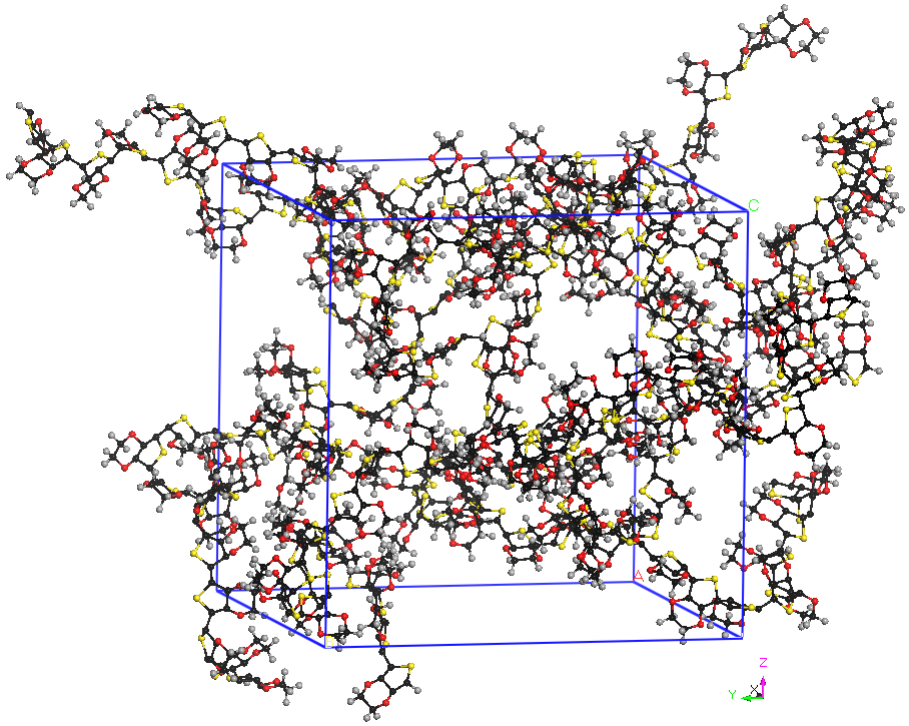

(a)

Figure 4.4: (a) Amorphous PEDOT

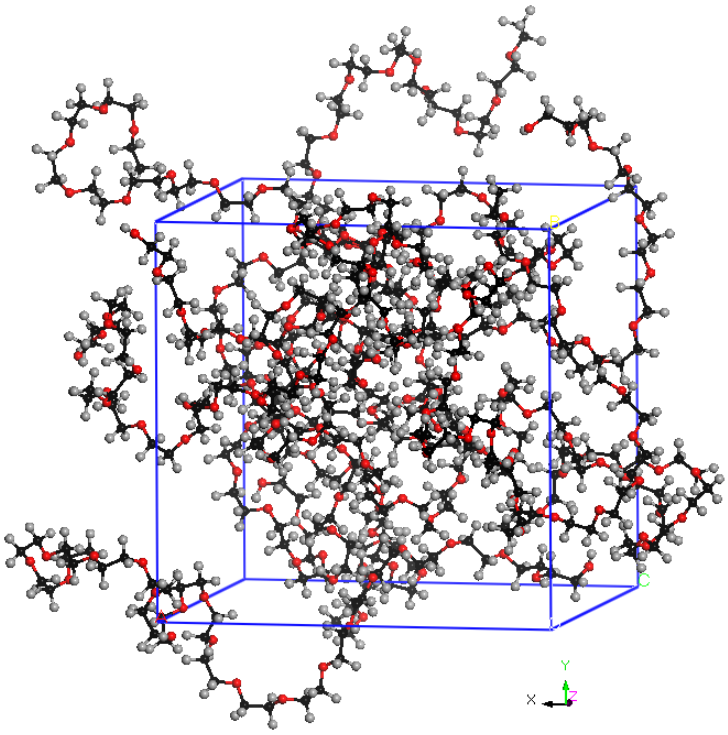

(b)

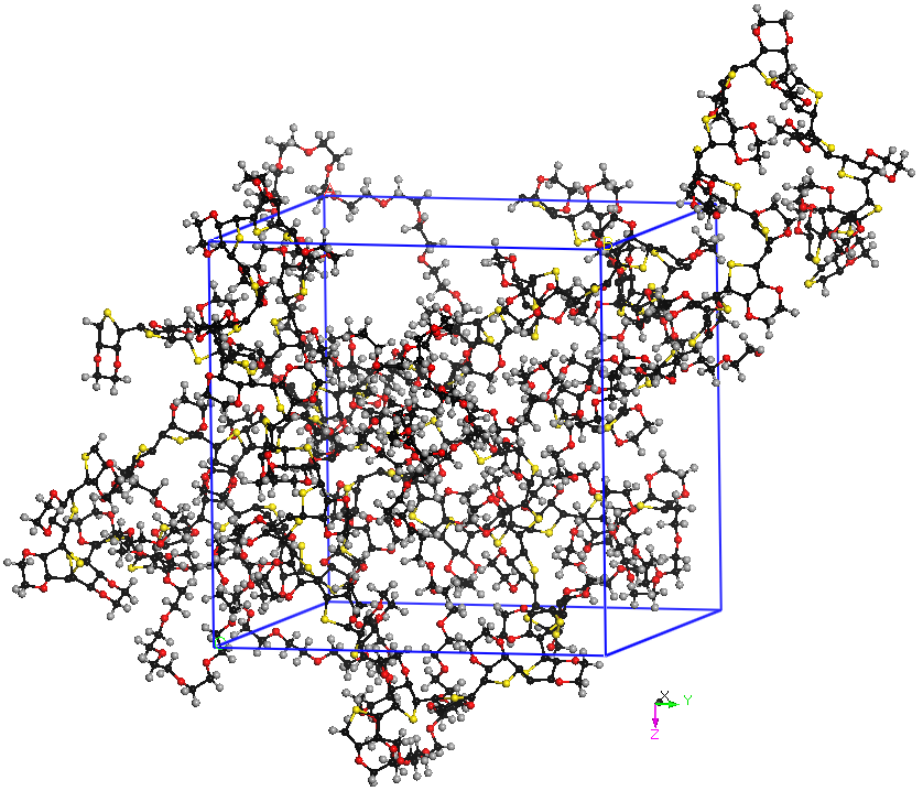

(c)

Figure 4.4: Continued. (b) Amorphous PEG and (c) Amorphous PEDOT-PEG

For PEDOT and PEG, the density was fixed at 1g/cm^3, while the known density value of 1.141g/cm^3 at 25°C for PEDOT-PEG doped with perchlorate and dispersed in propylene carbonate, was used [216]. The cell parameters varied for each system depending on the size of the polymer chains and density. The systems investigated in this study were for 20 units of PEDOT (Figure 4.4a), and PEG (Figure 4.4b), with 10 polymer chains present in the amorphous cell. For PEDOT-PEG (Figure 4.4c), 5 chains were present, with the co-polymer consisting of 40 units (20 for each polymer). The amorphous systems of PEDOT and PEG consisted of 2620 and 1420 atoms, respectively, while PEDOT-PEG consisted of 2010 atoms.

Using the PCFF force field, all of the starting structures were minimised in DL_POLY using the zero-temperature minimisation algorithm, with the target system reset to 10K. The exact same computer settings were used for the amorphous cell, as with the isolated chains (See Section 4.2.1). All simulations ran for 5000ps with a timestep of 0.001ps and equilibrium time of 100ps. For the amorphous cells, MSD plots were obtained, in order to measure the total diffusion of the polymer chains.

4.3 Results and Discussion

4.3.1 Physical Characteristics - Isolated Polymers

To begin with, a study was conducted on how the physical appearance of the polymers changed as a function of chain length. It was useful to investigate the pure polymers for this purpose, and compare this to the co-polymer, PEDOT-PEG. The polymers will undergo conformations as heat is applied over the number of steps that the dynamics simulation is run for. It is of interest to observe what shape the polymers will take, both on their own, and as a co-block polymer. Both the DL_POLY simulations with the PCFF force field and the Forcite simulations with the COMPASS27 force field will be shown for comparison purposes.

Figures 4.5 and 4.6 show the appearance of the PEDOT chains before and after the MD simulations are performed for the 20 unit structure (262 atoms) and the 120 unit structure (1562 atoms), respectively. In all cases, the polymers fold up independent of the force field and chain lengths. This is especially observed in the chain with 120 units, which clearly shows a preference for folding up. These results suggest that the PEDOT chains like to conform to remain close together and have an affinity for each other. This could partly be down to the shape of the PEDOT monomers and how they prefer to arrange themselves sterically. Intermolecular forces could also play a part in why the PEDOT chains prefer to fold and remain close together as opposed to making use of the space that is available. We obviously expect longer chains to have increased flexibility and, therefore, have more freedom to move and conform.

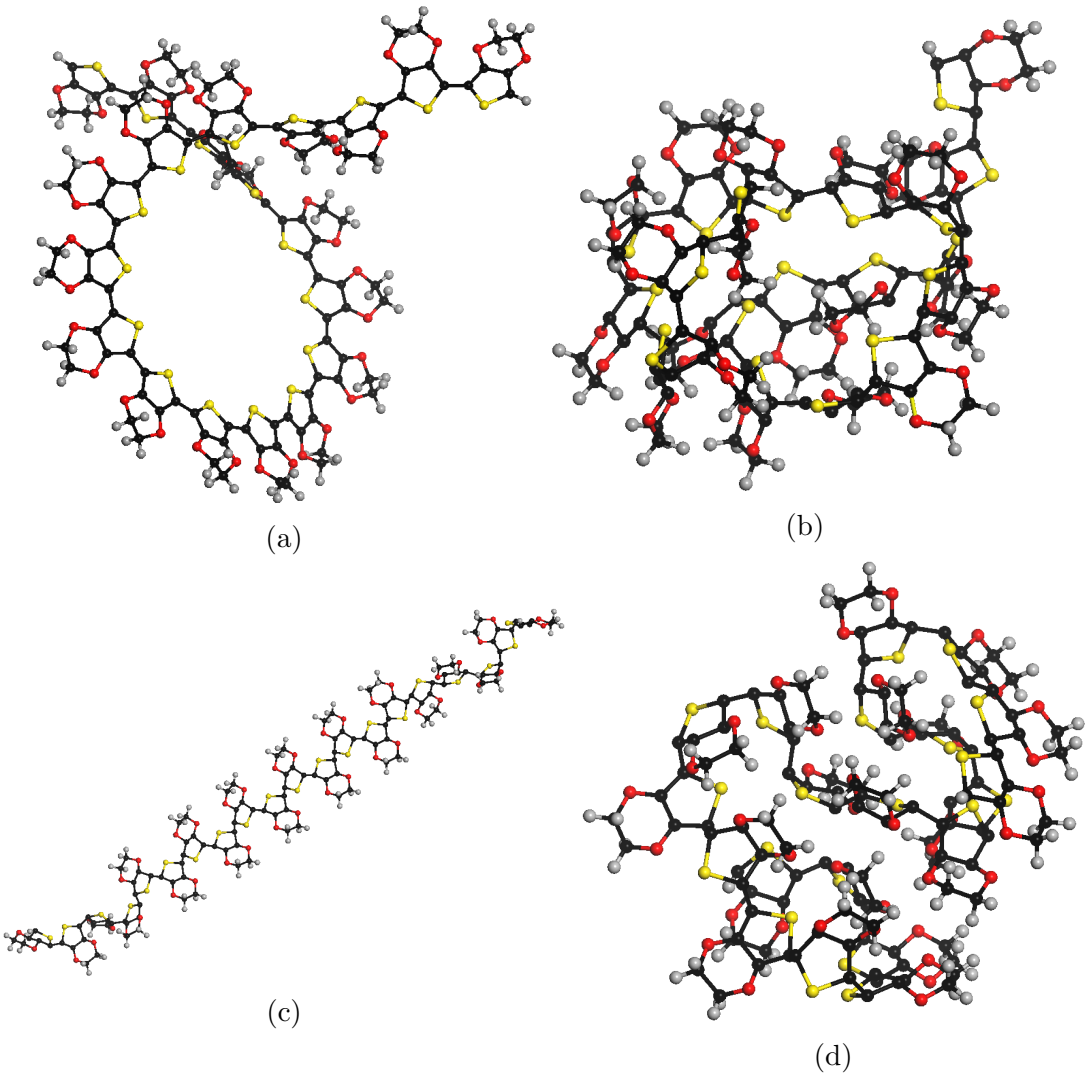

Figure 4.5: 20 unit chain of PEDOT (a) before and, (b) after simulation using the PCFF force field as well as (c) before and, (d) after simulation using the COMPASS force field

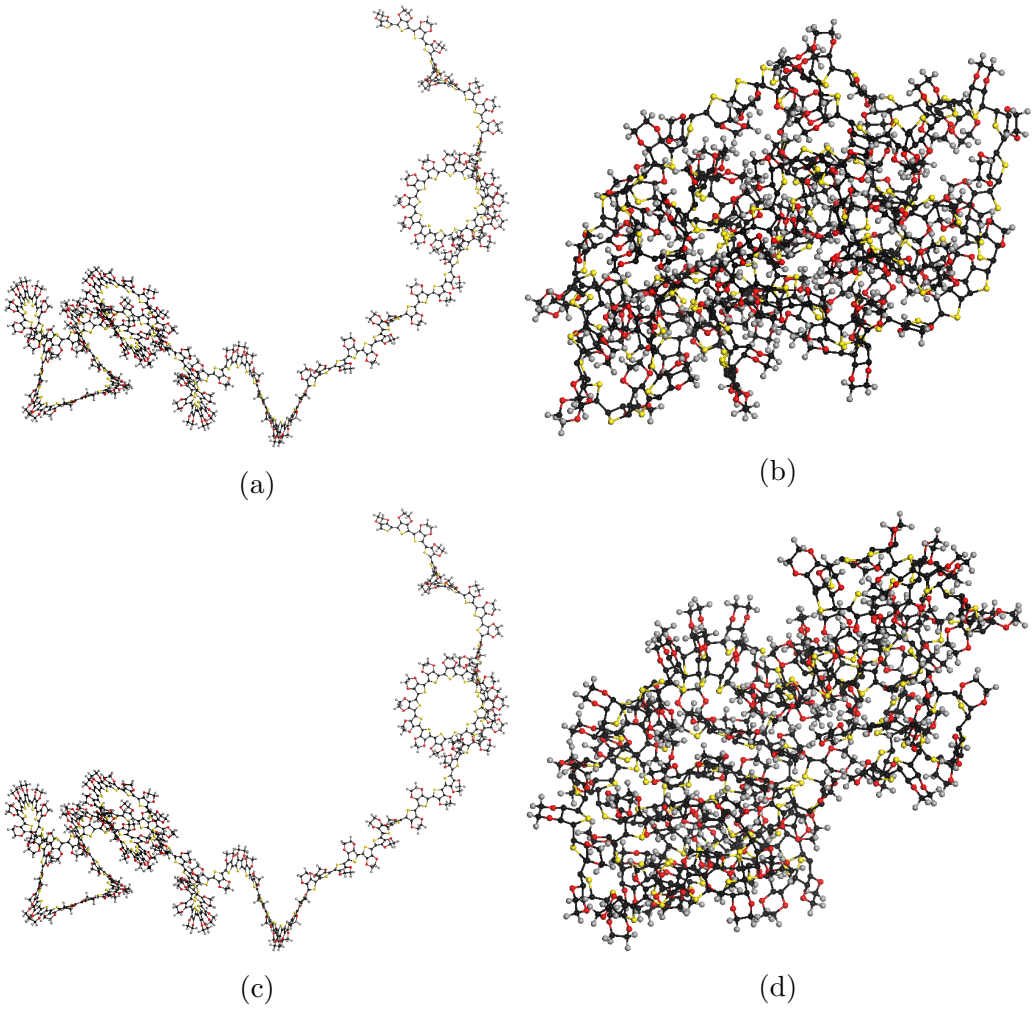

Figure 4.6: 120 unit chain of PEDOT (a) before and, (b) after simulation using the PCFF force field as well as (c) before and, (d) after simulation using the COMPASS force field

Figures 4.7 and 4.8 show the appearance of the PEG chains before and after the MD simulation is performed for the 20 unit structure (142 atoms) and the 120 unit structure (842 atoms), respectively. Here, the 20 unit structure of PEG does fold up, but not to such a great extent as PEDOT. This is much more apparent for the COMPASS force field. It does undergo movement in the chains in terms of the atoms repositioning themselves, but in a way where the chain does not bend. This could be due to steric effects between the seed block. As the chain length increases, the polymer becomes more flexible resulting in the 120 unit structure of PEG folding up, similar to the PEDOT chains. This suggests that as the chain length of PEG is increased, the conformations of the chain change and the PEG units show more affinity for each other with a preference to fold up.

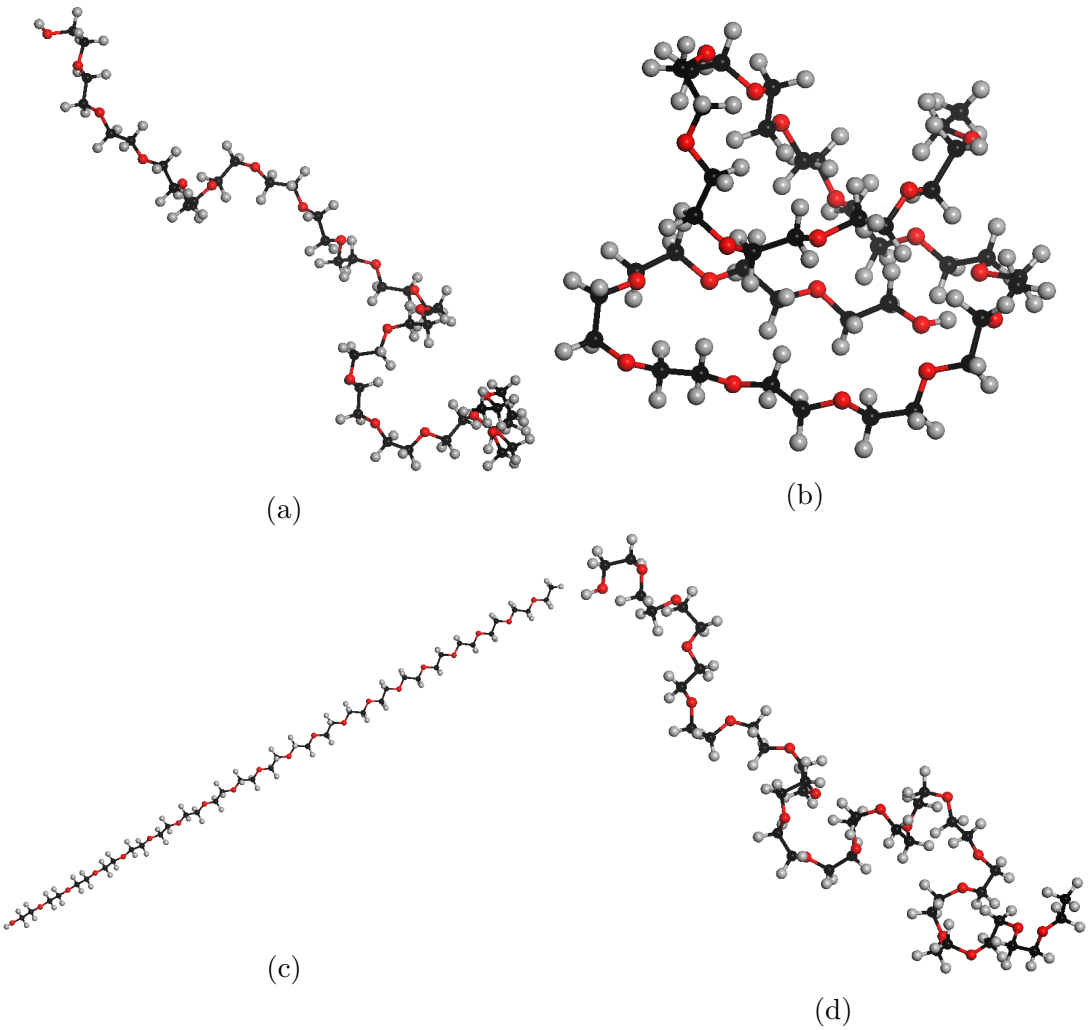

Figure 4.7: 20 unit chain of PEG (a) before and, (b) after simulation using the PCFF force field as well as (c) before and, (d) after simulation using the COMPASS force field

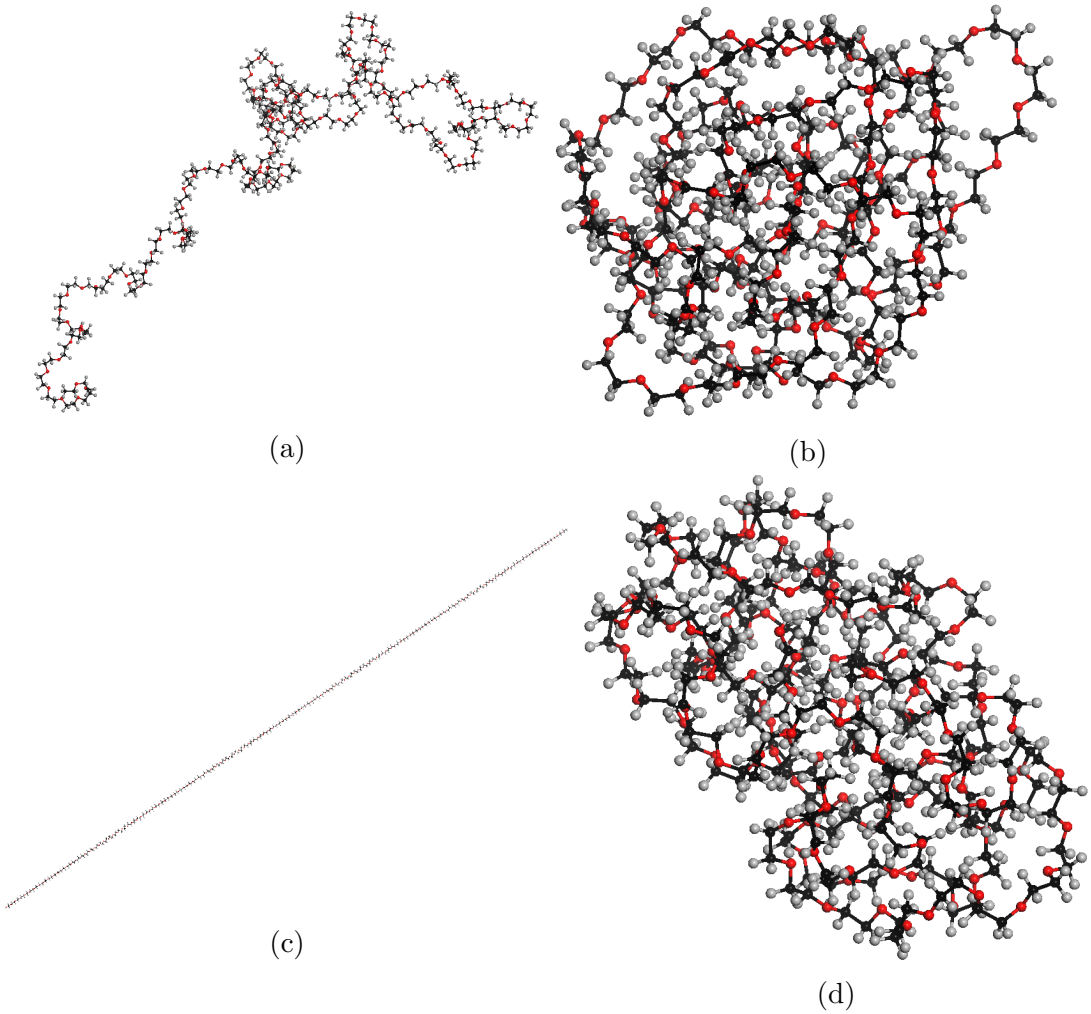

Figure 4.8: 120 unit chain of PEG (a) before and, (b) after simulation using the PCFF force field as well as (c) before and, (d) after simulation using the COMPASS force field

Figures 4.9 and 4.10 show the appearance of the PEDOT-PEG chains before and after the MD simulation is performed for the 40 unit structure (402 atoms) and the 160 unit structure (1602 atoms), respectively. In this case, the PEDOT segment of the co-block is highlighted in red, while the PEG segment is shown in blue. Once again, the chains show a preference for folding up, which is more apparent in the larger chains. In particular, the structure with 160 units shows a dense polymer structure. What is most noticeable in each case is the phase separation between the PEDOT and the PEG chains. Each of the different blocks (PEDOT and PEG) in the co-polymer clearly prefer to predominantly separate themselves rather than dispersing themselves amongst each other. This is more apparent in the 160 unit structure shown by Figures 4.10b and 4.10d. This phase separation is significant in understanding how the two different co-blocks may behave in the multi-block structure of PEDOT-PEG.

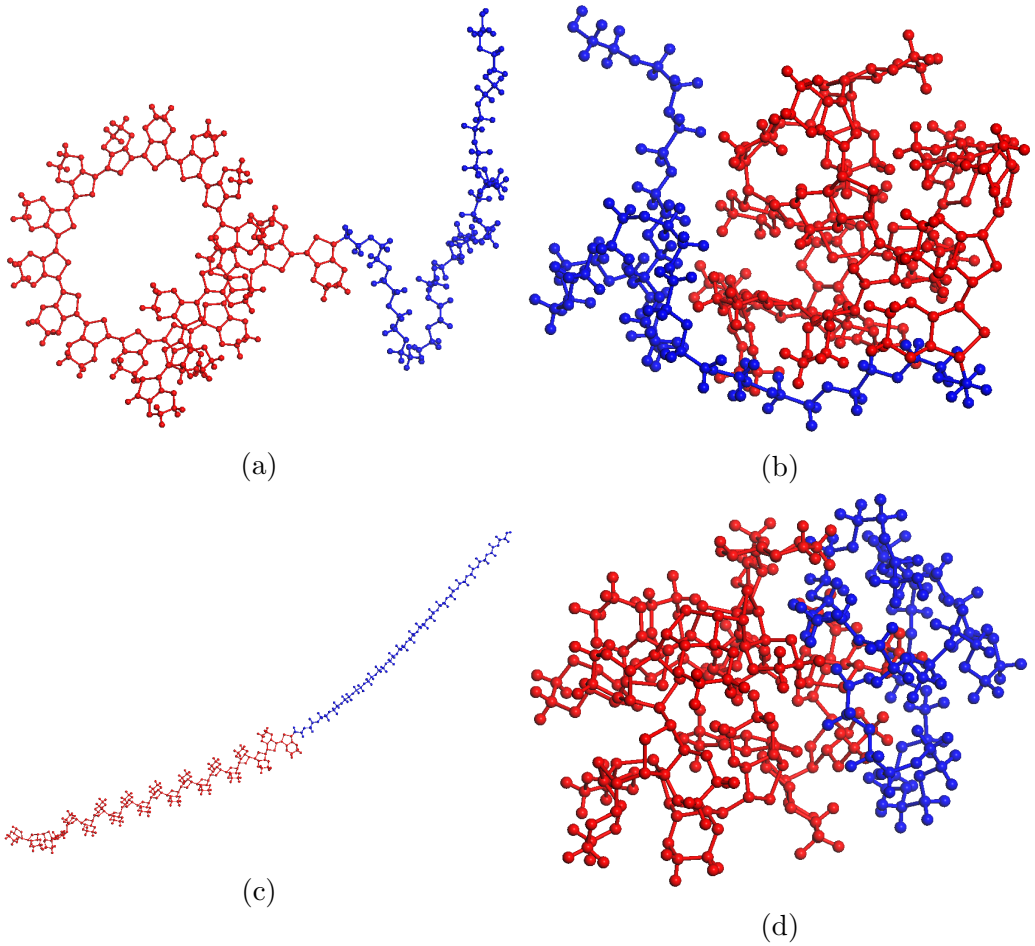

Figure 4.9: 40 unit chain of PEDOT-PEG (a) before and, (b) after simulation using the PCFF force field as well as (c) before and, (d) after simulation using the COMPASS force field

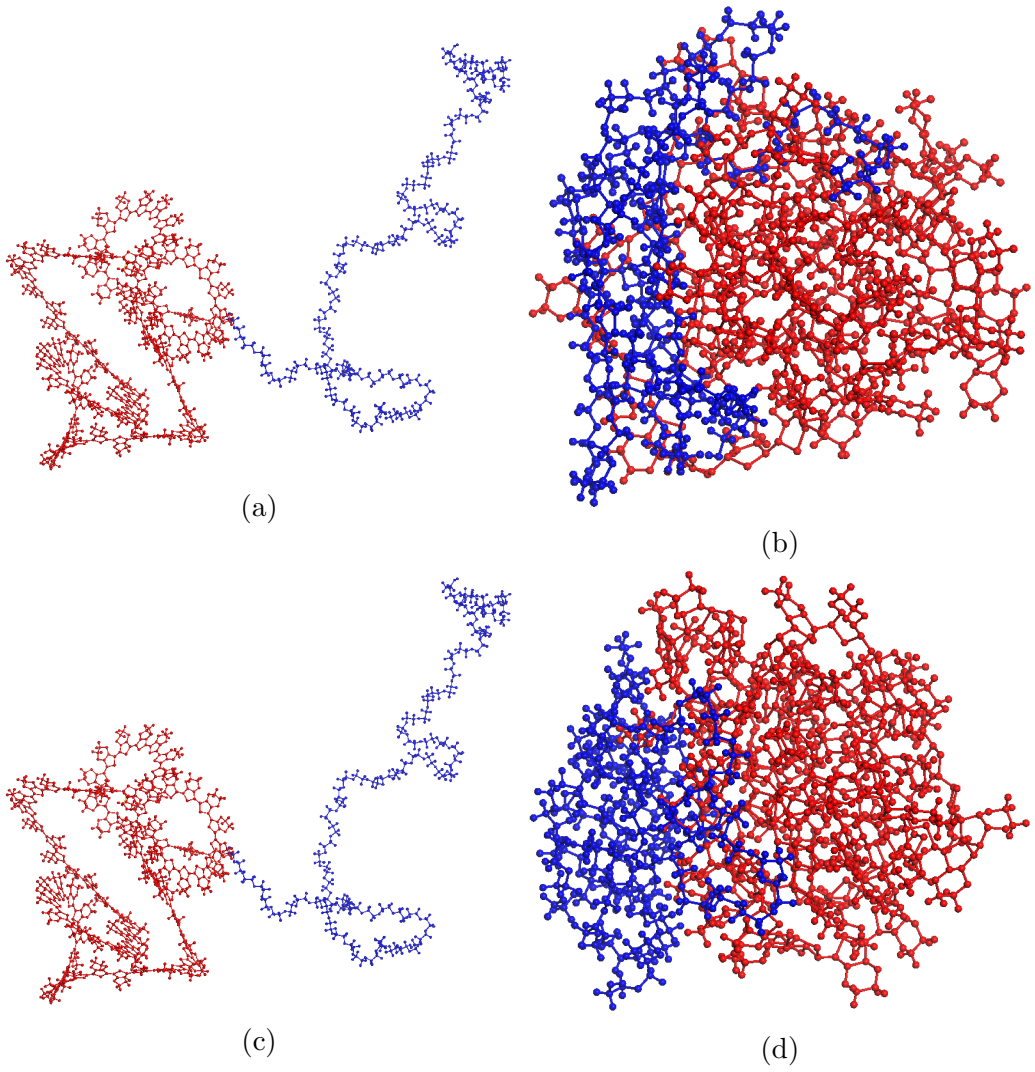

Figure 4.10: 160 unit chain of PEDOT-PEG (a) before and, (b) after simulation using the PCFF force field as well as (c) before and, (d) after simulation using the COMPASS force field

What is apparent is that both of the simulations performed using the PCFF and COMPASS27 force fields show similar results in terms of the physical appearance of the polymer chains. It is of interest to see how these compare with the amorphous polymers, which more closely resemble the experimental systems.

4.3.2 Physical Characteristics - Amorphous Polymers

The physical characteristics of the three amorphous polymer systems studied were observed. Only the PCFF force field was used in this case. For ease of comparison, each polymer was shown packed into the cell. The structure is shown for each case, both before and after the simulation is completed. Figures 4.11 to 4.13 show the amorphous structures of PEDOT, PEG and PEDOT-PEG.

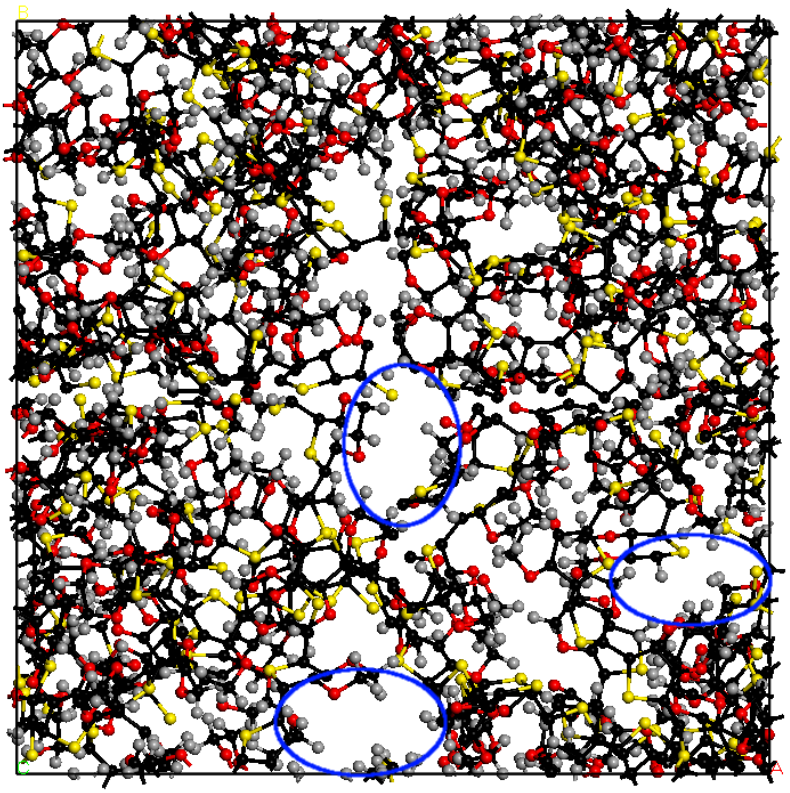

(a)

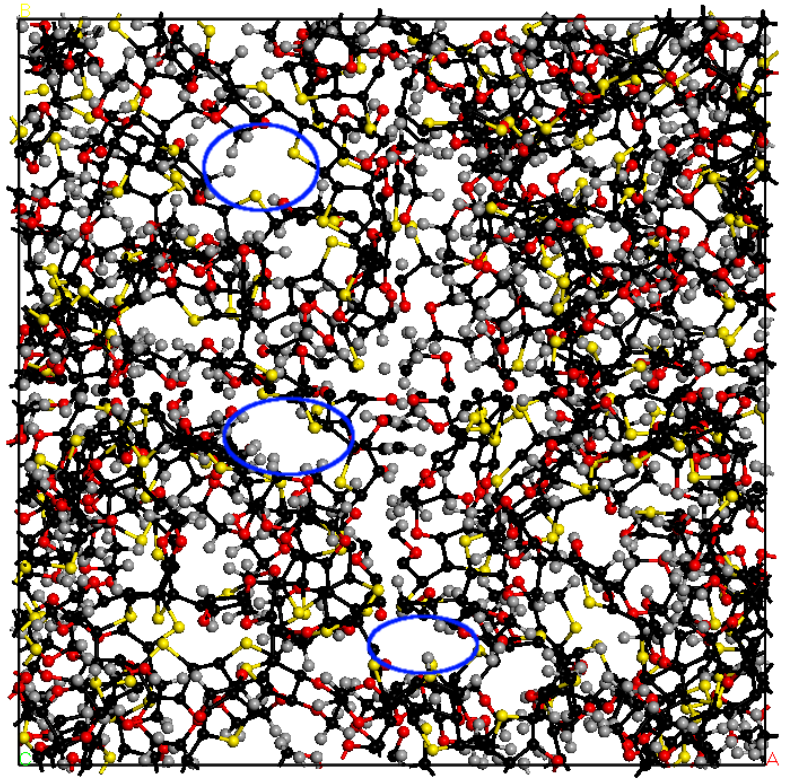

(b)

Figure 4.11: Amorphous PEDOT (a) before simulation and (b) after simulation using the PCFF force field. Highlighted in blue are examples of regions of open space within the system

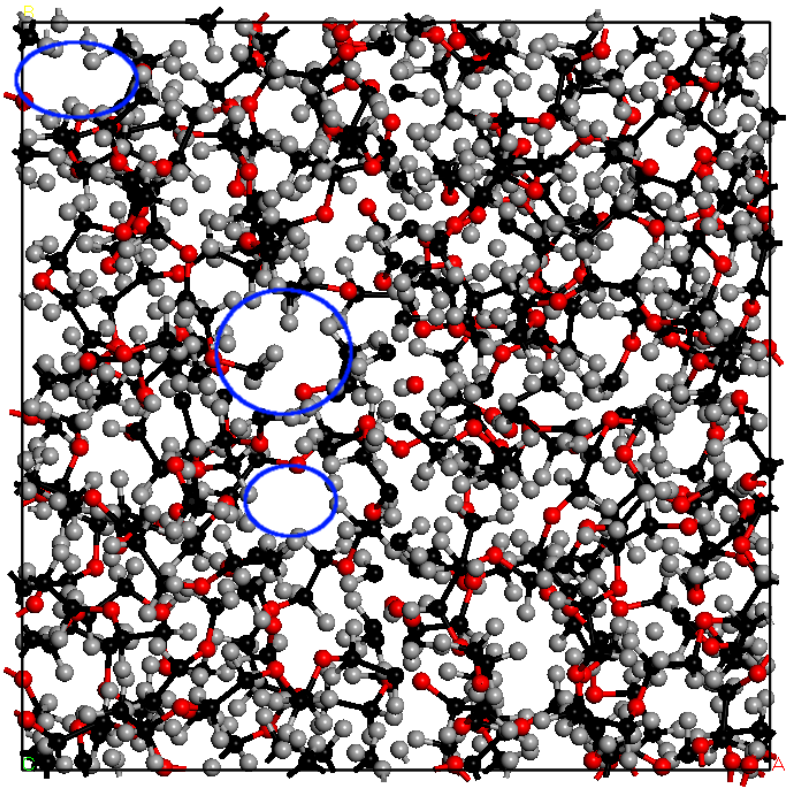

(a)

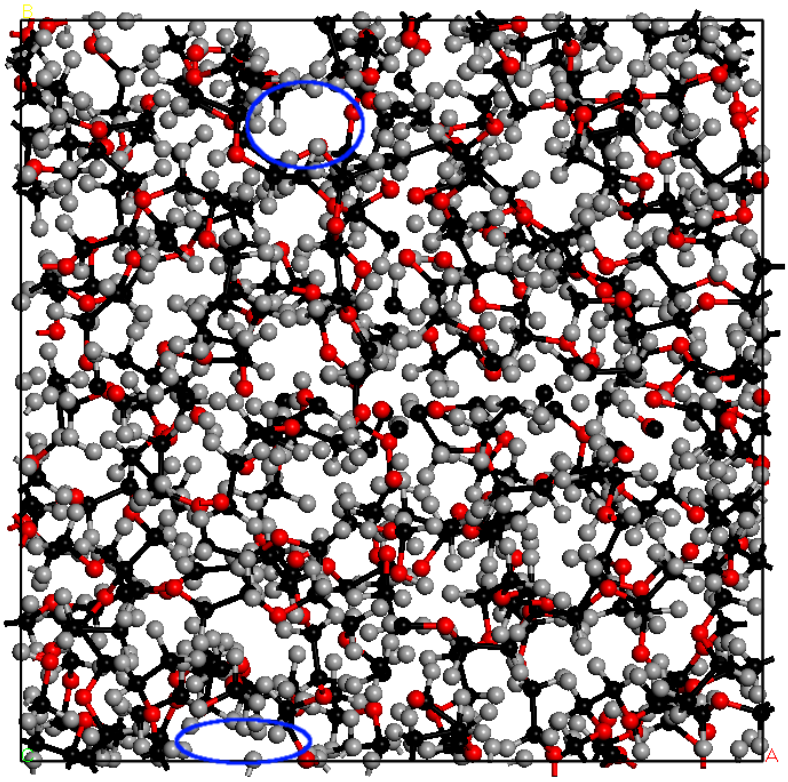

(b)

Figure 4.12: Amorphous PEG (a) before simulation and (b) after simulation using the PCFF force field. Highlighted in blue are examples of regions of open space within the system

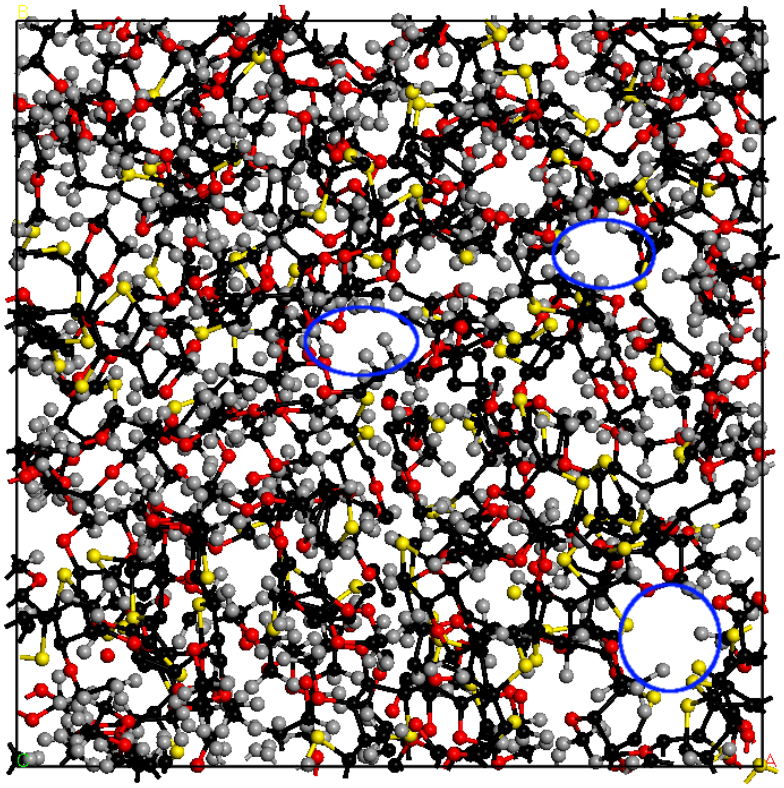

(a)

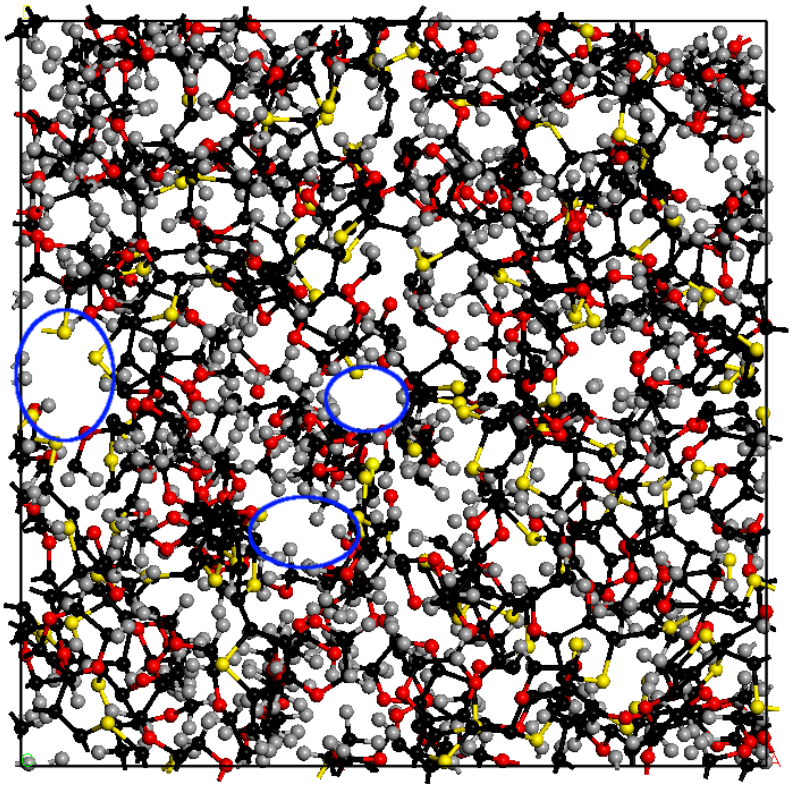

(b)

Figure 4.13: Amorphous PEDOT-PEG (a) before simulation and (b) after simulation using the PCFF force field. Highlighted in blue are examples of regions of open space within the system

In the case of amorphous PEDOT when packed into the cell, we see negligible differences between the structure before and after the simulation. One thing that is noticeable are the regions of open space present in the structure as highlighted in Figure 4.11. These open regions are visible both before and after the simulation, with the difference being the position of these regions. As the simulation progresses, the dense polymer rearranges in the cell, meaning that as the atoms are rearranged, the regions of free space are shifted around.

PEG and PEDOT-PEG appear to show the same pattern with regards to regions of space, as highlighted in Figure 4.12 and Figure 4.13. Again, these regions are shifted as the atoms rearrange themselves when the simulation progresses. PEDOT-PEG appears to show a greater amount of open space in the cell, which is likely due to the steric arrangement of the PEDOT segments of the chains.

What is perhaps of more interest is a comparison of the phase separation in the co-block polymer. For this purpose, the default structure was analysed, as opposed to being packed into the cell. The phase separation in PEDOT-PEG is shown in Figure 4.14. The PEDOT segments of the chain are highlighted in red, with the PEG segments highlighted in blue.

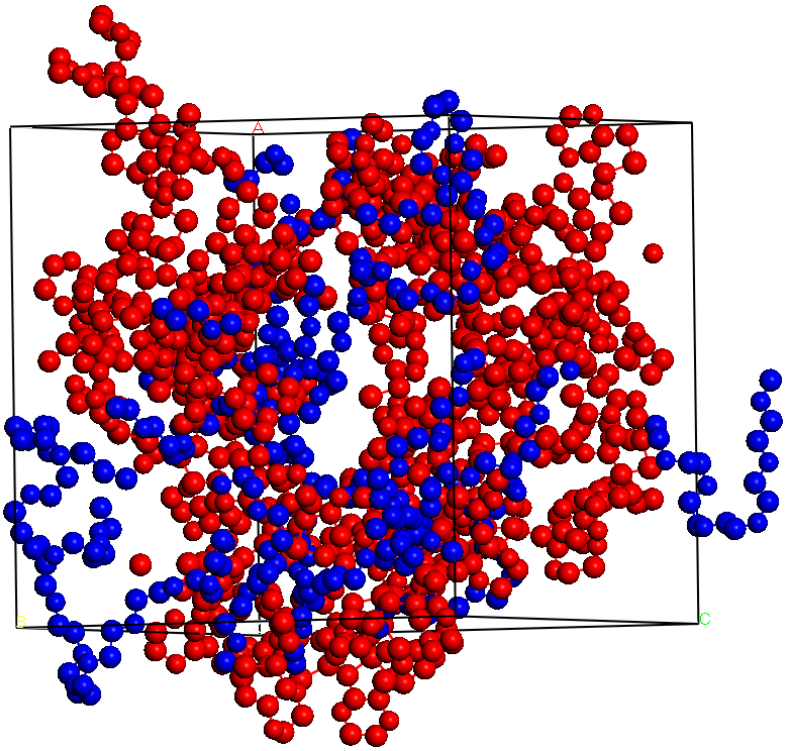

(a)

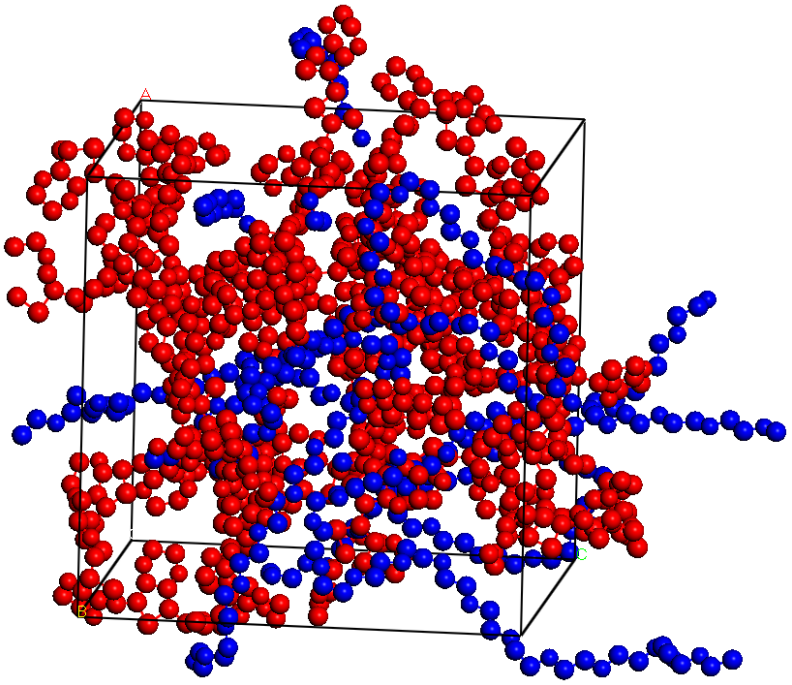

(b)

Figure 4.14: Amorphous PEDOT-PEG (a) before simulation (PCFF), and (b) after simulation (PCFF)

In both structures, a clear separation between the PEDOT and PEG segments of the polymer chain is observed. This shows that despite an increase in density, the two chain segments ideally prefer to remain separate, rather than be dispersed amongst each other. This phase separation is particularly prominent after the simulation has taken place with the strands of PEG clearly separating from PEDOT in terms of

steric arrangement. It even appears that the PEG segments are undergoing a lesser degree of folding after the simulation, which could be a way of the PEG segment separating itself from any neighbouring PEDOT segments.

While differences before and after the simulation appear to be very minor in PEDOT and PEG, the phase separation observed here for PEDOT-PEG is similar to that seen in Figures 4.9 and 4.10.

4.3.3 Bond distribution - Isolated Polymers

An analysis was conducted on some of the isolated polymer chains using both force fields to compare how the bonds in the polymer change over the course of the simulation. Differences between the different polymers are expected due to the way in which they conform, and obviously the different bonds present in the system. The early stages are more likely to show differences as the polymers bend and arrange themselves before reaching a point which is structurally preferable. In this case, only the results for the 20 unit structures of PEDOT and PEG are shown, along with the 40 unit structure (20 units for each block) for the co-block PEDOT-PEG. The bond distributions are reported every 1000ps up to the maximum run time of 5000ps, giving a total of 5 measurements. Figures 4.15 to 4.17 show the bond distributions in each case.

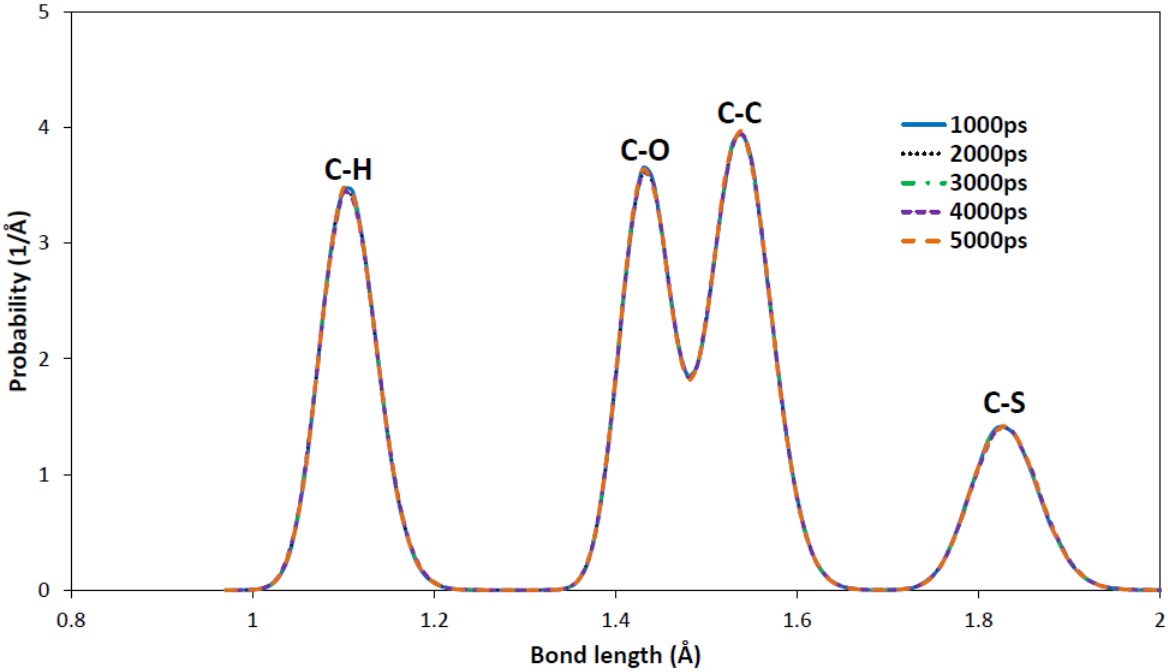

(a)

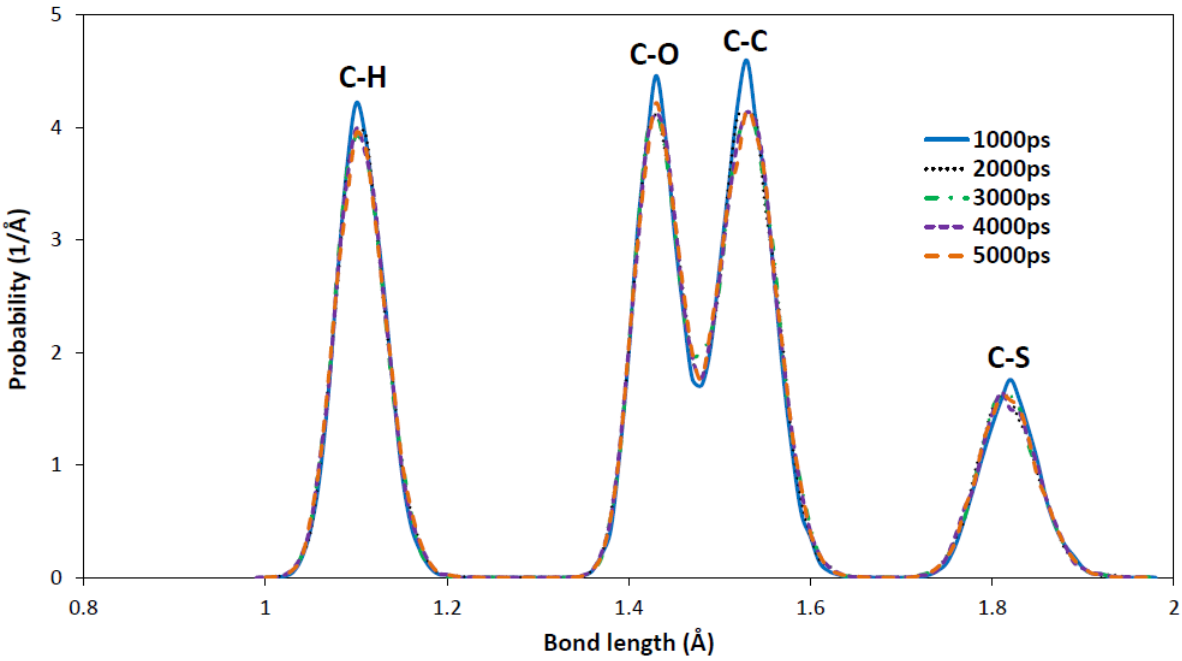

(b)

Figure 4.15: Bond distribution for $PEDOT_{20}$ using (a) the PCFF and (b) COMPASS force fields

From these plots, it can be determined which bonds are present in the system, and which peaks they correspond to on the graph. We know that for PEDOT, the bonds present are C-C, C-H, C-O and C-S. By analysing an animation of the PEDOT structure, the bond lengths could be measured at certain intervals. It was deduced that the peaks at around 1.1Å corresponded to the C-H bond, while the peaks at about 1.43Å were due to the C-O bond. Meanwhile, the peaks at about

1.53-1.54Å were for the C-C bond, with the peaks at about 1.81-1.83Å representing the C-S bond in the system. Table 4.3 details the final bond lengths for each polymer obtained in this study for both force fields. Comparison with experimental values is also conducted in Section 4.3.4.

For the PCFF force field, there is no change in the probability distribution as the simulation progresses for all three systems. A difference in the bond distribution is seen for the COMPASS force field. At 1000ps, the probability of the bonds are all slightly greater than for 2000ps onwards, after which they stabilise. A possible reason for the difference in values could be the rate at which the polymers fold up in the system or to which extent this occurs. Another explanation is due to the straight-chain starting structure of the polymers modelled in Materials Studio, which means that more conformations are required in order to achieve the folded shape. This will be discussed further at the end of this section.

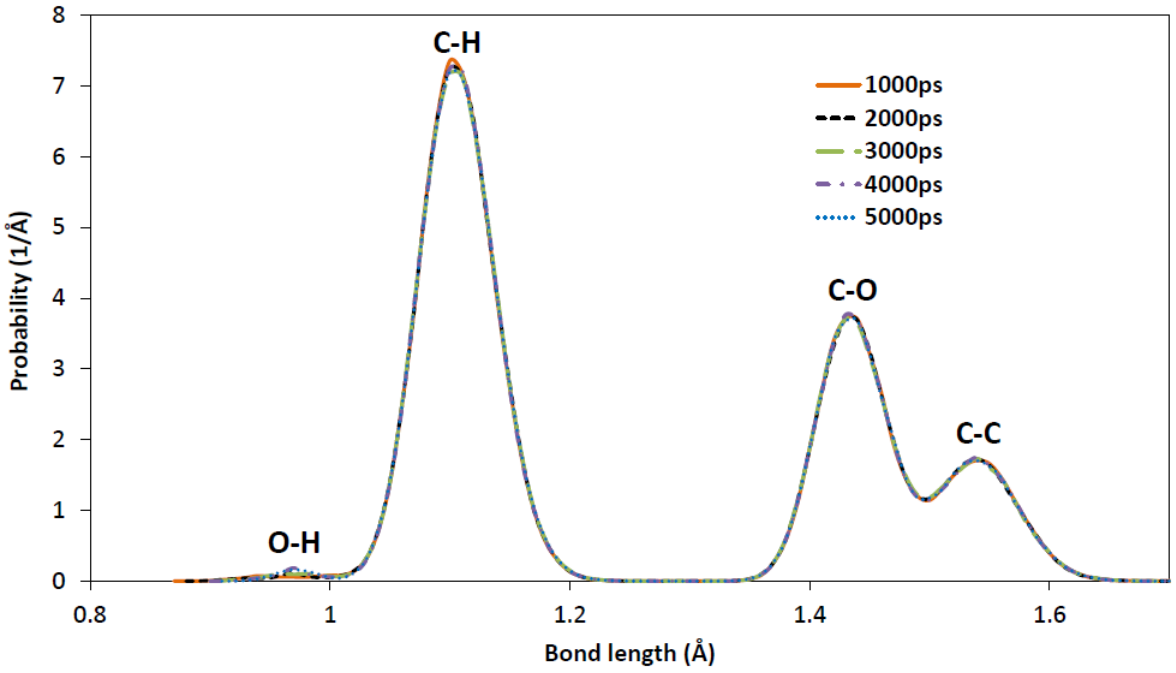

(a)

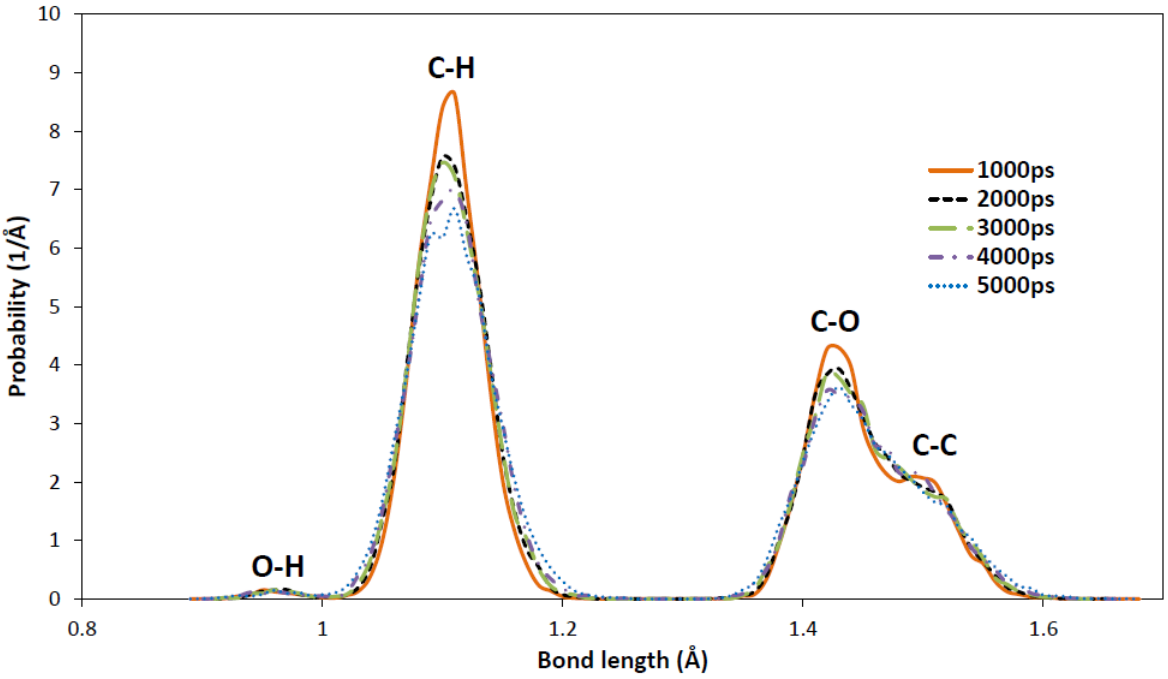

(b)

Figure 4.16: Bond distribution for PEG_{20} using (a) the PCFF and (b) COMPASS force fields

Measuring the bond distances of the output structure, firstly, small peaks were observed around 0.96-0.97Å assigned as an O-H bond. It was determined that the peaks at 1.1Å corresponded to the C-H bond. The peaks at 1.43Å are for the C-O bond, similar to PEDOT, while the peaks at 1.50-1.54Å are characteristic of the C-C bond. In the PEG chain, each O atom is attached to two C atoms, resulting in around twice as many C-O bonds as C-C.

Again, we see a difference between the PCFF and COMPASS force fields. The PCFF force field shows very little change between the different time frames of the simulation, while for COMPASS, there is a change in the probability shown every 1000ps. This could be explained by the difference in structures. The PCFF force field results in the PEG_{20} structure folding up. However, this is not seen to such an extent with the COMPASS force field, which also starts as a straight chain when MD simulations are initiated. Differences in this may be what leads to differing probabilities of bond distribution throughout the simulation.

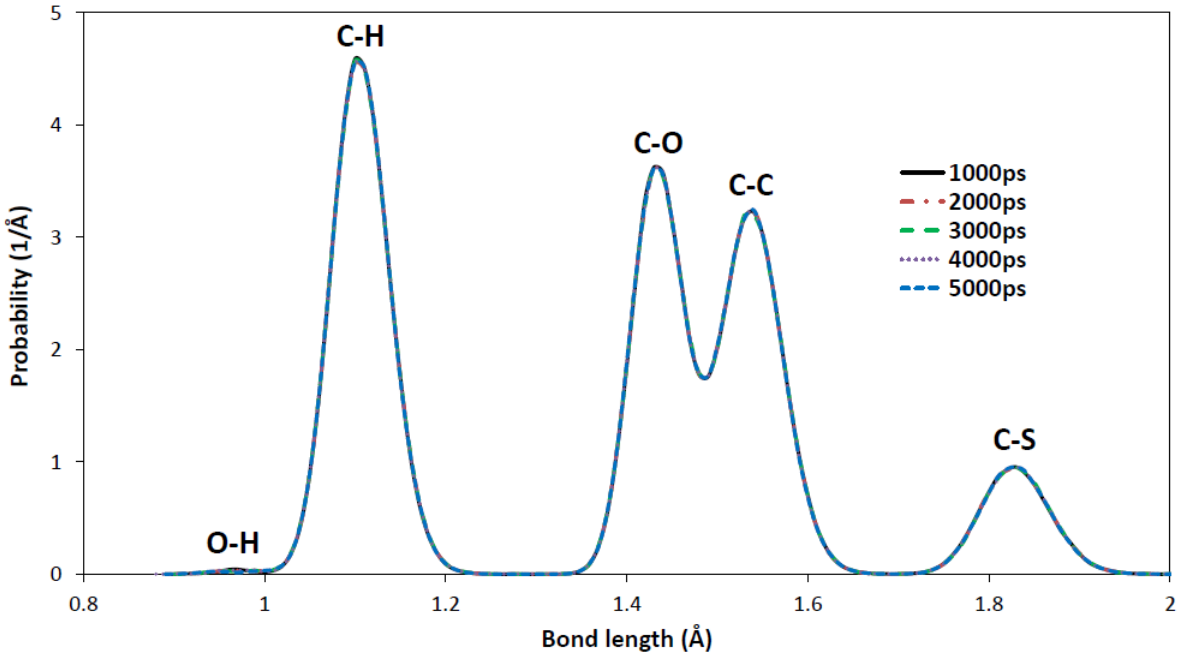

(a)

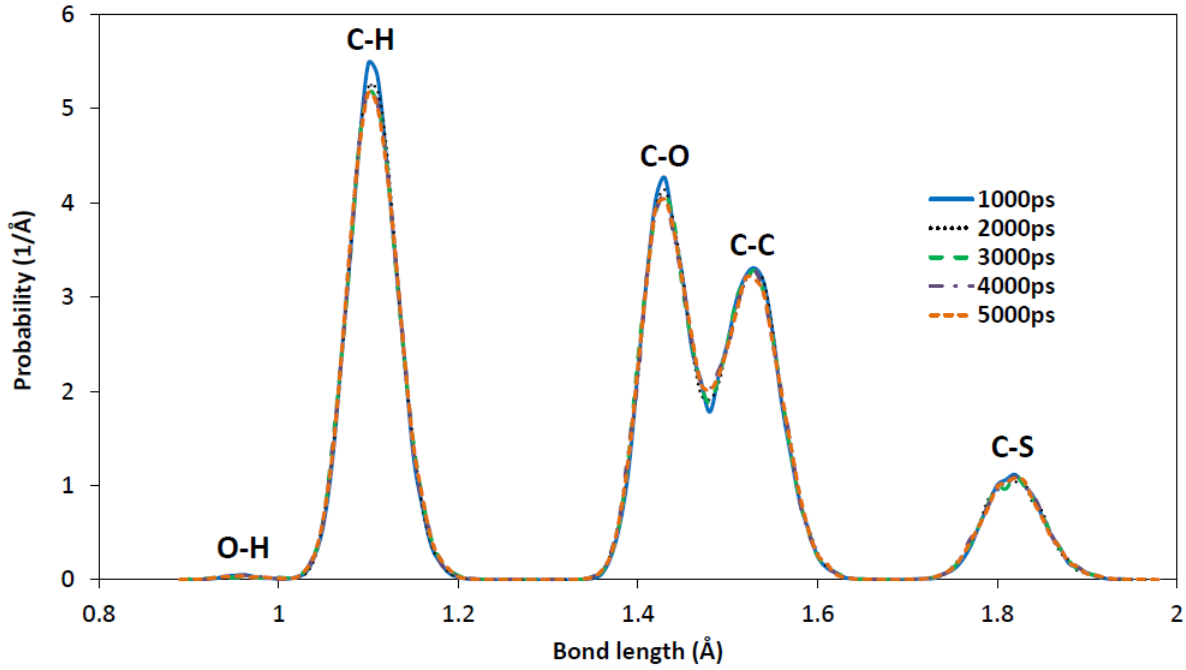

(b)

Figure 4.17: Bond distribution for PEDOT-PEG_{20} using (a) the PCFF and (b) COMPASS force fields

With PEDOT-PEG, we expect to see a combination of the previous plots, albeit with differences in probability. All of the above bonds identified for both the PEDOT and PEG bond distributions are seen here, with a total of 5 peaks observed. Each peak corresponds to the appropriate bond in either PEDOT or PEG, with a small peak present for the O-H bond at the end of the PEG chain, and the peaks at around 1.82-1.83Å for the C-S bond. The respective bond lengths for C-C, C-O and C-H are roughly the same for both polymers. The C-H bond is the most abundant in

PEDOT-PEG, with the second most abundant being the C-O bond. After this, the next most common is the C-C bond, since PEDOT contains more C-C bonds than PEG in a single unit. A smaller peak is then observed for the C-S bond, since this is only present in PEDOT. Finally, the O-H bond has a much smaller probability because only one of this bond is present in the whole system, at the end of the PEG chain. As seen for PEDOT, a slight difference between the first 1000ps and the rest of the simulation is seen in the COMPASS force field. Again, this can be explained by the straight-chain in the starting structure with the COMPASS force field.

As seen in all three polymer bond distributions, there are differences between the bond probabilities at different stages of the calculation. The first initial suggestion for this could be the straight-chain starting structure which the polymers had with the COMPASS force field. In comparison with PCFF, these starting structures were built with Zebedde, which gave a random distribution of the polymer chain. Furthermore, the polymers in DL_POLY also underwent a zero-temperature energy minimisation procedure before being run for the allocated simulation time. In comparison, the polymers using COMPASS underwent a geometry optimisation in Forcite to relax the structure. The differences in these two energy minimisation procedures are likely to reflect in the differences between the two force fields in the bond distribution plots.

4.3.4 Comparison of bond distances - Isolated Polymers v Amorphous Polymers

A brief comparison was made for the final bond distances of the isolated polymers, shown in the previous section, with the final bond distances obtained for the amorphous structures of PEDOT, PEG and PEDOT-PEG. Both the distances using PCFF and COMPASS are shown for the isolated polymers, and compared with the bond distances obtained for the amorphous polymers using the PCFF force field only. Table 4.3 shows the distances in this case.

Table 4.3: Bond distances in Å, obtained for both the isolated and amorphous polymers

Isolated						
Polymer	Force field	O-H	C-H	C-O	C-C	C-S
PEDOT	PCFF	N/A	1.10	1.43	1.54	1.83
PEDOT	COMPASS	N/A	1.10	1.43	1.53	1.81
PEG	PCFF	0.97	1.10	1.43	1.54	N/A
PEG	COMPASS	0.96	1.09	1.43	1.50	N/A
PEDOT-PEG	PCFF	0.97	1.10	1.43	1.54	1.83
PEDOT-PEG	COMPASS	0.96	1.10	1.43	1.53	1.82
Amorphous						
PEDOT	PCFF	N/A	1.10	1.43	1.54	1.83
PEG	PCFF	0.97	1.10	1.43	1.54	N/A
PEDOT-PEG	PCFF	0.97	1.10	1.43	1.54	1.82

In order to confirm that our calculated bond lengths are reliable, they were compared to experimental values. PEDOT in particular can be compared to experimental bond lengths in thiophene with C-S lengths of 1.835Å, C-C lengths of 1.532Å and C-H lengths of 1.117Å , while a C-O distance of 1.428Å in furans is also comparable [217]. Our PEDOT and PEDOT-PEG systems are in good agreement with these values for both force fields, and in the case of the isolated and amorphous polymers.

For PEG, experimental bond lengths in ethylene glycol are comparible with: C-O 1.420Å; C-C 1.530Å; C-H 1.093Å; and O-H 0.950Å [218]. Methoxy-ethane is also a good model for comparison, showing bond lengths of: C-O 1.412Å; C-C 1.540Å; and C-H 1.097Å [217]. Again, our PEG models show good agreement with these values, with only minor variations observed using the PCFF and COMPASS force fields. It should be noted that the calculated C-O values are slightly overestimated compared to the experimental ones. However, we are confident that the force fields used in this study accurately model the bond distances in PEDOT and PEG.

When comparing the force fields against each other, it appears that PCFF and COMPASS show minor variations themselves. COMPASS shows slightly underestimated values in comparison to PCFF and some of the experimental values, for example, C-S bond distances. The slight variation in results for COMPASS is reflected in the bond distribution plots, which showed variation between the different time frames of the simulation, particularly in PEG, while PCFF showed hardly any variation at each stage of the simulation. Perhaps the most noticeable variation is in the case of the C-C bond in PEG with COMPASS, which shows a noticeable underestimation with a distance of 1.5Å, compared to a value of 1.54Å with PCFF

and experimental bond distances of 1.53-1.54Å [217, 218].

Observing the amorphous polymers, which were ran using the PCFF force field, they resulted in bond distances almost identical to the corresponding isolated polymer using PCFF. Therefore, we can deduce that the PCFF force field is consistent when modelling polymers either as an isolated chain, or in a dense amorphous state. As the amorphous polymers reflect what would be expected in an experimental system, it is important to ensure that the polymer chains are correctly modelled, and are comparable to isolated chains and experimental distances.

4.3.5 MSD plots

To begin with, the amorphous cells of the pure polymers (PEDOT, PEG and PEDOT-PEG) were investigated, with the mean square displacement plotted for each case. The intention was to observe the diffusion in the pure polymer systems. The total MSD was plotted for each system. Figures 4.18 to 4.20 show the MSD plots for the three systems in question.

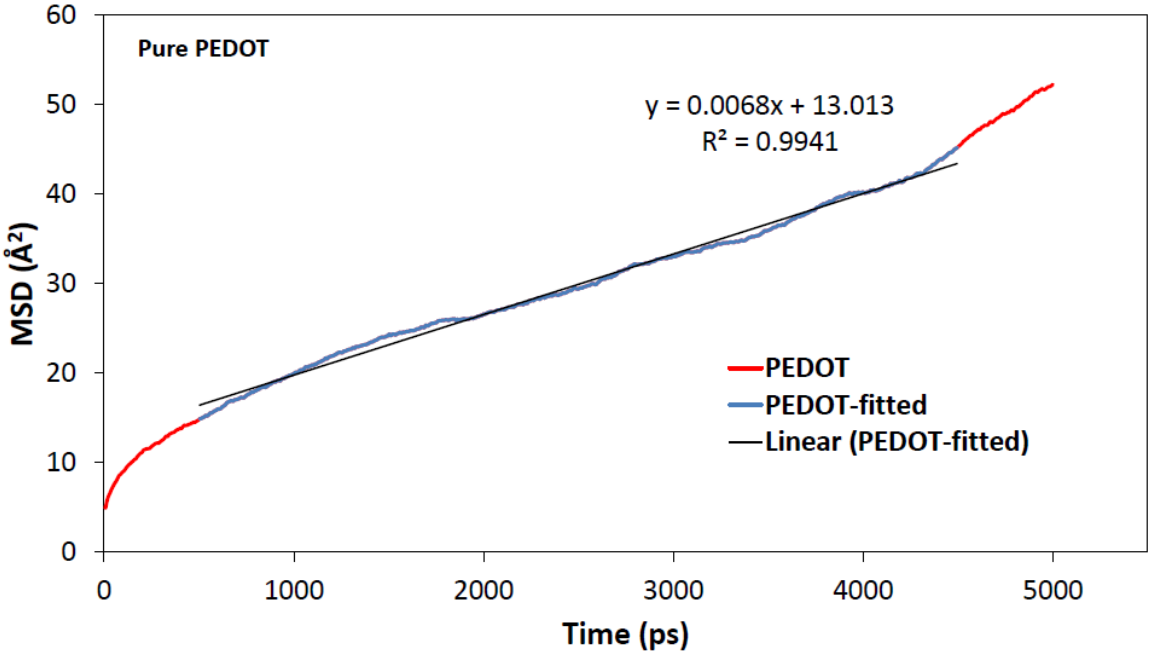

Figure 4.18: MSD plot for the amorphous cell of PEDOT

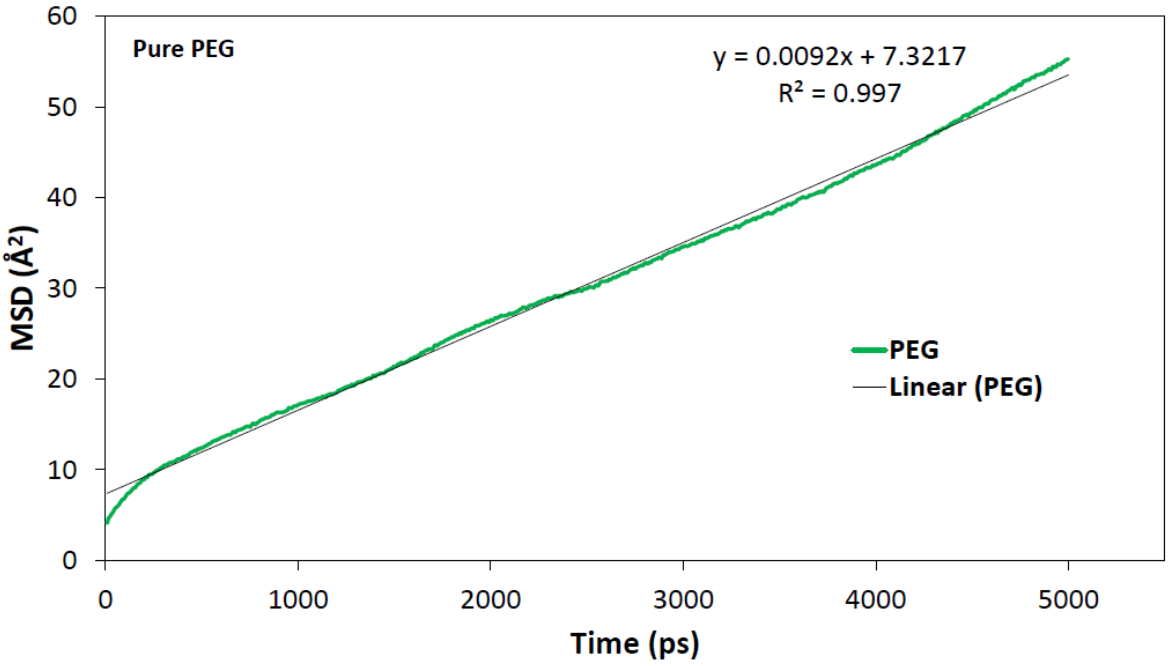

Figure 4.19: MSD plot for the amorphous cell of PEG

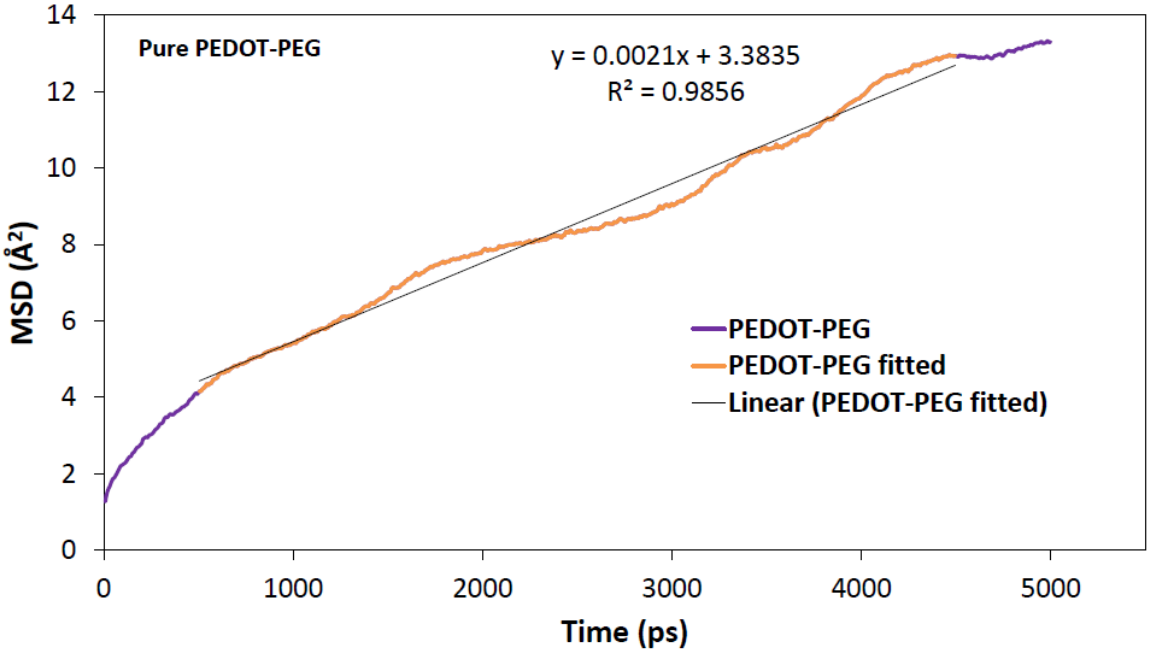

Figure 4.20: MSD plot for the amorphous cell of PEDOT-PEG

From the mean square displacement, the diffusion coefficient can be obtained. The diffusion coefficient is taken from the most linear part of the plot, from which a trend line can be fitted to obtain a linear equation. Any non-linear part of the plot was disregarded as this did not represent the true diffusive motion of the polymer. As can be seen on each of the graphs, the beginning, and usually the end of the MSD plot was not included in fitting the trend line. Equation (4.1) represents the diffusion over a distance for a three-dimensional system, according to Einstein's law.

$$< r^2 >= 6Dt + C \tag{4.1}$$

Here, $< r^2 >$ represents the mean square distance, t representing time, C is a constant, with D defining the rate of diffusion. Table 4.4 shows the diffusion coefficients calculated for all three of the polymers investigated in this study. The coefficients obtained from the gradient of the linear trend line were in units of $Å^2/ps$. As diffusion coefficients are often quoted in units of m^2/s and cm^2/s, the values have been converted into these units for comparison.

Table 4.4: Diffusion coefficients for PEDOT, PEG and PEDOT-PEG in an amorphous polymer cell

Polymer	No. chains	No. atoms	D ($Å^2/ps$)	D (m^2/s)	D (cm^2/s)
PEDOT	10	2620	1.1×10^{-3}	1.1×10^{-11}	1.1×10^{-7}
PEG	10	1420	1.5×10^{-3}	1.5×10^{-11}	1.5×10^{-7}
PEDOT-PEG	5	2010	3.5×10^{-4}	3.5×10^{-12}	3.5×10^{-8}

From these results (Table 4.4), it can be seen that out of all three of the amorphous polymer systems, the PEG chains have the highest rate of diffusion, with a diffusion coefficient in the order of 10^{-11} in m^2/s. This can possibly be explained by the chains of PEG being the least bulky, meaning that the system is less congested, allowing for faster displacement of the chains. The PEDOT-PEG chains have the slowest rate of diffusion, and this could be due to a bulkier system, with more dense packing. Each PEDOT-PEG chain contains 20 units of each block with 40 units in total, which may result in slower diffusion compared to a shorter chain.

It could be that the number of atoms in any particular chain has an effect on the rate of diffusion. We know that a single PEDOT chain contains 262 atoms, while an individual PEG chain only contains 142 atoms. Each PEDOT-PEG chain analysed in this case contains a total of 402 atoms. Therefore, there is a link between the number of atoms in any given chain and the diffusion coefficient, which can be seen by Figure 4.21. This could be further analysed as future work. The arrangement of atoms in the chain is also something that could be looked at, since bulkier structures will most likely have slower rates of diffusion. Bigger systems could be looked at for comparison, such as longer chain lengths and a greater number of chains in the system.

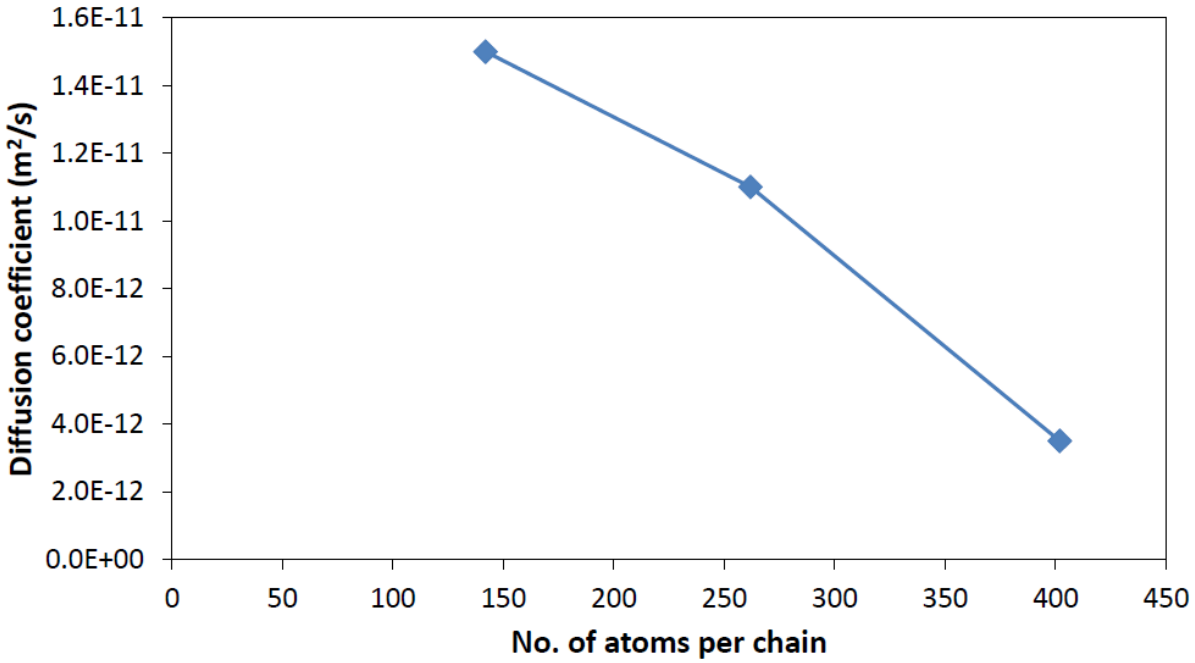

Figure 4.21: The number of atoms per polymer chain vs the diffusion coefficient

4.4 Conclusions

A theoretical study was conducted on the pure polymers of PEDOT, PEG and PEDOT-PEG using Molecular Dynamics. The aim was to observe various properties of the polymers, and make several comparisons including the force field used, the chain length, and also the number of atoms per chain. A brief study was made to compare two different geometries of PEDOT-PEG, the multi-block and tri-block. It was found that the multi-block structure was marginally more stable. Due to experiments being conducted using the multi-block structure, the decision was made to simulate this, as opposed to the tri-block geometry, despite a higher electrical conductivity.

The different polymers were ran for 5000ps using the packages DL_POLY and Forcite. The DL_POLY simulations used a PCFF force field, while the Forcite calculations were all run using the COMPASS force field. The isolated chains were observed to see how their shape and conformation changed throughout the simulation. It was found that the majority of the polymers folded up as the simulation progressed for both force fields, with the exception of the 20 unit chain of PEG for the COMPASS force field. While this example was bent in structure, it did not fold up to the same extent as the other chains. Furthermore, a phase separation was visible for PEDOT-PEG. Both chains showed that the PEDOT and PEG segments of the co-block polymer preferred to remain separate, although this was much more apparent in the 160 unit chain. This gives us an indication into how the polymer chains prefer to arrange themselves in space in the multi-block structure of

PEDOT-PEG.

The amorphous polymers were built using Materials Studio at a fixed density and simulated in DL_POLY. For the amorphous polymers, changes throughout the simulation were minimal. Regions of open space could be seen in each case and analysis showed that these regions changed as the simulation progressed, meaning that the bonds and atoms rearrange themselves during the simulation.

A bond distribution analysis was carried out on the shorter chains for the PEDOT, PEG, and PEDOT-PEG polymers. Each polymer was analysed using both of the force fields (PCFF and COMPASS) to see if there was a difference between the two. The bond distribution was recorded every 1000ps with a peak representing a bond in the system and the probability (height of peak) indicating how abundant that particular bond was in the polymer. By doing this, all of the peaks could be assigned to a particular bond in the system allowing us to see which bonds were most prevalent. The C-C bond was the most common in PEDOT, while the C-H bond was most common in PEG. PEDOT-PEG would essentially show a combination of the two previous plots, and here, the C-H bond again had the greatest probability. Another observation was that between each 1000ps of the simulation in PCFF, no difference was seen in the distribution. However, minor differences were observed for COMPASS in terms of the bond probability, which was most apparent in PEG. A suggestion for this could be due to the polymer structure not folding up to such an extent in the COMPASS force field. Other possibilities could be down to the straight-chain starting structure produced by the polymer builder in Materials Studio, meaning that more conformations of the polymer are required to achieve the folded up state.

The bond distances obtained were also compared with experimental values. It was found that the calculated distances agreed well with the experimental distances. Furthermore, the amorphous polymers, which only used the PCFF force field, were found to give very similar bond distances to the corresponding isolated chain. This showed that the distances were reproducible regardless of whether the polymer was modelled as an isolated chain or in an amorphous densely packed state.

The final part of the analysis for the pure polymers was to measure the mean square displacement (MSD) of the amorphous polymer chains. This allowed us to investigate the diffusion of the PEDOT, PEG and PEDOT-PEG polymer chains. It was identified that the PEG chains had the highest rate of diffusion, with PEDOT-PEG chains having the lowest. A possible reason for this could be down to the PEG chains being less bulky, and, therefore, showing less steric hindrance, facilitating diffusion. The PEDOT-PEG chains also contained a greater number of atoms per chain, along with being less sterically favourable, which might explain the lower diffusion coefficient. A trend was found between the number of atoms per chain and the diffusion coefficient for the three systems studied. The lower the number of

atoms, the higher the rate of diffusion.

Chapter 5

Molecular Dynamics Analysis of Lithiated Polymers

5.1 Aims

In this chapter, the intention is to study lithium ion insertion in PEDOT-based co-block polymers for battery applications. An investigation into potential lithium coordination sites in PEDOT-PEG and PEDOT:PSS was performed, using Fourier Transform Infrared Spectroscopy (FTIR). These measurements were complemented with frequency calculations using ab initio simulations. By analysing various changes in the spectra between pure and lithiated samples, the coordination sites for lithium could be deduced.

A study was then conducted to analyse the behaviour of lithium when inserted into various polymers. The amorphous polymer systems simulated using molecular dynamics in the previous chapter, PEDOT-PEG, PEDOT and PEG, were all used again in this investigation. For the individual polymers, a single lithium ion was inserted for test purposes and for comparison with each other. For each polymer, LiI and LiCl salts were used for comparison. Various concentrations of the lithium salts were then added to PEDOT-PEG. The results obtained in this case were the radial distribution functions (RDF) and mean square displacements (MSD).

The RDF results provide coordination distances and coordination numbers, along with any ion pairing that may occur in the system. The MSD allowed diffusion coefficients to be obtained for lithium, and from this, the Li-ion conductivity could be calculated. The coordination distances and diffusion coefficients were compared with experimental values and previously published theoretical results.

5.2 Method

5.2.1 FTIR frequencies

In order to investigate lithium coordination in our polymer chains, it is useful to do a preliminary investigation to find out the preferred coordination sites. For this purpose, ab initio calculations were performed on monomers of PEDOT, PEG and PSS. In addition, Fourier Transform Infra-red (FTIR) spectroscopy was used to characterise PEDOT-PEG and PEDOT:PSS. The main aim was to obtain the FTIR spectra for these two co-polymers, and use frequency calculations in order to assign the peaks in the IR spectra.

Firstly, the FTIR spectra were obtained for the pure samples of PEDOT-PEG and PEDOT:PSS. This is to determine the purity of the sample as well as to assign the peaks in the spectra. In this exercise, possible coordination centres of the polymers were identified. Once pure samples of PEDOT-PEG and PEDOT:PSS were obtained, various concentrations of the salt, $LiPF_6$, were added. Interactions between the lithium salt and the polymer are expected to result in either a shift or creation of new peaks in the spectra. These peaks in theory should correspond to the coordination centres found in the pure polymers. This technique has been previously used, in particular, the study of the oligo(ethylene glycol)dimethacrylate gel with the LiTFSI salt [219].

The PEDOT-PEG sample, a commercial copolymer from Sigma-Aldrich, was initially a 1 wt.% dispersion in propylene carbonate (PC) and water [11]. The sample was casted onto a glass surface, and left at a temperature of 70 °C for a total of 10 hours, resulting in an evaporation of the propylene carbonate, leaving behind a thin black layer of pure PEDOT-PEG on the glass surface.

Four samples of the PEDOT-PEG copolymer were mixed with 11.35, 21.16, 37.95 and 54.69 wt.% of $LiPF_6$, respectively. In order to prepare these samples for FTIR analysis, these differing concentrations of $LiPF_6$ were mixed with the PEDOT-PEG and ultra-sonicated for a total of 90 minutes at a temperature of 60 °C, after which they were casted onto a glass surface before being left overnight at 70 °C. Once again, the propylene carbonate evaporated away leaving behind thin layers of a black solid. This represented the lithiated sample of PEDOT-PEG which could then be analysed using IR measurements.

The sample of PEDOT:PSS was a commercial composite from Sigma-Aldrich, which was dispersed in water. It constituted a 0.5 wt.% of PEDOT and a 0.8 wt.% of PSS. The pure sample of PEDOT:PSS was prepared by casting 30g of the dispersion in water onto a glass surface, and leaving the sample for 10 hours at a temperature of 70 °C. As a result, the water evaporated to leave behind 0.39g of a thin black layer on the glass surface. The samples were analysed by Thermal Gravimetric Analysis (TGA) to confirm that they were water-free.

One lithiated sample of PEDOT:PSS was prepared using 20 wt.% of $LiPF_6$. 0.1g of $LiPF_6$ was mixed with 30.76g of the pure sample dispersed in water, yielding a mixture of 0.1g $LiPF_6$ and 0.4g of the PEDOT:PSS composite in water. The resulting mixture was ultra-sonicated for 90 minutes at a temperature of 60 °C, after which it was casted onto a glass surface and dried overnight at 70 °C. This lead to all the water being evaporated off as confirmed by TGA, leaving behind a thin black layer weighing 0.5g, which was our lithiated polymer composite.

To assign the peaks obtained in the FTIR spectra for the pure and lithiated samples of PEDOT-PEG and PEDOT:PSS, the CRYSTAL09 [82] code was used to conduct the ab initio simulations. For the purposes of this study, only the monomers of PEDOT, PEG and PSS were investigated, as they provide the required frequency information in order to compare to the experimental data. By performing a vector analysis in conjunction with visual identification (using the graphical interface J-ICE [220]), the peaks were assigned. An animation of the structure at each frequency showed the vibrational modes.

In order to create the monomer models, they were first created using MarvinSketch [164] and energy minimised using the MMFF94 optimisation method, in order to calculate the lowest energy conformer. Using the coordinates from MarvinSketch, the CRYSTAL input file could be created using a symmetry point group of 1. A geometry optimisation was specified in the input with the BFGS algorithm and the basis sets were defined as: Sulphur - 86-311G* [221], Carbon - 6-311d11G [222], Oxygen - 8-411d11G [222], Hydrogen - 5-11G* [223] and Lithium - 61-1G [223]. All calculations were run using the B3LYP hybrid functional, performed self-consistently and converged to an energy of 10^{-7} Hartree. It should be noted that when lithium was inserted as a cation, the CHARGED keyword was used to indicate a charged system. The frequencies of the molecule were calculated for the geometry optimised structure.

With the calculated results obtained, and with the aid of a database of IR frequencies [224] to confirm the accuracy of the results, the spectra were interpreted. With each significant peak identified in the spectra, the wavenumber was compared with the equivalent frequency in the simulated results. The frequencies that were specific to each polymer were considered crucial when confirming its presence in the sample, and the IR database confirmed the reliability of the simulations.

5.2.2 Molecular Dynamics approach for lithium diffusion

The PCFF force field in combination with the DL_POLY package has been used to simulate the lithiated polymer systems, having shown good comparison with the COMPASS27 force field in the Forcite module in terms of the shape and conformations for the pure polymer chains.

In order to investigate lithium properties, amorphous cells of PEDOT, PEG and

PEDOT-PEG were constructed and simulated as described in Chapter 4. The fixed densities of 1g/cm^3 were left unchanged for PEDOT and PEG. The experimental density of 1.141g/cm^3 for PEDOT-PEG was used again [216]. As for the pure polymers described, the amorphous systems of PEDOT and PEG once again consisted of 2620 and 1420 atoms respectively with ten chains of the 20-unit polymer in the system, while PEDOT-PEG consisted of 2010 atoms with five chains that contained 20 units for each block (PEDOT and PEG representing a block each with 40 units in total for each chain) and the multi-block geometry analysed.

The main goal of this investigation is to measure lithium coordination and diffusion in the polymer. From this we can calculate key properties such as lithium conductivity and gain an idea into how well the polymer electrolytes store and transport lithium ions to determine energy storage and ion mobility in applications such as Li-ion batteries. By seeing how much lithium can be inserted into a system, the suitability of that polymer electrolyte can be assessed for energy storage, while higher diffusion coefficients result in higher conductivity.

For the PCFF force field used for the pure polymers, no interatomic potential parameters are provided for the van der Waals interactions of lithium ions with the polymer atoms. Therefore, a literature search was conducted to derive or obtain suitable potentials to obtain the best interaction for lithium ions. Some force fields such as CVFF contain parameters for lithium ions, which are based on the 12-6 Lennard-Jones functional form, shown by Equation (5.1) [129].

$$V_{ij}{}^{vdW}(R_{ij}) = \frac{A_{ij}}{R_{ij}{}^{12}} - \frac{B_{ij}}{R_{ij}{}^{6}} \tag{5.1}$$

Here, R_{ij} represents the internuclear distance. PCFF on the other hand uses the 9-6 Lennard-Jones functional form for calculating van der Waals forces. Equation (5.2) shows the 9-6 Lennard-Jones functional form.

$$V_{ij}(R_{ij}) = \epsilon_{ij}\left\{2\left(\frac{R^*_{ij}}{R_{ij}}\right)^9 - 3\left(\frac{R^*_{ij}}{R_{ij}}\right)^6\right\} + \frac{q_i q_j}{R_{ij}} \tag{5.2}$$

R_{ij} is the distance between ions i and j, while q_i and q_j represent the ionic charges. The pairwise parameters R^*_{ij} and ϵ_{ij} are formed from the intrinsic ion parameters, R^*_i, R^*_j, ϵ_i and ϵ_j using the combination rules which have been described by Waldman and Hagler [225]. R^* is the separation distance at the minimum energy, while ϵ controls the well depth for the van der Waals interaction energy between two like ions. R^*_{ij} and ϵ_{ij} can be represented by Equations (5.3) and (5.4).

$$R^*_{ij} = \left(\frac{R^*_i{}^6 + R^*_j{}^6}{2}\right)^{1/6} \tag{5.3}$$

$$\epsilon_{ij} = 2(\epsilon_i \epsilon_j)^{1/2} \frac{{R^*_i}^3 {R^*_j}^3}{{R^*_i}^6 + {R^*_j}^6} \tag{5.4}$$

Equation (5.2) has the advantage in that only the R^* and ϵ parameters are required to specify the functional forms of the van der Waals potential [129]. Studies of specific systems such as alkanes [226] and amide crystals [227] show that the repulsive $(R^*_{ij}/R_{ij})^9$ term gives a better fit to the experimental data, both in the gaseous phase and condensed phase, compared to the $(R^*_{ij}/R_{ij})^{12}$ term, which in these cases was overly repulsive. A study by Peng *et al.* [129] contains a new set of 9-6 force field parameters for a series of alkali metal cations and halide anions. Included in this were van der Waals 9-6 parameters for Li^+, Cl^- and I^-, required to simulate lithium diffusion using the 9-6 PCFF force field.

Previous van der Waals coefficients have shown much variation, particularly due to the differing approaches used to derive them. A solution to this is to derive non-bonding parameters from crystal structures. In many cases, experimental values for lattice energies and structures have been measured for simple ionic crystals. However, further data is required such as dispersion energies for ions in the crystals. In Peng *et al.*'s study, parameters are derived that obey physical properties for ions as well as accounting for crystal properties.

Parameters reported in the study were converted from A and B in the commonly used Lennard-Jones 12-6 potential to the R^* and ϵ quantities, used in the 9-6 potential. It is rare that enough data is available in order to determine A_{ij} and B_{ij}, and, therefore, these constants may be obtained from the intrinsic parameters A_i and B_i of individual species via a combination rule [225]. The B_i parameter is often known as the C_6 dispersion coefficient and represents the dispersion energy [129]. These intrinsic parameters for the Lennard-Jones 12-6 potential are related to the R^* and ϵ parameters by Equations (5.5) and (5.6).

$$R^*_i = 2^{1/6}\sigma_i = \left(\frac{2A_i}{B_i}\right)^{1/6} \tag{5.5}$$

$$\epsilon_i = \frac{{B_i}^2}{4A_i} \tag{5.6}$$

Where σ represents the separation distance at which the van der Waals potential is zero.

An evaluation of published van der Waals parameters (R^* and ϵ) and corresponding isoelectronic rare gas values for a series of alkali metal cations and halide anions showed large discrepancies and variation between different approaches. This was particularly apparent when observing a wide range of values for a single ion. For example, our particular ion of interest, Li^+ had R^* values ranging from 1.41Å as derived by Chandrasekhar *et al.* [228] to 2.66Å as found by Heinzinger *et al.* [229].

There is an even larger discrepancy with ϵ ranging from as low as 0.077 kJ/mol by Åqvist [230] up to 26.15 kJ/mol (Chandrasekhar *et al.* [228]). F^- shows even more extreme variation with Chandrasekhar *et al.* having obtained values considerably different to other researchers.

There are several possible explanations for the discrepancies as discussed by Peng *et al.* [129], and a lack of precision in deriving the parameters may be an issue. For example, many of the approaches involved fitting by means of ab initio calculations. While these may agree well with experiments, the London dispersion forces may only provide a small contribution, particularly in the case of ab initio Hartree-Fock calculations such as those conducted by Kisternmacher *et al.* [231].

A difficulty in determining dispersion components of van der Waals interactions in these systems has resulted in parameters that are possibly not determined with a great degree of accuracy, resulting in such a variation in values. While they may appear to work well for one particular type of methodology, a lack of transferability is a problem here.

Referring back to Equations (5.2) to (5.4), the approach was taken by Peng *et al.* [129] to derive appropriate van der Waals parameters that corrected for systematic errors and satisfied isoelectronic trends. The Waldman-Hagler combination rules [225] were selected for this procedure as they have shown to fit well with the properties of noble gases with a higher degree of accuracy compared to other expressions. Furthermore, they fit more accurately to the properties of organic crystals [232].

In order to derive these new parameters, Heinzinger *et al.*'s R^* and ϵ values were chosen as a starting point. This is because Heinzinger's set [229] was the only complete one for all of the alkali halide ionic crystals. The first step was to keep Heinzinger *et al.*'s ϵ values the same [129]. This was to ensure that the correct trend in van der Waals energy based on atomic size was maintained in order to satisfy Equation (5.7).

$$\begin{aligned} \epsilon(I^-) > \epsilon(\mathrm{Cl}^-) > \epsilon(\mathrm{Br}^-) > \epsilon(\mathrm{F}^-) \\ \epsilon(\mathrm{Cs}^+) > \epsilon(\mathrm{Rb}^+) > \epsilon(\mathrm{K}^+) > \epsilon(\mathrm{Na}^+) > \epsilon(\mathrm{Li}^+) \end{aligned} \tag{5.7}$$

The R^* values were adjusted to satisfy the isoelectronic relationship (where alkali metal cations, noble gases and halide anions form families of isoelectronic species) *i.e.* $R^*(\mathrm{F}^-) > R^*(\mathrm{Ne}) > R^*(\mathrm{Na}^+)$. The criteria in this case is to ensure that systematic deviations from the experiment in the crystal calculations are minimised. Despite an improvement in lattice constants and energies, the new parameters did not always obey the Slater-Kirkwood relationship, described by Equation (5.8).

$$C_6(F^-) = \left(\frac{\alpha_{F^-}}{\alpha_{Ne}}\right)^{3/2} C_6(Ne)$$
$$C_6(Na^+) = \left(\frac{\alpha_{Na^+}}{\alpha_{Ne}}\right)^{3/2} C_6(Ne) \tag{5.8}$$

This equation relates the dispersion coefficients of isoelectronic anions, cations and neutral noble gases. It allows the C_6 coefficients to be estimated for the ions, on the provision that the C_6 coefficients for the relevant noble gases are known, along with the polarisabilities of the noble gases and ions. The C_6 coefficients and polarisabilities for noble gases for this study were taken from experiments [233], [234], [162], while the polarisabilities for the ions were estimated by Deltour [235] who fitted experimental indices of refraction of alkali halide salt crystals.

With these new C_6 parameters derived by Peng *et al.* [129], along with the revised R^* values, the ϵ value for the ions can be determined by relating it to C_6 and R^* ($C_6 = 3\epsilon R^{*6}$). The new R^* and ϵ parameters still had shortfalls, with an underestimation of the lattice constants and overestimation of lattice energies, which suggested that the van der Waals interactions between the ions were not repulsive enough. In order to provide a better fit with the experimental data, Peng *et al.* scaled the ϵ parameters of the cations (by scaling the C_6 coefficients since they were proportional at a given R^*). A scaling factor of 2.9 for Li^+ and 1.5 for the remaining cations minimised the systematic errors in the calculated crystal data of the 20 alkali halide salt crystals. The proper relative magnitudes for the isoelectronic anions, neutrals and cations for R^*, ϵ and C_6 were all maintained.

The combination rules in this case can be used to work out the necessary van der Waals interactions required for each type of atom in the system. Firstly, the self-interaction R^* and ϵ values for the 9-6 van der Waals potentials must be defined. For example, if the K^+ self-interaction R^* and ϵ values are derived as 3.60Å and 0.72kJ/mol respectively, then combination rules will calculate the K^+ non-bonded interactions with all other atoms in the system. This bypasses the need to have to derive the relevant parameters for each specific ion-atom interaction in a system.

For our purposes, the parameters for Li^+, Cl^- and I^- were taken from Peng *et al.*'s study and employed with the PCFF force field. The R^* and ϵ values used in this work are shown in Table 5.1.

Table 5.1: Derived 9-6 van der Waals parameters, taken from Peng *et al.*'s study [129]

Ion	R^* (Å)	ϵ (kJ/mol)
Li^+	2.40	0.071
Cl^-	5.22	0.259
I^-	5.77	0.515

These new parameters were applied to the amorphous cells of PEDOT, PEG and PEDOT-PEG, with the intention of investigating lithium coordination and diffusion. Lithium ions were inserted manually into the structure. For each lithium ion inserted, a counterion needed to be present. Both iodine and chlorine were chosen in this case for comparison, with a particular focus on iodine, where it is known experimentally that Li-O separations of about 2Å can be obtained in PEO/LiI solutions [236]. For test purposes, a single Li^+ cation along with either an I^- or Cl^- anion was inserted into the amorphous polymer cell.

As with the pure amorphous polymer systems, the starting structures were minimised with the zero-temperature minimisation algorithm, with the target system reset to 10K. The system was again equilibrated for the first 100 timesteps, with a value of 100% in the system density of particles used for the density variation. The temperature was rescaled for every step during the equilibration procedure. A timestep of 0.001ps was used with the NVE ensemble and the Velocity Verlet algorithm. The long-ranged and short-ranged interactions cutoff was set to 12Å. A value of 1×10^{-6} for the Ewald sum was used to calculate the electrostatic forces, using an automatic parameter optimisation. Each system ran for a total of 5000ps. The majority of these parameters were left unchanged for all simulations performed in this study. The only variant in terms of the system parameters was the short and long range cutoff values, which were adjusted for certain systems.

MSD plots were obtained for each system to determine the lithium diffusion coefficient. RDF plots were also obtained in order to compare the Li-O separations in each case, with a comparison also made between the LiI and LiCl salts.

5.3 Results and Discussion

5.3.1 Ab initio simulations of monomers to compliment FTIR measurements of co-polymers

To determine the Li-interactions with PEDOT-PEG and PEDOT:PSS, an experimental FTIR study was undertaken. To begin with, the pure PEDOT-PEG spectrum was investigated. Figure 5.1 shows the FTIR spectrum along with the experimental frequencies for each significant peak.

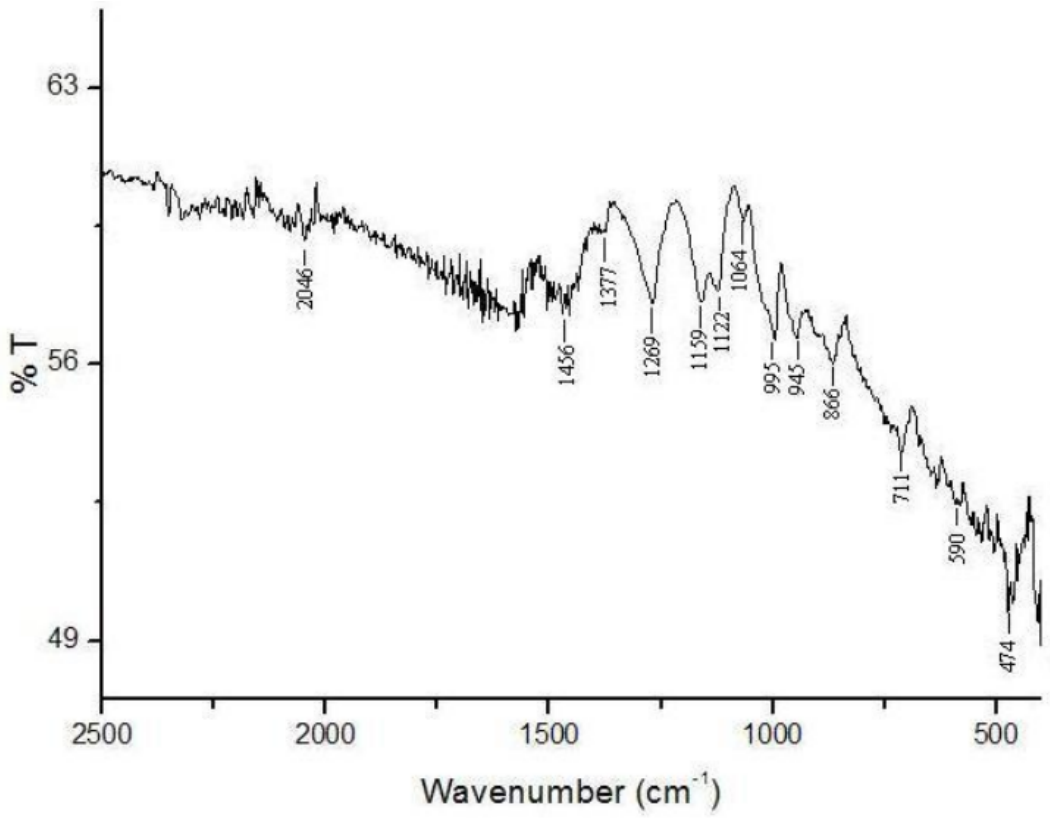

Figure 5.1: FTIR spectrum of pure PEDOT-PEG

Using the CRYSTAL09 code and the graphical user interface J-ICE to interpret the spectrum, Table 5.2 shows the frequencies that were assigned to the different vibrational modes. Figure 5.2 shows the PEDOT and PEG monomers which were used in order to calculate the frequencies.

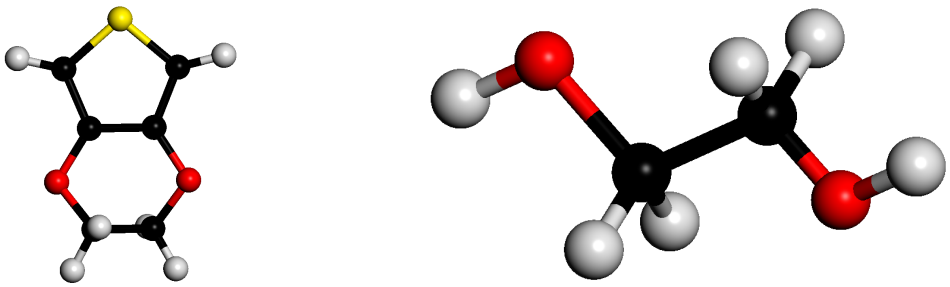

(a) PEDOT monomer (b) PEG monomer

Figure 5.2: Structures of (a) PEDOT and (b) PEG. Carbon atoms are displayed in black, with hydrogen atoms in grey, oxygen atoms in red and sulphur atoms in yellow

Table 5.2: Experimental and calculated frequencies (cm^{-1}) for PEDOT-PEG

Exp. Freq.	Calc. Freq.		Mode	
	PEDOT	PEG	PEDOT	PEG
474	483	N/A	C-C bend	N/A
590	560	N/A	C-S bend	N/A
711	724	N/A	C-C bend	N/A
866	847	837	C-S stretch	C-H bend
945	951	N/A	C-H twist	N/A
995	N/A	986	N/A	C-C stretch
1064	1073	N/A	C-C stretch	N/A
1122	1120	1069	C-H twist	C-O stretch
1159	1154	1157	C-O stretch	C-H twist
1269	1271	1292	C-H twist	C-H bend
1377	1388	N/A	C-H bend	N/A
1456	1448	1485	C-C stretch	C-H bend

There are several peaks in this table which allow us to confirm the purity of the sample. With previous experiments conducted on thiophenes, it is suggested that multiple bands of different intensities would be seen ranging from 1200 to 1555cm^{-1} [224], which is confirmed both experimentally and theoretically. These bands are associated with various C-H modes and C-C stretches. Another key identification is the experimental peak shown at 1159cm^{-1}, interpreted as a C-O stretch by calculations. This also gives reasonable agreement with previously conducted experiments on furans, which suggest that a C-O stretch would be present between 1075-1100cm^{-1} [224]. Along with the C-O stretch, another key peak is present at 866cm^{-1}, which is due to a C-S stretch. With these comparisons, we are confident that PEDOT is present in this pure sample of PEDOT-PEG.

With regards to PEG, the main thing we are looking for is a C-O stretch. This is seen on the spectrum at 1122cm^{-1}, and also computationally at 1069cm^{-1}. The peak at 1122cm^{-1} also corresponds to PEDOT which showed a vibrational mode computationally at 1120cm^{-1}. Hence, some peaks overlap. This is observed in this case. It is useful to use calculations in order to distinguish between the PEDOT and PEG vibrational modes. The other key peaks identified are the C-C stretch at 995cm^{-1}, C-H twisting at 866cm^{-1} and 1159cm^{-1}, and C-H bending at 1269cm^{-1} and 1456cm^{-1}. With all this information, we are confident that PEG is also present in the sample, and that the spectrum does indeed show that we have pure PEDOT-PEG.

We are confident that water is not present in our samples. The TGA analysis confirmed that water was not present in the sample. In the experimental spectrum of water, peaks would be observed at around 600cm^{-1}, 1600-1680cm^{-1}, and 3550cm^{-1}

[237]. The peaks at 600cm^{-1} and 3550cm^{-1} would be very broad, while the peak at around 1600-1680cm^{-1} would be sharp. While a peak at 590cm^{-1} was identified in the above spectrum, it was deduced to be from the C-S bending mode in PEDOT. Meanwhile, no sharp peak is observed around 1600-1680cm^{-1}, nor are any peaks present from 3000-3550cm^{-1} which can be seen in Figure 5.5. Therefore, we can rule out any of the peaks in this spectrum being due to water.

The pure PEDOT:PSS spectrum was then analysed. The peaks were assigned once again using the calculations from CRYSTAL along with the graphical interface programme J-ICE. The presence of PEDOT and PSS in the sample was confirmed. Figure 5.3 shows the FTIR spectrum for the pure sample of PEDOT:PSS.

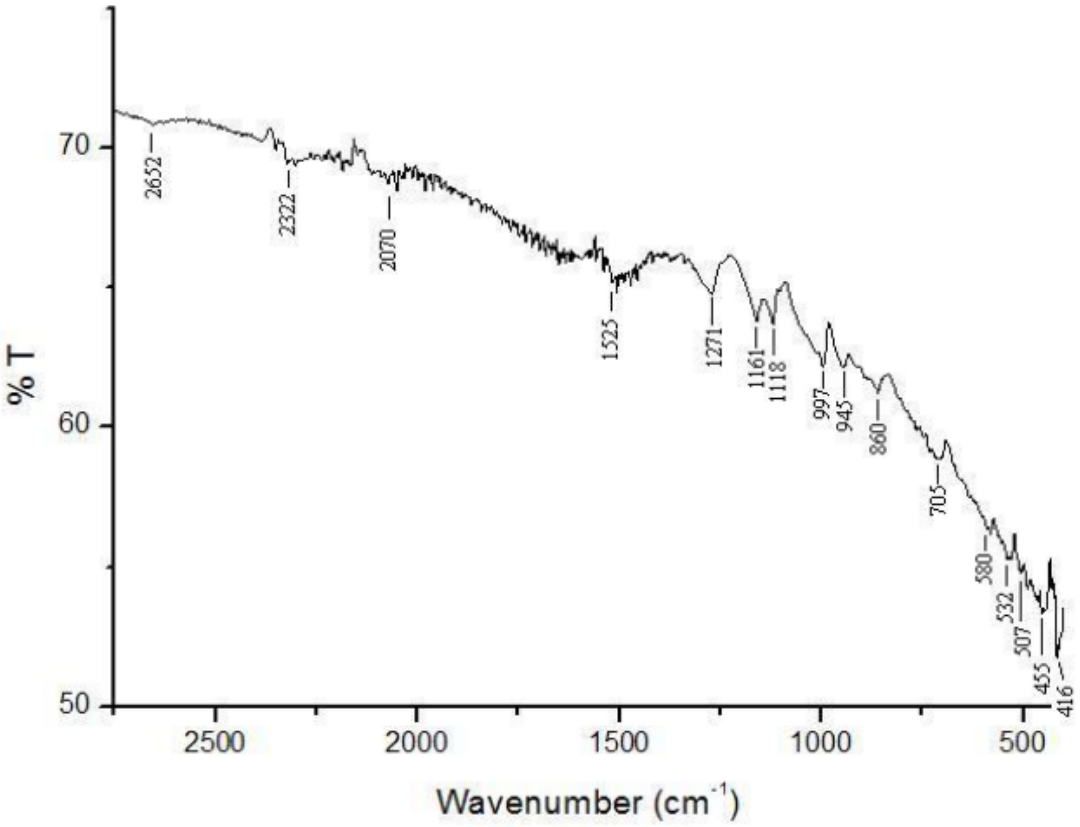

Figure 5.3: FTIR spectrum of pure PEDOT:PSS

Figure 5.4 shows the structure of the polystyrene sulphonate monomer used in the simulations. Table 5.3 shows the frequencies that were assigned for the spectrum.

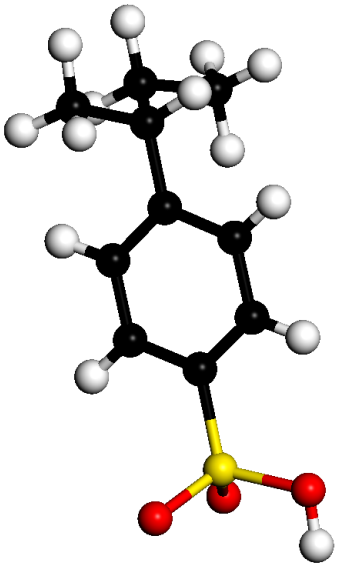

Figure 5.4: Structure of the PSS monomer. Carbon atoms are displayed in black, with hydrogen atoms in grey, oxygen atoms in red and sulphur atoms in yellow

Table 5.3: Experimental and calculated frequencies (cm^{-1}) for PEDOT:PSS

Exp. Freq.	Calc. Freq.		Mode	
	PEDOT	PSS	PEDOT	PSS
416	N/A	422	N/A	C-C bend
455	443	N/A	C-O bend	N/A
507	483	N/A	C-C bend	N/A
532	524	527	C-H twist	C-S stretch
580	560	567	C-S bend	C-H bend
705	724	714	C-C bend	S-OH stretch
860	847	859	C-S stretch	C-H bend
945	951	N/A	C-H twist	N/A
997	N/A	1002	N/A	C-H bend
1118	1120	1112	C-H twist	C-S stretch
1161	1154	1167	C-O stretch	C-H bend
1271	1271	1244	C-H twist	S-O stretch
1525	1524	1528	C-C stretch	C-H bend

Once again, the main peaks that result from PEDOT are present, and comparison with these significant peaks in the previous spectrum confirm that once again, PEDOT is identified in the sample. Several of the peaks provide evidence for determining PSS in the sample, but the main peak of interest is the one shown on the spectrum at $705cm^{-1}$. Using calculations, this was identified to result from an S-OH stretch, in the sulphonate group of PSS. The typical range for an S-OH stretch would be around $840 - 880cm^{-1}$ [224]. However, we are still confident on the relia-

bility of this assigned peak as it was confirmed by vector analysis. Other important peaks are those situated at 1118cm^{-1} and 1271cm^{-1}, which correspond to a C-S stretch and an S-O stretch respectively. With these results, it is apparent that the sulphonate group associated with PSS is present, and, therefore, the spectrum can be assumed to correspond to the sample of pure PEDOT:PSS. It should be noted that the hydrogen atom was used in the sulphonate group in the calculations of PSS in order to maintain a neutral system. This is why an S-OH stretch is detected.

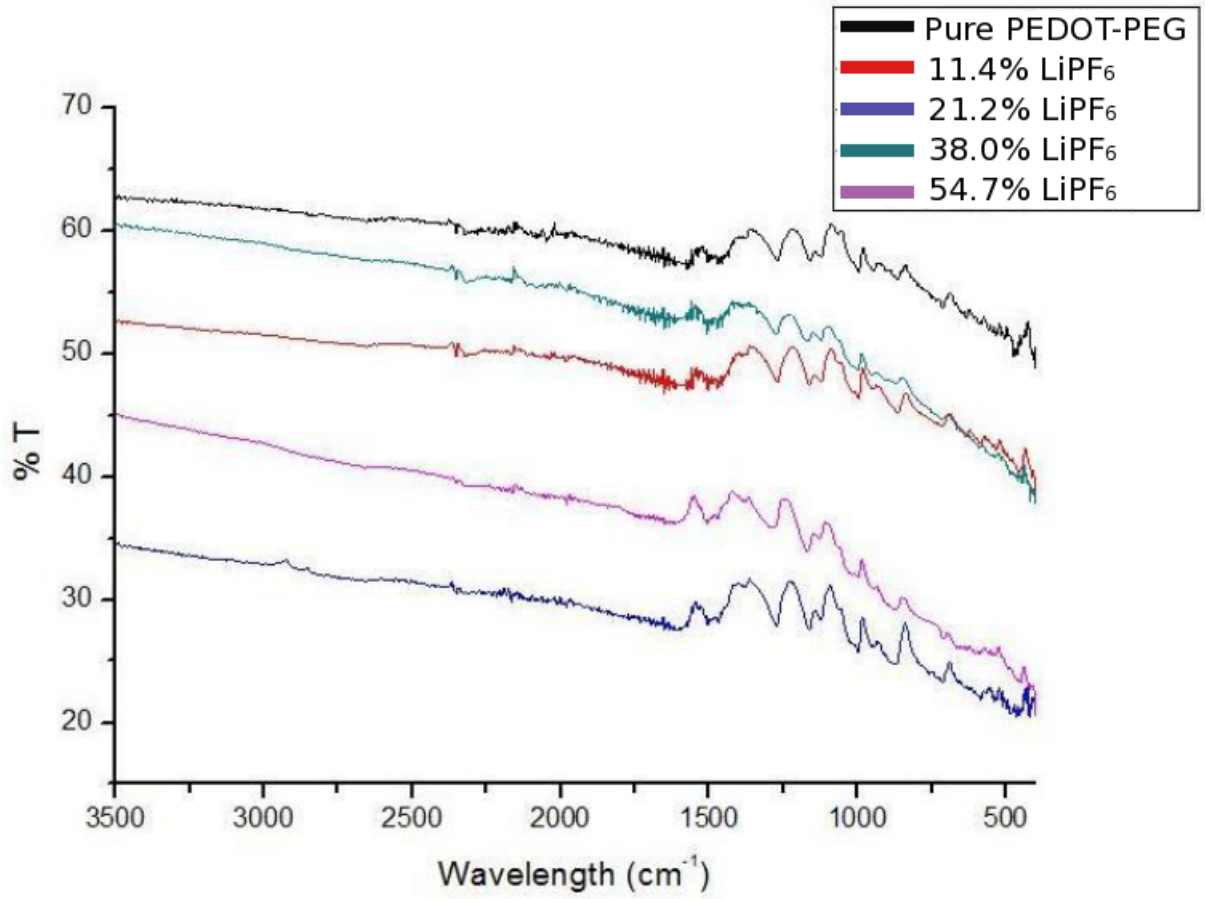

Figure 5.5: FTIR spectra of lithiated PEDOT-PEG for various concentrations of $LiPF_6$

Secondly, the effect of the insertion of lithium on the IR spectra was analysed. With PEDOT-PEG, 4 different concentrations of $LiPF_6$ were used, these being 11.4, 21.2, 38.0 and 54.7 wt.%. The main aim here was to see if any shifts in the coordination bands in these co-polymers were identified, or even the creation of new peaks. Figure 5.5 shows the spectrum of pure PEDOT-PEG along with the spectra for all of the lithiated samples for comparison.

The first thing observed in these spectra is that no peak is present from around 3000 to 3500cm^{-1} which confirms that no water is in the sample. Upon comparison of the spectra, it is noticed that no changes are present in any of the cases, even with increasing concentrations of lithium. It is anticipated that the most favourable coordination centre in the composite is on the PEG chain. While we would have

expected either a shift in the C-O stretch or the creation of a new peak with regards to this band, neither is observed in any of the lithiated samples. This result was not completely unexpected. A suggestion as to why this is the case is perhaps explained by previous studies carried out by Bernson *et al.* [238]. In the latter study, it was proposed that in chains of $(PEG)_n \geq 20$, the presence of lithium in the structure was no longer detected by FTIR measurements. Experimentally, we are obviously looking at larger polymer chains, and so the explanation in the study by Bernson seems plausible for the lack of change in the FTIR spectra for each of the increasing concentrations of the lithiated PEDOT-PEG samples analysed. In order to test our theory that lithium shows affinity for the PEG chain, a geometry optimisation was carried out using CRYSTAL, on the monomer of PEG. Figure 5.6 shows the energy change when a lithium ion migrates from its original location (Figure 5.6c) to the coordination centre, in this case, the oxygen atom.

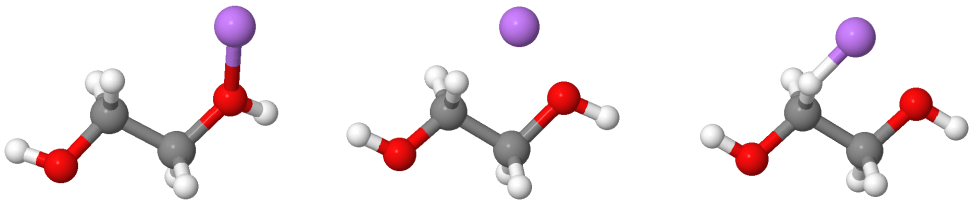

(a) $\Delta E = 0$ kJ/mol (b) $\Delta E = +40.43$ kJ/mol (c) $\Delta E = +118.67$ kJ/mol

Figure 5.6: Lithium ion migration in PEG monomer, with energy values in kJ/mol. Lithium ion is shown in purple, with oxygen atoms represented in red, carbon atoms in grey and hydrogen atoms in white

As observed, the energy decreases as lithium is drawn towards the oxygen atom. This calculation suggests that lithium does coordinate to the PEDOT-PEG copolymer, but as previously mentioned, it appears to be only detected in chains of $(PEG)_n < 20$. It is also likely that lithium ions coordinate to the oxygen atoms in the PEDOT segment of the copolymer, but, this is also undetected in the FTIR spectra.

In the PEDOT:PSS composite, the pure sample was compared with a sample of 20 wt.% $LiPF_6$. Once again, the spectra were assessed in order to see if any noticeable changes were present with the insertion of lithium. Figure 5.7 shows the spectra of pure PEDOT:PSS alongside the lithiated sample.

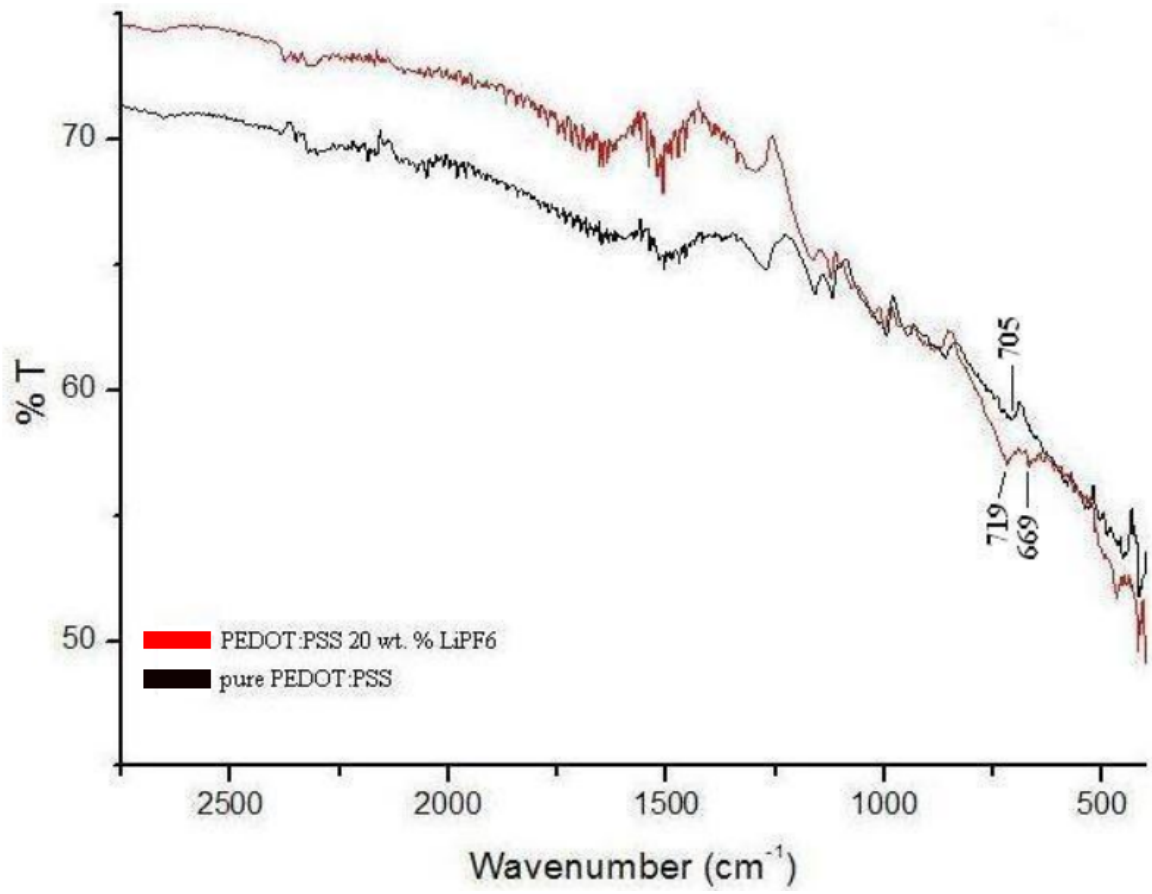

Figure 5.7: FTIR spectra of lithiated PEDOT:PSS compared with the pure sample

Here, the lithiated PEDOT:PSS sample is represented in red. The key observation in this case was the creation of a new peak in the lithiated sample present at 669cm^{-1}. This new peak is situated close to the IR absorption band at 705cm^{-1} in the pure spectrum, now given as 719cm^{-1} in the lithiated spectrum. This was characterised as an S-OH stretch in the initial pure sample. To investigate further, we used the aid of calculations to simulate a lithiated sample of PSS. What we observed here was a clear lithium interaction with the sulphonate group at a frequency of 646cm^{-1}. The lithiated peak downshifted compared to S-OH. This is in agreement with a frequency at 669cm^{-1} experimentally which suggests the peak at 719cm^{-1} is for the SO_3^- group as seen at 705cm^{-1} in the pure spectrum.

As a coordination centre that contains a negative charge, the sulphonate group appears to be a very likely site in which lithium ions prefer to sit. The distance between the lithium ion and the SO_3^- group is suggested to be 1.87Å computationally and this strongly suggests that the lithium ion has an affinity for this group in PSS. It is, therefore, suggested that the creation of a second peak at 669cm^{-1} in the lithiated spectrum of PEDOT:PSS is caused by the lithium interacting with the sulphonate coordination centre in PSS. This provides good evidence that this is where lithium prefers to sit in this composite polymer.

It cannot be disregarded of the possibility that the peak at 669cm^{-1} might correspond to water, in particular, an Li-OH mode. However, no peaks in the 3000cm^{-1}

region and above were observed, as well as the lack of a sharp peak around 1600-1680cm^{-1} corresponding to H_2O bending. This suggests that in all probability, the peak at 669cm^{-1} was not due to water.

5.3.2 Molecular Dynamics investigation of lithium diffusion in polymer electrolytes

Testing of van der Waals potentials in DL_POLY

Before performing the MD simulations, adequate testing of the potentials obtained from the study of Peng *et al.* [129] was required to ensure they were suitable for our models. In order to do this, the potentials were input into the PCFF force field, and several tests were performed. PEG was used as the model system here. The Li-O coordination distances were observed visually for a single lithium ion, along with the Li-Cl and Li-I distances if possible. The Li-O distances could be compared to published results to assess the suitability of the potentials employed. The Li-anion distances were checked mainly to see if they were considered reasonable. The main set of parameters tested in this study were the newly derived parameters for lithium, chlorine and iodine.

A system of PEG_{20} consisting of 2 chains was considered as the reference system. Initially, the LiCl salt was chosen. Each test system was ran for a total of 50ps. Using the initial parameters (R^* and ϵ) as seen in Table 5.1, Li-O coordination distances as low as 1.99Å were observed. These distances compared well with published experimental values, with Li-O separations of 2.07-2.10Å seen in neutron diffraction isotopic substitution (NDIS) experiments performed on PEO/LiI [236, 239] and PEO/LiTFSI [240]. These coordination distances also compared well with other computational studies, with values of 2.1Å [241] and 2.02-2.20Å [242] obtained using $PEO-LiPF_6$/$PEO-LiBF_4$ salts respectively. A reasonable Li-Cl distance of 2.2Å was seen in this case. In this particular example, the lithium ion is coordinating to at least 4 neighbouring oxygen atoms. A higher number would be expected for larger PEG systems.

The chlorine R^* and ϵ parameters were re-fitted in this test system to observe how the local geometry changed. Reducing the R^* value tended to have an adverse effect on coordination number and distances. The same issue was also seen when the ϵ value was increased. Though sometimes a shorter Li-O distance was seen at certain points in the calculation, this was usually at the expense of coordination number or distances between other nearby oxygen atoms. Re-fitting these parameters essentially lead to an imbalance in the system with potentially unknown consequences for bigger systems. Tests were also made by fitting the oxygen van der Waals parameters. In one case, where both the oxygen and chlorine ϵ values were reduced, a coordination distance as low as 1.88Å was seen, however, with a lower

coordination number of three.

The decision was, therefore, made to use the derived potentials from Peng *et al.* for chlorine. Due to the tests for these parameters being positive, the derived parameters for iodine were also used, with no further fitting. The coordination distances shown in the test PEO-LiI system were promising with values as low as 1.88Å in some cases, which also compared well with experiments (2.07-2.10Å [236, 239, 240]) and published calculations (2.02-2.20Å [241, 242]). An Li-O coordination number of six was also seen in this test.

Finally, the experimental isoelectronic rare gas parameters as shown in [129] were also fitted for comparison. For the chlorine anion, though the Li-O coordination number seemed reasonable (around 5), an imbalance in terms of coordination distances was seen. Furthermore, the rare gas parameters showed a lower coordination number (around 4) as well as an imbalance in Li-O distances for iodine. Again, it was deduced that the newly derived parameters from Peng *et al.* were the most suitable for the polymers to be analysed in this study, with no re-fitting required.

Radial distribution functions

One area of keen interest in the study of lithium in polymers is the coordination distance. It is expected that lithium will likely coordinate to the oxygen atoms, both of which are present in PEDOT and PEG, due to these oxygen atoms being coordination centres. Figure 5.8 shows an example of a simulated system of PEG with a lithium ion coordinating to multiple oxygen atoms.

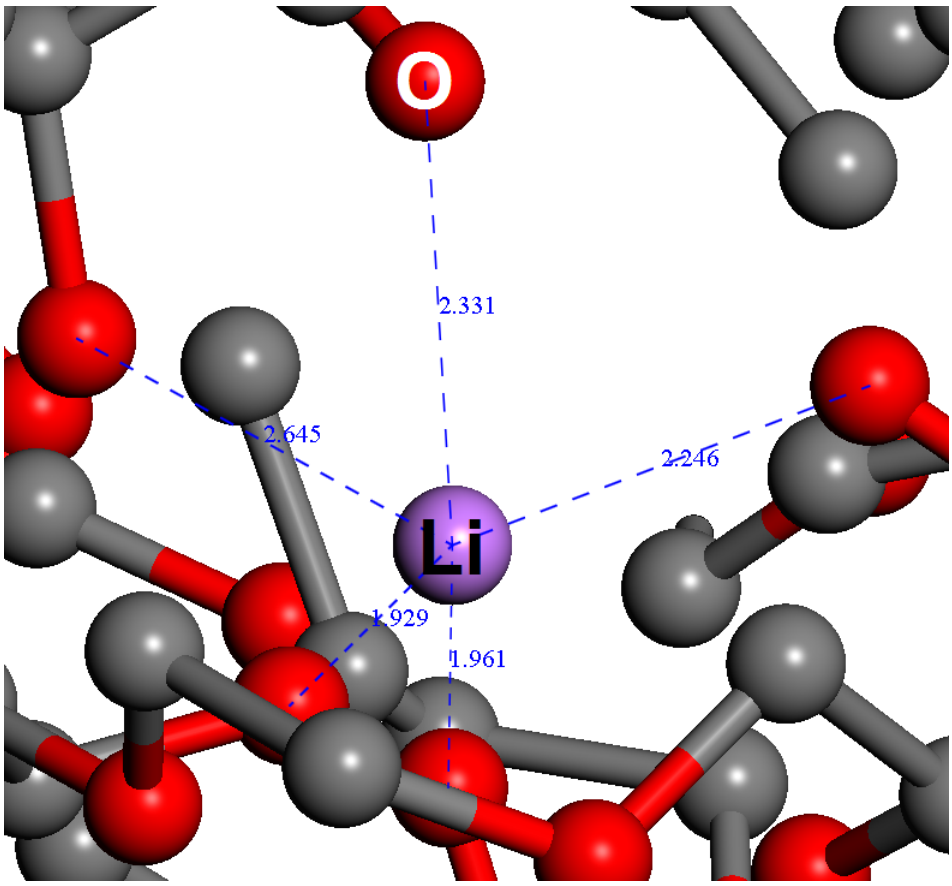

Figure 5.8: Lithium ion coordinating to ether oxygen atoms in PEG/LiI system. The oxygens are represented in red, with the lithium ion in purple. Carbon atoms are displayed in grey, with hydrogen atoms removed for ease of viewing. The blue lines indicate some of the oxygen atoms the lithium ion is coordinating to, with bond distances given in Å

The average Li-O coordination distance is of interest in each of the studied systems. This is not plausible to measure by visual examination. In order to investigate this, the radial distribution functions between lithium and oxygen will be analysed. Ion pairing is also a possibility in these systems, particularly with increasing concentrations of cations and anions. To investigate this, the Li-I and Li-Cl bond distances will be compared. Initially, only a single lithium ion was inserted into the amorphous systems of PEDOT (2620 atoms), PEG (1420 atoms) and PEDOT-PEG (2010 atoms). A further investigation was then conducted for the PEDOT-PEG system only, analysing the effect of increasing lithium concentration upon the RDF. The PEDOT and PEG systems contained 10 chains of each polymer, with a density of 1g/cm^3 while the PEDOT-PEG system contained 5 chains of each polymer component in the multi-block copolymer, with a density of 1.141g/cm^3. Figures 5.9 to 5.12 show the RDF plots for PEG and PEDOT.

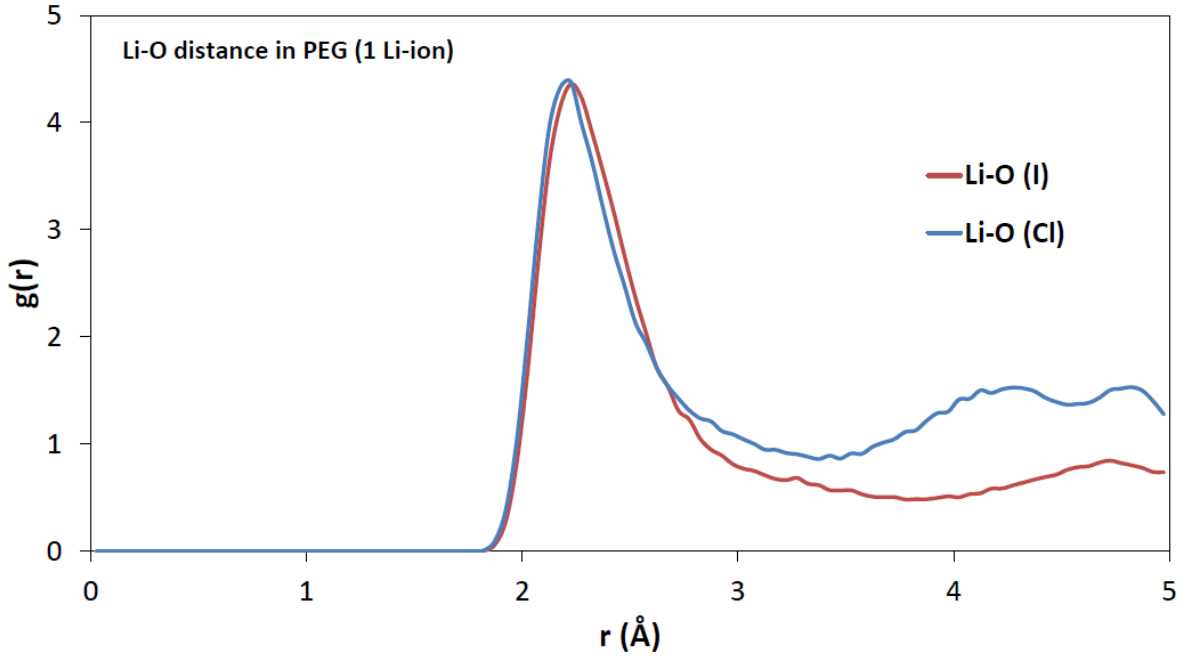

Figure 5.9: RDF plot for Li-O distances in PEG with 1 lithium ion

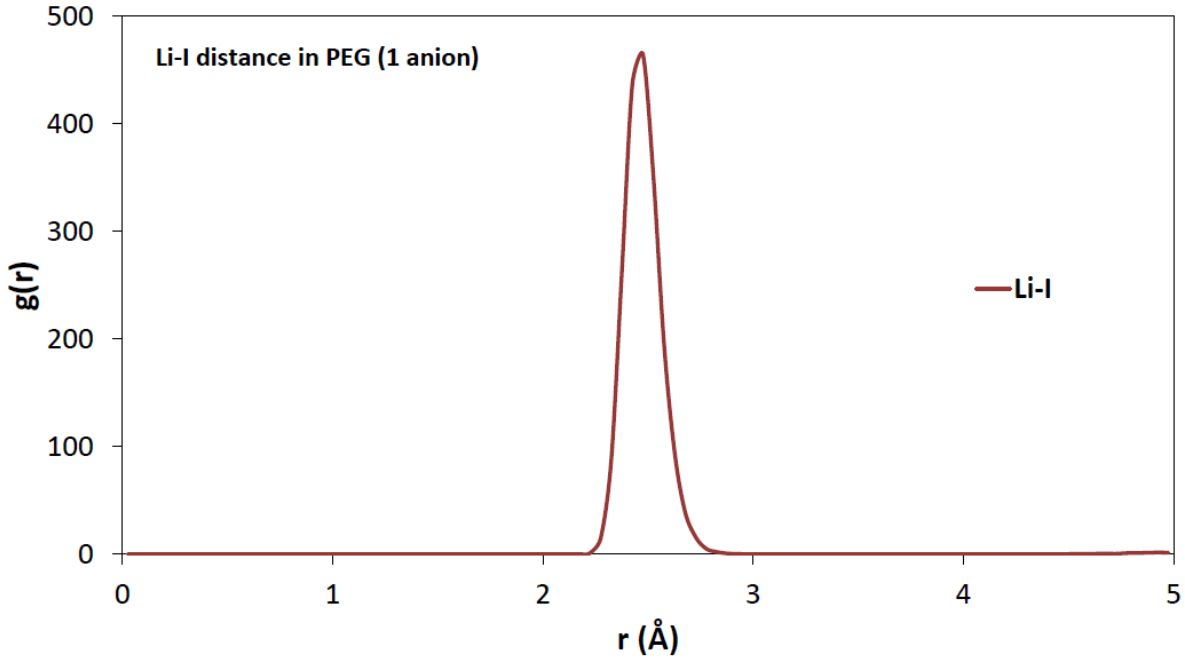

Figure 5.10: RDF plot for Li-I distance in PEG with 1 anion. In this case, no RDF was observed for Li-Cl suggesting that these ions did not interact in the system

The intention with PEG was to observe the coordination distances and compare them to published values. In this case, the Li-O pair distance was analysed with both iodine and chlorine-based salts. In a PEG system consisting of 20 units per chain, and 10 chains, the average coordination distance for lithium with an ether oxygen atom was around 2.23Å for both the iodine and chlorine salts (See Figure 5.9). Both of the RDF plots in this case give a very similar distribution. This value

can be compared to MD calculations of lithium in PEO with Li-O separations of around 2.1Å with an $LiPF_6$ salt [241], and 2.02-2.20Å for a $LiBF_4$ salt [242]. It can also be directly compared to neutron diffraction isotopic substitution (NDIS) experiments performed on PEO/LiI [236, 239] and PEO/LiTFSI [240] which as mentioned previously gave Li-O separations of 2.07-2.10Å . The calculated Li-O value is slightly overestimated compared with the experimental value but in the same range as other calculations.

A reason for this overestimation could be due to the force fields used in this study. Despite this, as seen in Figure 5.8, Li-O distances as short as 1.93Å are observed. Though the average distance is slightly overestimated, this is somewhat expected with higher coordination numbers in larger systems. Another reason could be due to only a single lithium ion being present in the PEG system. Hence, systems with higher salt concentrations were investigated (Figure 5.15).

What we can also investigate for the lithium interaction with the polymers is the coordination number, which can be deduced from the g(r) peak intensity. We know that the RDF, or g(r), is calculated by Equation (5.9).

$$\mathbf{g(r) = n(r)/(\rho 4\pi r^2 \Delta r)} \tag{5.9}$$

$\mathbf{n(r)}$ is the mean number of atoms present in a shell that has a width of $\mathbf{\Delta r}$, with $\mathbf{r}$ representing the interatomic distance. ρ is the mean atom density in this case. For Figure 5.9, we can approximate and relate the value of g(r) directly to the height of the peak. With a coordination number of approximately 4.4 with both lithium salts, we can presume that the average coordination number for Li-O in PEG is slightly higher than 4.

Also under investigation was the Li-I separation in the system, with which we could compare to published values. It should be noted that for the PEG system, the RDF for the Li-Cl distance did not give a peak, due to a lack of interaction between the two ions. This was possibly due to the ions being placed far apart and not able to interact in this particular example. We expect ion pairing to have an influence, particularly for more saturated systems. Ideally, it is desirable for the cation-anion separations to be as large as possible, since the anion will have a bearing on the Li-O coordination distances in the polymer.

It was discovered that the average separation for Li-I in PEG was around 2.48Å. This can be compared to other MD simulations on PEO; in the study by Brandell *et al.*, an Li-P (for $LiPF_6$) separation of around 3.4Å was calculated [241]. Borodin's study on PEO/$LiBF_4$ showed Li-B separations also of around 3.4Å [242]. For Borodin's analysis of PEO with LiI melts, a Li-I separation of around 2.9Å was calculated [236]. It is clear that our result differs from these values, with a shorter Li-I distance. It can be expected that a smaller separation in LiI compared to $LiPF_6$ and $LiBF_4$ is possible, due to the size of the anions. Again, the difference between

the Li-I value in our work and Borodin's could be due to the force field employed. Future work could be to analyse the same system, using a different force field i.e. COMPASS.

The next system to be investigated was PEDOT. While PEG is known for its ionic conductivity, it is still of interest to see whether lithium ions coordinate to the oxygen atoms present also in the PEDOT polymer.

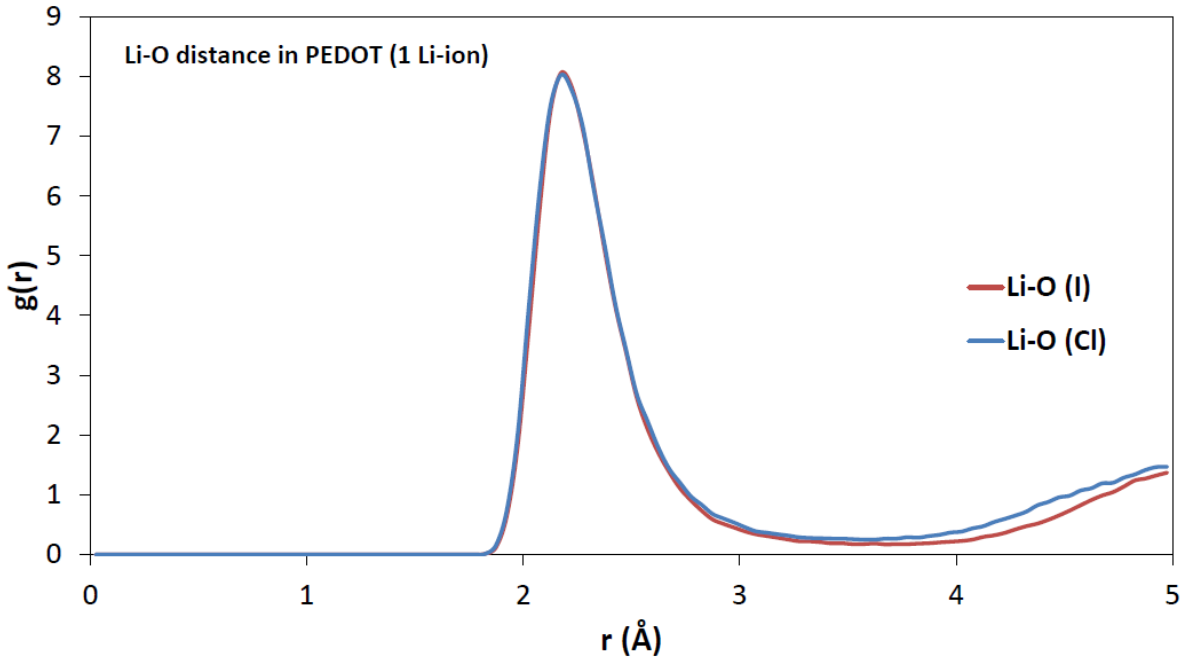

Figure 5.11: RDF plot for Li-O distances in PEDOT with 1 lithium ion

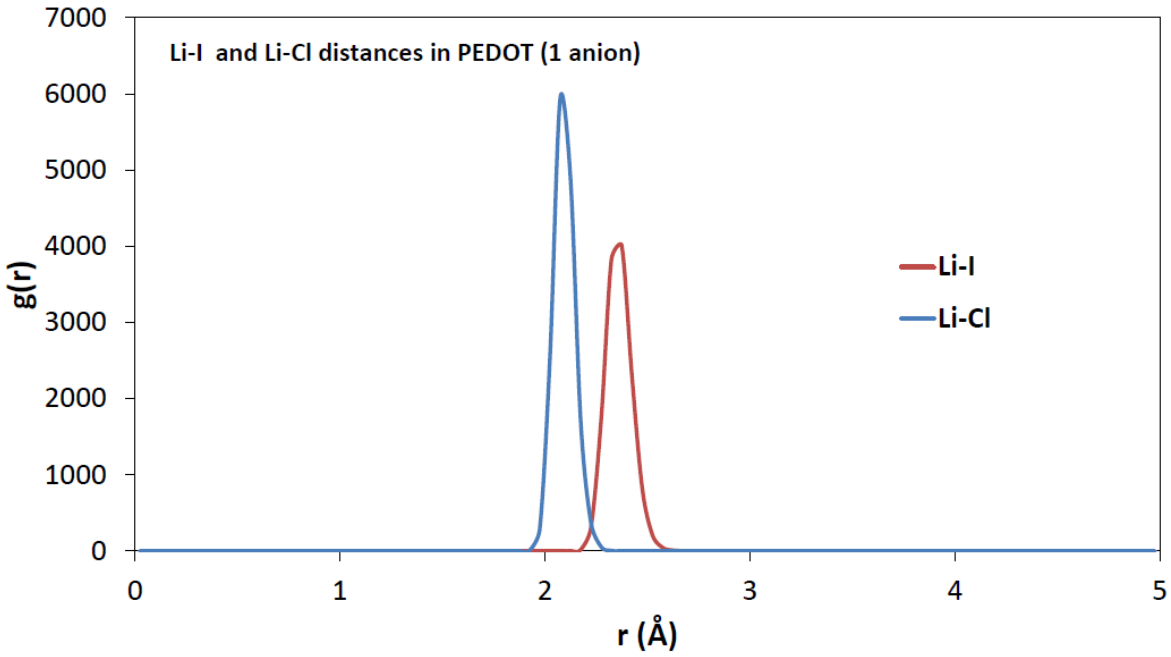

Figure 5.12: RDF plot for Li-I and Li-Cl distances in PEDOT with 1 anion

In both cases of PEDOT (iodine and chlorine salts, Figure 5.11), the Li-O sep-

aration is seen at 2.18Å. This suggests that the lithium ion is showing affinity for the oxygen atoms in the PEDOT system, with even shorter distances than seen in PEG.

In terms of coordination number, a g(r) value of approximately 8 is observed for Li-O in PEDOT. It therefore appears that the average Li-O coordination number in PEDOT is 8, a value which is double that of PEG. One possible suggestion for the higher coordination number in PEDOT could be the fact that there are around twice as many oxygen atoms in the system compared to PEG. Each PEDOT unit will contain two oxygen atoms. This means that a greater number of oxygen atoms are available for the lithium ion to coordinate to. It could be that as lithium coordinates to an oxygen atom in PEDOT, it could be coordinating to both of the oxygen atoms in that particular unit. Alternatively, the lithium ion may sit between two neighbouring oxygen atoms from different PEDOT units. This could be why the coordination number for PEDOT is almost double that of PEG. For future work, it would be of interest to see how the coordination number of PEDOT changes with increasing lithium concentration.

For comparison, both the Li-I and Li-Cl separations were plotted. It is expected that the Li-I separation will be similar to that in PEG. A separation here of 2.38Å shows that there is a shorter Li-O distance in PEDOT compared to a separation of 2.48Å in PEG. In comparison, the Li-Cl separation is noticeably smaller compared to Li-I in PEDOT, with a value of 2.08Å (No Li-Cl separation was seen in PEG due to no interaction between these two ions). A reason for this could be due to the size of the anion. Iodine has a larger ionic radius than chlorine, and bond distances shorter for Li-Cl than Li-I are observed. Figure 5.13 shows lithium coordinating to oxygen atoms in the PEDOT cell.

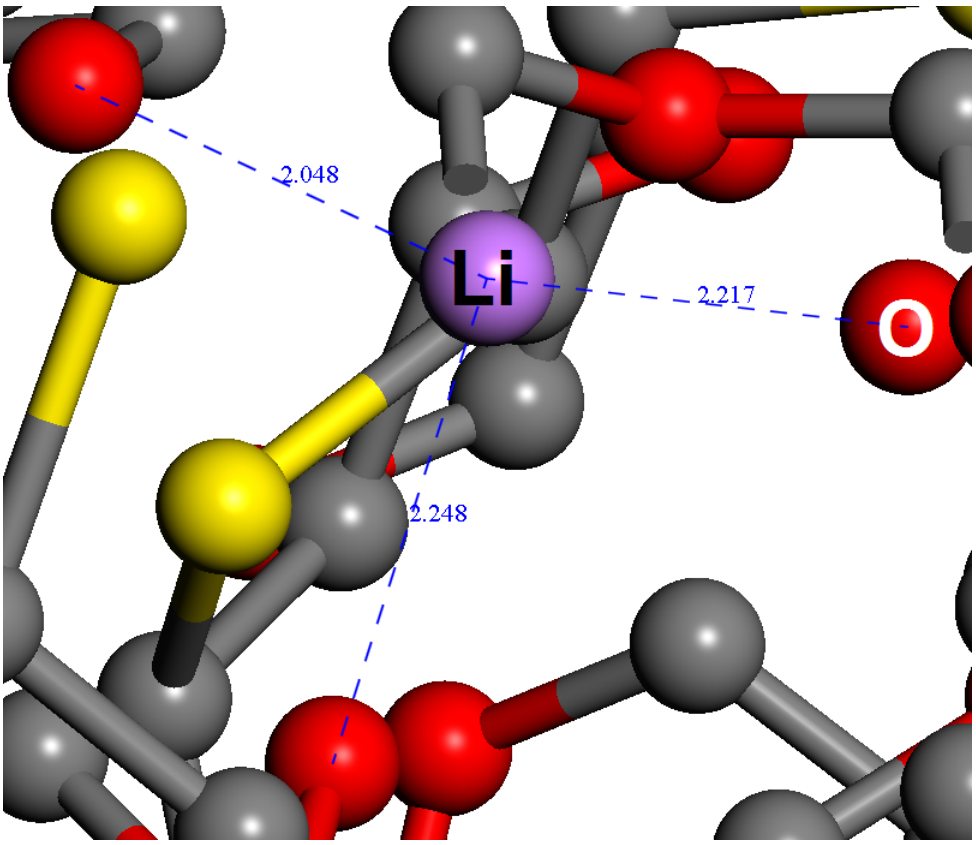

Figure 5.13: Lithium ion coordinating to oxygen atoms in PEDOT/LiCl system. The oxygens are represented in red, with the lithium ion in purple. Sulphur atoms are displayed in yellow, with carbon atoms displayed in grey, and hydrogen atoms removed for ease of viewing. The blue lines indicate some of the oxygen atoms the lithium ion is coordinating to, with bond distances given in Å

The next part of the analysis involved a study of PEDOT-PEG. In this case, increasing amounts of lithium were inserted into the structure with the RDF plots obtained in each case to compare how g(r) changed as a function of lithium and anion concentrations. As we anticipate PEG to be a good source of coordination centres in the multi-block copolymer, published experimental and calculated results will be used for PEG for comparative purposes. Figure 5.14 shows a single lithium cation coordinating to oxygen atoms in PEDOT-PEG.

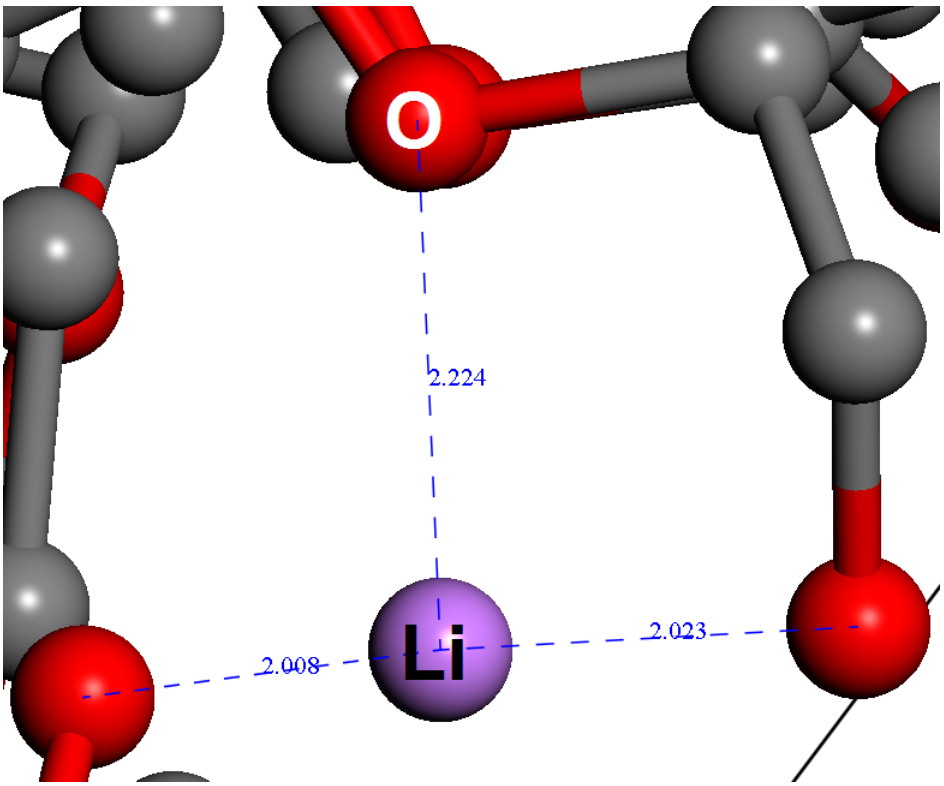

Figure 5.14: A single lithium ion coordinating to oxygen atoms in PEDOT-PEG/LiCl system. The oxygens are represented in red, with the lithium ion in purple. Sulphur atoms are displayed in yellow, with carbon atoms displayed in grey, and hydrogen atoms removed for ease of viewing. The blue lines indicate some of the oxygen atoms the lithium ion is coordinating to, with bond distances given in Å

In this particular example, we can see lithium coordinating to at least three oxygen atoms in the PEDOT-PEG co-block polymer. We expect that lithium ions will coordinate to the oxygen atoms in both the PEDOT and PEG chains. From Figure 5.15, it can be observed that an average coordination number in PEDOT-PEG for an LiCl concentration of 0.23 wt.%, is close to 3, which is lower than both PEG (Figure 5.9) and PEDOT (Figure 5.11). Issues such as ion pairing may have a bearing on this observation.

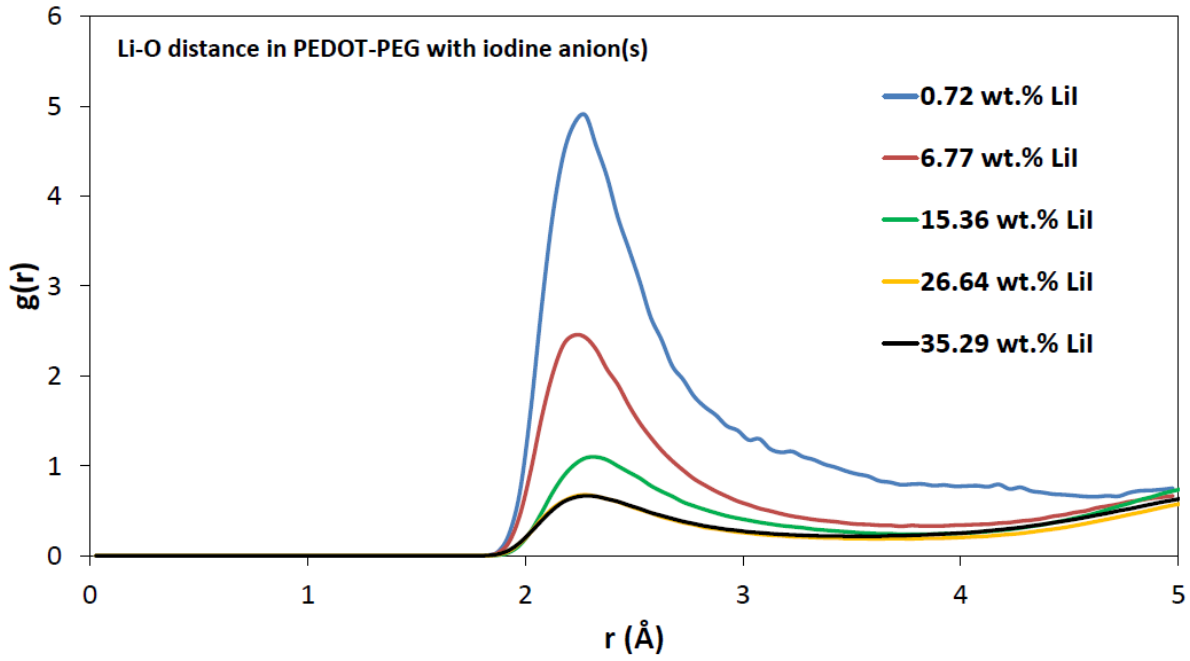

(a)

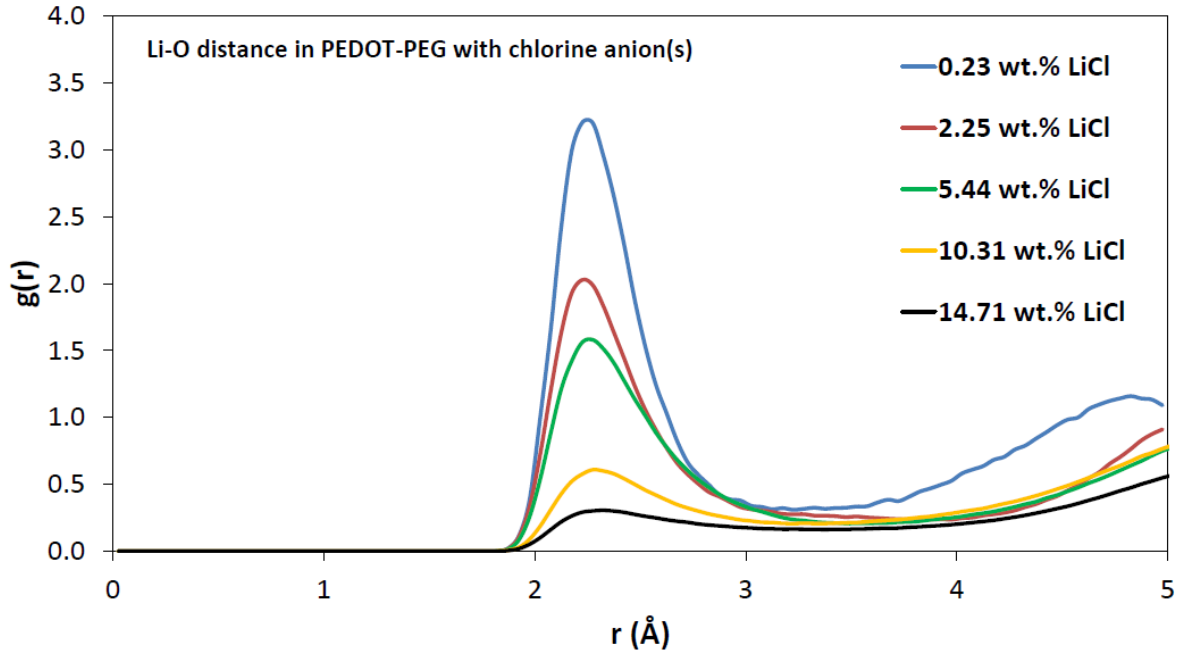

(b)

Figure 5.15: RDF plots for Li-O distances in using (a) an LiI and (b) an LiCl salt

Figure 5.15 shows the RDF plots for the Li-O separation using the two salts in PEDOT-PEG. What is first apparent is that there is no noticeable change in the nearest neighbour bond distance as the lithium concentration is increased. This is true for both salts. Each peak is present at around 2.23-2.28Å. This is very close to the value observed in the case of the PEG system, while being slighter greater than the value for PEDOT. Once again, comparing to calculated values with published ones for PEO (2.1Å with an $LiPF_6$ salt [241], 2.02-2.20Å for a $LiBF_4$ salt [242]) and experimental data (2.07-2.10Å for PEO/LiI [236, 239] and PEO/LiTFSI [240]),

we do see a slight overestimation in the Li-O separation with an iodine and chlorine salt. Hence, the Li-ion concentration is not a plausible explanation to the slightly larger Li-O distance.

The main pattern we see with regards to both PEDOT-PEG/Li systems observed is a reduction in coordination number as the amount of lithium salt increases. With the addition of more lithium salt, the coordination number is reduced in almost each case, with the slight exception of the LiI system where no further reduction is seen as we go from 26.64 wt.% LiI to 35.29 wt.% LiI. Other observations are that on average, the coordination number is higher for each Li concentration in the PEDOT-PEG/LiI system compared to the LiCl system. For example, with the LiCl salt, a coordination number of around 3.2 for a single cation (0.23 wt.% LiCl) is observed, while for the LiI salt with a single cation (0.72 wt.% LiI), a value of around 4.9 is obtained.

The average Li-O bond distance and coordination numbers obtained for PEDOT-PEG at each Li concentration are shown in Table 5.4 for each salt.

Table 5.4: Lithium-Oxygen coordination numbers in PEDOT-PEG for increasing lithium salt concentrations

LiI salt	
Concentration (wt.%)	Li-O average coordination no.
0.72	4.9
6.77	2.5
15.36	1.1
26.64	0.7
35.29	0.7
LiCl salt	
0.23	3.2
2.25	2.0
5.44	1.6
10.31	0.6
14.71	0.3

From these values, we can see that for small concentrations of lithium, the LiI salt results in higher coordination numbers than LiCl. For increasing LiI concentrations, this value stabilises with an average coordination number of around 0.7. A possible explanation for the smaller coordination numbers with increasing concentration could be due to ion pairing in the system. In some cases, lithium ions may coordinate to nearby anions, and as a result, diffusion and coordination to ether oxygens in PEG may be inhibited. While this is something that ideally should be minimised,

it cannot be prevented entirely, since naturally, a cation will show a greater affinity for a nearby anion than any surrounding oxygen atoms. This becomes more likely as a greater number of anions and cations are inserted into the system, since there is less chance of the anion and cation avoiding each other.

In order to further investigate this potential ion pairing in the system, the RDF plots were obtained for the Li-I and Li-Cl separation distances at each different concentration of the anion, as seen in Figure 5.16.

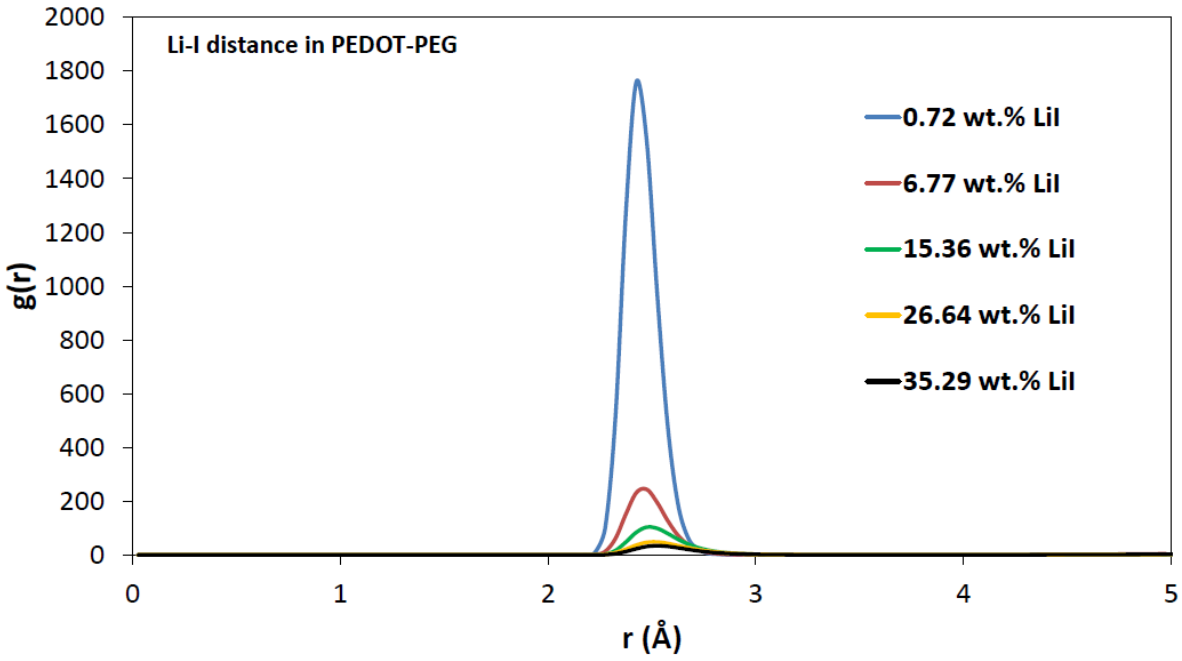

(a)

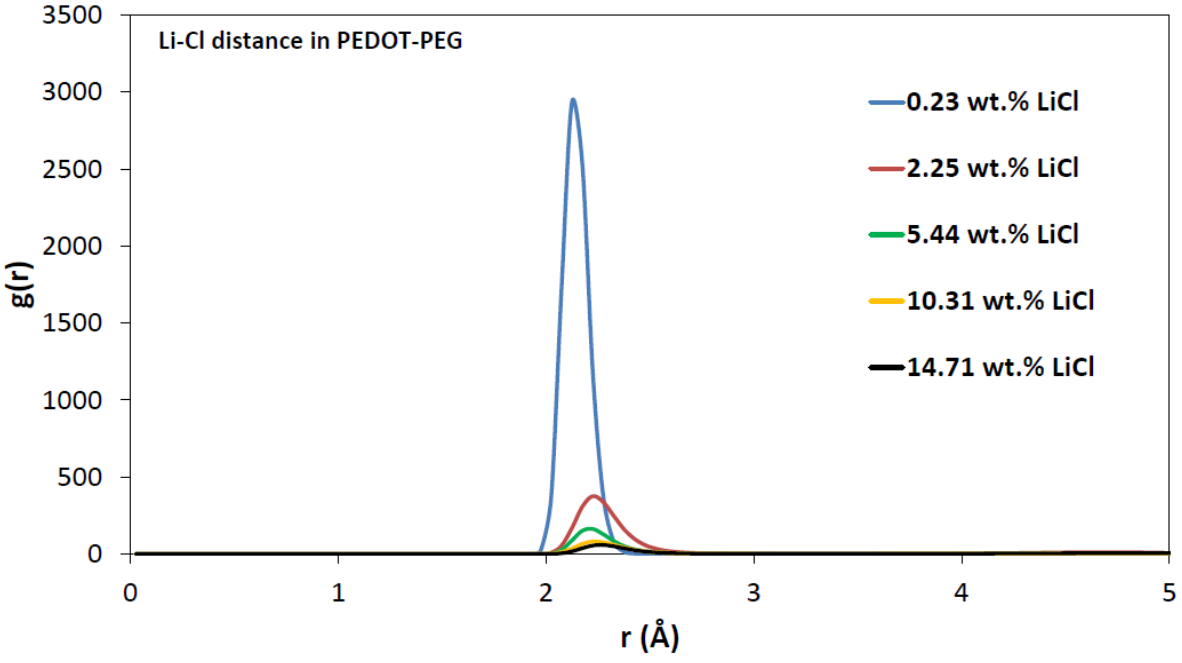

(b)

Figure 5.16: RDF plots for (a) Li-I and (b) Li-Cl distances in PEDOT-PEG

The first observation for the Li-I separation are that distances increased gradually with increasing anion concentration from about 2.43 to 2.53Å. Li-Cl distances of 2.13 to 2.28Å were obtained, again with a gradual increase with increasing anion concentration. On average, these values were lower than other lithium-salt systems studied including Li-P in PEO/$LiPF_6$ [241] and Li-B in PEO/$LiBF_4$ [242], which had separations of around 3.4Å , and an Li-I in PEO/LiI [236] separation of 2.9Å. This can be explained by ionic radius, since lithium would be able to approach individual anions easier than the other salts mentioned above.

What is particularly apparent, and was also seen for the Li-anion RDF plots in PEG and PEDOT are that the g(r) values are much greater than seen for the Li-O coordination RDFs. While the g(r) value here does not directly give the coordination number, it does give us information about the nature of the ion pairing in the system. In the case of ion pairing such as that studied here, the atoms are in-equivalent, and can be referred to as N_A and N_B of each. Therefore, g(r) can be represented by Equation (5.10).

$$g(r) = \frac{\sum_{frames} d(r)}{N_f d_{uni}(r)} = \frac{V}{4\pi N_f N_A N_B r^2 \delta r} \sum_{frames} \sum_{i} \sum_{j \neq i} \delta(r - r_{ij}) \tag{5.10}$$

The g(r) function is in fact a ratio of the number of pairs seen at a particular distance and what would be expected in a uniform distribution. In relation to the above RDF plots for the Li-anion interactions, the number of nearest neighbours varies from 1 at the lowest lithium salt concentration to between values of around 4-6 at the highest concentrations. The uniform equivalent in this case increases by a factor of several thousand at the highest concentrations. Therefore, the bottom component of the g(r) ratio becomes much larger at these high concentrations, therefore meaning that g(r) for the ion pairs is reduced as the concentration of lithium salt increases.

A reason for the LiI salt having a greater Li-O coordination number at each stage compared to LiCl could be the degree to which ion pairing occurs. As mentioned previously, chlorine has a smaller ionic radius than iodine, which allows it to approach the lithium ions more closely. It is therefore likely that a greater degree of ion pairing occurs in the PEDOT-PEG/LiCl system. This is supported by the RDF plots for the Li-Cl distance, which show a greater coordination number on average, when compared to the equivalent coordination numbers in the Li-I system. This suggests that a greater number of lithium ions are bonding with chlorine, compared to iodine. This in turn means that less lithium ions are coordinating to ether oxygens in PEDOT-PEG for the LiCl system in comparison to the LiI system.

In order to visualise the ion pairing occurring in the system, the animation of the simulations were viewed. As a particular set of examples, the cases of the 0.72

wt.% LiI and 26.64 wt.% LiI systems were viewed, along with the 0.23 wt.% LiCl, and 10.31 wt.% LiCl systems for comparison. The final frame of the simulation in each case is shown in Figures 5.17 to 5.20.

As can be seen from Figures 5.17 to 5.20, significant regions of ion pairs occur, which may prevent these lithium ions from coordinating with oxygen atoms in the system. Even in the case of a single ion pair, these remain in close contact throughout the whole simulation which may inhibit lithium diffusion. As this becomes more prominent at higher lithium salt concentrations, this could be what gives a lower average percentage of Li-O coordination in systems with greater salt concentration. It could be that to improve this, bulkier anions may need to be used i.e. $LiPF_6$, as lithium will bind less strongly to these, and thus Li-O coordination may improve. This is future work which can be conducted on PEDOT-PEG, along with PEDOT to investigate whether lithium diffusion may improve with bulkier anions.

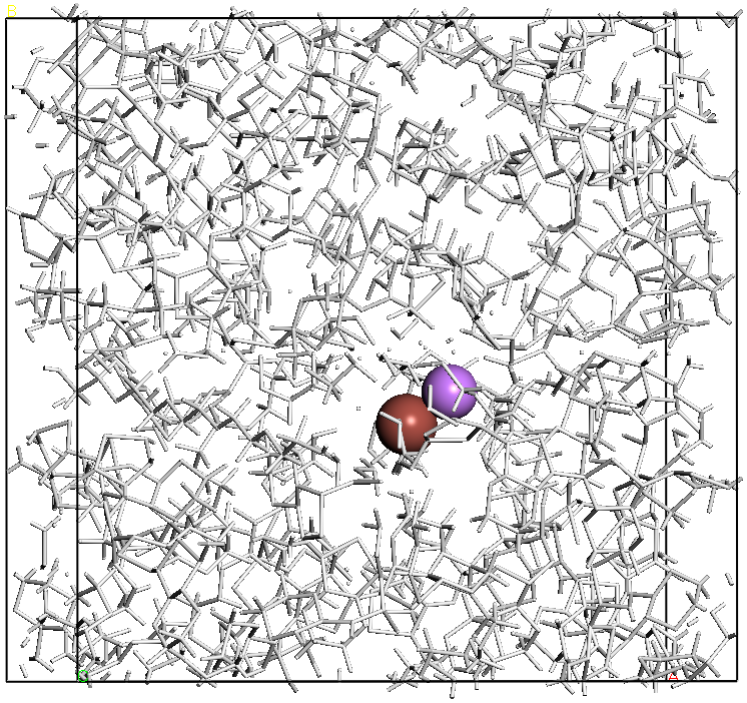

Figure 5.17: Region of ion pairing in PEDOT-PEG with 1 lithium ion and 1 iodine ion (0.72 wt.%). The lithium ion is shown in purple, with the iodine ion shown in brown. The polymer matrix is shown in white

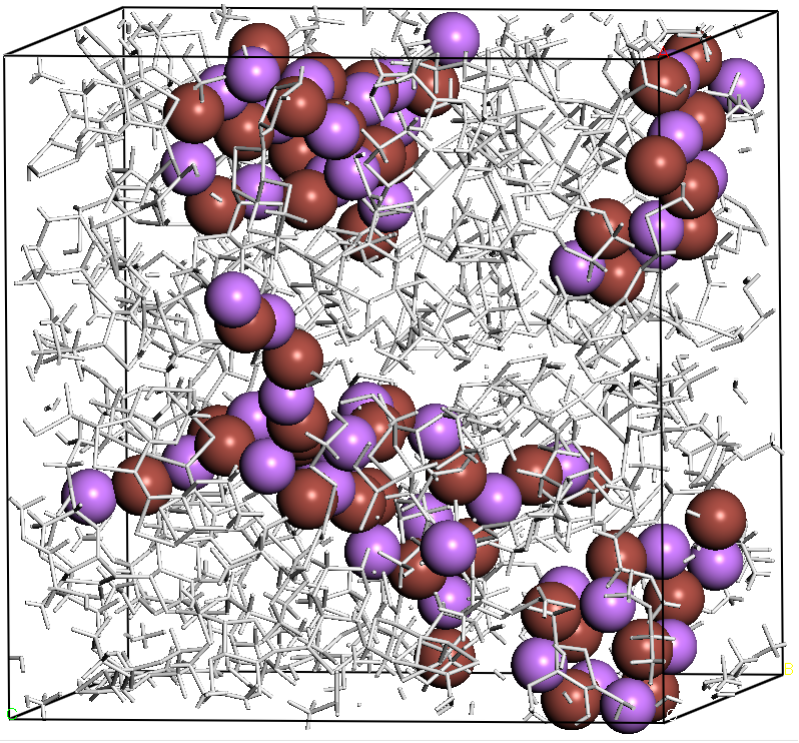

Figure 5.18: Region of ion pairing in PEDOT-PEG with 50 lithium ions and 50 iodine ions (26.64 wt.%). The lithium ions are shown in purple, with the iodine ions shown in brown. The polymer matrix is shown in white

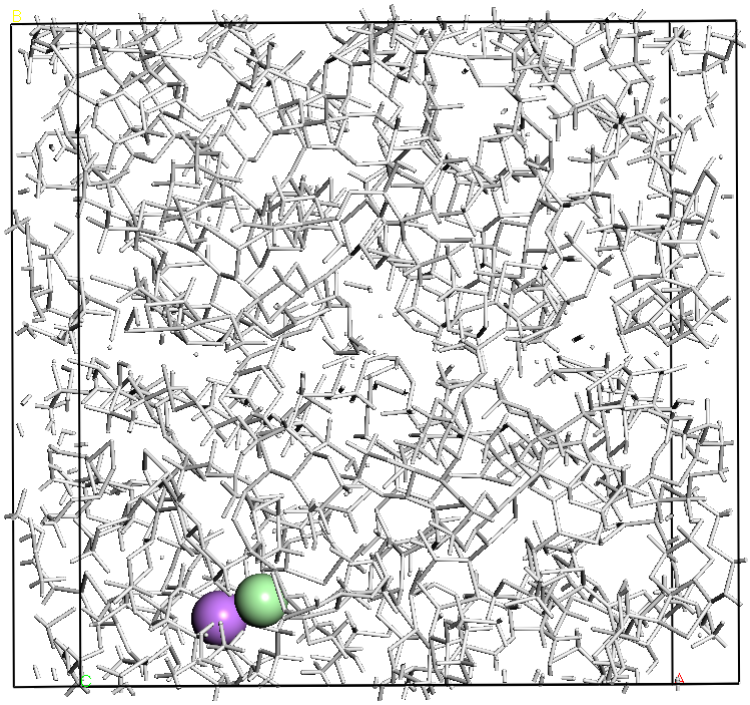

Figure 5.19: Region of ion pairing in PEDOT-PEG with 1 lithium ion and 1 chlorine ion (0.23 wt.%). The lithium ion is shown in purple, with the chlorine ion shown in green. The polymer matrix is shown in white

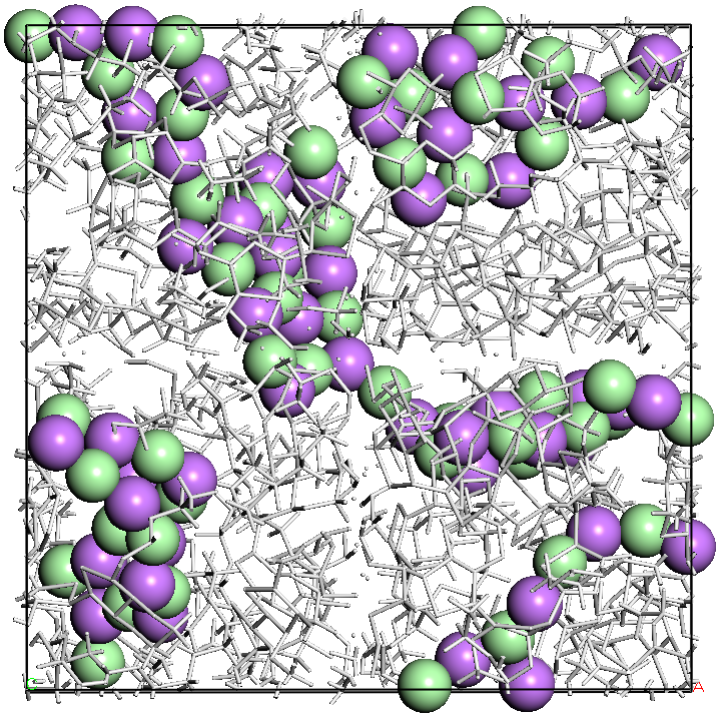

Figure 5.20: Region of ion pairing in PEDOT-PEG with 50 lithium ions and 50 chlorine ions (10.31 wt.%). The lithium ions are shown in purple, with the chlorine ions shown in green. The polymer matrix is shown in white

Mean square displacement plots

In order to further investigate the properties of these polymers in terms of their performance in a battery, the ionic diffusion will be investigated. In this part of the study, the mean square displacements for lithium in the polymers PEG, PEDOT and PEDOT-PEG were investigated. An analysis in terms of lithium concentration, diffusion and conductivity was then conducted on PEDOT-PEG as this is our main system of interest with regards to potential use in our proposed battery. To begin with, a single lithium ion was inserted into the polymer structure, with two different counterions, i.e. iodine and chlorine. The total MSD is shown for lithium in both cases to show the differences between the two. Diffusion coefficients have been calculated for lithium in each case, and are shown in Tables 5.5 and 5.7. Figures 5.21 and 5.22 show the MSD plots for PEG and PEDOT, with a single lithium ion.

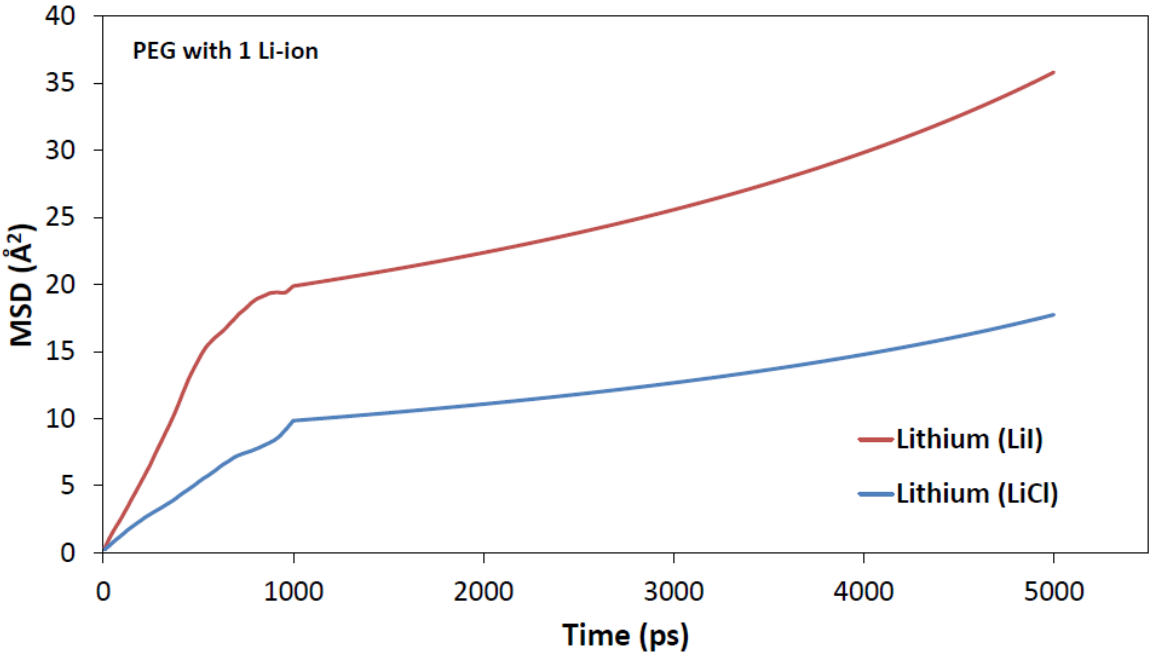

Figure 5.21: MSD plots for a single lithium ion in PEG, with both LiI and LiCl salts

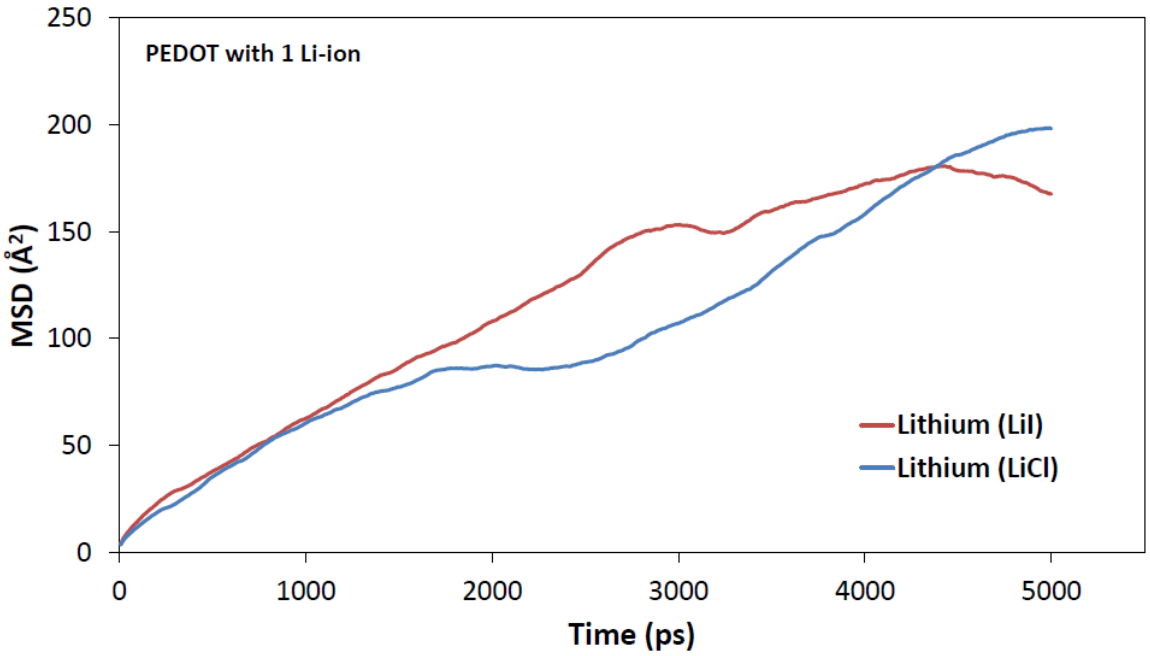

Figure 5.22: MSD plots for a single lithium ion in PEDOT, with both LiI and LiCl salts

In the case of PEG, the MSD value is noticeably greater with the LiI salt, by almost a factor of two compared to the LiCl salt. A steeper gradient is also observed for LiI. PEDOT on the other hand shows plots that are not linear for some of the simulation time. However, at the most linear section of the plots in each system, a much steeper line is seen in comparison to PEG.

In order to better understand any trends that may be present, the diffusion coefficients were calculated from the linear part of each MSD plot, with any non-linear section of the plot disregarded as this does not represent the true diffusive motion of the ionic species. The diffusion is calculated by using the equation $< r^2 >= 6Dt + C$, where D is equal to the diffusion coefficient. Table 5.5 shows the diffusion coefficients calculated for a single lithium ion in PEG and PEDOT. Diffusion coefficients were initially calculated in $Å^2/ps$. For the purposes of this study and the table, they have been converted to m^2/s and cm^2/s, as these are the units more commonly used for diffusion and conductivity measurements experimentally.

Table 5.5: Diffusion coefficients for a single lithium ion in PEG and PEDOT

Polymer	Salt	D ($Å^2/ps$)	D (m^2/s)	D (cm^2/s)
PEG	LiI	5.8×10^{-4}	5.8×10^{-12}	5.8×10^{-8}
PEG	LiCl	2.8×10^{-4}	2.8×10^{-12}	2.8×10^{-8}
PEDOT	LiI	7.8×10^{-3}	7.8×10^{-11}	7.8×10^{-7}
PEDOT	LiCl	8.5×10^{-3}	8.5×10^{-11}	8.5×10^{-7}

It is apparent from this table that lithium in PEDOT is giving higher diffusion coefficients than lithium in PEG, which would initially suggest a higher ionic conductivity in PEDOT. However, it is important to consider that this result is only for a single lithium ion, and, therefore, no significant conclusion can be drawn as to which of these polymers is the most conductive. PEG is the more widely used polymer in terms of lithium conduction in batteries. However, a more detailed study would be required involving a greater concentration of lithium in each to draw more realistic conclusions.

The diffusion coefficients obtained here can be compared to molecular dynamics studies of lithium diffusion in PEO, along with experimental NMR studies. Our diffusion coefficients for lithium in PEG range from 2.8 to $5.8\times10^{-12}m^2/s$, which is comparable to values of 4.4 to $7.1\times10^{-12}m^2/s$ obtained by molecular dynamics studies of Li^+ in PEO using a "Two-Body force field" [242]. Furthermore, they are comparable to dynamics properties studied by NMR, with lithium diffusion coefficients in the order of 10^{-12} to $10^{-11}m^2/s$ for both a $LiCF_3SO_3PEG_{10}$ and $LiN(CF_3SO_2)_2PEG_{10}$ system [243]. These values tend towards $10^{-12}m^2/s$ at 300K and below. Another NMR analysis of lithium diffusion in $LiCF_3SO_3PEG_{10}$ at 23.5°C showed a value very close to $10^{-12}m^2/s$, with zero water content [244]. The latter would be a better benchmark value for the calculation.

From these diffusion coefficients, the molar conductivity for lithium was calculated. In order to do this, the Nernst-Einstein equation is used, to establish the relationship between molar limiting conductivity (Λ_m^0) and the diffusion coefficient (D). The Nernst-Einstein equation is shown by Equation (5.11).

$$\Lambda_m^0 = z^2 \mathrm{D} \left(\frac{\mathrm{F}^2}{\mathrm{RT}} \right) \tag{5.11}$$

Here, z is the charge of the ion under investigation. T is the temperature in Kelvin. F is Faraday's constant (9.6485×10^4 Coulomb mol^{-1}) and R is the gas constant (8.31446 J $\mathrm{K}^{-1}\mathrm{mol}^{-1}$). F^2/RT is known as the proportionality constant at a given temperature in units of s·S mol^{-1}. Molar limiting conductivity is usually quoted in units of S $\mathrm{cm}^2\mathrm{mol}^{-1}$. In this case, the values will be displayed in both S $\mathrm{m}^2\mathrm{mol}^{-1}$ and S $\mathrm{cm}^2\mathrm{mol}^{-1}$, for an absolute temperature of 300K. Table 5.6 shows the molar conductivities for a single lithium ion in PEG and PEDOT.

Table 5.6: Molar limiting conductivities (Λ_m^0) for lithium in PEG and PEDOT

Polymer	Salt	Λ_m^0 (S $\mathrm{m}^2\mathrm{mol}^{-1}$)	Λ_m^0 (S $\mathrm{cm}^2\mathrm{mol}^{-1}$)
PEG	LiI	2.18×10^{-5}	0.22
PEG	LiCl	1.06×10^{-5}	0.11
PEDOT	LiI	2.89×10^{-4}	2.89
PEDOT	LiCl	3.17×10^{-4}	3.17

The conductivities for PEDOT are greater by a magnitude of 1, when compared to PEG. This is expected, since the diffusion coefficients in PEDOT were also greater by a magnitude of 1. In the case of PEG, the LiI salt gives a conductivity which is approximately double the value of the LiCl salt. This was also reflected in terms of the rate of diffusion. The conductivities for PEDOT are similar with both of the salts used.

This initial investigation allows us to compare diffusion and conductivity of PEG and PEDOT as separate polymers. We are mainly interested in the multi-block PEDOT-PEG, particularly with differing concentrations of lithium. Figures 5.23 to 5.27 show the MSD plots obtained for PEDOT-PEG with each different lithium salt concentration. Initially, only a single lithium ion was inserted, with both the anion MSD plots shown as a comparison. The remainder of the MSD plots focus on the lithium diffusion with each different salt used.

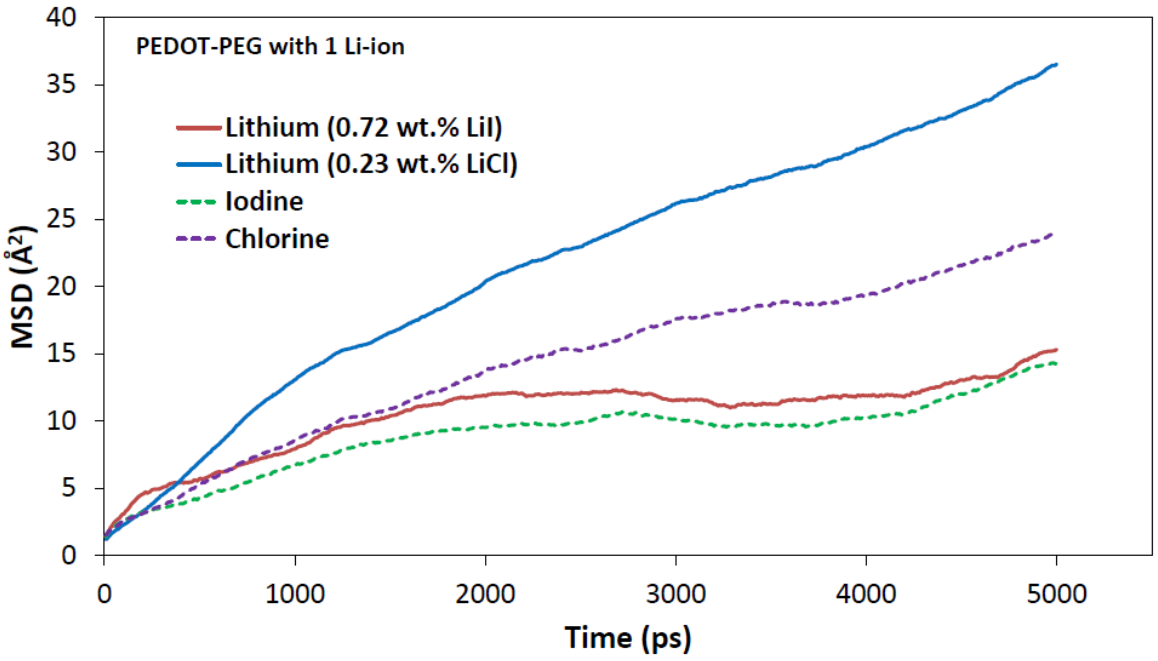

Figure 5.23: MSD plots for a single lithium ion, with both an iodine (0.72 wt.% LiI), and a chlorine anion (0.23 wt.% LiCl) present in PEDOT-PEG (MSD plots for anions shown by dashed lines)

It can be observed that in the case of a single lithium ion, a steeper gradient and, therefore, a higher diffusion coefficient is seen for lithium with a chlorine anion. This is also seen whereby the chlorine anion itself has a steeper MSD plot than the iodine anion. As we are mainly focused on lithium ion diffusion in PEDOT-PEG, only the lithium MSD plots are shown hereafter.

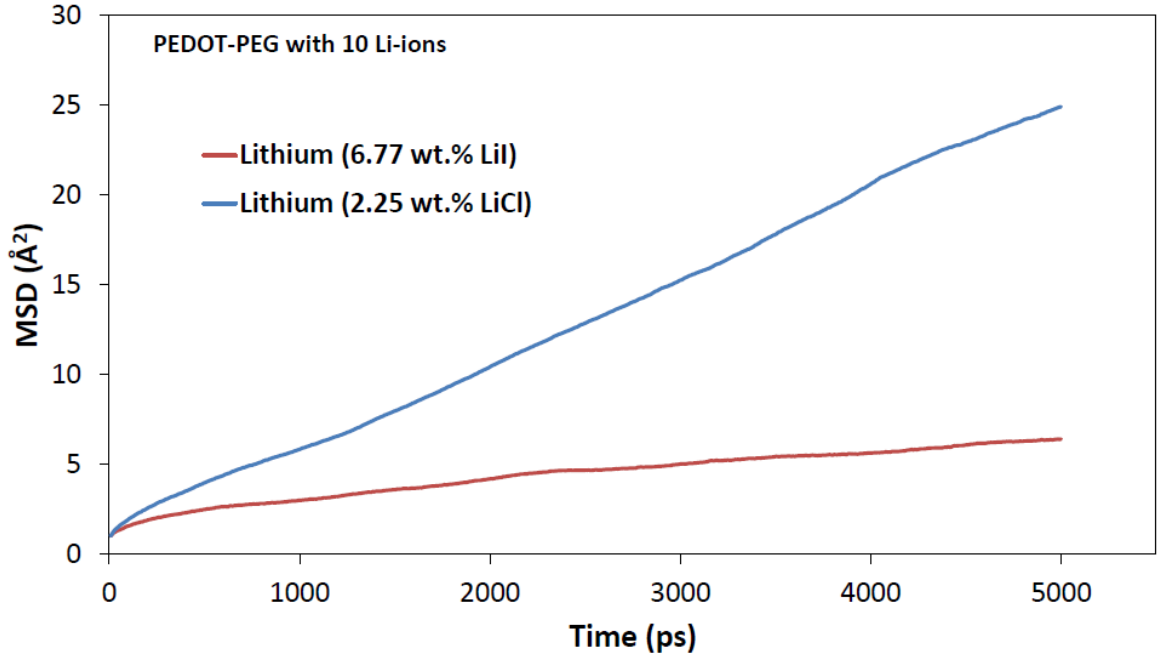

Figure 5.24: MSD plot for 10 lithium ions in PEDOT-PEG (6.77 wt.% LiI, 2.25 wt.% LiCl)

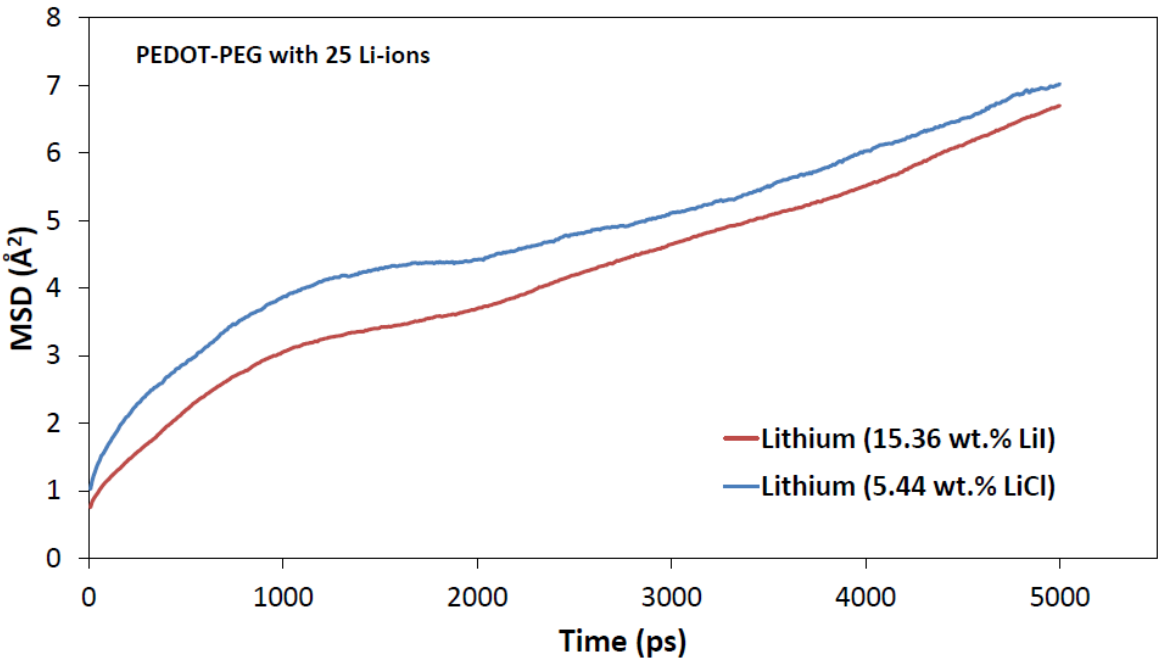

Figure 5.25: MSD plot for 25 lithium ions in PEDOT-PEG (15.36 wt.% LiI, 5.44 wt.% LiCl)

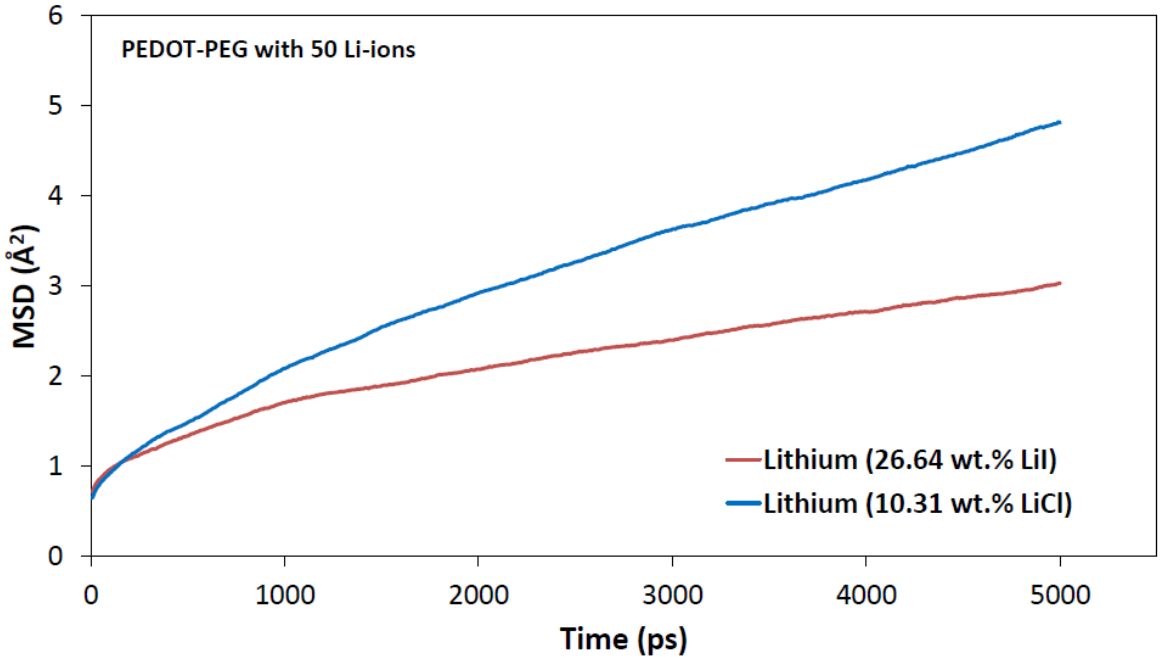

Figure 5.26: MSD plot for 50 lithium ions in PEDOT-PEG (26.64 wt.% LiI, 10.31 wt.% LiCl)

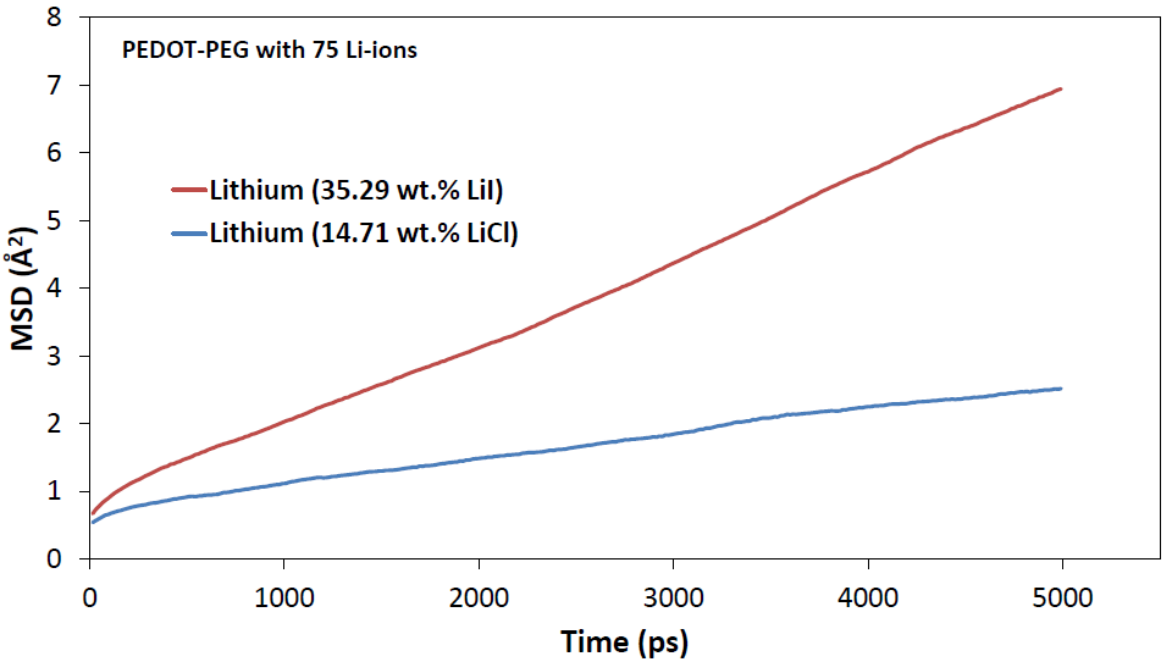

Figure 5.27: MSD plot for 75 lithium ions in PEDOT-PEG (35.29 wt.% LiI, 14.71 wt.% LiCl)

From all of the above plots, a few key observations have been made. For the majority of lithium concentrations, the LiCl salt system is showing the steepest gradient, resulting in higher diffusion rates than for the LiI salt system. The only exception to this is in the case of 75 lithium ions inserted into the PEDOT-PEG system containing 2010 atoms (35.29 wt.% LiI, 14.71 wt.% LiCl). Table 5.7 shows the diffusion coefficients for lithium in each scenario.

Table 5.7: Diffusion coefficients (D) for lithium in PEDOT-PEG. Lithium concentration is shown also as a weight percentage of the salt in the PEDOT-PEG system

Lithium (Iodine salt)				
No. of Li-ions	Li salt conc. (wt.%)	D ($Å^2$/ps)	D (m^2/s)	D (cm^2/s)
1	0.72	7.2×10^{-4}	7.2×10^{-12}	7.2×10^{-8}
10	6.77	1.3×10^{-4}	1.3×10^{-12}	1.3×10^{-8}
25	15.36	1.6×10^{-4}	1.6×10^{-12}	1.6×10^{-8}
50	26.64	5.0×10^{-5}	5.0×10^{-13}	5.0×10^{-9}
75	35.29	2.0×10^{-4}	2.0×10^{-12}	2.0×10^{-8}
Lithium (Chlorine salt)				
1	0.23	9.2×10^{-4}	9.2×10^{-12}	9.2×10^{-8}
10	2.25	8.0×10^{-4}	8.0×10^{-12}	8.0×10^{-8}
25	5.44	1.5×10^{-4}	1.5×10^{-12}	1.5×10^{-8}
50	10.31	1.2×10^{-4}	1.2×10^{-12}	1.2×10^{-8}
75	14.71	6.0×10^{-5}	6.0×10^{-13}	6.0×10^{-9}

The diffusion coefficients for each system were plotted as a function of lithium salt concentration, as seen in Figure 5.28. The D values are given in m^2/s, meaning they are directly comparable to the experimental values.

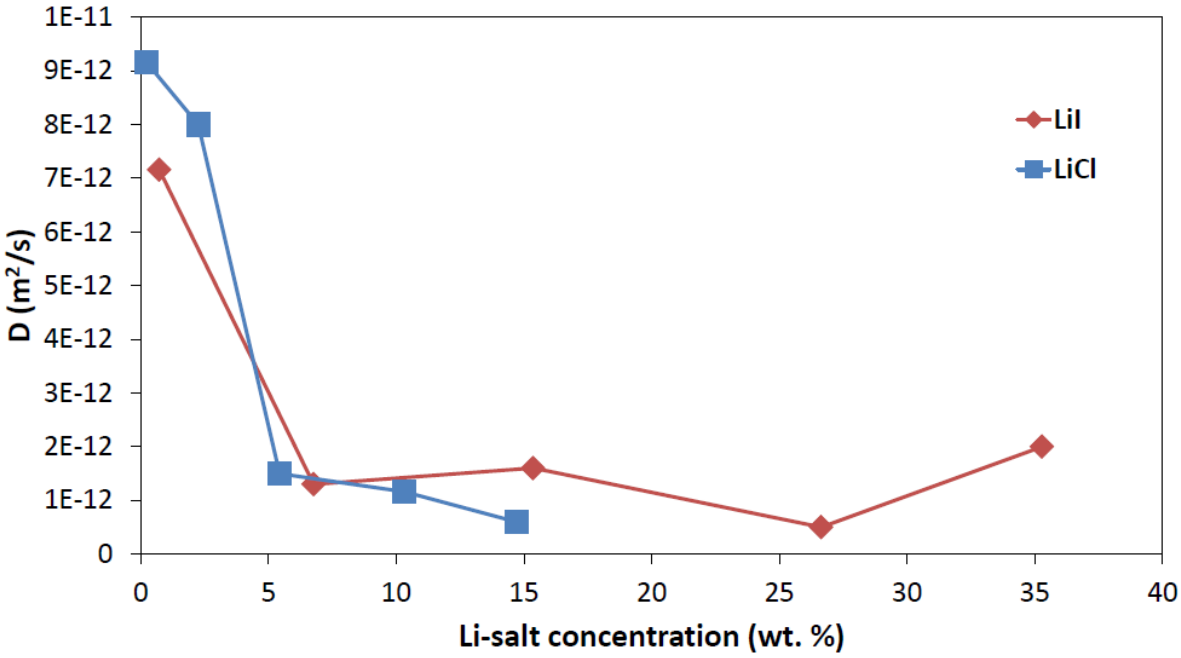

Figure 5.28: Lithium concentration vs diffusion coefficient for PEDOT-PEG

From Figure 5.28, it appears that for the LiI salt, even at low Li-ion concentrations, the diffusion coefficient falls toward a value of $1\times10^{-12}m^2/s$. This is confirmed by the sharp decrease from 0.72 to 6.77 wt.% LiI. The diffusion coefficient then stabilises around $1\times10^{-12}m^2/s$. This could be an induction of ion pairing.

On the contrary, the LiCl salt shows a different trend. As lithium concentration is increased, the diffusion coefficient decreases at each stage. This decrease is sharp as we go from 0.23 to 5.44 wt.% LiCl, with a gradual decrease from this point onwards. A possible reason for this trend is that as more lithium is inserted into the structure, the system shows higher ion pairing, leading to a reduction in ion mobility, meaning that lithium diffuses at a slower rate. LiCl systems are commonly used, particularly from an experimental point of view, with the PEDOT-PEG sample analysed earlier in this study being perchlorate doped. The weight and ionic radius of the anion may have a bearing on the simulation, along with ion-pairing.

These diffusion coefficients were compared to calculated MD values, as well as the experimental NMR diffusion coefficients obtained for PEG, as shown previously. In the case of the MD simulations of lithium in PEO using a "Two-Body force field", values of 4.4 to $7.1\times10^{-12}m^2/s$ were obtained [242]. Values ranging from 5.0×10^{-13} to $9.2\times10^{-12}m^2/s$ have been calculated for PEDOT-PEG for all of the different lithium concentrations. Particularly in the case of lower lithium concentrations, we see a good agreement with published calculated results. Furthermore, when comparing to the previously mentioned NMR-based diffusion coefficients for

$LiCF_3SO_3PEG_{10}$ and $LiN(CF_3SO_2)_2PEG_{10}$, these values tended towards $10^{-12}m^2/s$ at 300K and below [243], [244]. These also agree reasonably well with the calculated values for PEDOT-PEG.

The next stage was to investigate the ionic conductivity for PEDOT-PEG with increasing lithium concentration. Table 5.8 shows the conductivity values at each concentration for both the LiI and LiCl salts.

Table 5.8: Molar limiting conductivities (Λ_m^0) for lithium in PEDOT-PEG. Lithium concentration is shown also as a weight percentage of the salt in the PEDOT-PEG system

Lithium (Iodine salt)			
No. of Li-ions	Li salt conc. (wt.%)	Λ_m^0 (S m^2mol^{-1})	Λ_m^0 (S cm^2mol^{-1})
1	0.72	2.67×10^{-5}	0.27
10	6.77	4.85×10^{-6}	0.05
25	15.36	5.97×10^{-6}	0.06
50	26.64	1.87×10^{-6}	0.02
75	35.29	7.46×10^{-6}	0.07
Lithium (Chlorine salt)			
1	0.23	3.42×10^{-5}	0.34
10	2.25	2.99×10^{-5}	0.30
25	5.44	5.60×10^{-6}	0.06
50	10.31	4.33×10^{-6}	0.04
75	14.71	2.24×10^{-6}	0.02

As can be observed from Table 5.8, the same trend as reported for the diffusion coefficients is seen here. This is expected since F^2/RT acts as a constant, meaning that the conductivity is directly proportional to the diffusion coefficient.

In terms of comparison with the individual polymers, PEG and PEDOT, we can directly compare with PEDOT-PEG for a single cation. What is apparent is that PEDOT shows both higher diffusion coefficients and thus higher conductivities than both PEDOT-PEG and PEG. Meanwhile, PEDOT-PEG shows a higher conductivity than PEG for a single cation with each salt. As the ion concentration increases in PEDOT-PEG, these values become lower than those obtained for PEG. It is interesting to note however that for 10 lithium cations (6.77 wt.% LiI, 2.25 wt.% LiCl), the conductivity is still higher for PEDOT-PEG than in the case of a single cation for PEG. In fact, the results are in between PEG and PEDOT with the latter showing higher Li-ion diffusion rates.

5.4 Conclusions

The composite polymers, PEDOT-PEG and PEDOT:PSS were analysed using both FTIR spectroscopy and ab initio calculations. The spectra for both the pure samples of the polymers were characterised using frequency calculations with the CRYSTAL code, and then the accuracy of the calculations was confirmed using previous experimental results. These pure spectra were then compared alongside the spectra for the lithiated polymers. No changes were observed experimentally for the PEDOT-PEG sample, and this was suggested to be down to the chain length, which meant that lithium was not detected on the FTIR spectra for chains of $(\mathrm{PEG})_n \geq 20$. Computationally, however, lithium ions showed affinity for the oxygen atom on a PEG monomer, which is known to be a significant coordination site for the copolymer. In the PEDOT:PSS composite, the creation of a second peak was observed experimentally. From calculations, it was deduced that this was caused by the interaction of lithium with the sulphonate group in PSS. This indicates that this group is the preferred site for lithium in this composite polymer.

A molecular dynamics study was also performed on the polymers PEG, PEDOT, and the multi-block structure of the co-block PEDOT-PEG. An RDF analysis was conducted to measure the lithium-oxygen coordination number and distances in each of these polymers. Also analysed were the cation-anion separations in the system, and the potential extent of ion pairing. Li-O separations of around 2.23Å in PEG, 2.18Å in PEDOT and 2.23-2.28Å in PEDOT-PEG were obtained. It was found that these values were slightly higher than previously published calculated and experimental data. Ion pairing was also found to occur, for example, in PEDOT-PEG, Li-Cl and Li-I separations of 2.13-2.28Å and 2.43-2.53Å were calculated respectively. It was determined that with a smaller average separation for Li-Cl observed, a smaller coordination number for Li-O was also seen, indicating that a greater degree of ion pairing occurred in this system. With increased ion pairing, it can be deduced that there will be a decrease in the amount of lithium coordination.

Further molecular dynamics studies were carried out, analysing the MSD, and in turn, diffusion and conductivities for lithium in PEG, PEDOT and PEDOT-PEG. It was found that in the case of a single lithium ion, PEDOT showed diffusion coefficients and conductivities a single order of magnitude higher than in PEG. Other observations showed that values for PEDOT were similar in the case of both salts (LiCl and LiI) whereas the LiI salt in PEG had values of approximately double that of the LiCl salt. Importantly, the diffusion coefficients obtained for PEG agreed well with both published calculated MD data, and experimental NMR data.

A study was then carried out on PEDOT-PEG analysing how diffusion and conductivities changed as a function of lithium concentration. With the LiCl salt, diffusion, and thus conductivity decreased at each stage where the lithium concentration was increased, while the values tended to fluctuate for the LiI salt. The

general decrease in these values overall suggested that ion pairing might be having a noticeable effect, particularly with a more densely-packed system, where it becomes more difficult for Li^+ cations and Cl^-/I^- anions to avoid each other. Once again, the diffusion coefficients for PEDOT-PEG generally agreed well in comparison to published values for PEG.

Perhaps a result of a surprising nature, it was shown than the conductivity for PEDOT considering a single cation was greater than that observed for PEG and PEDOT-PEG. PEDOT-PEG also demonstrated a higher conductivity than PEG in this instance. It was expected that PEG would be a preferable coordination site for lithium ions, particularly as a model material. However, the result observed here may suggest that lithium ions shows greater diffusion in PEDOT. Of course, this result is inconclusive since only a single cation was tested in this case. As a future study, it is worth investigating the conductivity of lithium in PEDOT as a function of concentration. It could be that the distribution of oxygen atoms in PEDOT are preferable for hosting cations, and may even lead to reduced ion pairing. As a bulkier structure, it could also be that PEDOT arranges itself in a way where ion pairing is less common due to steric hindrance.

Overall, this study has given us an insight into the potential use of PEDOT-PEG as a battery material, with these calculated values being of use when considering the performance aspects. Good ionic conductivity is a highly desirable property of a polymer electrolyte, and it is useful to understand how this is affected with increasing lithium concentration. In terms of battery storage, a good lithium-ion capacity is also desirable. Striking a balance between the both is a potential challenge, with which, further studies can be conducted. To conclude, studies on PEDOT-PEG have shown that it indeed is an attractive prospect as a mixed conducting polymer in batteries, demonstrating conductivity values comparable to systems that are currently employed in solid state batteries, such as PEG.

Chapter 6

Designing a Low-profile Antenna for Integration with a Battery

With the issue of antenna mismatch and dramatic efficiency reduction of antennas in the presence of proximal metal planes, there is a need for a fully integrated antenna-battery system. Conventionally, batteries are wrapped in a hermetic metal seal, meaning there must be a separation from the antenna(s) to avoid degradation in efficiency.

With the proposed system, the design is intended to be extremely thin and lightweight, while aiming to maintain acceptable antenna input match and radiation efficiency. With this integrated design, we have considered low-profile applications which include sensors, home monitoring systems and lightweight portable radio for use in the military. There is also interest in using thin integrated antenna-batteries for security purposes.

The antenna design is based on a planar layered battery design to use for our integrated antenna, similar to that used by Nagatomo [30]. Figure 6.1 shows the battery design proposed in this case.

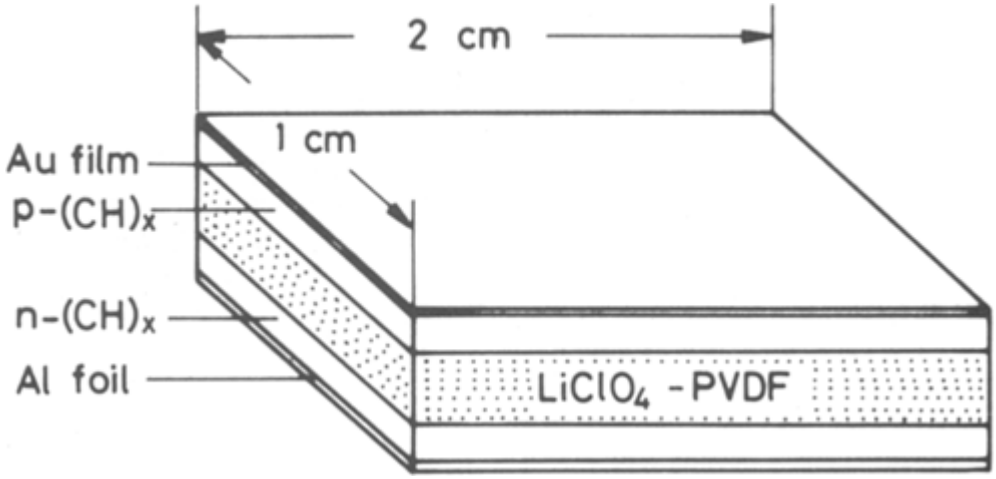

Figure 6.1: All-plastic polyacetylene battery design fabricated by Nagatomo

This design of battery consisted of a polyacetylene film as the electrode active

material, with $LiClO_4$/PC in a polyvinylidene fluoride (PVDF) film as the electrolyte. A gold film was present on top of the battery, with an aluminium foil present underneath, to act as the current collectors. Polyacetylene was seen as an attractive choice for an electrode, due to its high energy and power density. This battery was ultra-thin, with the two polyacetylene films being about 70μm thick, with the electrolyte thickness of between 30-150μm. The gold film was 2000Å thick, while the aluminium sheet was around 100μm in thickness.

For our design, we are interested in a battery that does not contain metal, therefore, the intention is for the polymer electrolyte films to also act as the current collectors. For the purposes of our initial integrated antenna-battery system, we treat both the polymer films and electrolyte as the antenna substrate, while the metallic films normally associated with the battery would essentially be the conducting layers containing a slot antenna.

6.1 Methodology and Results

6.1.1 Starting structure - Simulations

The CST Microwave Studio® package Transient Solver was used to perform all of the simulations in this study. As the aim was to simulate a wideband antenna, the starting structure was based on a coplanar waveguide-fed slot dipole by Nithisopa [78] which was developed to function on a substrate structure close to the battery design proposed by Nagatomo. Nithisopa, designed and simulated a CPW-fed slot antenna for wideband application, to function at the 2.4GHz frequency. Alterations were made to the slot on each side of the antenna, resulting eventually in an asymmetric design that was demonstrated to be suitable for wideband applications. The design was low-profile, small and lightweight, with a CPW feeding whereby the side-plane conductor is ground and a centre strip is what carries the signal.

Nithisopa's first design was a symmetrical structure based on RT/Duroid 5880. It consisted of a thickness of 1.575mm with a dielectric constant (ε_r) of 2.2, and was designed to have a transmission line impedance of 50Ω. Figure 6.2 shows the dimensions of the symmetrical CPW-fed antenna design.

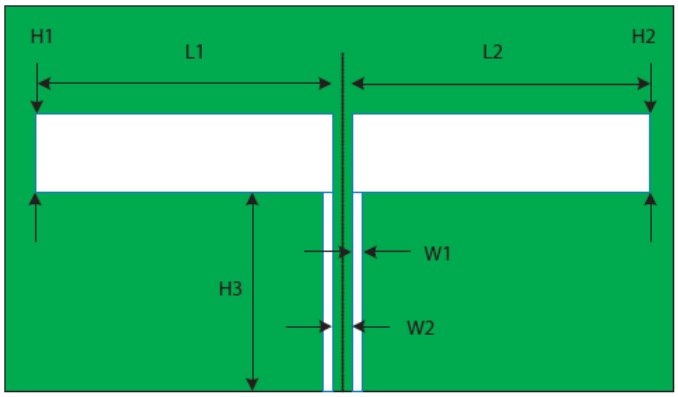

Figure 6.2: The first symmetrical CPW-fed slot antenna proposed by Nithisopa

Here, the total length of the antenna was 80mm, with the width of each slot dipole (H1, H2) of 10.5mm. The length of each slot dipole (L1, L2) was 38.8mm. The gap (W1), width of centre strip (W2) and length of CPW line (H3) had values of 0.5mm, 2.4mm and 23mm, respectively. The symmetric antenna shows a bandwidth (-10dB) of 1.0 GHz, and a return loss at 2.4GHz of -48dB.

Nithisopa then went on to alter the previous design by reducing the width of both slots (H1, H2) to 9.5mm and changing the length of L1 to 43.8mm and L2 to 33.8mm, as shown in Figure 6.3.

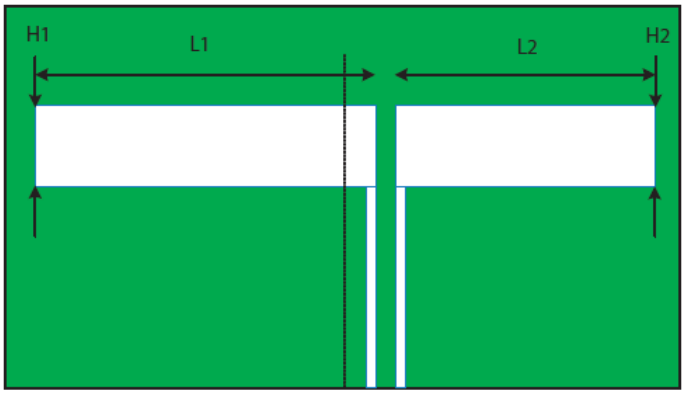

Figure 6.3: The second asymmetrical CPW-fed slot antenna proposed by Nithisopa

This asymmetric structure had a bandwidth (-10dB) of 0.8GHz and return loss at 2.4GHz of -35dB.

The final step involved an alteration of the width of the slots, with H1 reduced to 7.8mm and H2 reduced to 4.1mm. In Nithisopa's simulation, a bandwidth (-10dB) of 1.65GHz was achieved, with a return loss at 2.4GHz of -15.5dB. This showed a significant increase in bandwidth over the initial symmetrical design, and demonstrated that an antenna of this design could be used in wideband applications.

Ideally, we would like to design an integrated antenna-battery that gives us the greatest amount of bandwidth possible. Efficiency is also very important in ensuring that the antenna is performing adequately. Nithisopa's final asymmetric design in this study, therefore, was used as the starting point in our designs to simulate

and create an antenna that could be suitably used with a battery while giving us efficiencies that are usable despite high losses.

The slot antenna consisted of two asymmetric slots cut into an upper plane of metal. The thickness of the substrate was 1.575mm, with a relative dielectric constant (ε_r) of 2.2. The ground plane was 0.018mm thick, made up of a copper film with a conductivity of 5.8×10^7 S/m. The slots used for the feed (W1) and the gap between the two feed slots (W2) were 0.5mm and 2.4mm respectively. The length of the CPW feed line (H3) was 23mm. The left slot had a height (H1) and width (L1) of 4.1mm and 33.8mm. The right slot had a height (H2) and width (L2) of 7.8mm and 43.8mm. Figure 6.4 shows the dimensions and simulated S_{11} results along with the farfield patterns for this design using a copper conductor for the metal plane:

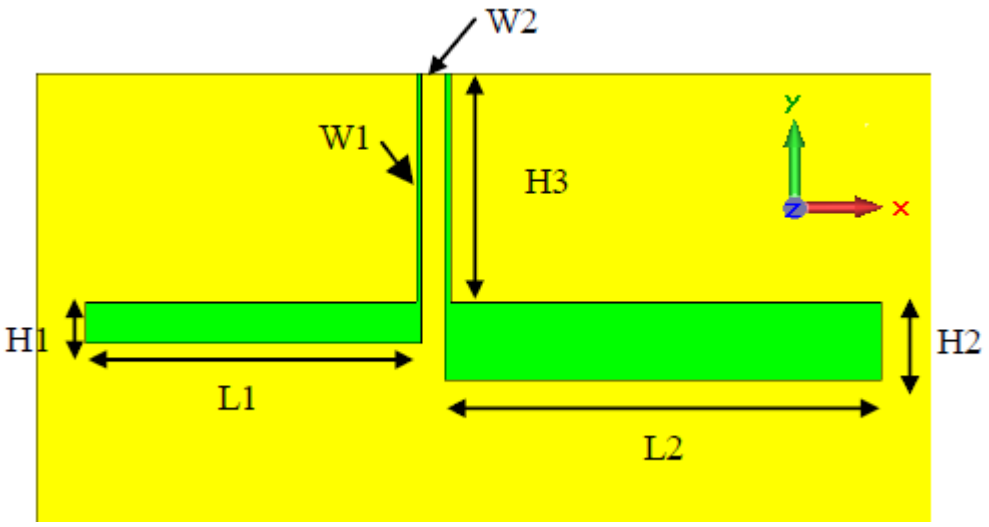

(a)

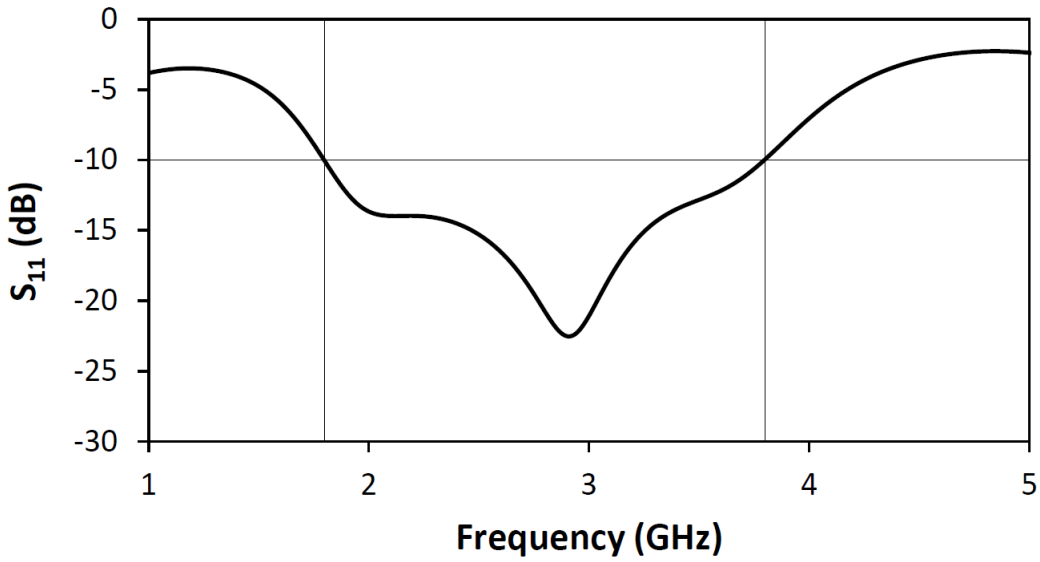

(b)

Figure 6.4: (a) Initial dimensions and (b) S_{11}, for antenna-battery prototype, based on Nithisopa's design

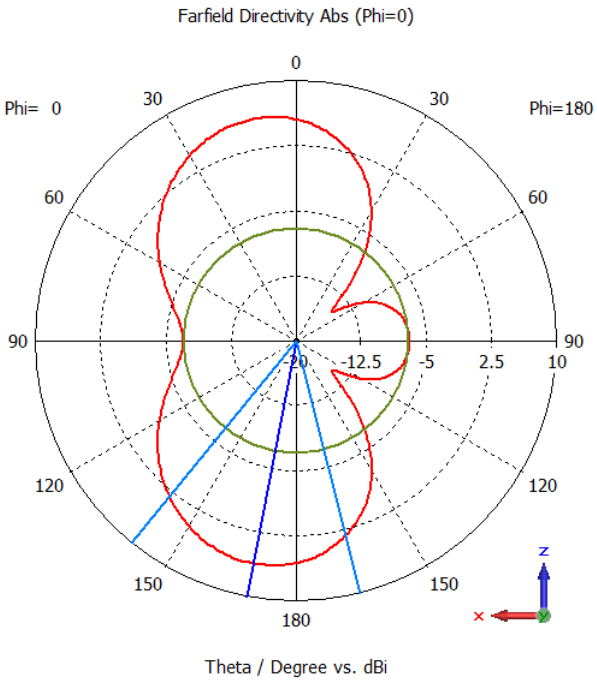

(c) Phi=0° as a variation of Theta.

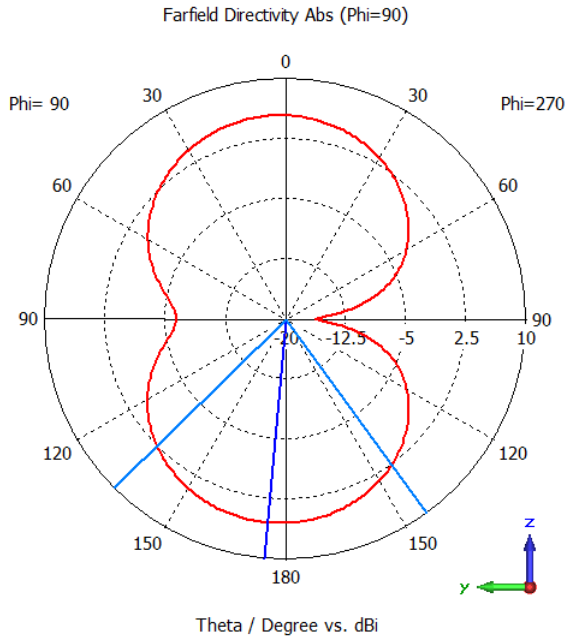

(d) Phi=90° as a variation of Theta

Figure 6.4: Continued. (c), (d) Simulated farfield Directivity patterns for initial antenna design at 2.9GHz

The matched operating band is indicated in the S_{11} results of Figure 6.4b. The -10dB fractional bandwidth was simulated to be about 70% and the antenna simulated total efficiency was -0.87dB with a gain of 5.2dB.

6.1.2 Initial measurements

With the simulation for Nithisopa's asymmetric antenna design showing good bandwidth and usable efficiency, a measurement was performed to establish whether an antenna of this design could show a good match with simulations. For test purposes, a Mylar substrate was used, with a thickness of 0.025mm and a dielectric constant of 3.2. A single copper film was used for the ground plane, with the slot dipole inside. The measurement is compared with the simulation to assess whether they match at the resonant frequency. Figure 6.5 shows the antenna that was synthesised for the measurements. Figure 6.6 shows the experimental setup for this antenna, giving an indication of how the antenna was mounted in the anechoic chamber. Figure 6.7 shows the S_{11} results for both the simulation and measurement with a Mylar substrate.

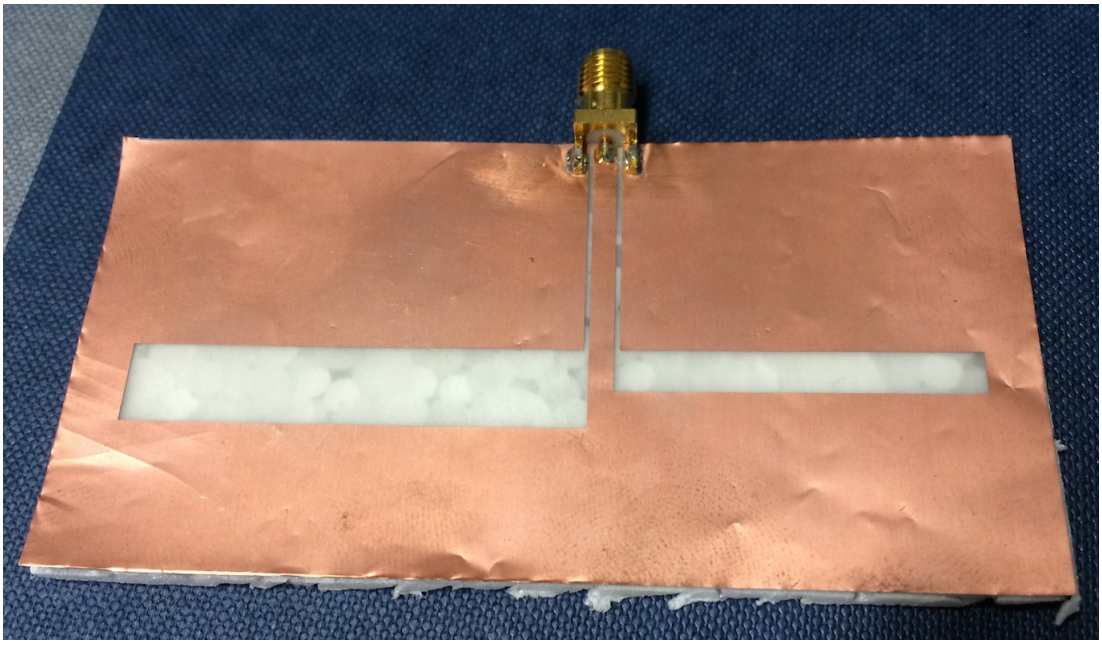

Figure 6.5: Synthesised asymmetric antenna with Mylar substrate

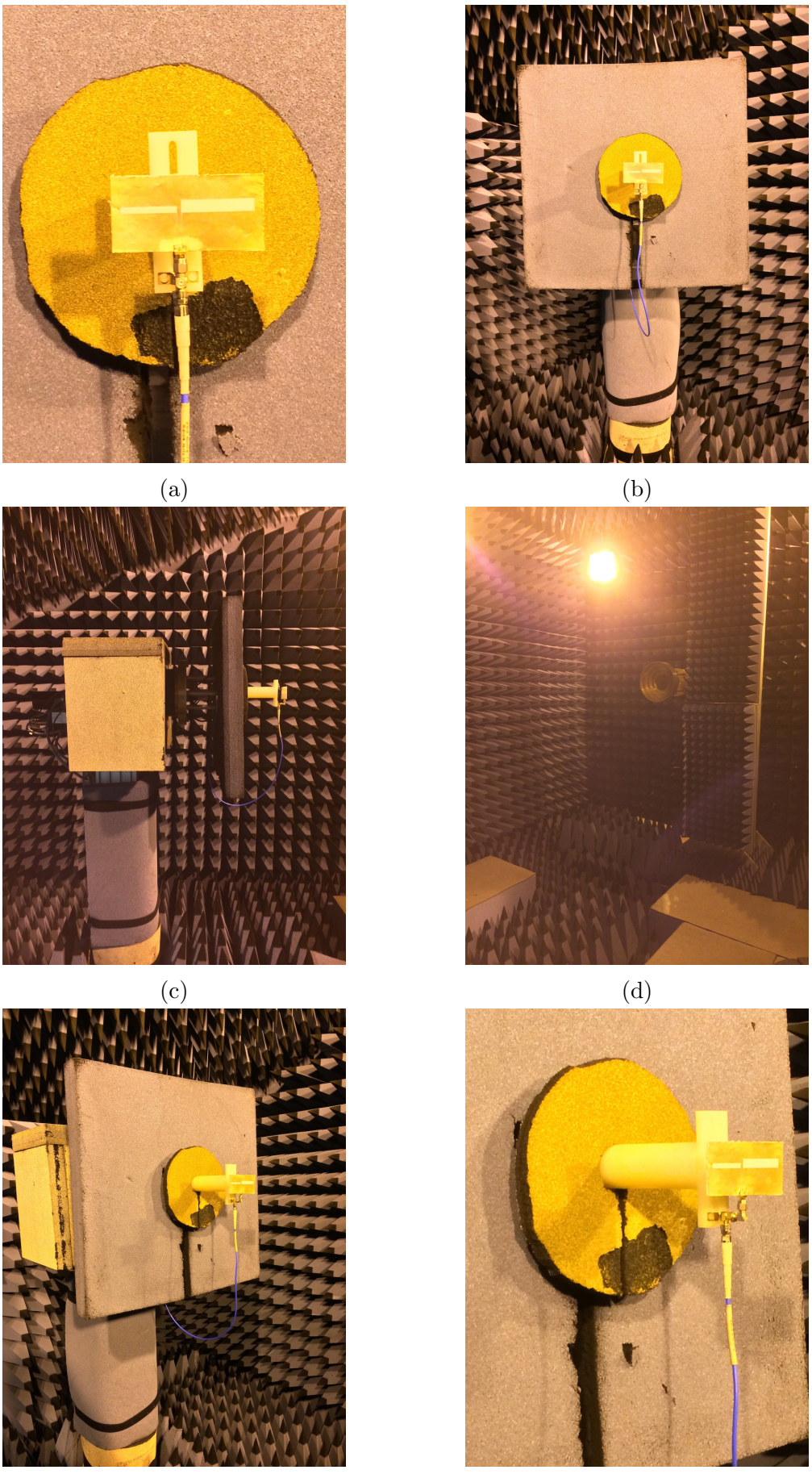

(a) (b) (c) (d) (e) (f)

Figure 6.6: Experimental setup for Mylar antenna, showing how it was mounted in the anechoic chamber

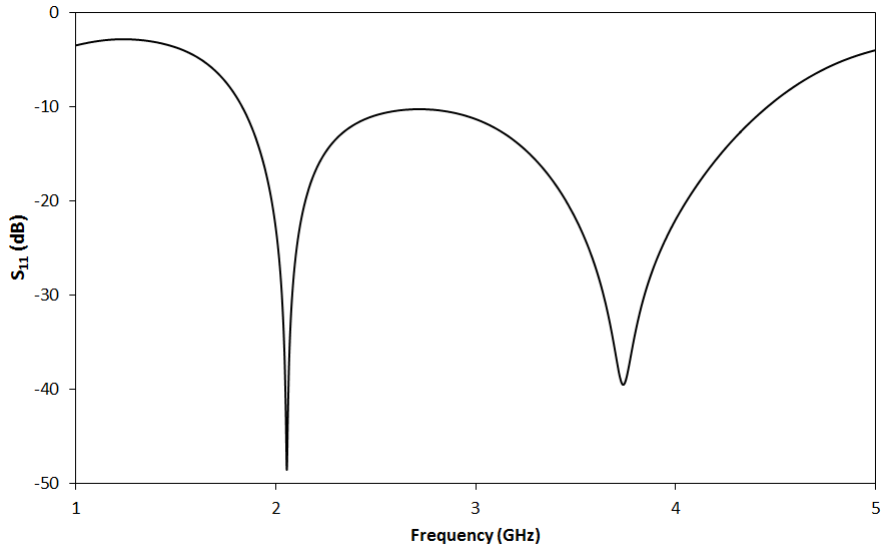

(a)

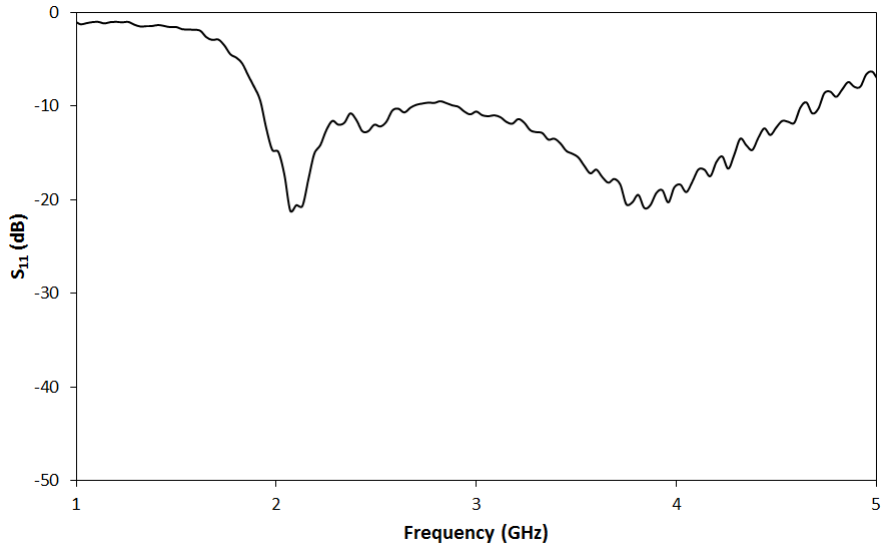

(b)

Figure 6.7: (a) Simulated S_{11} and (b) Measured S_{11}, for antenna-battery prototype, using a Mylar substrate

It can be seen that there is a good match between simulation and experiment for the antenna design with a Mylar substrate. The simulation shows the resonant frequency to be 2.1GHz, which agrees well with the measurement observed at 2.1GHz. The simulated radiated farfield indicates a gain of 4.0dB and an efficiency of -0.996dB at the resonant frequency, values of which can be considered usable in mobile applications. Radiation patterns were obtained both for the simulation and measurement, however, they cannot be compared due to the disruption encountered during the radiation pattern measurements. It was discovered that due to the setup of the apparatus in the anechoic chamber, part of the measured pattern was blocked by the pedestal to which the antenna was attached (See Figure 6.6). The issue with the pedestal meant that the radiation patterns could not be related back

to the simulation results. In this case, the antenna was vertically polarised. As a result of this issue, for all subsequent measurements, the antenna was placed on a raised pedestal to ensure that this would not happen again. Figure 6.8 shows the simulated and attempted measured radiation patterns for the antenna design with a Mylar substrate.

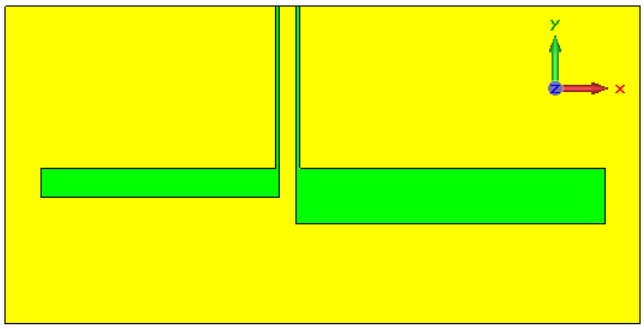

(a)

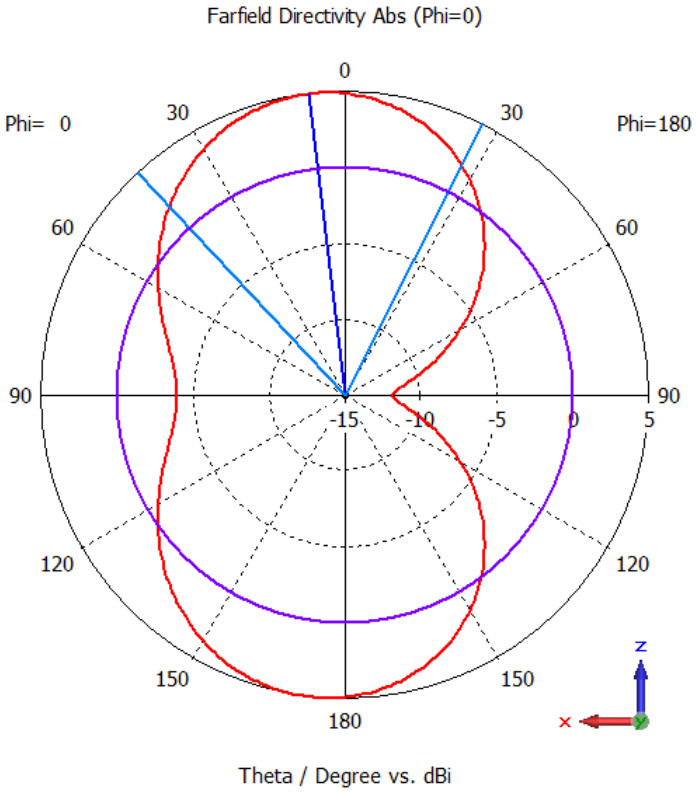

(b) Phi=0° as a variation of Theta

Figure 6.8: (a) Simulated antenna design and (b) Simulated farfield Directivity pattern for asymmetric antenna which was vertically polarised, using a Mylar substrate at 2.1GHz

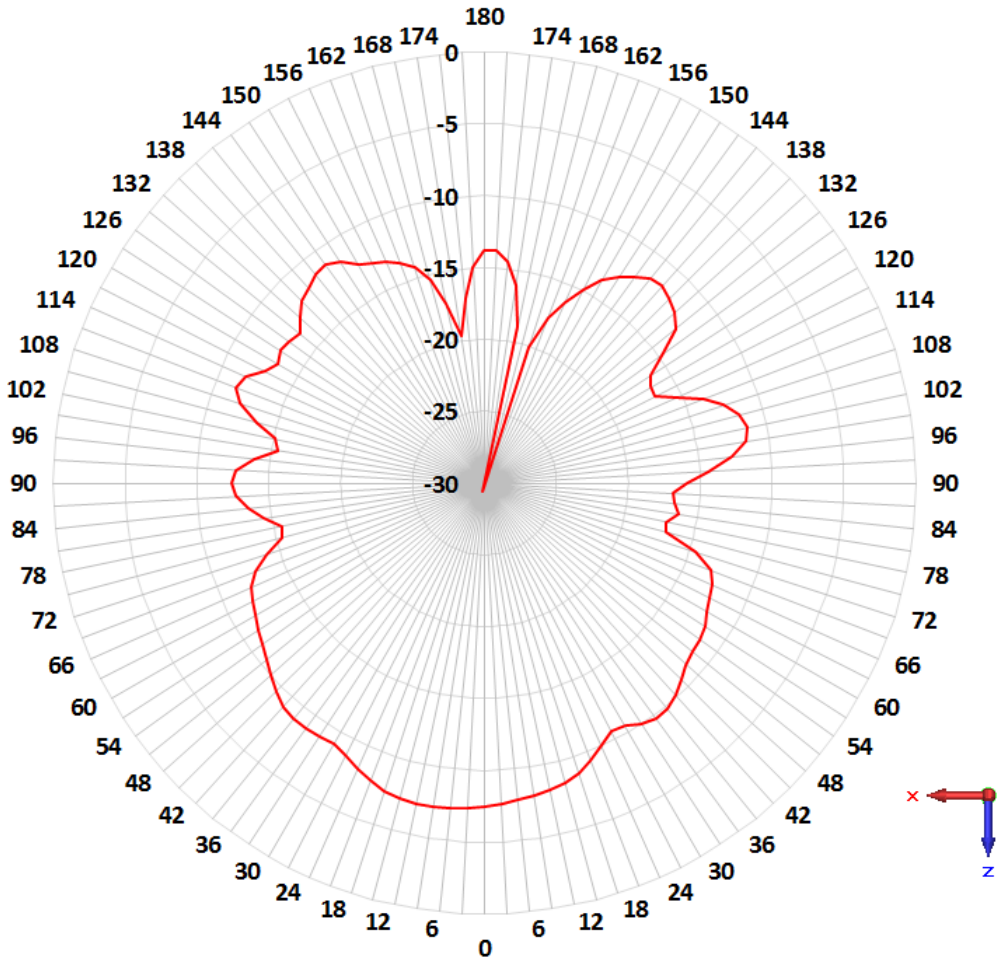

(c)

Figure 6.8: Continued. (c) Measured farfield Directivity pattern for asymmetric antenna which was vertically polarised, using a Mylar substrate at 2.1GHz

6.1.3 New structure

After testing that an asymmetric antenna of this design can give results both in terms of simulation and measurement, the next stage was to alter the design in Section 6.1.1, in order to improve properties and develop a structure more closely resembling the material parameters of a battery. To create a low-profile structure with low surface area, end caps were added to each slot to reduce the antenna length. For the left slot, the cap had a height (H4) of 18.1mm and a width (W3) of 7mm. The cap at the end of the right slot was of height (H5) 18mm and width (W4) 24mm. These values were obtained via a parameter sweep on CST to select the optimum bandwidth. Figure 6.9 shows the dimensions and S_{11} results for the end-loaded design along with the radiation patterns.

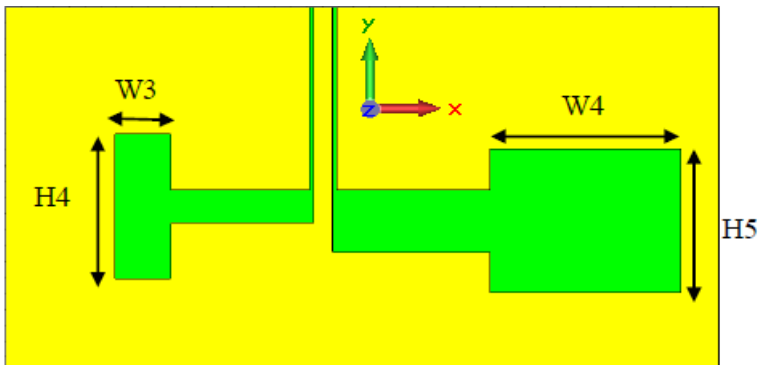

(a)

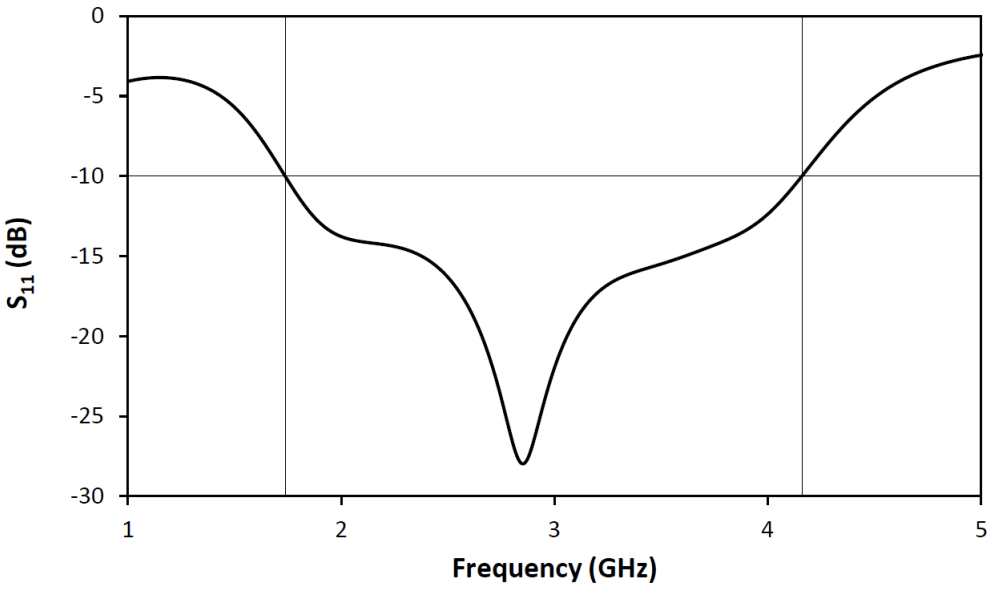

(b)

Figure 6.9: (a) Dimensions and (b) S_{11} of end-loaded design

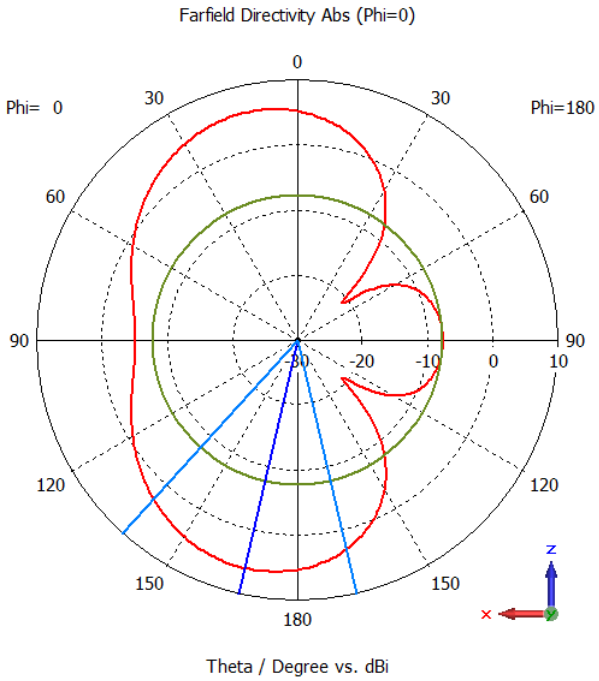

(c) Phi=0° as a variation of Theta

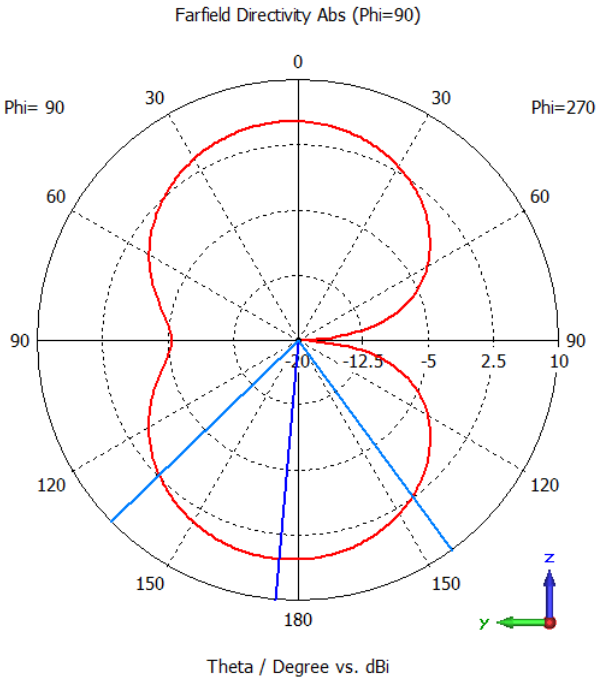

(d) Phi=90° as a variation of Theta

Figure 6.9: Continued. (c) and (d) Simulated farfield Directivity patterns at 2.9GHz for end-loaded design

Simulation of the modified structure showed an improvement in bandwidth of 85%, and a total efficiency of -0.47dB was observed along with a gain of 5.4dB, which compares well with the original structure. It should be noted that our modified designs use the original frequency range chosen by that of Nithisopa, purely due to the fact that there was no specific application in mind at this point.

6.1.4 Conductivity sweep

Conducting polymer conductivities are lower than the bulk copper which was used in the original design. To assess the effect of reducing conductivity, a parameter sweep was performed on our new structure in order to see the effect that conductivity of the ground plane had upon the bandwidth of the structure. In this case, the parameter, n, was defined as 5.8×10^{n} S/m. For each test, the power n was reduced by 1, to see how the S_{11} parameters changed. Figure 6.10 shows the resulting S_{11} for the antenna structure at each different conductivity of the ground plane, while Table 6.1 shows the percentage bandwidth in each case.

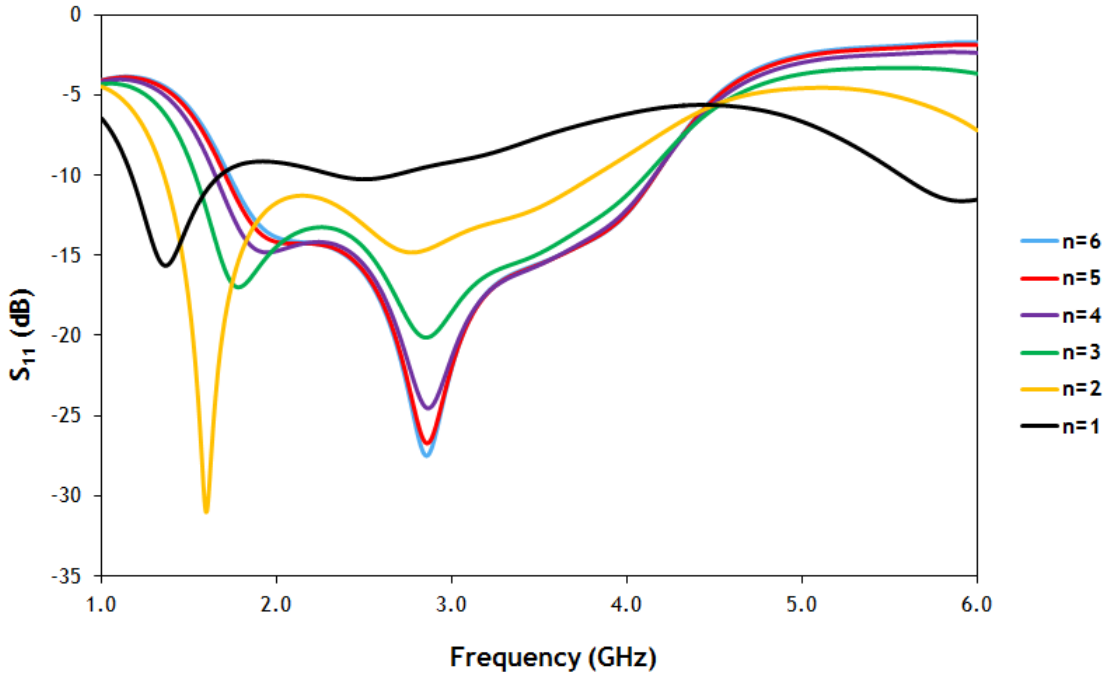

Figure 6.10: S_{11} at different ground plane conductivities

Table 6.1: Power to which conductivity is raised compared to percentage bandwidth

n	Fractional bandwidth (%)
6	85
5	86
4	87
3	91
2	92
1	37

It was observed that the antenna maintained a relatively high bandwidth for conductivities down to that of 5.8×10^{2} S/m whilst lower values resulted in a significant loss of bandwidth. Looking at the S_{11} parameters and Table 6.1, there is

a significant change as the conductivity is reduced from 5.8×10^2 S/m to 5.8×10^1 S/m. A loss of bandwidth of 55% is seen which is a noticeable reduction. The lowest conductivity value for the conducting plane at which the high bandwidth was maintained is closer to conductivity values quoted for several polymer electrolytes, such as polyaniline (10×10^2 S/m in some cases [12]). This demonstrates that polymer electrolytes could be a viable candidate material to use for the ground plane of the antenna, though it should be recognised that radiation efficiency is also affected. Table 6.2 gives us an overview of how the gains and efficiencies are altered when n is changed.

Table 6.2: Power to which conductivity is raised compared to gain and efficiency

n	Gain (dB)	Efficiency (dB)
6	5.0	-0.9
5	4.9	-1.0
4	4.7	-1.3
3	4.0	-1.9
2	-0.6	-4.8
1	-5.4	-8.9

6.1.5 Addition of a lower ground place

The next stage of the investigation required the addition of a second ground plane, representing the lower battery terminal. This lower ground plane was added progressively as illustrated in Figure 6.11. The intention was to cover as much of the base as possible with conductor, while retaining a good bandwidth. We wished to find the minimum rectangular slot size for the ground plane that gave sufficient efficiency and bandwidth, as opposed to designing a more complex slot configuration that would perhaps yield better results at the expense of fabrication complexity.

The process began by inserting a conducting layer of 0.018mm thickness in stages from the lower edge of the bottom layer. Once again, a parameter sweep was conducted, with the width of conducting layer referred to as g, being the varying factor. This ensured that at each stage of the addition, the optimum bandwidths could still be maintained. Figure 6.11 shows the stages of the addition, with the radiation patterns and efficiencies shown.

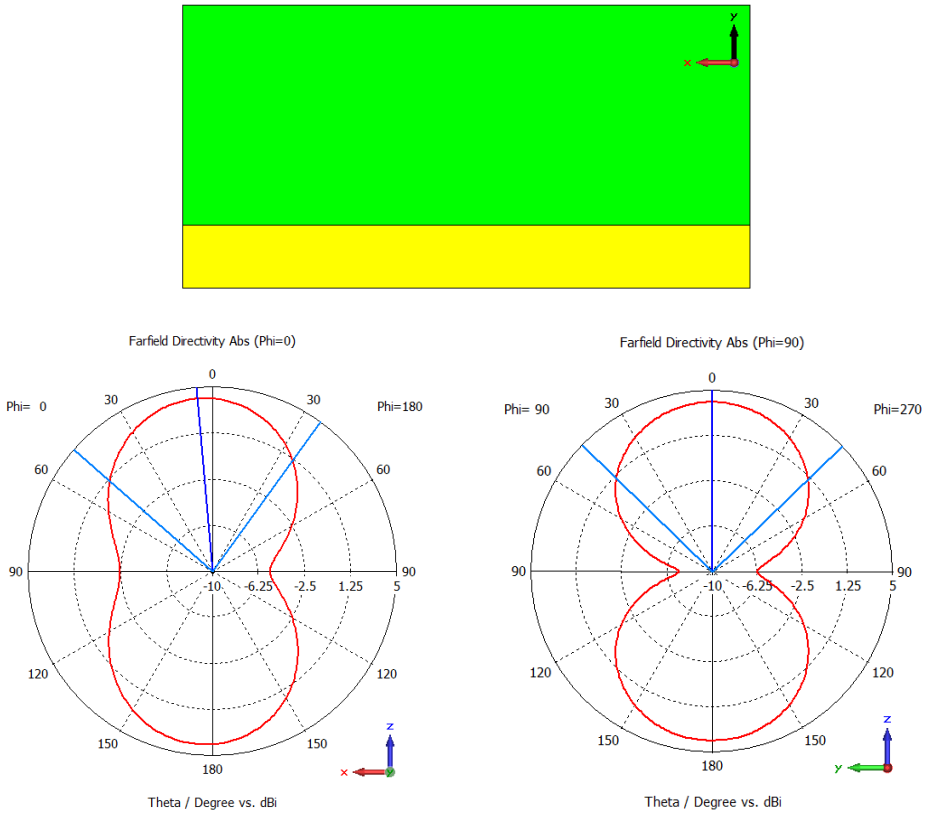

(a) Bandwidth = 95%, Efficiency = -5.1dB

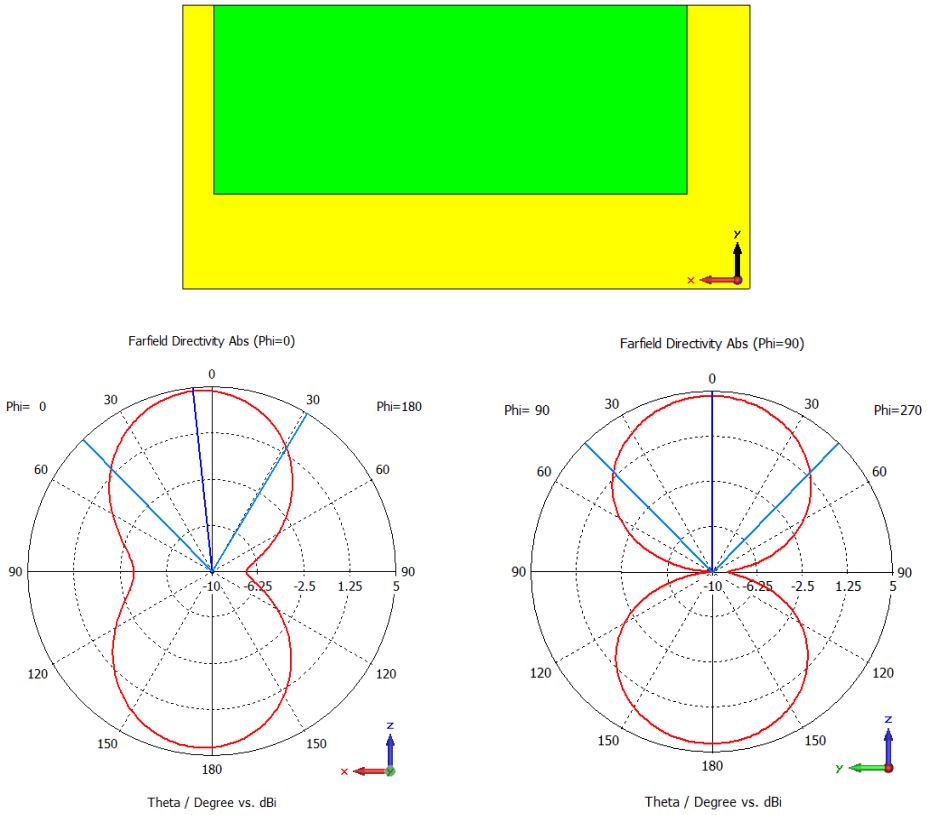

(b) Bandwidth = 87%, Efficiency = -5.1dB

Figure 6.11: Addition of lower ground plane (conductor shown in yellow) along with farfield Directivity at both Phi=0° and Phi=90°, respectively, as a variation of Theta

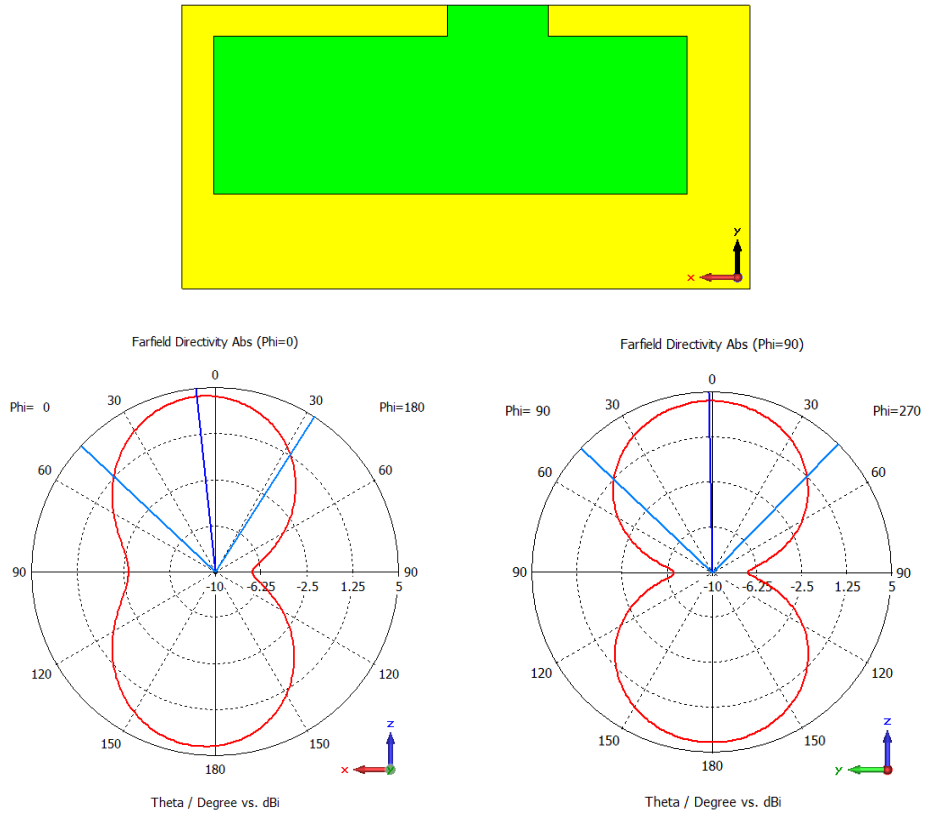

(c) Bandwidth = 93%, Efficiency = -5.2dB

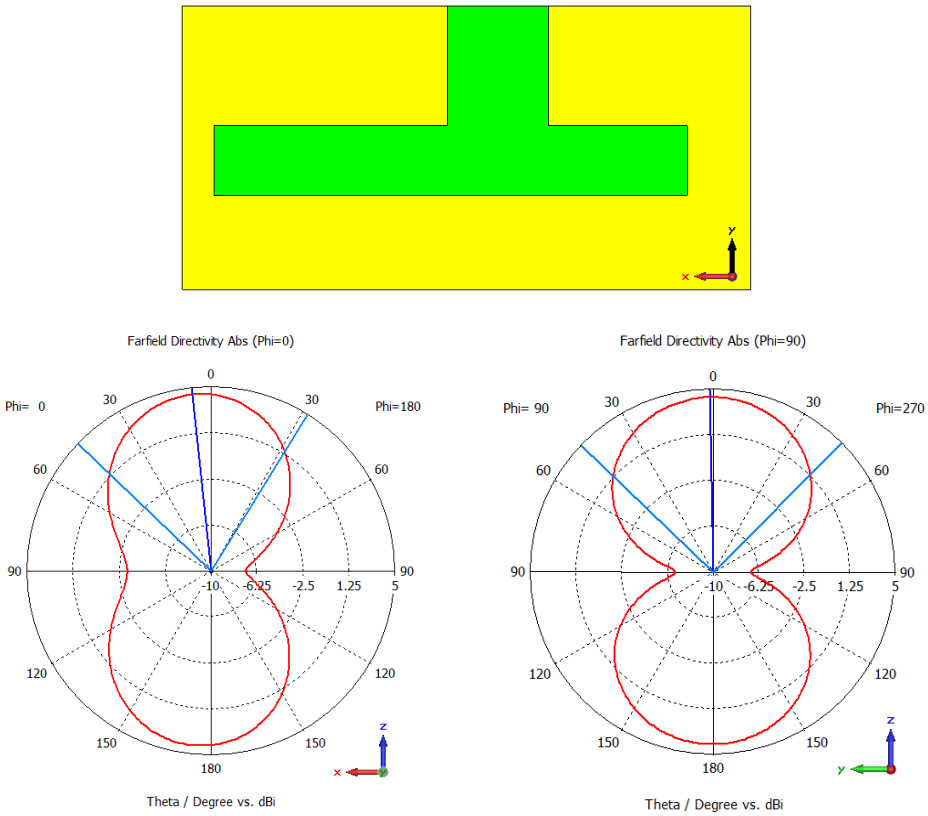

(d) Bandwidth = 86%, Efficiency = -4.6dB

Figure 6.11: Continued.

It should be noted that a ground conductivity of 5.8×10^2 S/m was chosen, similar to that of polymer electrolytes such as polyaniline. In this situation, it merely represented a test case, rather than giving optimum performance, particularly in terms of efficiencies. The conductor was inserted in stages with one sheet added at a time, to gain a better insight into how the bandwidth would change with each parameter. As a greater amount of the surface was covered and enclosed with the conducting film, a structure closer to that of an all-plastic solid state battery was obtained. At this point, further parameter sweeps were conducted, mainly for parameters g and l, to ascertain the maximum extent of lower battery terminal area before the antenna performance is lost. By keeping parameter l constant, parameter g was decreased, enclosing the slots seen in the middle of the structure. Figure 6.12 shows the dimensions to be altered for the purposes of this study, and Table 6.3 shows the effect of decreasing parameter g upon the bandwidth of the structure, with all other parameters kept constant.

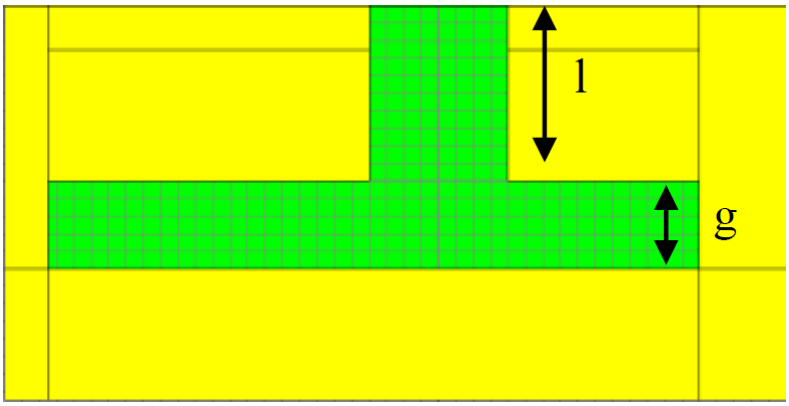

Figure 6.12: Dimensions for the slots on the bottom ground plane

Table 6.3: Effect of reducing height of slots beneath dipole (g) upon fractional bandwidth (the lower the height, the more enclosed the lower plane)

g height (mm)	Lower frequency (GHz)	Upper frequency (GHz)	Centre frequency (GHz)	Fractional Bandwidth (%)
21	1.38	3.81	2.60	94
16	1.40	3.80	2.60	93
11	1.41	3.61	2.50	88
6	1.35	3.72	2.50	95
1	2.75	3.60	3.19	27

By performing these multiple simulations, it was deduced that the slot on the bottom ground plane located directly underneath the CPW feed was necessary to avoid total mismatch (S_{11} > -10dB). However, there was no requirement for a slot beneath the dipole to be present, and by taking this away completely, an input

bandwidth of 27% is achieved, which could still be considered wideband. However, due to a significant reduction in efficiency down to a value of -13.6dB, the antenna essentially became a resonator, and therefore this particular ground plane configuration was not pursued any further. Figure 6.13 shows the design in which the slot beneath the dipole is removed, along with the resulting S_{11} and farfield patterns.

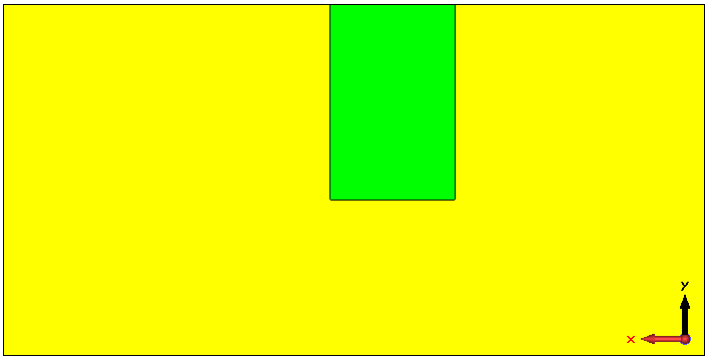

(a)

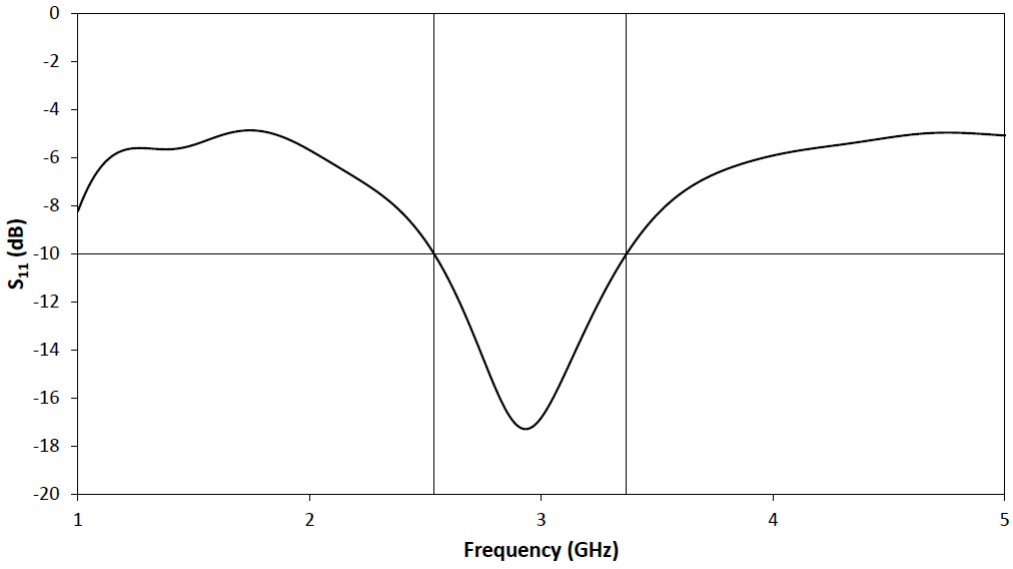

(b)

Figure 6.13: (a) Lower ground with the slot beneath the dipole removed and (b) S_{11}

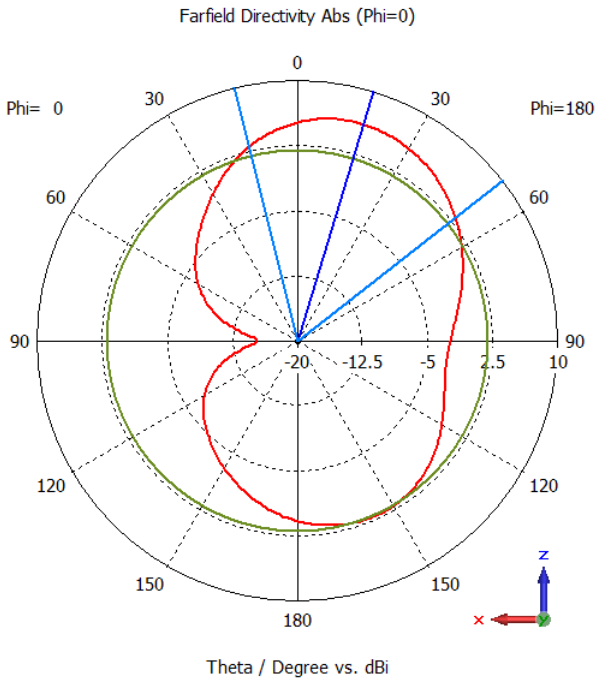

(c) Phi=0° as a variation of Theta

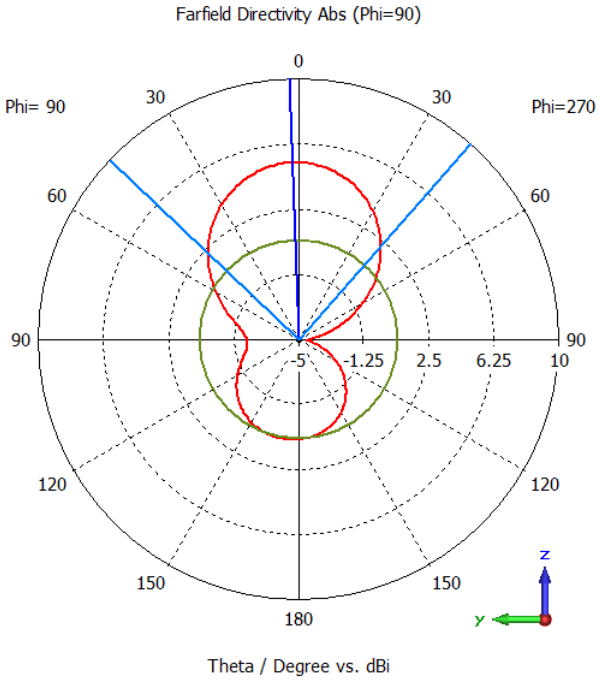

(d) Phi=90° as a variation of Theta

Figure 6.13: Continued. (c) and (d) Farfield Directivity patterns at 2.9GHz with the slot beneath the dipole removed on the lower ground

6.1.6 Design modification to replicate battery parameters

The next parameter to investigate is the thickness of the substrate. In Nagatomo's proposed polyacetylene battery, the total structure thickness was about 0.4mm. Around 0.3mm of this consisted of the polyacetylene and electrolyte layers with the

remaining thickness due to the metallic films deposited on the top and the bottom of the structure. It is of keen interest to create an antenna-battery that is ultra-thin. Therefore, to obtain an antenna design closer to these proposed batteries, the thickness of the substrate was reduced from 1.575mm to 0.3mm. It is also important to assess whether the antenna would still function well with anode/cathode conductivity values closer to metal, so for this purpose, we increased the current value of 5.8×10^2 S/m to a value of 3×10^5 S/m, which has been achieved in a laboratory environment by the copolymer PEDOT:PSS, after being doped with sulphuric acid. Though this value is still significantly lower than that of bulk copper, it allows us to establish a middle ground in terms of conductivity, should the concept of using polymer electrolytes as the ground plane be pursued further. It is also useful to know the permittivity and conductivity of the electrolyte substrate.

The ionic conductivity of the substrate in this case was taken from a study of poly(vinylidene fluoride-co-hexa fluoro propylene)/poly (methyl methacrylate) (PVDF-HFP/PMMA) using lithium perchlorate as the salt, along with varying concentrations of propylene carbonate [245]. This value was of the order of 0.1 S/m. Based on a study of PVDF permittivity [246], it has been calculated that ε_r is about 3 at 1MHz, which was used as an initial assumption for the simulations. A few modifications were made to the slots in the lower ground plane, with the width of the slot beneath the dipole reduced to 1mm. This ensured that the lower ground plane was sufficiently enclosed while providing us with optimum antenna performance. Figure 6.14 shows the dimensions that have been altered in this investigation, with Table 6.4 summarising the changes made to the antenna to resemble parameters more closely associated with a battery. Figure 6.15 then goes on to show the optimum S_{11} and farfield results obtained.

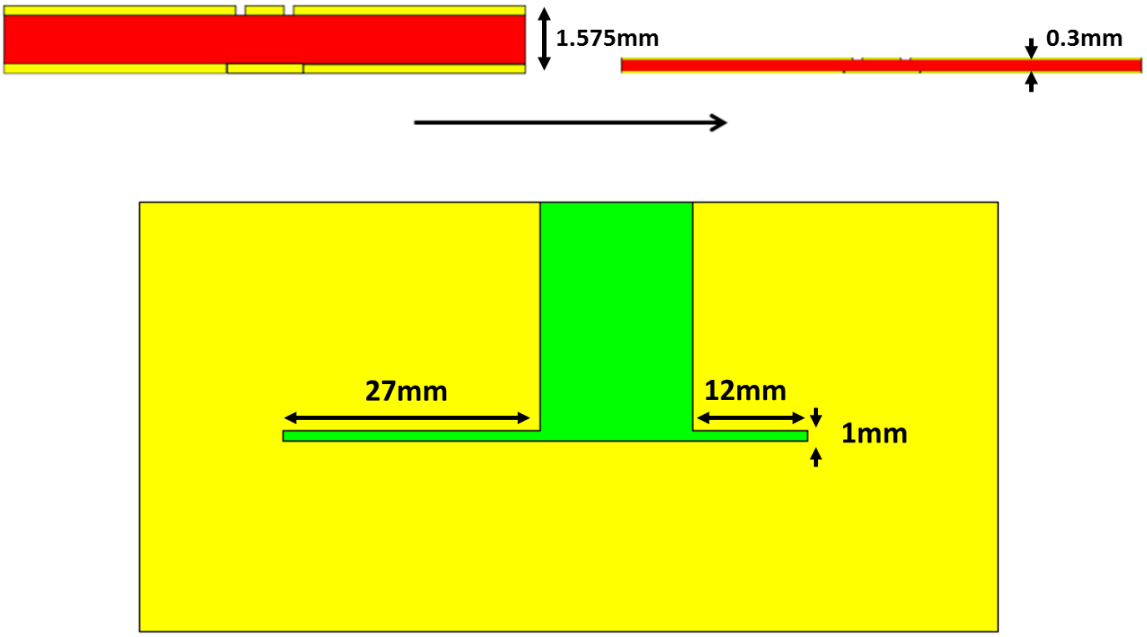

Figure 6.14: Diagram showing new dimensions of antenna for the substrate and lower ground

Table 6.4: Original and modified parameters for antenna-battery

Parameter	Original value	New value
Substrate thickness (mm)	1.575	0.300
Ground conductivity (S/m)	5.8×10^{2}	3.0×10^{5}
Substrate conductivity (S/m)	0	1.0×10^{-1}
Substrate permittivity (ε_r)	2.2	3.0
Optimum bandwith (%)	92	66

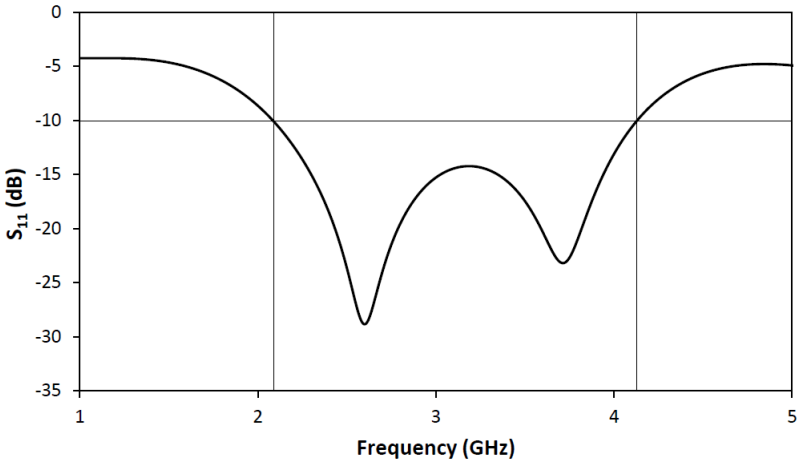

(a)

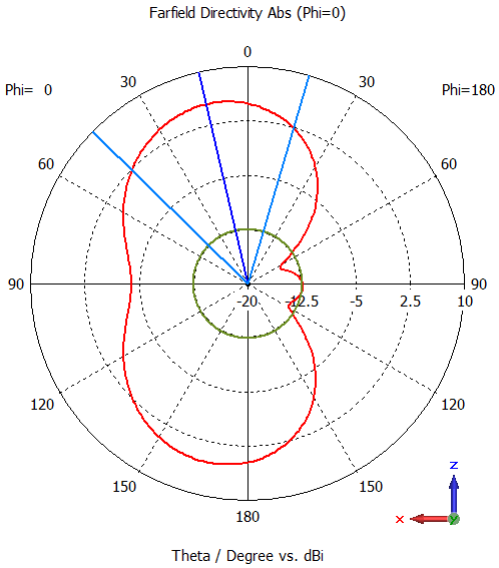

(b) Phi=0° as a variation of Theta

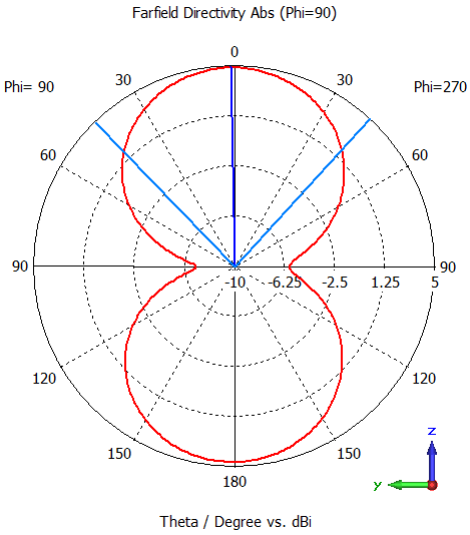

(c) Phi=90° as a variation of Theta

Figure 6.15: (a) S_{11}, (b) and (c) farfield Directivity patterns obtained with new parameters for antenna-battery

It was found that using these parameters, an optimum bandwidth of around 66% was achieved with a lower ground plane. A total efficiency of around -4.1dB with a gain of around 1.3dB was obtained. Once again, we obtain usable efficiencies in terms of our potential application, even with parameters more closely resembling a solid state battery. Further investigation should allow us to obtain more accurate battery parameters, particularly by measuring candidate materials to use in the potential design.

6.1.7 Radiation pattern analysis

The radiation patterns for the antenna were simulated for the design with the lower ground plane as shown in Figure 6.12. The effect of changing the width of the centre slot beneath the dipole upon the farfields was observed for two frequencies in the S_{11} matched bandwidth. Table 6.5 shows the gain and efficiency results for this analysis.

Table 6.5: Effect of decreasing the slot width on the lower ground plane upon gains and efficiencies at 2.3GHz and 3.4GHz

Width of slot (mm)	Gain (dB) at 2.3GHz	Efficiency (dB) at 2.3GHz	Gain (dB) at 3.4GHz	Efficiency (dB) at 3.4GHz
16	2.3	-2.9	4.1	-1.9
11	2.3	-2.9	4.2	-1.8
6	1.5	-3.7	4.2	-2.0
1	0.2	-4.8	2.6	-3.3

What is observed here is that reducing the slot width on the bottom ground plane does not make any real difference initially, particularly going from 16mm to 11mm. As the lower ground plane becomes more enclosed, however, we see a reduction in efficiency and gain, beginning with the pattern at 2.3GHz. In fact, the efficiency at 3.4GHz remains largely unaffected, until we reach a slot width of 1mm. In this case, the gain and efficiency is noticeably reduced for both of the observed frequencies. This pattern is expected when increasing the area covered by the ground plane, and as the results in Section 6.1.5 showed, by enclosing the slot beneath the dipole entirely on the lower ground plane, a significant reduction in efficiency was seen. Therefore, we expect to see a reduction in efficiency with a decrease in the width of the slot beneath the dipole. It is important to note, however, that despite the reduction, these gains and efficiencies are still usable and something which can be worked with to develop our design further.

The variation in antenna gain with substrate loss was also of interest owing to the high frequency loss of the electrolyte material. A study was performed by increasing the tan δ value (and therefore the dielectric loss) for the antenna substrate and observing the changes in the farfield patterns at two frequencies within the S_{11} bandwidth. In this case, the lower ground plane slot width beneath the dipole was kept constant at 1mm. Table 6.6 shows the change in gain and efficiency as a result of the substrate loss.

Table 6.6: Effect of increased tan δ of substrate upon gains and efficiencies at 2.6GHz and 3.7GHz

tan δ	Gain (dB) at 2.6GHz	Efficiency (dB) at 2.6GHz	Gain (dB) at 3.7GHz	Efficiency (dB) at 3.7GHz
0.0009	3.3	-2.2	3.0	-2.7
0.009	3.2	-2.3	3.0	-2.7
0.09	2.6	-2.9	2.7	-3.1
0.9	-1.8	-7.3	-3.0	-8.8

Here, it can be seen that the antenna maintains its efficiency for a loss tangent of up to 0.09, with a slight reduction of gain and efficiency observed at both of the frequencies of interest. However, as the tan δ value is increased up to a value of 0.9, significant reductions in gain and efficiency occur. We see a decrease from -2.9 to -7.3dB at 2.6GHz, and a decrease from -3.1 to -8.8dB at 3.7GHz. This pattern of decreasing efficiency with increasing loss tangent is expected, as ultimately, a greater substrate loss will result in a less efficient antenna. However, this result shows that the substrate loss can be increased to a certain point where the gains and efficiencies could still be considered usable. It is expected that the candidate battery material, which will become the substrate, will be fairly lossy, and so it is important to ensure that the antenna design can accommodate this and still maintain good performance as a result. With polymer electrolytes showing good potential to be used in a battery, it is of interest to measure the permittivity and dielectric loss of a sample, and analyse whether the antenna will maintain its performance with these measured parameters.

Figures 6.16 and 6.17 show all the farfield patterns in this part of the study, with both Phi=0° and Phi=90° shown as a variation of Theta.

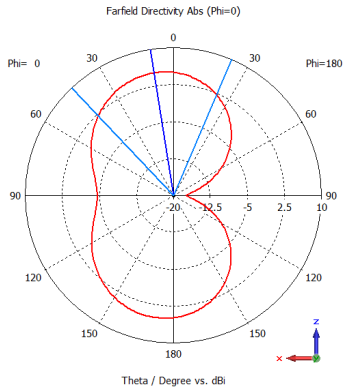

(a) Slot width 16mm, 2.3GHz, Phi=0°

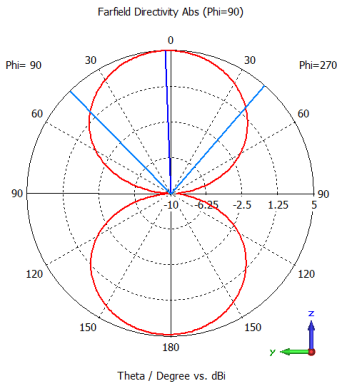

(b) Slot width 16mm, 2.3GHz, Phi=90°

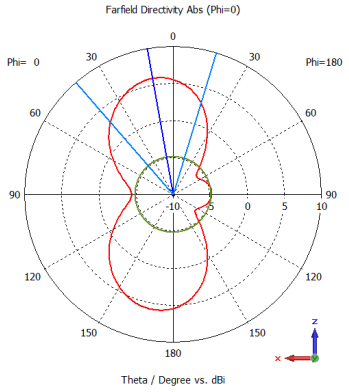

(c) Slot width 16mm, 3.4GHz, Phi=0°

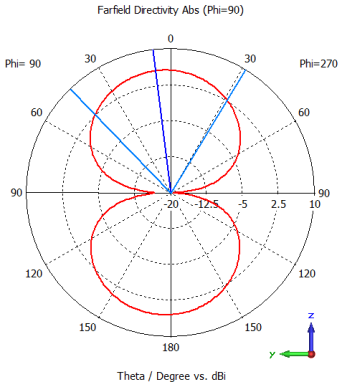

(d) Slot width 16mm, 3.4GHz, Phi=90°

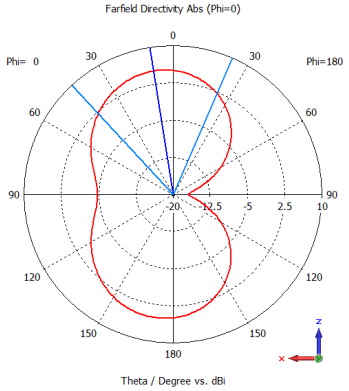

(e) Slot width 11mm, 2.3GHz, Phi=0°

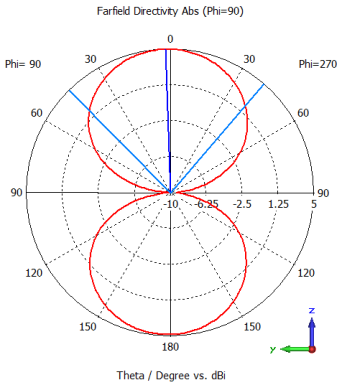

(f) Slot width 11mm, 2.3GHz, Phi=90°

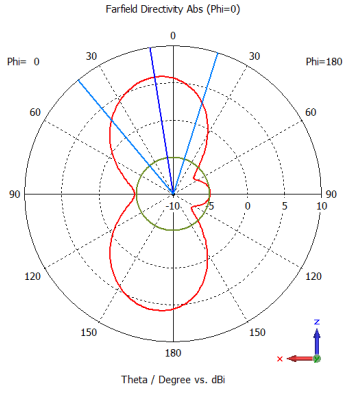

(g) Slot width 11mm, 3.4GHz, Phi=0°

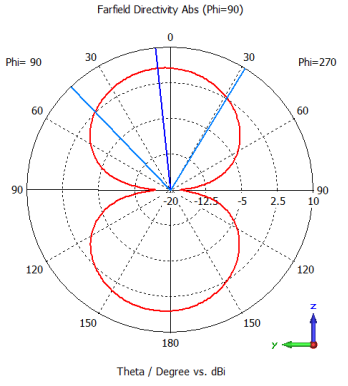

(h) Slot width 11mm, 3.4GHz, Phi=90°

Figure 6.16: Farfield Directivity patterns as a result of altering the lower ground plane slot width at 2.3GHz and 3.4GHz

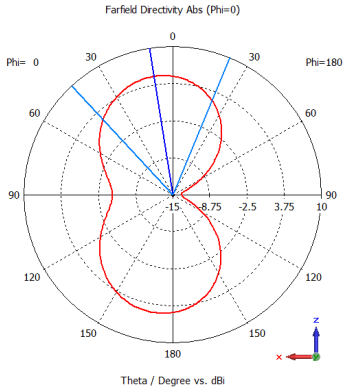

(i) Slot width 6mm, 2.3GHz, Phi=0°

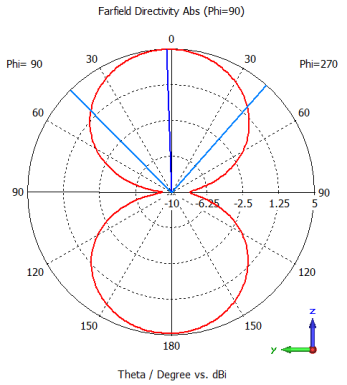

(j) Slot width 6mm, 2.3GHz, Phi=90°

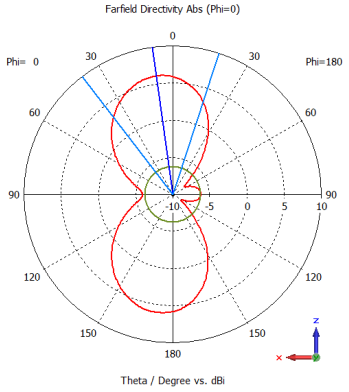

(k) Slot width 6mm, 3.4GHz, Phi=0°

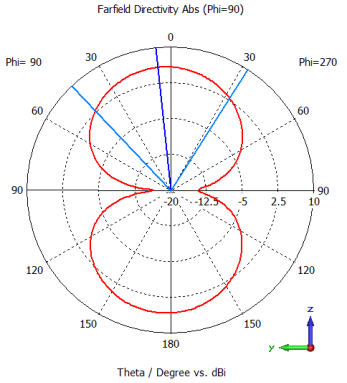

(l) Slot width 6mm, 3.4GHz, Phi=90°

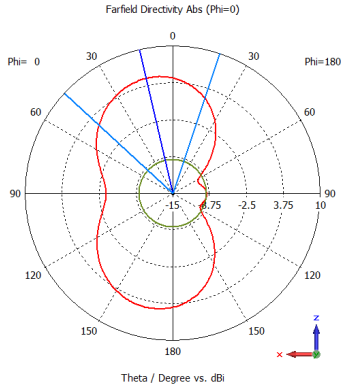

(m) Slot width 1mm, 2.3GHz, Phi=0°

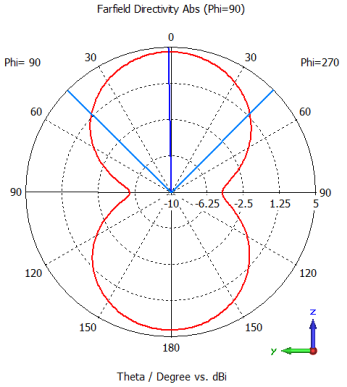

(n) Slot width 1mm, 2.3GHz, Phi=90°

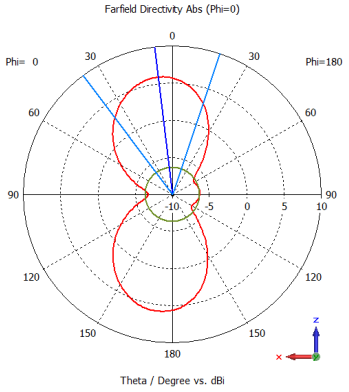

(o) Slot width 1mm, 3.4GHz, Phi=0°

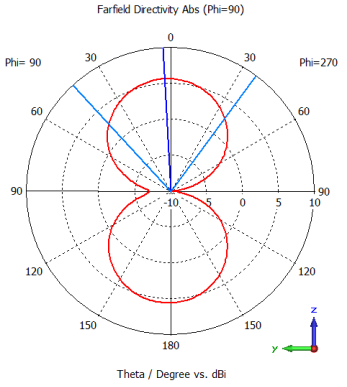

(p) Slot width 1mm, 3.4GHz, Phi=90°

Figure 6.16: Continued.

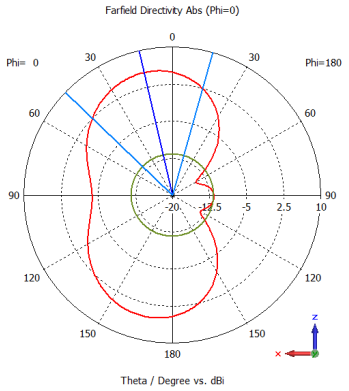

(a) tan δ = 0.0009, 2.6GHz, Phi=0°

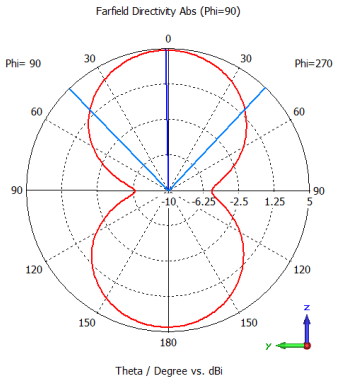

(b) tan δ = 0.0009, 2.6GHz, Phi=90°

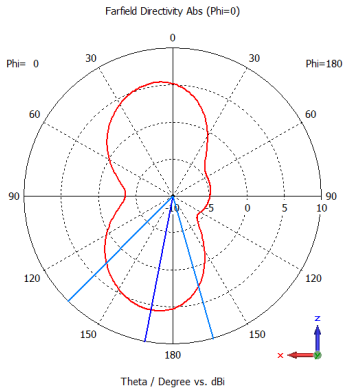

(c) tan δ = 0.0009, 3.7GHz, Phi=0°

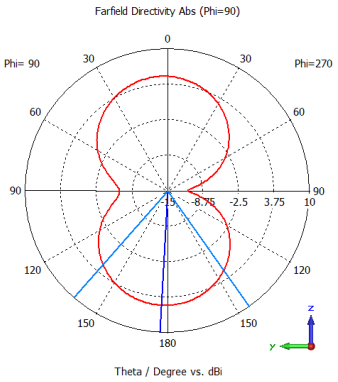

(d) tan δ = 0.0009, 3.7GHz, Phi=90°

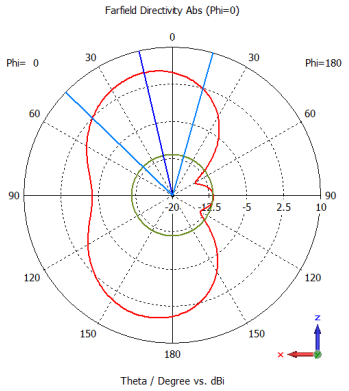

(e) tan δ = 0.009, 2.6GHz, Phi=0°

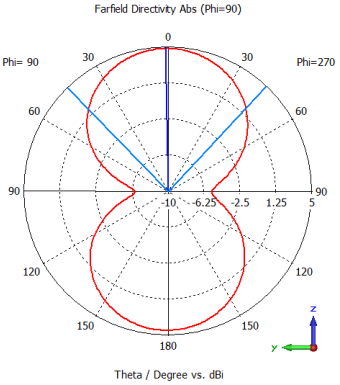

(f) tan δ = 0.009, 2.6GHz, Phi=90°

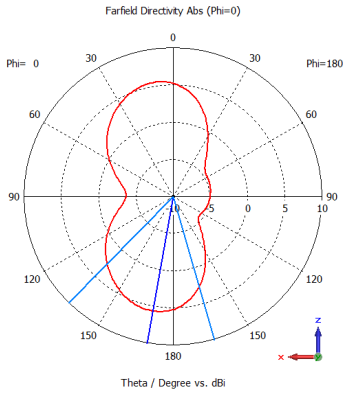

(g) tan δ = 0.009, 3.7GHz, Phi=0°

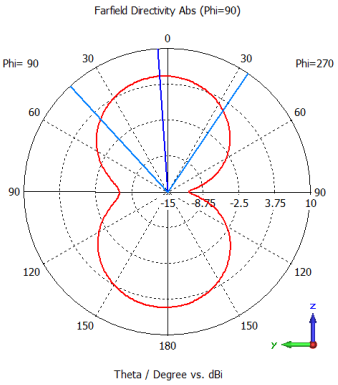

(h) tan δ = 0.009, 3.7GHz, Phi=90°

Figure 6.17: Farfield Directivity patterns as a result of substrate loss (tan δ)

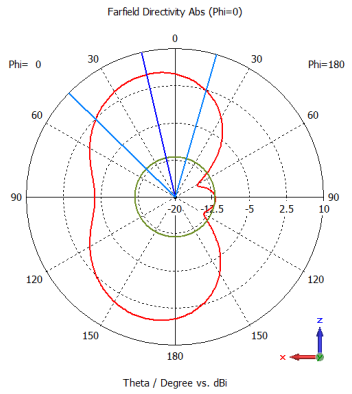

(i) tan $\delta = 0.09$, 2.6GHz, Phi=0°

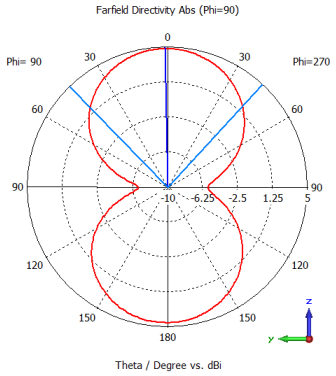

(j) tan $\delta = 0.09$, 2.6GHz, Phi=90°

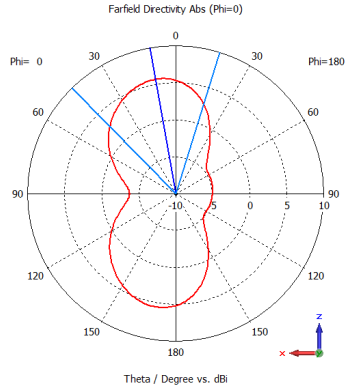

(k) tan $\delta = 0.09$, 3.7GHz, Phi=0°

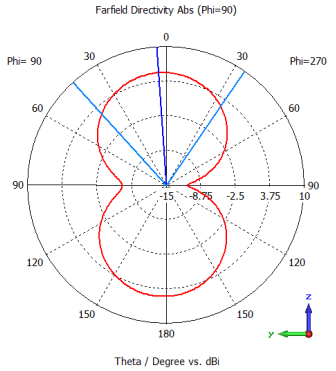

(l) tan $\delta = 0.09$, 3.7GHz, Phi=90°

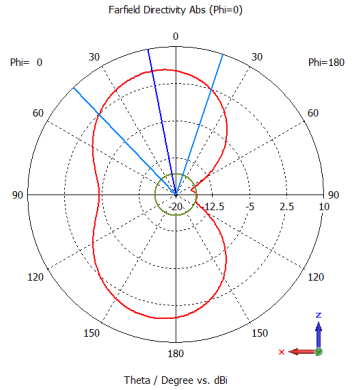

(m) tan $\delta = 0.9$, 2.6GHz, Phi=0°

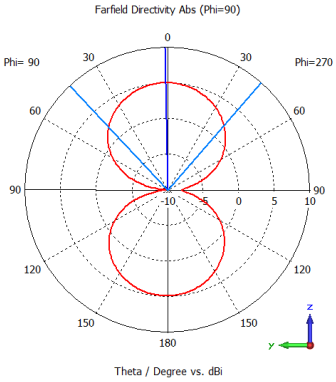

(n) tan $\delta = 0.9$, 2.6GHz, Phi=90°

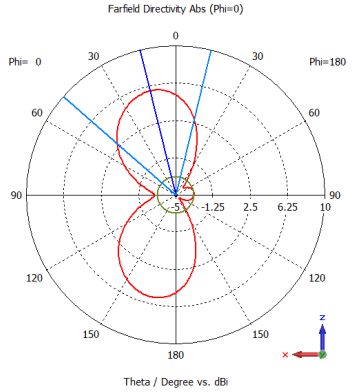

(o) tan $\delta = 0.9$, 3.7GHz, Phi=0°

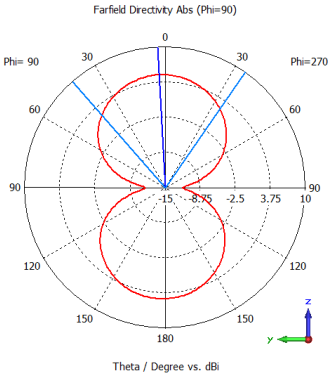

(p) tan $\delta = 0.9$, 3.7GHz, Phi=90°

Figure 6.17: Continued.

6.2 Conclusions

Simulation has indicated the possibility to create a fully integrated antenna-battery system in the microwave band, based on polymer battery material properties taken from the literature. By creating a structure that is wideband and shows reasonable gain and efficiency results even with relatively lossy substrates, close to that of a planar polymer battery, an antenna with reasonable efficiency can be designed.

Research into conducting polymers shows that we can still achieve high conductivities, which are not far off that of metals. This shows promise in terms of creating a non-metallic battery. Results showed that the antenna could maintain its performance down to a value of $5.8\text{x}10^2$ S/m, which covers a range of polymer electrolytes that possess conductivities around this value and higher.

By adding a second ground plane to the bottom of the structure, we were able to see how the antenna performed with two current collectors. Once again, good bandwidth values were obtained with slots cut into the bottom current collector. It was observed that the slot beneath the feed was necessary for the antenna to function, but a large proportion of the slot below the dipole could be taken away.

To simulate conditions as close as possible to an actual polymer battery, the substrate thickness was set to 0.3mm and given an ionic conductivity value of 10^{-3} S/cm. The relative permittivity (ε_r) of the electrolyte substrate was assumed to be 3. Good bandwidth and reasonable gain was obtained with values of 66% and 1.7dB respectively.

The farfield dependence on the width of the lower ground plane slot was assessed as well as the loss tangent (tan δ) value of the substrate. The trend for slot width showed that as it was reduced, the gain and total efficiency decreased as would be expected. Similarly, as the loss tangent was increased, a reduction in both gain and total efficiency occurred, with a drastic reduction in performance shown at a tan δ value of 0.9.

Chapter 7

Simulation and Measurements of an Ultra-thin Low-Profile Antenna operating at the Bluetooth Frequency

With the advent of new proximity location systems operating with Bluetooth links to smart phones, for instance the Tile tag [247], there is interest in creating extreme low-profile and integrated antenna-battery components for use at 2.45GHz. The battery and antenna are typically the bulkiest components in a transceiver system and it is therefore of interest to combine them and ideally use novel digital fabrication technologies to realise them using low-profile conducting polymer films.

Following on from the design principle of the antenna in Chapter 6, the intention was to develop an antenna with performance optimised on a better representation of a battery. Furthermore, with the majority of the work being simulations up to this point, it is important to perform some experimental measurements on a prototype design to validate the reliability of these simulations. With the previous work, a measurement had been conducted on an asymmetric antenna with a single conducting ground plane. Our intended design will consist of two ground planes, leading to a partially enclosed or sandwiched structure. Nagatomo's design [30] of solid state battery is used as the basis of the design process, with the intention of designing a battery similar to this, while also functioning as an antenna structure.

The previous antenna design will be modified, giving a smaller and much thinner structure. Printed electronics are highly desirable as a future fabrication process, and so an ultra-thin design will be pursued. One thing of high interest in this study, and dictated by the thin battery structure, is to assess the antenna performance with two conducting ground planes in close proximity to one another with only a very thin substrate between them. If it can be demonstrated that an antenna can still maintain good functionality, then our intended ultra-thin design will be a viable

one.

Another new consideration in this study is a target frequency range, particularly for our simulated systems. Much electronics have been developed specifically for the Bluetooth frequency range at 2.45GHz, and so this presents a good opportunity to tailor our antenna for a specific application. Home monitoring systems and wireless sensors are all potential uses for an ultra-thin portable antenna.

7.1 Methodology and Results

7.1.1 Integrated Antenna-Battery structure

Starting with the previous structure design (Chapter 6) [248], in which the antenna substrate was sandwiched between two ground planes, a new design was proposed. The new antenna design is a symmetric slot antenna cut into a conducting film, with an electrolyte substrate underneath, followed by a second conducting layer, also with slots present. The conducting films are used to represent the anode and cathode of a solid state battery. Furthermore, they will also act as the battery terminals, providing the electrical conductivity needed for the battery to function. Figure 7.1 shows the integrated antenna-battery design proposed.

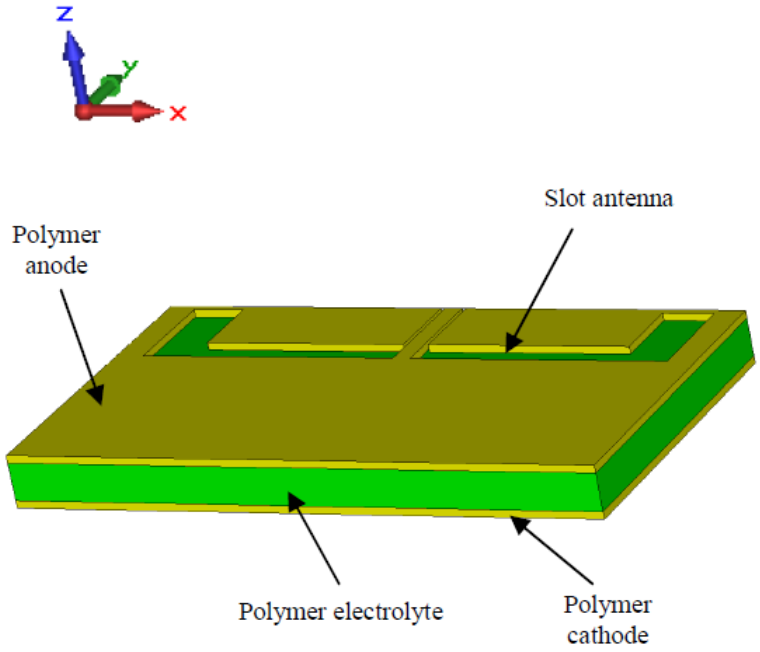

Figure 7.1: Integrated antenna-battery design for Bluetooth application

The CST Microwave Studio® package Transient Solver was used to perform the required simulations for this investigation. The slot dipole antenna consisted of two symmetric slots cut into an upper conducting plane. The antenna structure is derived from that of [248] (See Chapter 6), and is based on Nithisopa's CPW-fed

slot dipole [78], and redesigned for the 2.45GHz frequency band. The substrate had a thickness of 0.3mm, with a relative permittivity (ε_r) of 3.

Both the upper and lower ground planes had a thickness of 0.018mm and Figure 7.2 shows the structure geometry. The dipole slots in this particular structure were symmetrical, with a width and length (W1) and (L1), of 35mm and 4.1mm respectively. The end caps, or folded sections, on each slot were each of length (L2) and width (W2), 14.1mm and 7mm. The width of the feed slots (W3) was 0.5mm, with the gap between the two (W4) being 2.4mm. The CPW feed line for the antenna consisted of a length (L3) of 11mm. Slots were also present on the bottom ground plane with the slot beneath the coplanar wave guide feed of a length (L4) of 12mm and width (W5) of 16mm. The slot beneath the dipole was of a length (L5) 3mm and width (W6) 70mm.

The antenna itself had an overall width of 80mm with an overall length of 45mm. The substrate was initially simulated with a low-loss tan δ value of 0.0009. A conductivity value of 1000 S/m was applied to the two conducting planes as might be expected for a good conducting polymer electrolyte. Figure 7.2a and Figure 7.2b show the upper and lower plane views of the structure along with the associated length and width parameters. Figures 7.3a to 7.3c show the simulated S_{11} results, and the associated farfield results at 2.45GHz respectively.

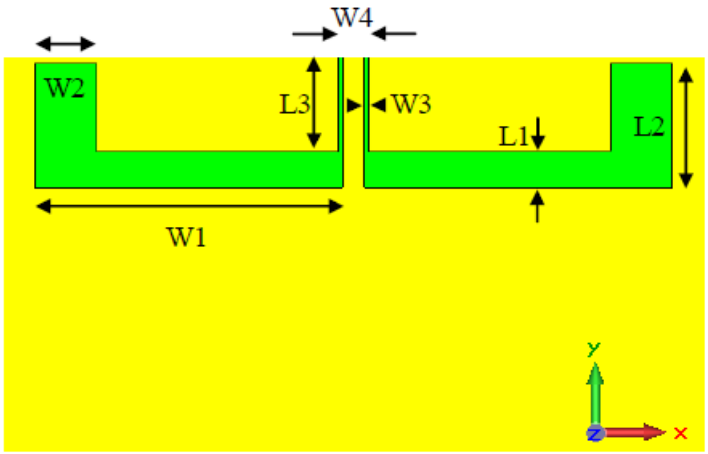

(a)

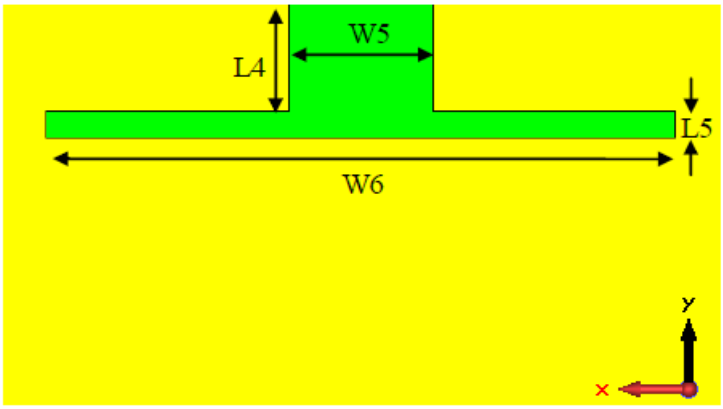

(b)

Figure 7.2: Dimensions for slot antenna, (a) top plane, and (b) bottom plane

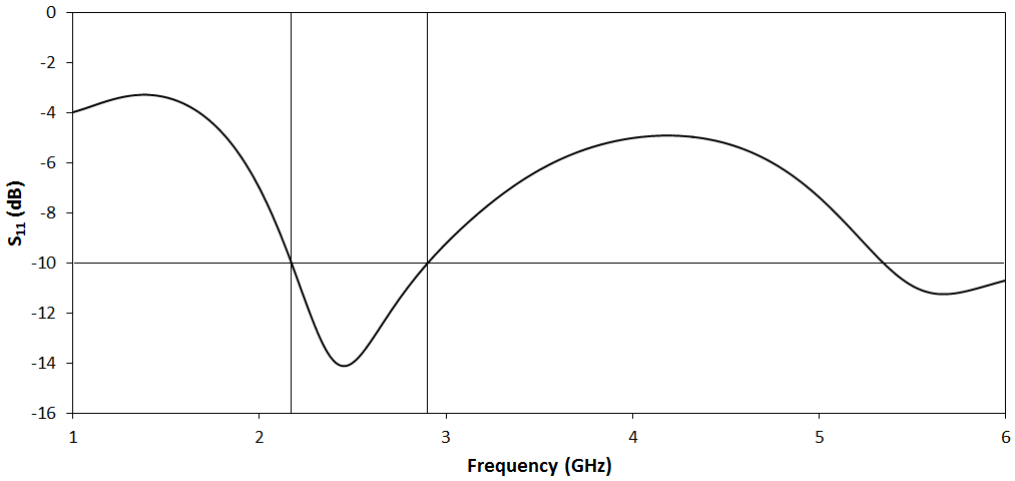

(a)

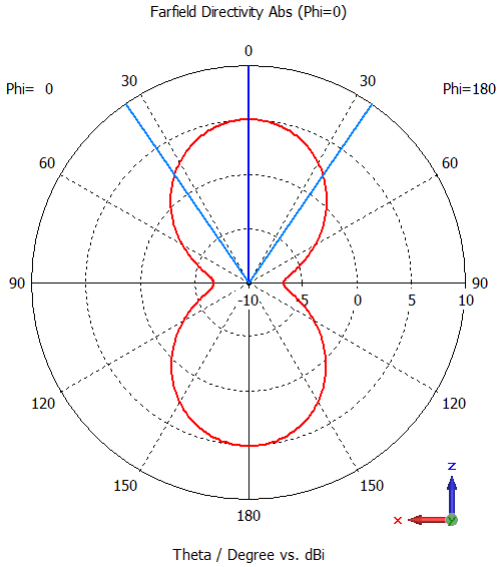

(b) Phi=0° as a variation of Theta

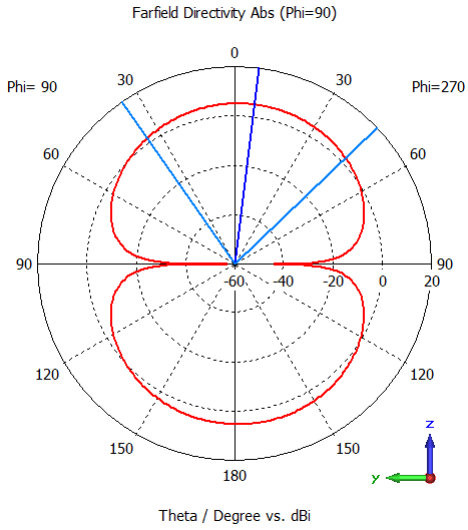

(c) Phi=90° as a variation of Theta

Figure 7.3: (a) Simulated S_{11}, (b) and (c) Simulated farfield Directivity at 2.45GHz

The matched operating band is indicated in the S_{11} results of Figure 7.3a. We can see that the structure is noticeably lossy with an out of band loss of about 4dB. However, with our low range application in mind, this is not a concern. The -10dB fractional bandwidth was calculated to be about 28%. The antenna radiation patterns in Figures 7.3b and 7.3c are those expected for a narrow slotted dipole and are symmetrical in the forwards and backwards direction because no mounting substrate is included in the simulation. The simulated total efficiency was -2.3dB with a gain of 2.8dB. This can be compared to the previous study in Section 6.1.7 [248] where efficiencies of about -2.2dB and gains of about 3.3dB at 2.6GHz were obtained.

The loss tangent (tan δ) of the substrate was then altered from 0.0009 to 0.9, as might be anticipated for a battery electrolyte. Here, although the directivity is unaffected, we observed a reduction in gain to 0.3dB because of a reduction in efficiency to -4.8dB. Once again, comparing this to the previous study in Section 6.1.7 [248] where an efficiency of -7.3dB at 2.6GHz was simulated for a loss tangent of 0.9, a noticeable improvement was achieved. Figure 7.4 shows the simulated S_{11} parameters and farfield results respectively for the antenna with a substrate dielectric loss tangent of 0.9.

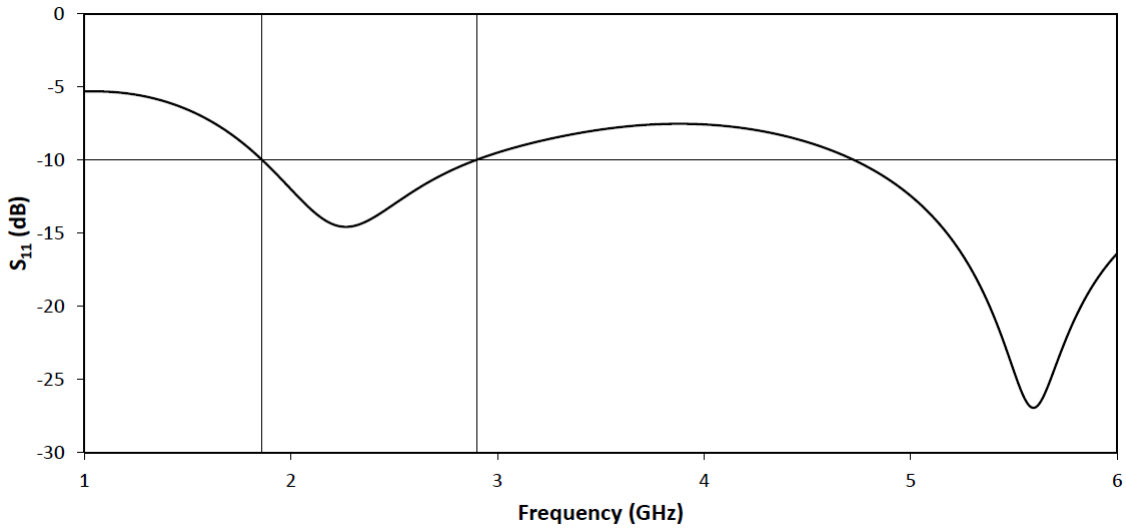

(a)

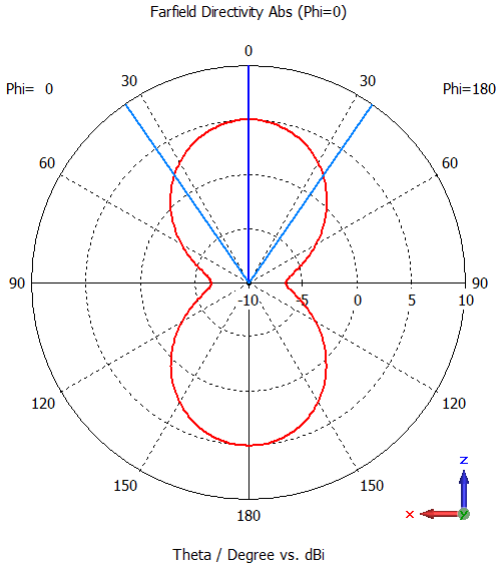

(b) Phi=0° as a variation of Theta

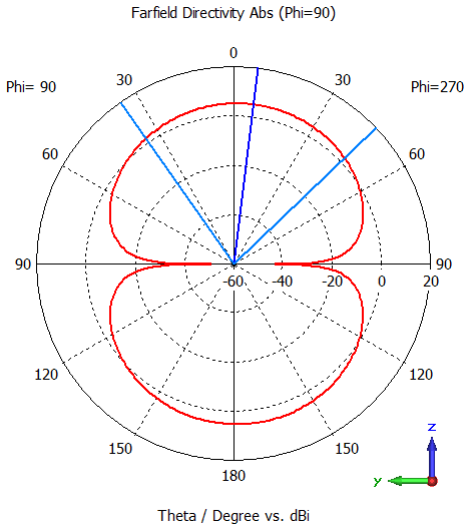

(c) Phi=90° as a variation of Theta

Figure 7.4: (a) Simulated S_{11} and (b), (c) Simulated farfield Directivity at 2.45GHz

Table 7.1 shows a summary of the results obtained from the initial structure of Figures 7.2 to 7.4 compared with the results obtained from the previous study in Section 6.1.7 [248].

Table 7.1: Effect of loss tangent of substrate upon bandwidth, gain and efficiency

tan δ	Fractional bandwidth (%)	Gain (dB) (Figs. 7.2-7.4)	Efficiency (dB) (Figs. 7.2-7.4)	Gain (dB) [248]	Efficiency (dB) [248]
0.0009	28	2.8	-2.3	3.3	-2.2
0.9	44	0.3	-4.8	-1.8	-7.3

7.1.2 Dielectric loading

The low-profile slotted design is affected by dielectric loading when mounted on structures. It is expected that potential applications of our antenna will involve mounting on several different structures and surfaces i.e. walls, plastic. Therefore, it is important to ascertain the overall effect that certain surfaces will have upon the performance of the antenna and whether it will retain a good degree of functionality. A simulated investigation was carried out to ascertain how the antenna match and efficiency were altered when the antenna-battery was placed on a dielectric block of relative permittivity (ε_r) 2.3 and tan δ 0.09. With no specific surface at this stage, this is an initial investigation into how dielectric loading will affect the structure, with the intention of testing the antenna on specific surfaces both by simulation and experiment.

The antenna bandwidth and efficiency underwent a change upon dielectric loading and a few adjustments were made to the antenna in order to allow it to function again at 2.45GHz. The width of the antenna was reduced from 80mm to 75mm, while the width of the slots (W6) beneath the dipole were reduced from 70mm to 55mm. The substrate material parameters were kept constant with the tan δ at 0.9. Figure 7.5 shows the amended material parameters of the antenna along with how it was loaded onto a dielectric material in the simulation.

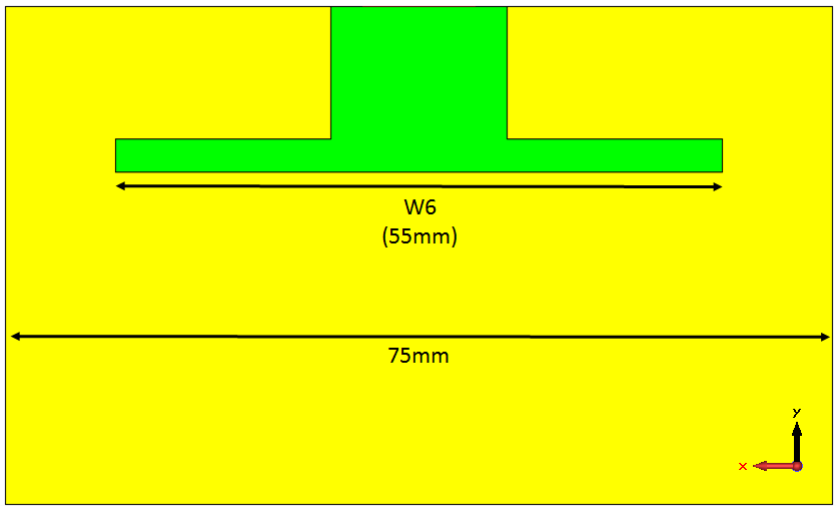

(a)

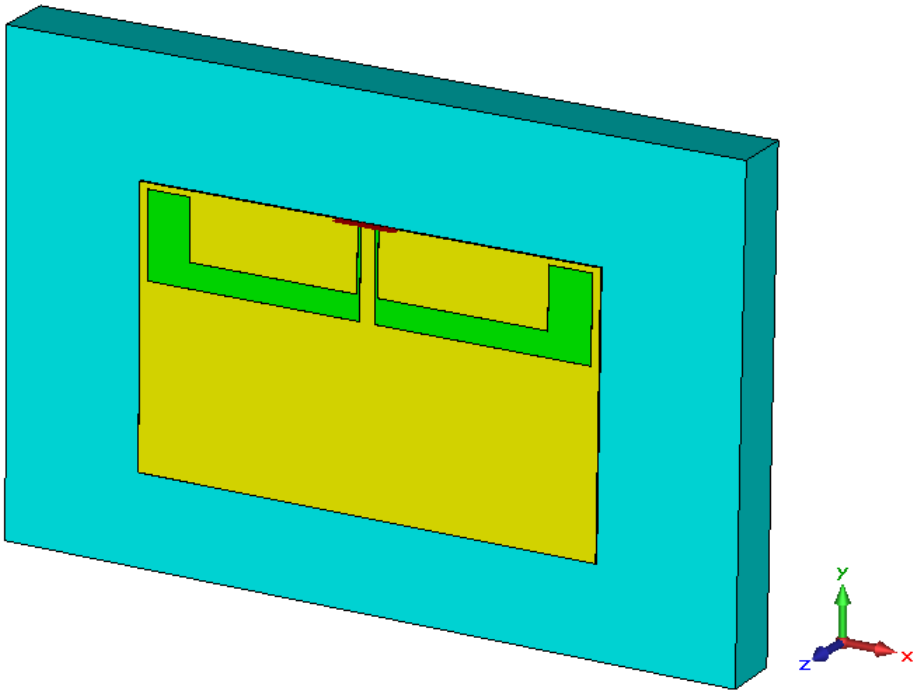

(b)

Figure 7.5: (a) Bottom plane of new structure showing altered dimensions and (b) antenna mounted onto dielectric block

When mounted onto the dielectric block with the altered dimensions, a fractional bandwidth of 55% was observed, with an efficiency of -6.3dB and a gain of -1.7dB. This still gives a slight improvement in gain and efficiencies compared to the results shown in Section 6.1.7 [248], in which the structure was not mounted onto any dielectric material. Figure 7.6 shows the S_{11} and farfield results for this antenna mounted onto the dielectric block. We notice that the presence of the dielectric block has introduced a degree of asymmetry to the radiated beams.

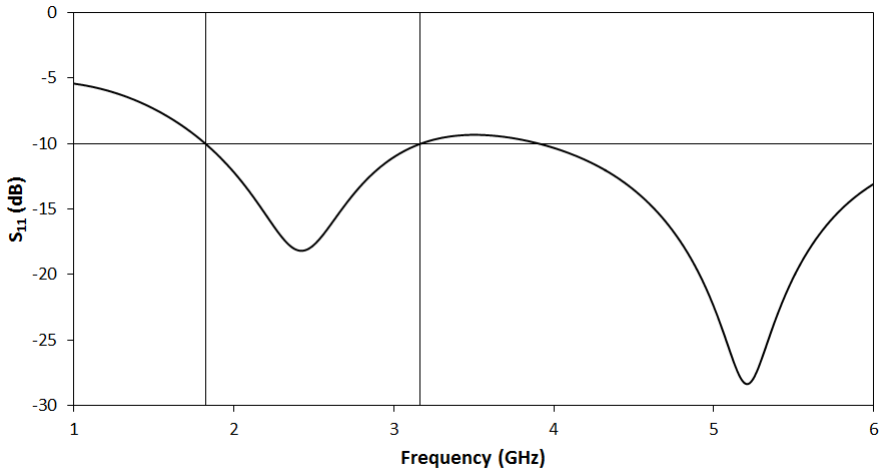

(a)

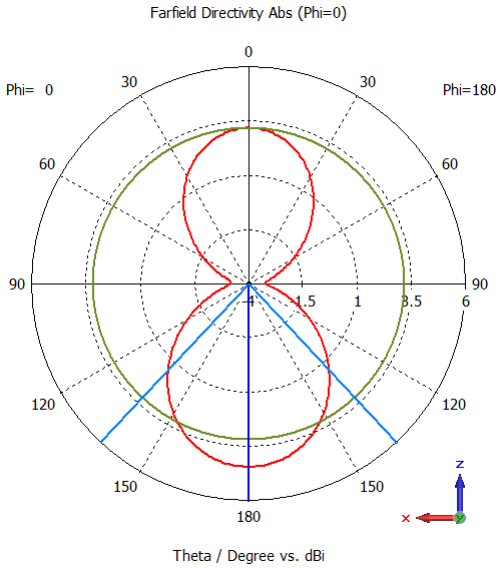

(b) Phi=0° as a variation of Theta

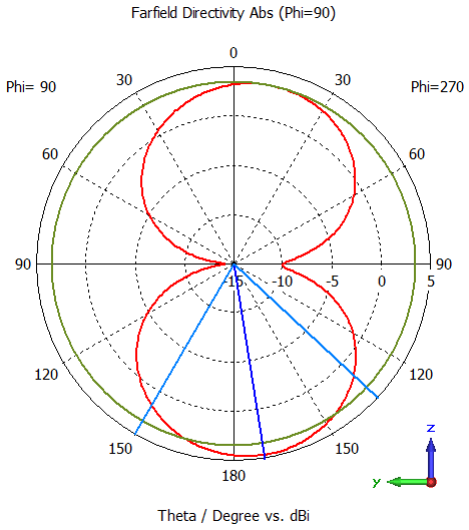

(c) Phi=90° as a variation of Theta

Figure 7.6: (a) Simulated S_{11} and (b), (c) Simulated farfield Directivity at 2.45GHz for antenna mounted onto a dielectric block

With these results considered, it does appear to be possible to create a functioning antenna that can be loaded onto a dielectric material, albeit with a loss of efficiency. By optimising the structure or material that we use, we can create a design that not only mirrors a battery, but also offers potentially useful antenna efficiency and bandwidth. It is interesting to observe how antenna performance will change, particularly with substrate parameters associated with battery materials, and that when mounted on representative battery materials, the thin antenna offers gain values which compare favourably with those of existing mobile technology.

7.1.3 Sample measurement

It was desirable to create a sample of material as would be used in the polymer battery to form an electrode. A pellet of PEDOT:PSS, a highly conductive polymer electrolyte, was synthesised for this purpose. The dimensions of the pellet were a width of 25mm and a thickness of 3mm [167]. The chemical structure and appearance of PEDOT:PSS is shown in Figure 7.7.

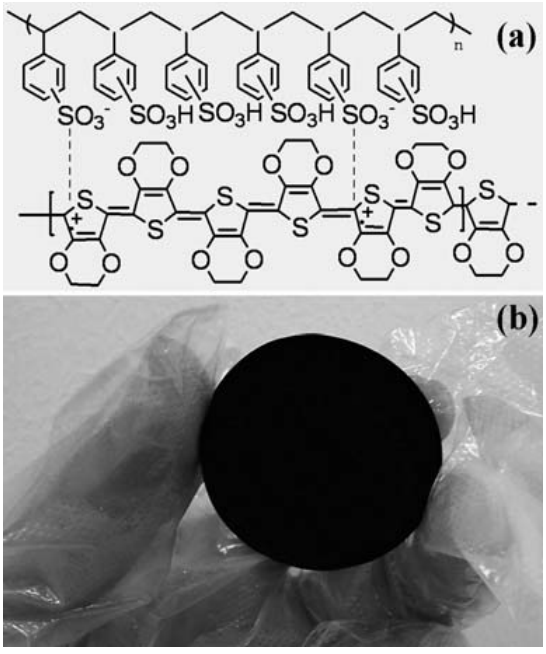

Figure 7.7: (a) Structure of PEDOT:PSS and (b) an example of a PEDOT:PSS aerogel pellet [249]

The permittivity of the PEDOT:PSS sample was measured by placing a Coplanar Waveguide (CPW) track on top of the material and calculating the phase constant and effective permittivity of the line directly from the S_{21} measurement, since it was well matched to 50Ω [167]. Using the approximation that the effective permittivity of a CPW is the average of the air and dielectric region allowed a figure of $\varepsilon_r = 4.3$ and $\tan\delta = 0.13$ for the relative permittivity and loss tangent to be obtained.

These measured material values were applied to the antenna-battery substrate and simulated. The underlying dielectric material was still present and remained

unchanged. The permittivity (ε_r) of the antenna substrate was increased from 3 to 4.3, while the tan δ value of 0.9 was reduced to 0.13. The main observations were a reduction in bandwidth from 55% to 44%, which is to be expected when decreasing the loss tangent. More importantly, an improvement in efficiency with a value of -4.63dB was observed, with an increase in gain to 0.02dB. Figure 7.8 shows the S_{11} and farfield results for the structure simulated with the experimental parameters. Table 7.2 gives a summary of the comparison of simulation results for the antenna mounted onto the dielectric block with both the initial assumptions and the results obtained from the experimental data.

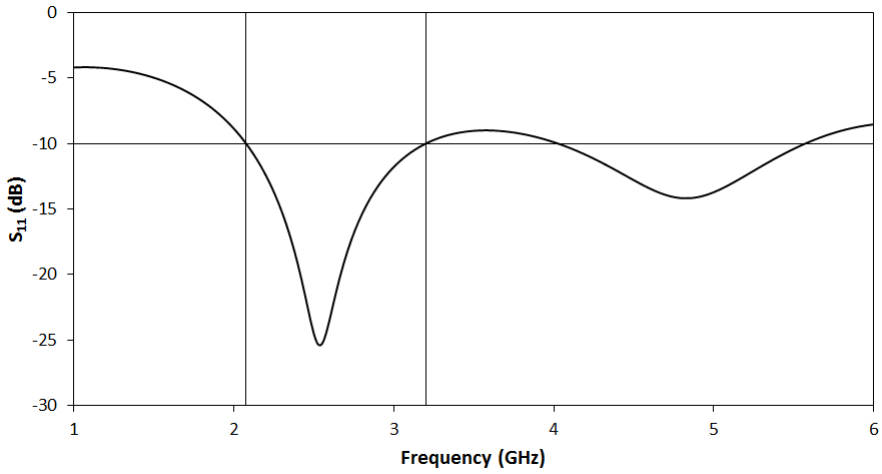

(a)

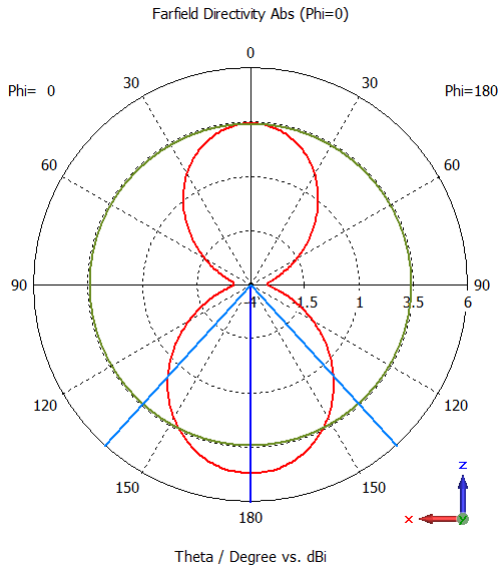

(b) Phi=0° as a variation of Theta

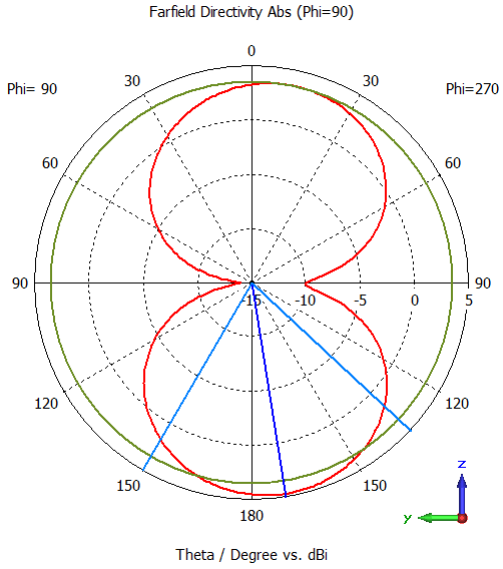

(c) Phi=90° as a variation of Theta

Figure 7.8: (a) Simulated S_{11} and (b), (c) Simulated farfield Directivity at 2.45GHz for antenna with the measured PEDOT-PSS dielectric properties

Table 7.2: Comparison of initial assumptions for antenna with PEDOT:PSS parameters (obtained from measurement) in the presence of dielectric material

Permittivity (ε_r)	tan δ	Bandwidth (%)	Gain (dB)	Efficiency (dB)
3	0.9	55	-1.7	-6.3
4.3	0.13	44	0.02	-4.6

The results show an overall improvement in performance using the experimental parameters for PEDOT:PSS obtained through measurement. This suggests that PEDOT:PSS may be a useful candidate material to use for our antenna-battery. In order to investigate the possibility of an integrated structure further, it is important to perform some experimental measurements on a design similar to our system of interest, to gauge whether our simulated results will match.

7.1.4 Measurements

In order to assess the reliability of our simulations, it is necessary to perform some experimental measurements. The first step in this study was to observe whether an antenna with two copper ground planes could still function, despite being very close together due to an ultra-thin substrate. For this purpose, a double-sided copper clad film with a Mylar substrate in the middle was chosen. The Mylar substrate has a thickness of 0.045mm. The permittivity (ε_r) of the Mylar was 3.2, and it had a loss tangent (δ) value of 0.005. It should be noted that the dimensions of the antenna from Figure 7.2 were used for this study, as opposed to the slightly altered dimensions in Figure 7.5, due to the fact the earlier antenna design was optimised to function at 2.45GHz in free space. Figure 7.9 shows the antenna fabricated.

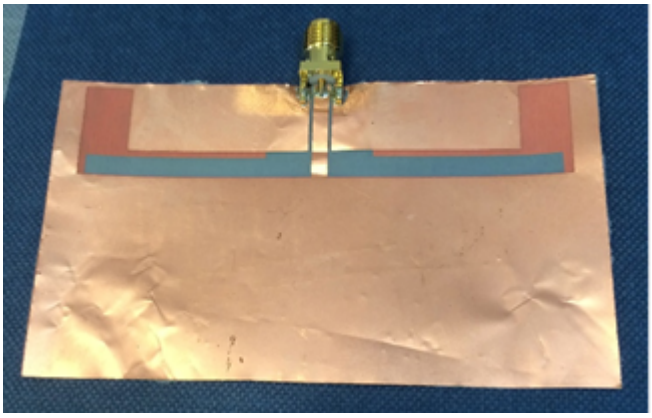

Figure 7.9: A photo of the fabricated Mylar antenna used in this study

The antenna with a Mylar substrate was both simulated and measured first of all, in free space, with S_{11} parameters and farfield patterns obtained in each case. This was to ensure that we could get a good match between simulation and experiment before any further tests were conducted. Figure 7.10 shows the experimental setup for the synthesised antenna in the anechoic chamber, where measurements for the radiation patterns took place. Figure 7.11a shows the simulated and measured S_{11} parameters for the antenna in free space, while Figure 7.11b shows the simulated and measured farfield patterns, also in free space.

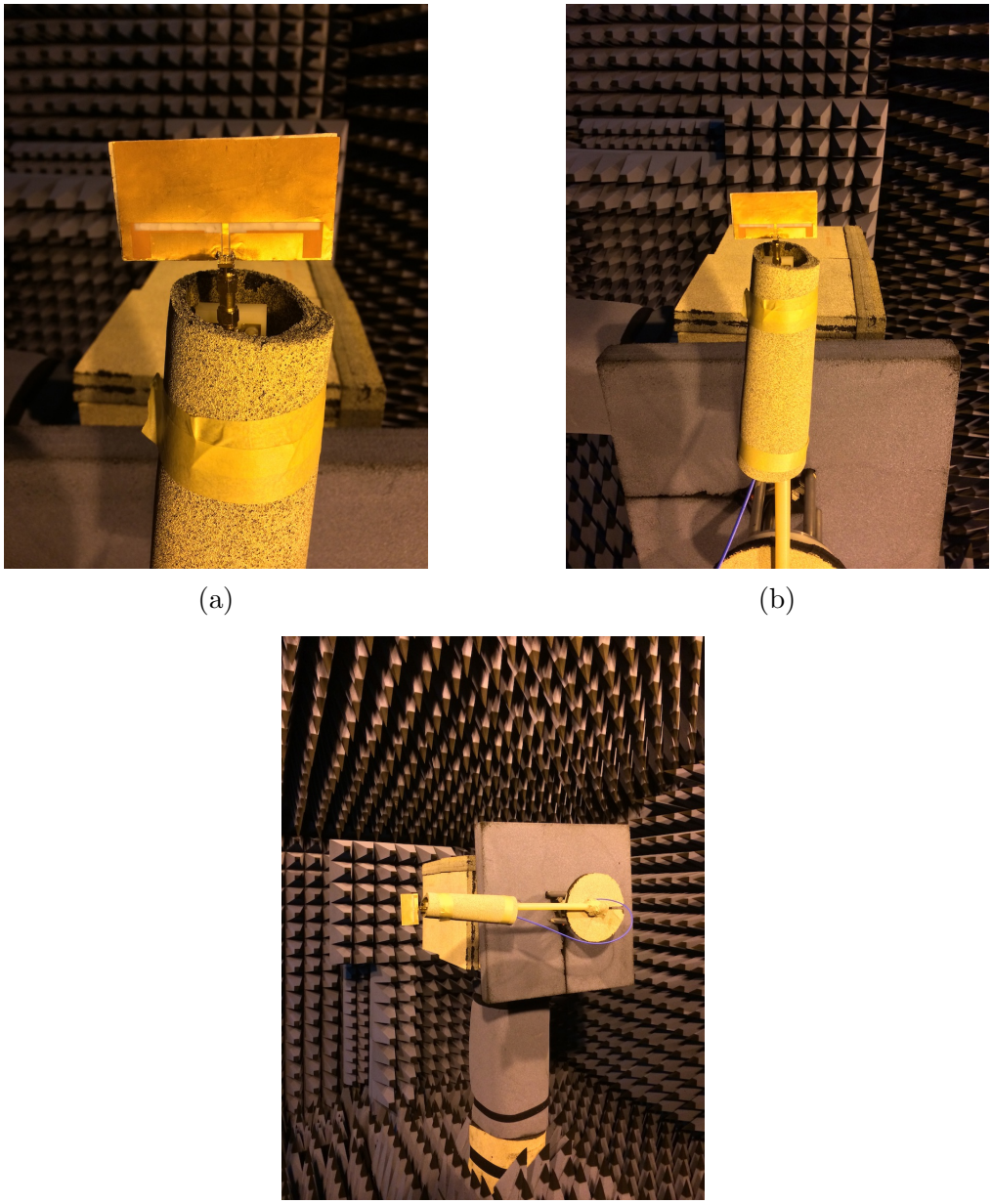

(a) (b)

(c)

Figure 7.10: Experimental setup of the antenna in the anechoic chamber

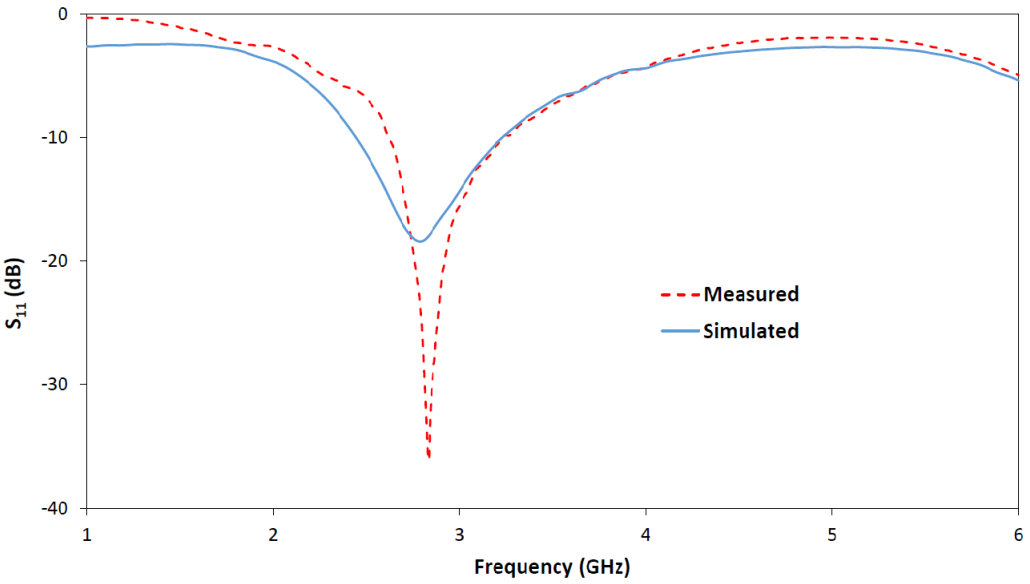

(a)

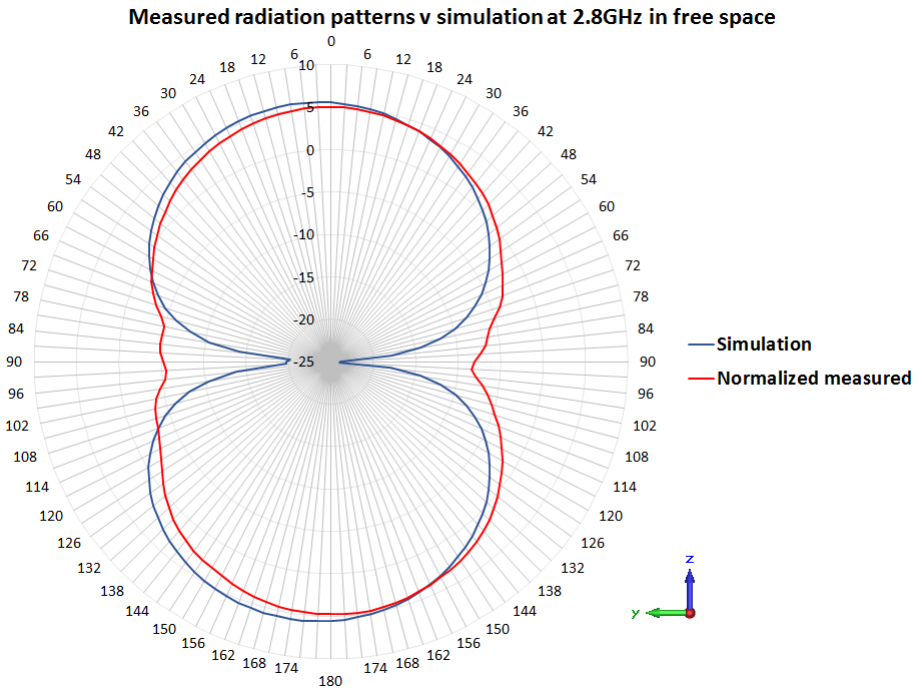

(b)

Figure 7.11: (a) Simulated and measured S_{11} and (b) Simulated and measured farfield Directivity patterns at 2.8GHz for antenna with a Mylar substrate (Phi=90°).

Key points to note here are a slight shift in the resonant frequency to around 2.8GHz, with a percentage error of 12.5% compared to the original frequency of 2.45GHz. This is caused by the Mylar film (which was not present in the initial simulations in Section 7.1.1) and is not a concern in this instance. What is apparent is that for both the S_{11} parameters and farfield patterns, the simulated and measured results show a good match with each other. This suggests that the simulations are accurate. The fractional bandwidth calculated for the simulation was 28%, while

the measured results gave a value of 22%. The gain and total efficiency was obtained for the simulation in this case with values of 5.3dB and -0.40dB respectively. What is most interesting about these results is that they demonstrate that an antenna can still function well with two conducting copper ground planes close together, with only a separation of 0.045mm between them. Having worked in free space, it is of interest to investigate the structure undergoing dielectric loading.

The next stage involved mounting the antenna onto a variety of different surfaces, with differing dielectric properties. The surfaces tested were MDF, PVC, copper and human flesh. Figure 7.12 shows the antenna being tested on each of these surfaces.

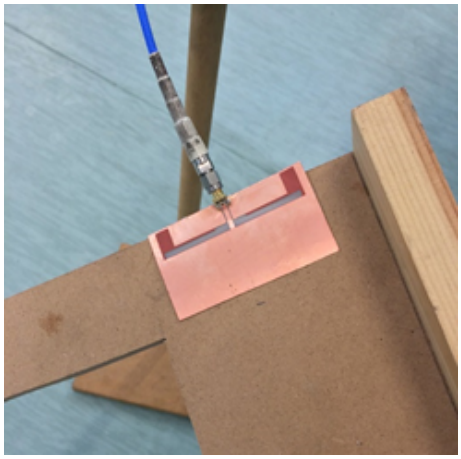

(a) MDF

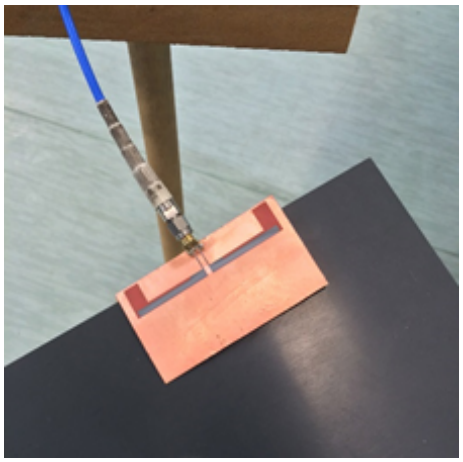

(b) PVC

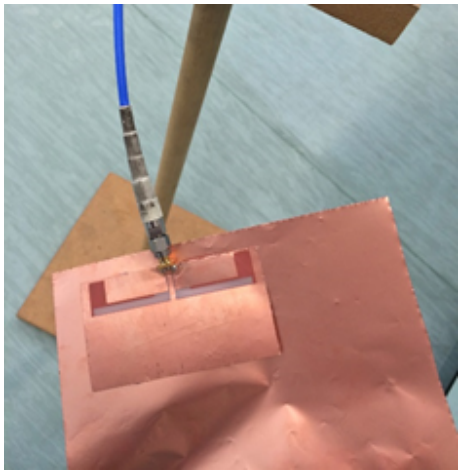

(c) Copper

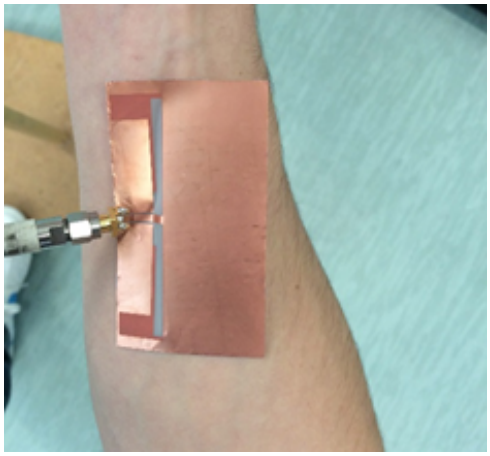

(d) Human flesh

Figure 7.12: Antenna mounted on different surfaces.

In each situation, the antenna was mounted both directly onto the material of choice as well as 2.3mm above it. In order to create this 2.3mm separation, a polystyrene layer was used. The polystyrene layer was cut to ensure it had the same overall dimensions as the antenna (80×45mm), and had a thickness of 2.3mm. Figure 7.13 shows the polystyrene layer used in this instance, attached to the back of an antenna. The main intention here is to observe how much effect the material has upon the antenna performance with regards to proximity, and more importantly,

whether we see a match between simulation and experiment. The relative permittivity of expanded polystyrene is approximately 1, making it appear as air to an electromagnetic field.

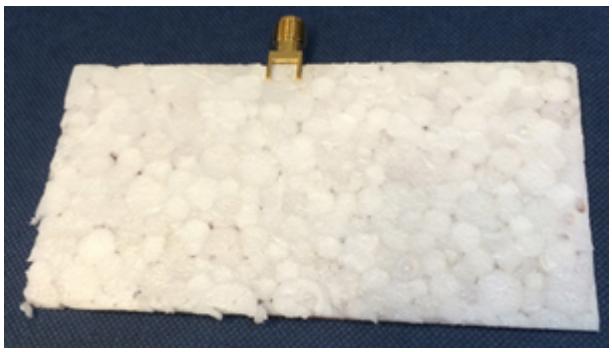

Figure 7.13: A photo of the polystyrene layer

MDF

Medium-density fibreboard or MDF, is a common wooden material in everyday use, which makes it an interesting surface to test our antenna on. While a permittivity can be assumed for the material we are analysing, simulations can help us deduce a value which is more accurate in that it gives us a good match between the simulated and measured S_{11} parameters. With tan δ values that can start around 0.023 [250] for certain MDF samples, in this case, a value of 0.02 was chosen as an initial assumption. Figure 7.14 shows the simulated and measured S_{11} results both for a 2.3mm separation between the antenna and the surface, and with direct mounting on the surface. Figure 7.15 shows the simulated farfield results in each of these cases.

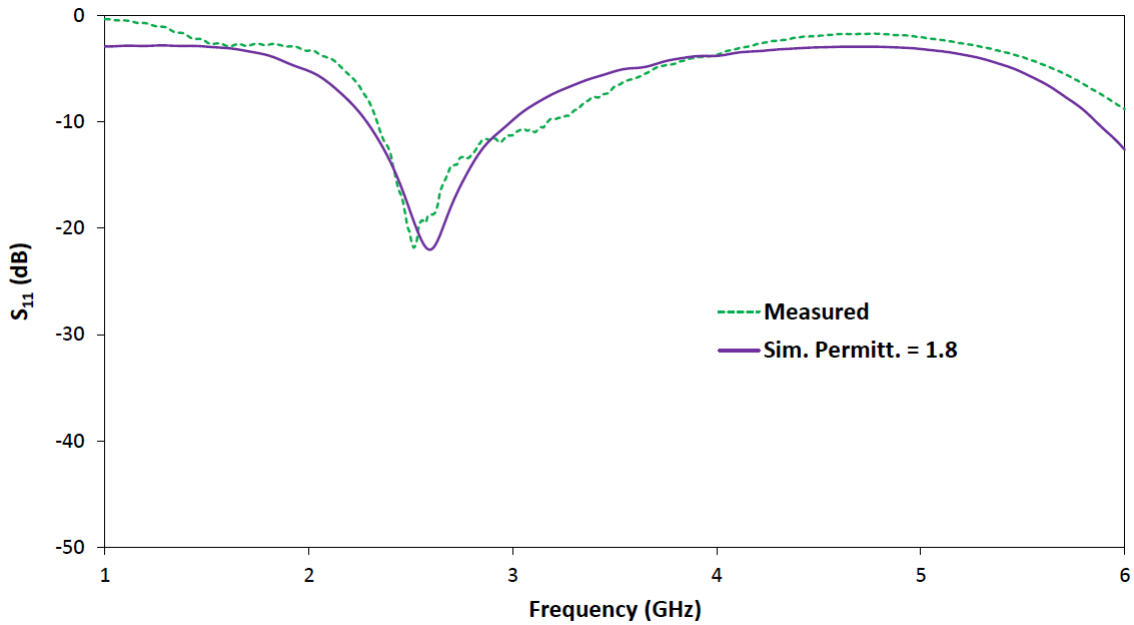

(a) Antenna mounted 2.3mm above MDF

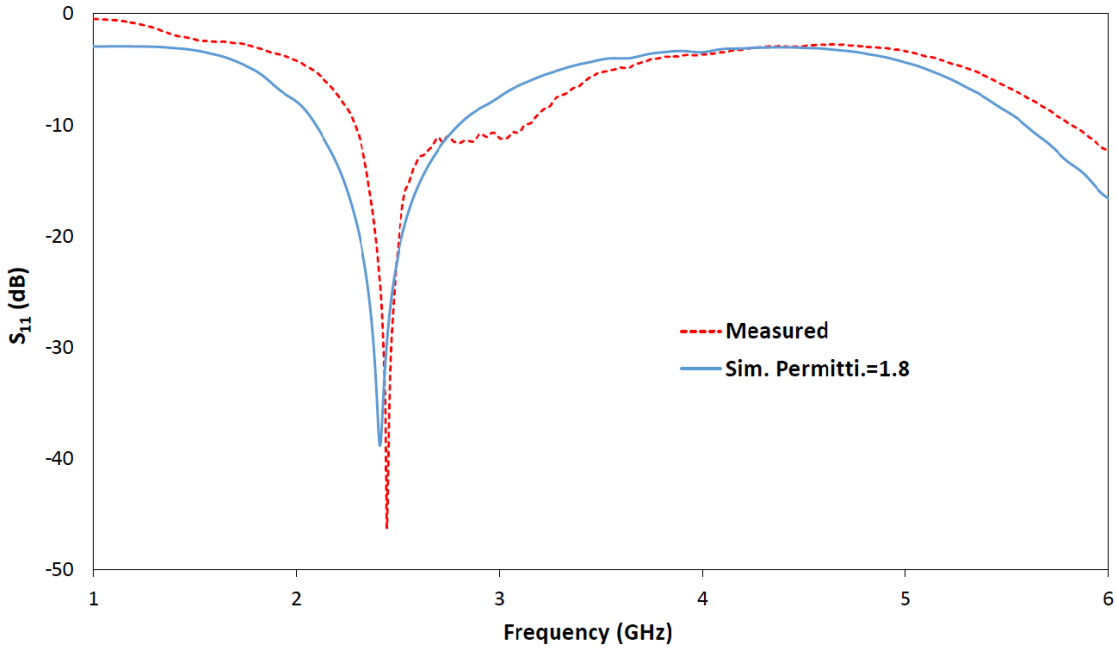

(b) Antenna directly mounted on MDF

Figure 7.14: Simulated and measured S_{11} for the antenna on MDF

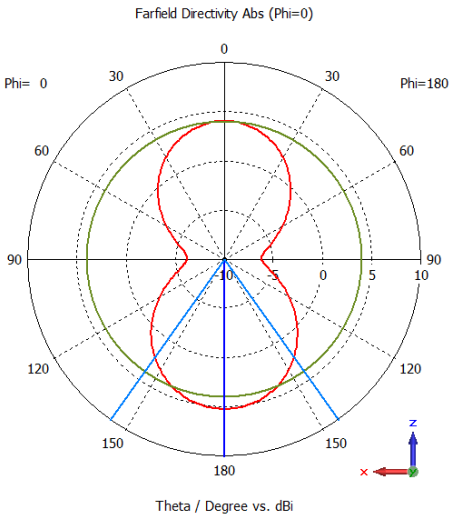

(a) 2.3mm above MDF, Phi=0°

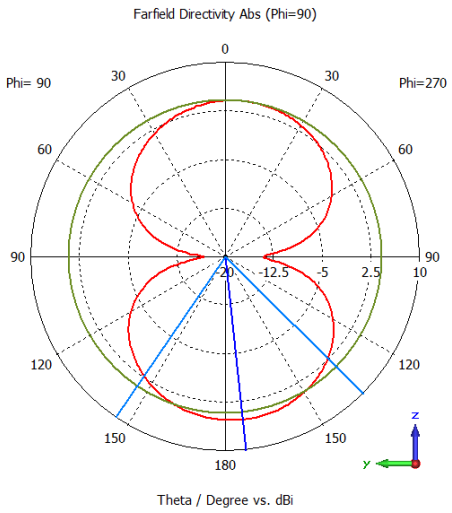

(b) 2.3mm above MDF, Phi=90°

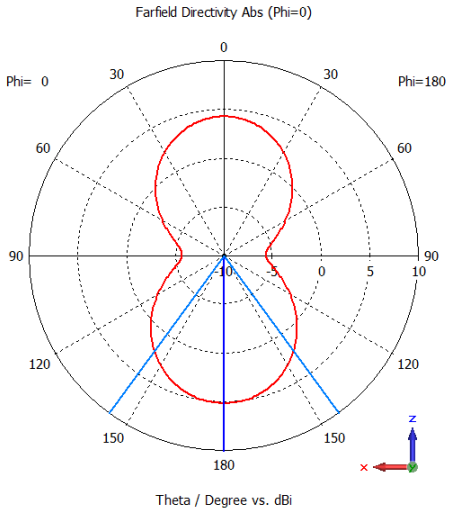

(c) Directly on MDF, Phi=0°

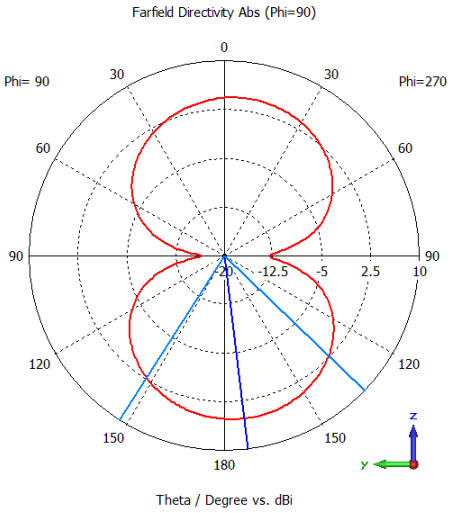

(d) Directly on MDF, Phi=90°

Figure 7.15: Simulated Directivities for the antenna mounted on MDF

Firstly, what we can deduce from the S_{11} results is that in both cases, we get a good match between simulation and experiment. Using the measured results, and comparing them to simulations, the relative permittivity of the material (ε_r), in this case MDF, was determined to be about 1.8. This was confirmed from getting a good match in both of scenarios tested. From the simulated farfield patterns, a gain of 4.65dB and an efficiency of -0.77dB was obtained when the antenna was mounted 2.3mm above the MDF surface. A gain of 4.37dB and efficiency of -0.8dB was obtained when the antenna was mounted directly onto the material. It is expected that as the antenna is in closer contact with the underlying dielectric material, the gain and efficiency will be reduced. However, these simulated values suggested that they may be usable in certain applications.

PVC

Polyvinyl chloride, or PVC, is another commonly used material, with many applications. As antennas are likely to come into contact with plastics such as this, it is useful to assess how our fabricated design performs, compared to simulations. Once again, a relative permittivity was deduced using simulations and comparing to the measured results. It is known that the loss tangent decreases noticeably at higher frequencies [251], dropping to around 0.05 as the frequency reaches up to the 100kHz mark. Therefore, it is assumed that at around 2.45GHz, the tan δ value will be relatively low-loss. A value of 0.0005 was chosen in this case, simply as an initial value for a low-loss substrate. The antenna was again measured 2.3mm above the PVC surface using a polystyrene layer for the measurements, and then mounted directly onto the surface. Figure 7.16 shows the measured and simulated S_{11} results in both cases, while Figure 7.17 shows the farfield patterns.

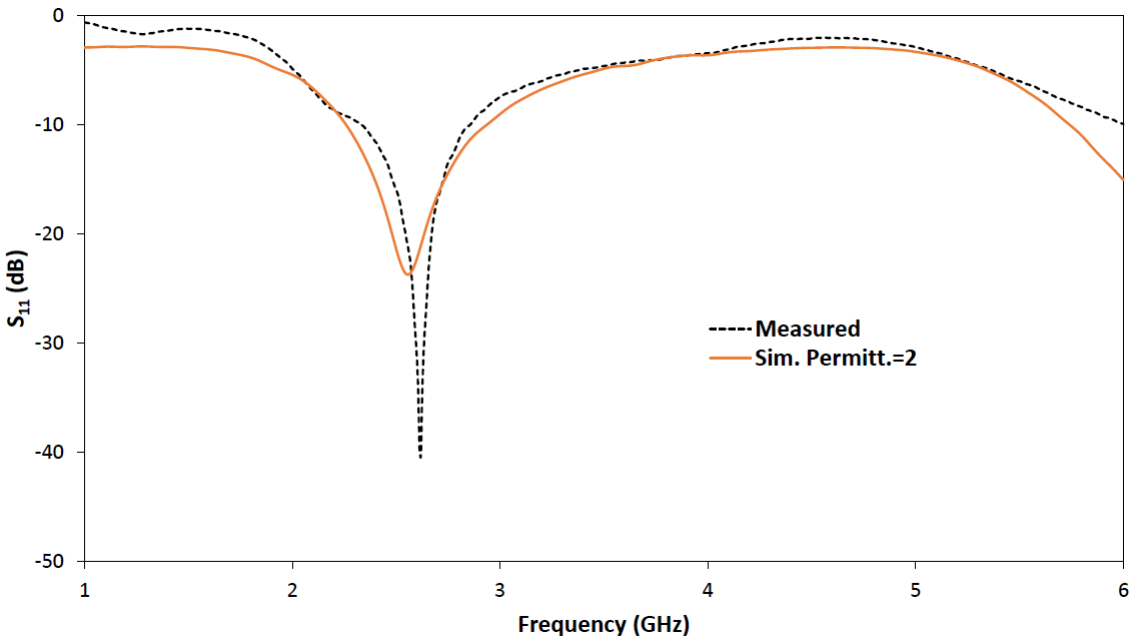

(a) Antenna mounted 2.3mm above PVC

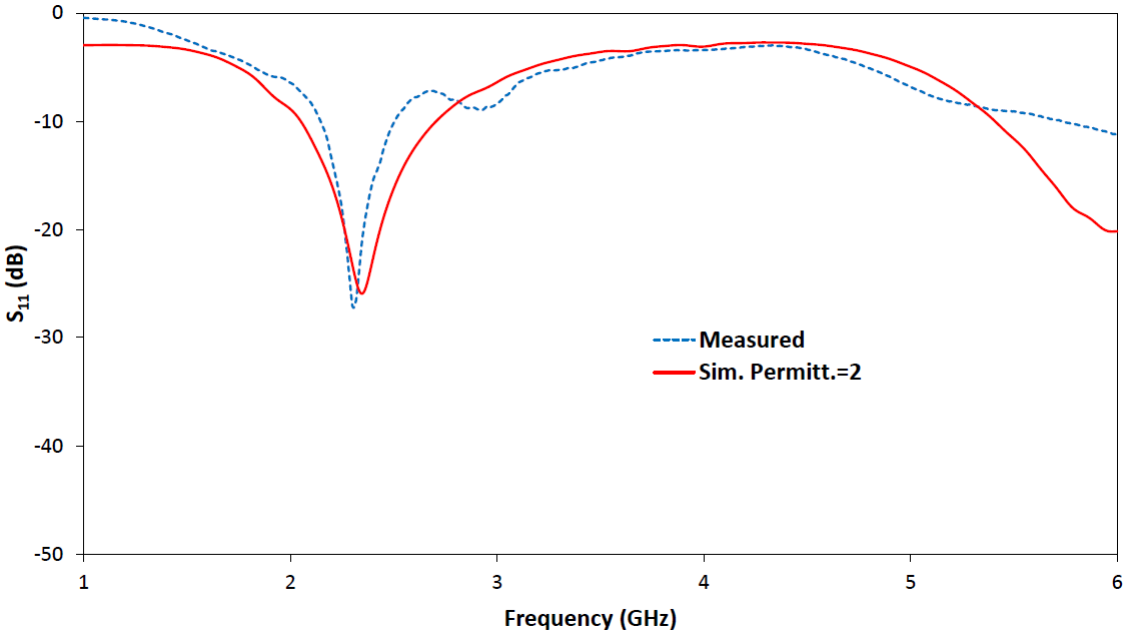

(b) Antenna directly mounted on PVC

Figure 7.16: Simulated and measured S_{11} for the antenna on PVC

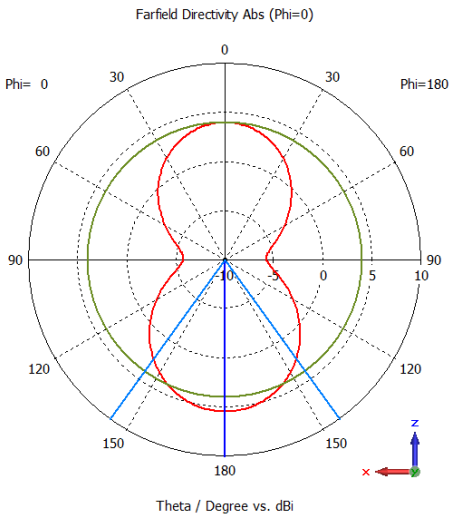

(a) 2.3mm above PVC, Phi=0°

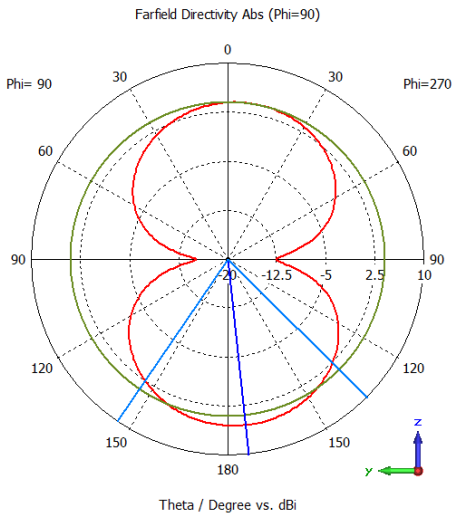

(b) 2.3mm above PVC, Phi=90°

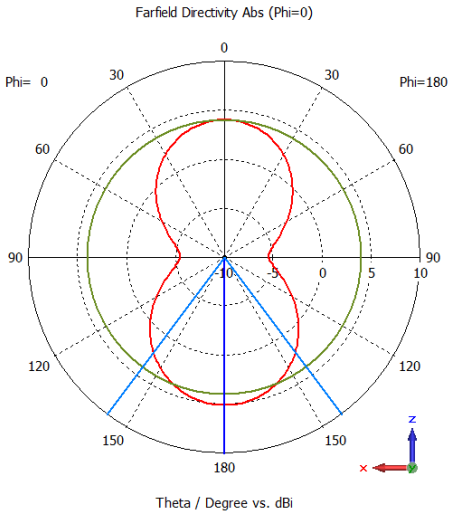

(c) Directly on PVC, Phi=0°

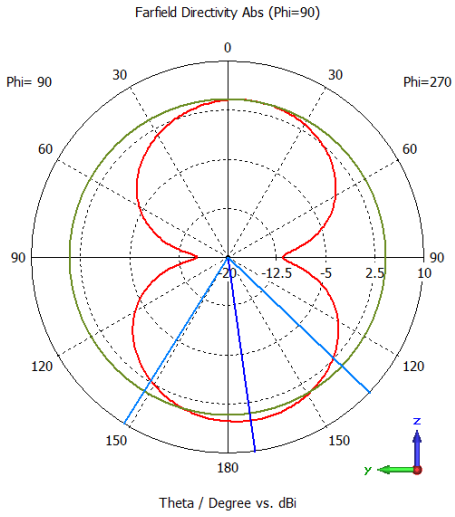

(d) Directly on PVC, Phi=90°

Figure 7.17: Simulated Directivities for the antenna mounted on PVC

Again, we see a good match between simulation and experiment in both of the scenarios. By comparing simulations to experiments, the relative permittivity (ε_r) was determined as 2 for the sample of PVC tested. The simulated farfield patterns showed a gain of 4.82dB and efficiency of -0.64dB when the antenna was mounted 2.3mm above the PVC surface. When mounted directly onto the material, a gain of 4.57dB and efficiency of -0.6dB was observed.

Copper

The antenna was then mounted onto bulk copper. It is expected that unlike the previous materials, copper will cause a significant degradation in the antenna performance. Despite this, a comparison was still made with the simulation. As the material parameters for copper were already stored in the CST database, there was no need to make any assumptions with regards to the material parameters. Figure 7.18 shows the simulated and measured results obtained both with a 2.3mm

separation and direct mounting on the copper surface.

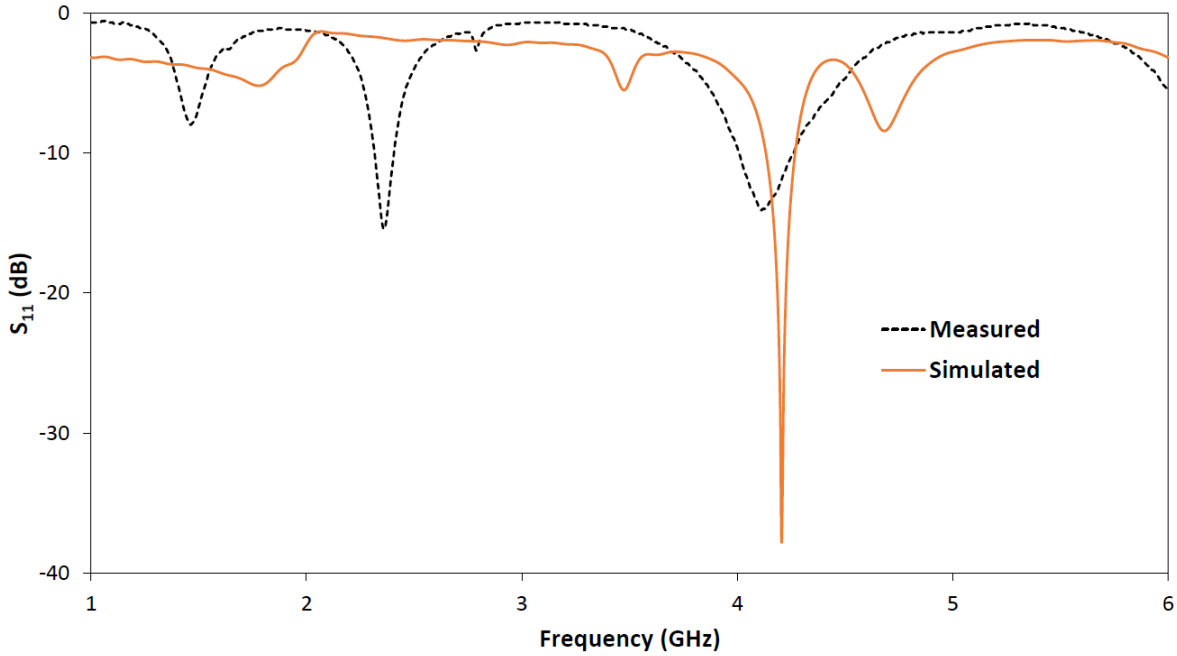

(a) Antenna mounted 2.3mm above copper film

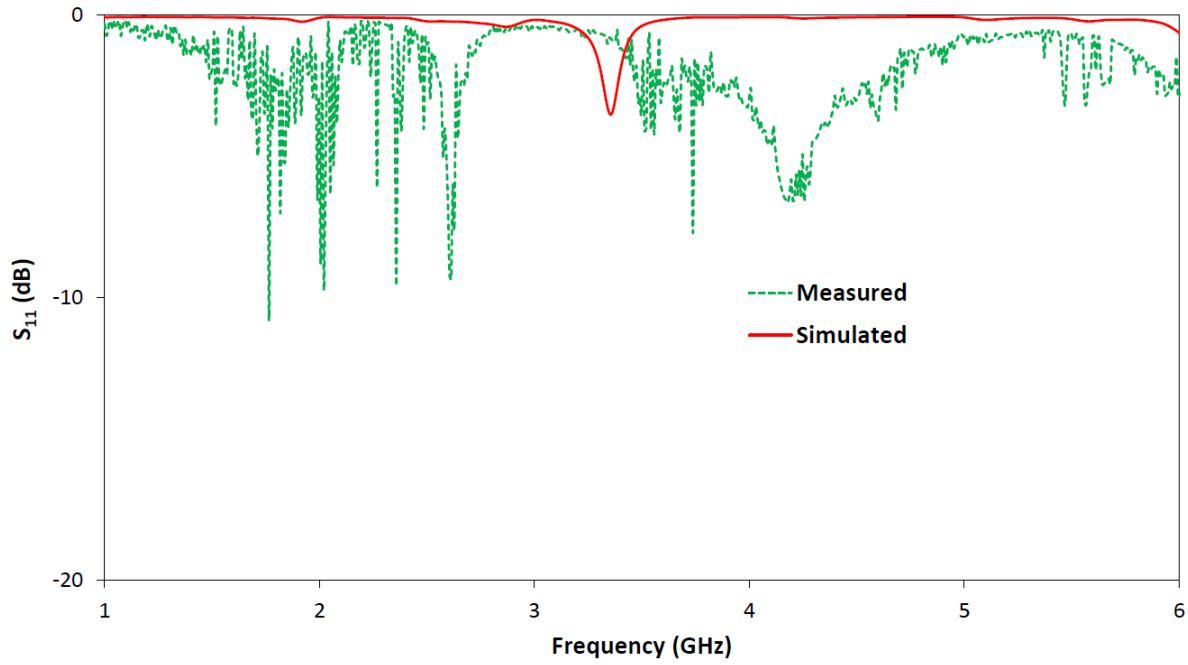

(b) Antenna directly mounted on copper film

Figure 7.18: Simulated and measured S_{11} for the antenna on copper

As expected, the copper caused a degradation with regards to the antenna performance. This was particularly noticeable when the antenna was in direct contact with the copper film. This made it difficult to give a good comparison between simulation and measurements. With a 2.3mm separation, a null was observed at around 4.2GHz for both measurement and simulation. It was noted that we achieved a match in the measurement at the operating frequency of 2.45GHz. This was not

observed for the simulation with the pattern as a whole giving a poor match. With direct mounting on the copper surface, it is clear that the antenna S_{11} is completely degraded, with no grounds for comparison with the simulated result.

This result was ultimately expected, and can be related back to the overall aim of this research. It is known that the antenna performance is affected in the presence of proximal metal planes, with the result here confirming this. Hence, it is clear that there is a requirement for a non-metallic battery in our intended antenna-battery design in order for the antenna to function well.

Flesh

Another test was to see how the antenna behaved when mounted on human flesh. There is increasing interest in having antennas placed directly onto the skin and even as tattoos [252]. Therefore to design an antenna that can perform in this environment is desirable. However, it can be difficult to predict antenna performance on skin, due to a variety of factors e.g. increased muscle mass and moisture content. Based on an application used to calculate the dielectric properties of body tissues in the frequency range 10Hz-100GHz [253], the dielectric constant of dry skin at 2.4GHz was calculated to be 38.063 with a predicted loss tangent of 0.2835. These values were input into the simulation with the intention of comparing to the S_{11} measurements.

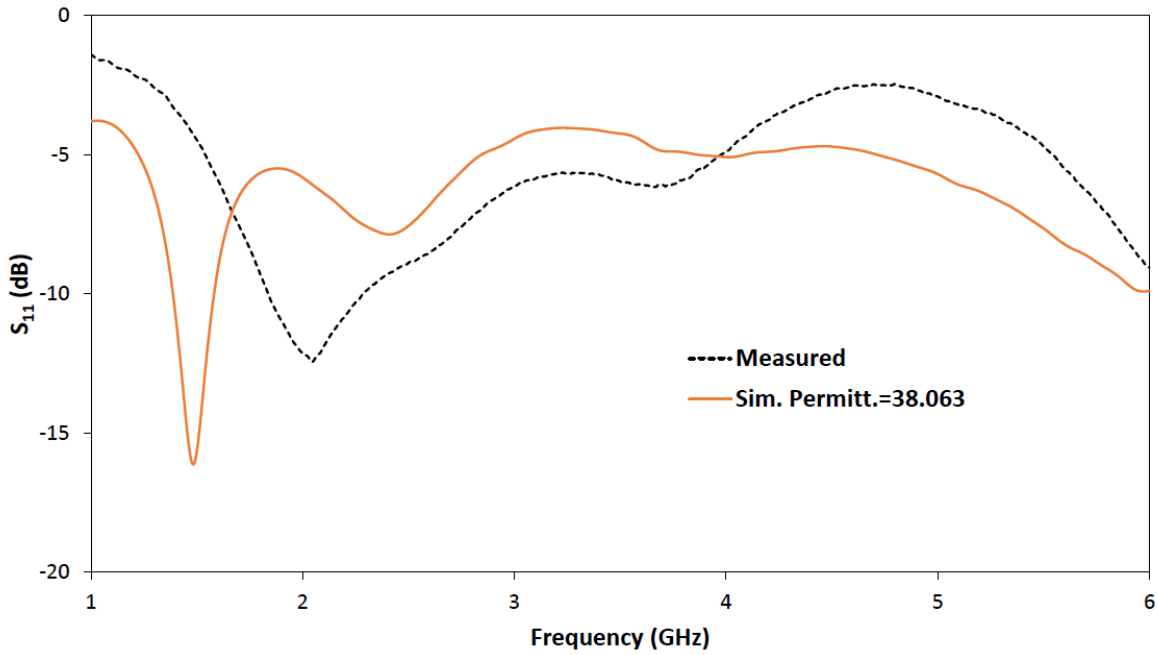

(a) Antenna mounted 2.3mm above human skin

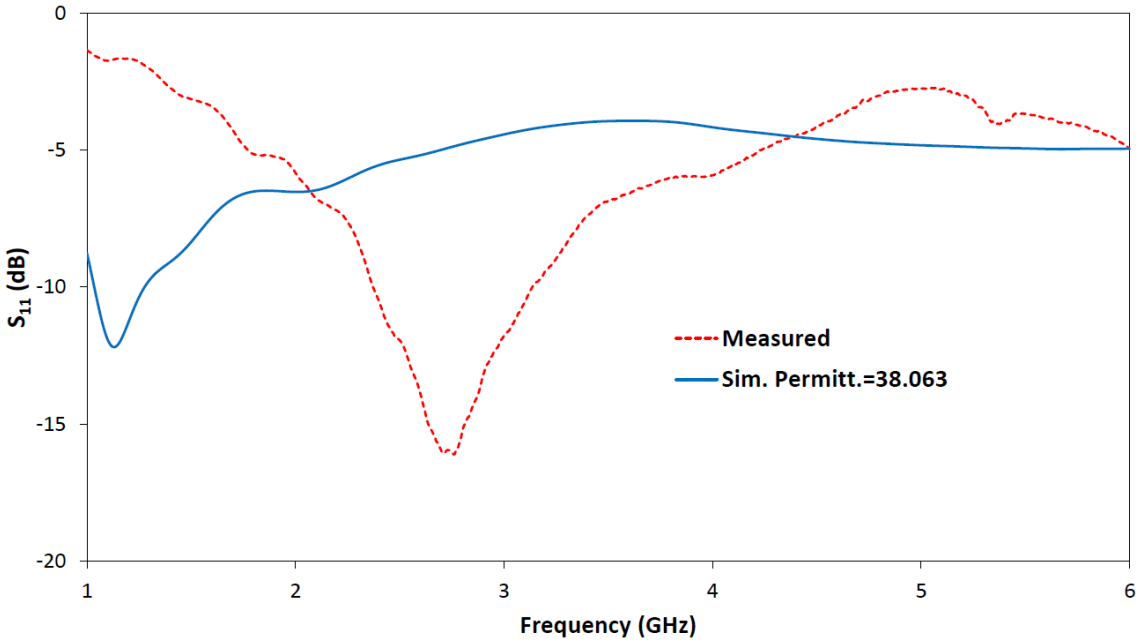

(b) Antenna directly mounted on human skin

Figure 7.19: Simulated and measured S_{11} for the antenna on skin with dry skin dielectric constant values

As can be seen from Figure 7.19, the simulated results do not match well with the measurements. This suggests that the initial dielectric parameters used for the simulations are not accurate. It is difficult to predict precise dielectric properties for a given individual for flesh due to several variables. To observe whether a better match could be obtained, the dielectric constant was altered in the simulations to values of 34 and 20, to see how the S_{11} changed, and whether we could get a better idea as to the dielectric parameters of the skin tested in this instance. Figure 7.20

shows the simulated results for these altered dielectric constant values compared with the measurements in each case, with a polystyrene layer and direct mounting on the surface of the skin.

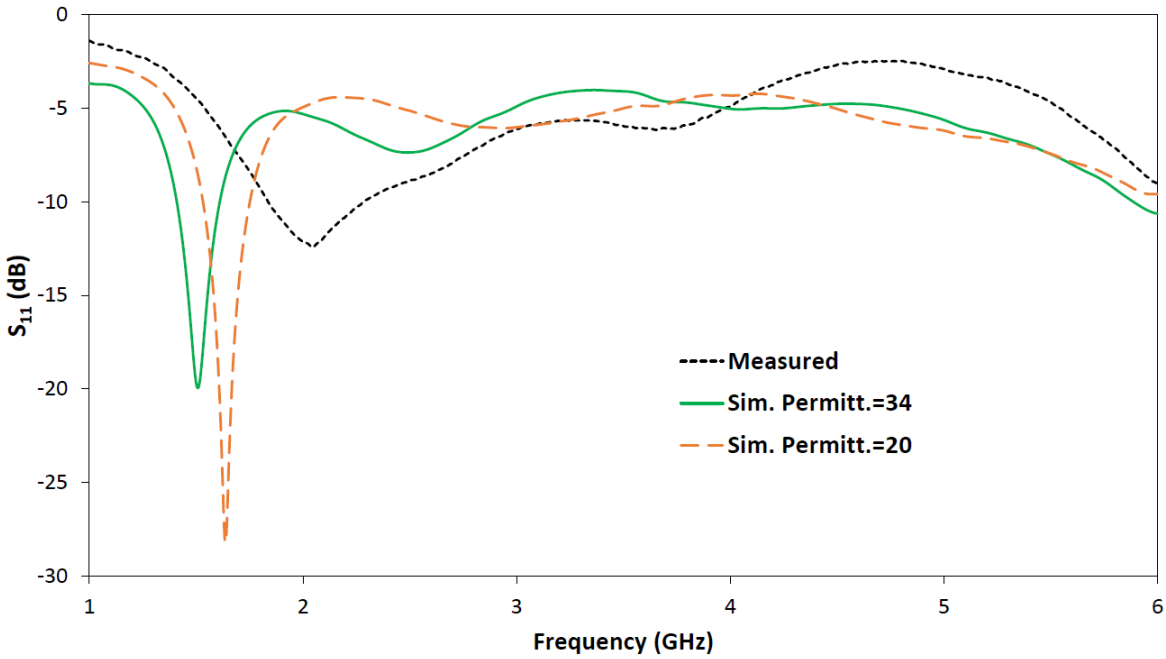

(a) Antenna mounted 2.3mm above human skin

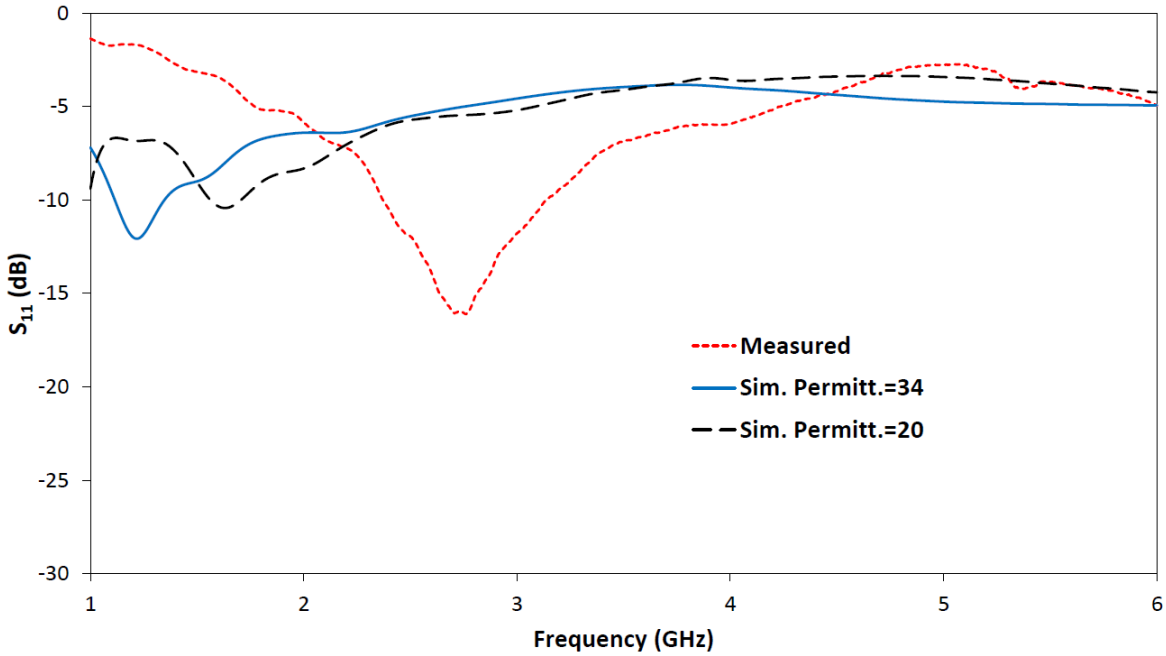

(b) Antenna directly mounted on human skin

Figure 7.20: Simulated and measured S_{11} for the antenna on skin, using altered dielectric constant values

Despite the change in permittivity, the S_{11} simulations still do not match with the experiments in either case. It should be noted, however, that as the permittivity was reduced, there was a slight shift in resonant frequency, towards the measured peak. This was not pursued further at this stage, but future work could be to try

and obtain a simulated pattern closer to the measured value, or to perform new measurements. It is clear that further adjustment of the dielectric properties in the simulation is required, which is something to consider if this work is revisited.

Bandwidths

A summary of the bandwidths obtained for the measurements and simulations of the antenna in free space, on MDF and PVC are shown in Table 7.3. It should be noted that bandwidths for the copper and flesh results were not calculated due to poor S_{11} comparison.

Table 7.3: Simulated and measured fractional bandwidths for antenna mounted on different surfaces

Simulated				
Surface	Low. freq. (GHz)	Upp. freq. (GHz)	Null freq. (GHz)	Fractional Bandwidth (%)
Free space	2.44	3.23	2.80	28
MDF (2.3mm separation)	2.28	2.99	2.59	27
MDF (Direct mounting)	2.10	2.80	2.40	29
PVC (2.3mm separation)	2.26	2.94	2.55	27
PVC (Direct mounting)	2.05	2.70	2.35	28
Measured				
Free space	2.62	3.23	2.84	22
MDF (2.3mm separation)	2.34	3.17	2.51	33
MDF (Direct mounting)	2.29	3.13	2.44	34
PVC (2.3mm separation)	2.33	2.86	2.62	20
PVC (Direct mounting)	2.15	2.51	2.31	16

What is first noticeable is that the majority of fractional bandwidths in each case could be considered usable for wireless applications where 10% is a nominally useful value. All of the simulated results are very similar between 27-29%. The measured results differed slightly from the simulations, with the results for MDF giving higher values, while the PVC bandwidths were lower for the measurements compared to simulations. The bandwidths for the measurements range from 16-34%. Despite the difference between the simulated and measured bandwidths, it is more important that they match around the null frequency, rather than having similar upper and lower frequencies at the point which they pass -10dB in the S_{11} patterns.

7.1.5 Capacitive plate study

Due to the presence of two capacitive plates for the antenna being in such close proximity with a separation of about 0.045mm, it was of interest to see if the end caps present for this design had any bearing upon the results. An additional brief simulated study was therefore conducted for the antenna with a Mylar substrate (Figure 7.9) to observe if these end caps had any effect. In addition, the slots on the lower ground plane were altered to be of identical width and length to the slot dipole on the upper ground plane. The new patterns are shown in Figure 7.21. In comparison with the original dimensions, as shown in Section 7.1.1, the length (L1) and width (W1) remained unchanged, however, with the end caps this time removed. The lower ground plane showed new dimensions with the length (L5) and total width (W6) of the slots beneath the dipole at 4.1mm, and 72.4mm, respectively, while the new length of the slot beneath the feedline (L4) was altered to 11mm. This ensured that the length and overall width (the total width including both slots and the gap between the feed) of the slots on the lower ground plane were identical to the dimensions on the upper ground plane.

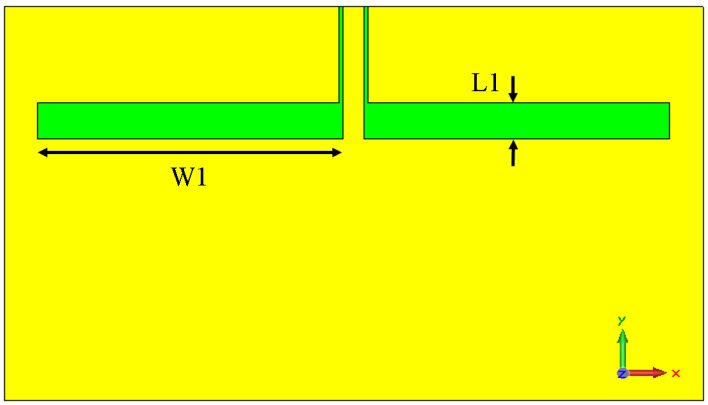

(a)

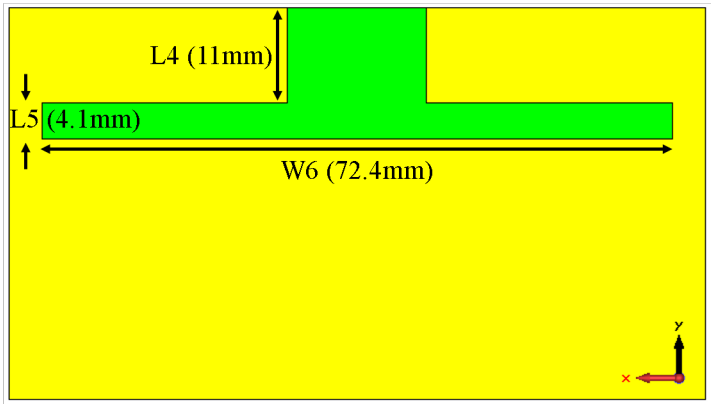

(b)

Figure 7.21: Altered dimensions for simulated Mylar antenna for (a) the upper ground plane, and (b) the lower ground plane

For this study, the simulated S_{11} parameters were shown for the new structure, and compared alongside the original structure for the antenna with a Mylar substrate, containing the end caps. The S_{11} plots are shown in Figure 7.22.

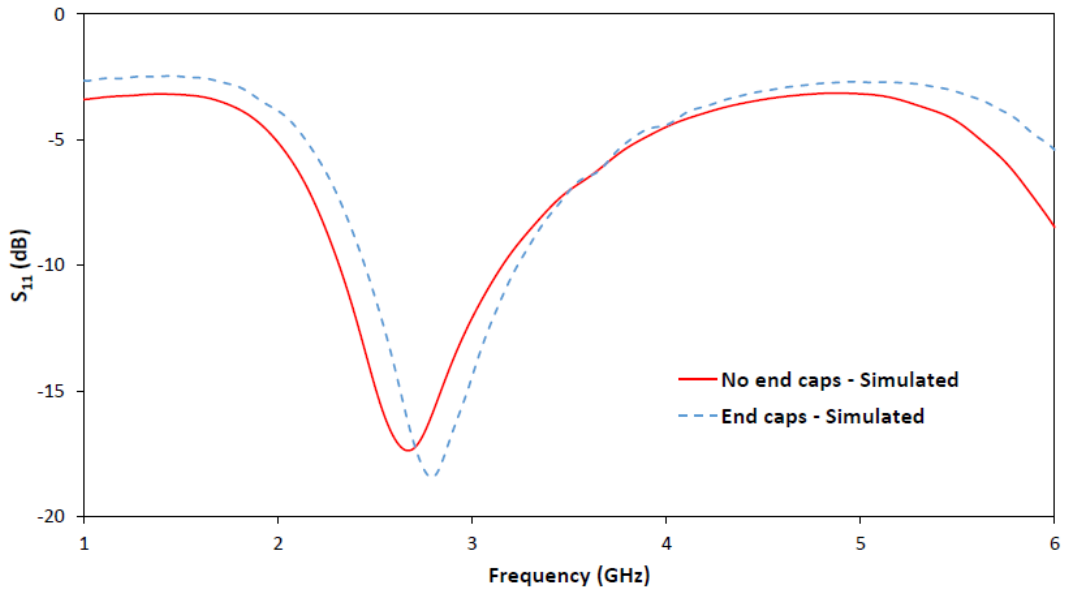

Figure 7.22: Simulated S_{11} for the altered structure with no end caps (Figure 7.21), compared with the simulated S_{11} for the previous structure containing the end caps (Figure 7.9)

As can be seen from the results, the design gives a similar plot to the original study, however, with a slight shift in resonant frequency. It was perhaps expected that due to the two capacitive ground planes being in such close proximity, the end caps would have a negligible effect. This is not the case, since we see a slight downshift in frequency when these end caps are removed. It could be that altering the dimensions on the lower ground plane to be identical to the upper ground plane slot configuration may have had an effect. In theory, however, this effect should have also been negligible. One positive to take from this study is that removing the end caps shifts the resonant frequency closer to the initial target frequency of 2.45GHz.

7.2 Conclusions

The feasibility of producing extremely low-profile composite polymer-battery antenna devices for active short range systems such as Bluetooth has been indicated by simulation. Material measurements of a candidate polymer sample indicate that losses may not be prohibitively high, though further studies using appropriately treated polymer samples will be required before validation with antenna structures. This technology is proposed for use in short range location finding and security applications where very low-profile or covert tags may be beneficial.

In addition to simulations, measurements were performed on a Mylar prototype antenna with two ground planes and an ultra-thin substrate. The antenna was

measured in free space, with S_{11} and farfield results obtained. The measured results for the prototype compared well with the equivalent simulated design.

The antenna was then mounted on a variety of surfaces being MDF, PVC, copper and flesh. The S_{11} patterns were measured in this case, and compared with simulations. In each case, the antenna was measured with a 2.3mm separation between the surface, by means of a polystyrene layer. This layer was then removed, allowing the antenna to be mounted directly onto the chosen surface. For MDF and PVC, all of the measured S_{11} patterns matched well with their equivalent simulations. As expected, copper caused a significant degradation for the patterns, noticeably in the measurements. This was not a surprise as we know that proximal metal planes cause interference with the antenna performance. Meanwhile, a match could not be obtained for when the antenna was mounted on flesh. This could be due to inaccuracies in the simulated dielectric parameters for human skin, or the measurements themselves. Further measurements and simulations may be required in order to investigate further.

Simulated and measured bandwidths were obtained and compared for the prototype antenna, with values considered usable for wireless applications. Overall, the measured and simulated results for the prototype indicate that we can design and build a fully functioning antenna whereby two ground planes are in close proximity as a result of an ultra-thin substrate, with usable bandwidths and efficiencies shown throughout. Therefore, it is feasible for our integrated antenna-battery to be of an ultra-thin design.

A final study focused on comparing the effect of the end caps of the slot dipole upon the S_{11} patterns, for the ultra-thin Mylar prototype. This design involved two capacitive plates in very close proximity due to a very thin substrate. It was therefore anticipated that removing the end caps, as well as ensuring the slot dipole configuration was identical for both the upper and lower ground planes, would have a negligible impact on the S_{11} patterns. While the results were similar when compared with the structure containing the end caps, a slight downshift in the resonant frequency was observed for when the end caps were removed. This result was slightly unexpected, however, removing the end caps did result in a shift closer to the initial target frequency of 2.45GHz.

Chapter 8

Conclusions and Future Work

In this study, a detailed analysis has been performed on both battery materials and antenna systems, to determine their suitability as an integrated, compact, ultra-thin component. By studying the systems separately, information can be obtained specifically relating to the performance of these materials, indicating how the integrated system may function.

In terms of the battery material, the system of choice being a mixed conducting co-block polymer, PEDOT-PEG was studied in order to obtain information about lithium coordination and lithium conduction properties. Detailed studies were also performed on the pure polymers, PEG and PEDOT, to investigate properties such as the physical characteristics and bond lengths.

For the antenna systems, a suitable design of antenna needed to be chosen, one which could be easily mounted onto a battery substrate without significant reduction in efficiency and bandwidth. Modifications were made to the simulated antenna in order to assess performance using parameters associated with battery materials such as conducting polymers. A prototype was also constructed using a Mylar substrate. This prototype was then mounted onto a variety of surfaces, both computationally and experimentally. Potential applications such as a printed antenna placed on a wall require the antenna to maintain performance in the case of mounting onto different surfaces.

8.1 Acetylene

With polyacetylene being considered a model material with regards to conducting polymers, a detailed ab initio study was performed on the acetylene molecule. This was predominantly a study of the effect of the dispersion correction using DFT functionals (BLYP), along with an analysis of the electrostatic properties in acetylene. The effect of hybridisation was also discussed, which involved introducing a certain degree of Hartree-Fock exchange added to the DFT functional (B3LYP).

The dispersion correction, initially derived by Grimme was applied to two dif-

ferent polymorphs of acetylene, namely the low temperature orthorhombic and high temperature cubic structures. A newly derived method for the solid state was also applied to the pure DFT BLYP functional. Lattice parameters and energies were calculated. It was found that the cubic structure of acetylene was better represented by the BLYP and B3LYP functionals in terms of lattice parameters, with Grimme's dispersion correction (BLYP-D) and the newly derived solid state correction (BLYP-DS) underestimating these values. On the contrary, both the pure and Grimme-corrected functionals (BLYP, B3LYP and BLYP-D) incorrectly modelled the orthorhombic structure, resulting in a tetragonal structure instead. This was corrected by the BLYP-DS method, which resulted in the expected orthorhombic symmetry, along with a good agreement with the experimental values.

In the case of each polymorph, the pure functionals significantly overestimated the lattice energies. The energies were improved noticeably with the BLYP-D approach, with further improvement shown by the newly derived BLYP-DS functional. The orthorhombic structure in particular showed good agreement with experiments.

A study of the electron density using the pure BLYP functional showed an over-delocalisation when the Grimme correction was applied, as seen in a Mulliken population analysis and electron density distributions. The BLYP-DS approach localised the electron delocalisation.

With electric field gradients known to be sensitive to the local structure as well as electron density, quadrupole coupling constants (QCC) were calculated for the two different types of atoms in acetylene (carbon and hydrogen). It was discovered that the QCC values were method dependant, with the LDA and HF approaches shown for comparison. LDA gave values similar to the BLYP and B3LYP functionals, while HF showed an overestimation for the carbon atom and an underestimation for the hydrogen atom. Comparing BLYP with BLYP-D and BLYP-DS, it was observed that the dispersion correction had little effect on the QCC values. It was identified, however, that the QCCs are influenced by the basis set, with an augmented method resulting in a value of almost four times that of the original basis set in the case of hydrogen. Meanwhile, the augmented method resulted in a value of approximately double the original basis set in carbon.

In summary, the newly derived solid state dispersion correction improved most of the properties calculated in this investigation. Having been derived by studying the transferability of the BLYP-DS functional to other hydrogen-bonded systems, it has demonstrated to perform either as well, or even better than the pure BLYP and BLYP-D functionals.

This greater understanding of the electrostatic and lattice properties would prove useful should polyacetylene have been chosen as a potential battery material. However, due to issues such as stability in a laboratory environment, other mixed conducting polymers were pursued.

8.2 Polymer Electrolytes - A study of both pure and lithiated systems

With mixed conducting polymers of great interest for a non-metallic battery, due to offering both electrical and ionic conductivity, PEDOT-PEG was chosen as a good potential candidate material. The PEDOT phase of the polymer is known to offer good electrical conductivity, while PEG is considered a model material with regards to ionic conductivity. A theoretical study was conducted on this co-block polymer, investigating its performance both as a pure and lithiated polymer. Two of the known geometries of PEDOT-PEG, the multi-block and tri-block configuration, were briefly compared, with the multi-block found to be marginally more stable. Since experiments were performed using the multi-block geometry, the decision was made to investigate this structure for the remainder of the simulations. In order to understand how properties changed when forming the co-block polymer, studies were also performed on the pure PEDOT and PEG polymer systems.

8.2.1 Pure Polymers

With Molecular Dynamics (MD) simulations being chosen to model these polymers, a force field comparison was made. Two different approaches to constructing the polymers were used, with the PCFF and COMPASS force fields being compared. The PCFF force field was used in the DL_POLY software, while the COMPASS force field was used with Forcite, in the Materials Studio package. Initially, the isolated chains were analysed, in terms of their physical shape and conformations. Two different chain lengths were investigated (20 and 120 units for PEDOT and PEG, 40 and 160 units for PEDOT-PEG), and it was found for the three different polymers simulated, both force fields modelled the polymers in a similar fashion.

A further investigation of the pure polymers involved looking at the bond distribution for the 20 unit isolated chains and the amorphous systems. These plots allowed the bond distances to be determined, along with the probability of finding that bond in the system. For the isolated systems, the distribution was plotted for every 1000ps of the simulation (with a total run time of 5000ps per system). It was found that for the PCFF force field, there was no change after the first 1000ps onwards in terms of the bond probability. On the contrary, minor differences were obtained for COMPASS which were most apparent in PEG. This could possibly be down to the polymer structure not folding up to the same extent with this simulation approach. Furthermore, the systems constructed for use with the COMPASS force field in Forcite had a straight chain starting structure, and were optimised using the Forcite geometry optimisation procedure. Meanwhile, the systems in DL_POLY using the PCFF force field were built as a random polymer distribution and optimised using a zero-temperature energy minimisation method. This resulted in the

fact that the majority of the polymers folded up during the course of the simulation with the exception of a 20 unit chain of PEG using the COMPASS force field.

The bond distances for the isolated 20 unit polymer chains and amorphous systems were compared with experiments. It was found that all the systems gave good agreement with the experimental values.

A result of interest was a phase separation observed in PEDOT-PEG. For both of the different chain lengths as well as each force field, it was evident that the PEDOT and PEG phases of the co-block polymer preferred to remain separate during the simulation. This behaviour is helpful in understanding how this polymer may conduct electrons as well as lithium ions in the battery.

In addition, the mean square displacement (MSD) was calculated for the amorphous polymer chains. From these plots, the diffusion coefficient could be obtained for the PEDOT, PEG and PEDOT-PEG polymer chains. It was discovered that the PEG system had the highest rate of diffusion, with PEDOT-PEG resulting in the lowest rate. This was deduced to be down to the PEG chains being the least bulky, resulting in less steric hindrance, which in turn would facilitate diffusion. A trend was identified between then number of atoms per polymer chain and the diffusion coefficient. PEDOT-PEG, which showed the lowest rate of diffusion, had the greatest number of atoms per chain, while PEG, which had the highest rate, in turn, contained the smallest number of atoms per chain.

8.2.2 Lithiated Polymers

In order to investigate lithium conduction in mixed conducting polymers, both ab initio calculations performed alongside experimental measurements, and MD simulations were undertaken. The aim of the ab initio study was to investigate coordination sites of PEDOT-PEG. For comparison, the composite polymer PEDOT:PSS was also investigated in this case. MD simulations were performed on PEG, PEDOT and then focusing on PEDOT-PEG, in order to analyse coordination numbers and distances. The lithium diffusion coefficients were then obtained, which in turn allowed the ionic conductivity to be calculated for these systems.

The pure and lithiated PEDOT-PEG and PEDOT:PSS polymers were investigated using FTIR spectroscopy. Ab initio simulations were performed, with frequency calculations used to help characterise the peaks on the IR spectra. In the case of PEDOT-PEG, no change in the FTIR spectra was observed when lithium ions were inserted into the polymer. A similar study showed that lithium was not detected in FTIR spectra for chains of $(\mathrm{PEG})_n \geq 20$. This was assumed to be the case also with PEDOT-PEG. A brief ab initio simulation was performed on a PEG monomer, which confirmed that the lithium ion showed an affinity for the oxygen atom, which is known to be a significant coordination centre in PEG. For the lithiated IR spectrum of PEDOT:PSS, a second peak was observed experimentally, not

seen in the pure PEDOT:PSS spectrum. By using ab initio calculations, it was identified that this second peak was a result of the interaction of lithium with the sulphonate group in the PSS phase of the polymer. Therefore, it was suggested that this functional group in PSS acted as the preferred coordination site for lithium, in the composite polymer PEDOT:PSS.

Using MD calculations, the radial distribution functions for the lithiated polymers could be obtained. Two different salts were used for this study (LiI and LiCl). Furthermore, a more detailed analysis was conducted on PEDOT-PEG whereby different concentrations of each salt were used. The intention was to observe both coordination numbers and distances for the Li-O separation in the polymer. Separations of 2.23Å in PEG, 2.18Å in PEDOT and 2.23-2.28Å in PEDOT-PEG were obtained. Coordination numbers of 4.4 and 8 were observed for PEG and PEDOT, respectively. For differing concentrations of the salts in PEDOT-PEG, coordination numbers ranged from 0.3 up to 4.9. A decrease in Li-O coordination number was observed with increasing lithium salt concentration, suggested to be due to ion pairing.

In order to calculate the conductivity of the system, MSD plots were obtained for the lithiated polymers. The diffusion coefficient obtained from these plots could then be used to calculate the ionic conductivity. Again, PEG and PEDOT were investigated using both the LiI and LiCl salts, with PEDOT showing diffusion coefficients and conductivities a single order of magnitude higher than PEG. Both salts in PEDOT gave similar results, while the LiI salt in PEG gave diffusion coefficients twice those of the LiCl salt. The diffusion coefficients for PEG agreed well with published calculated MD data, along with experimental NMR results. The diffusion coefficients obtained for PEDOT-PEG were also found to agree well with published results for PEG.

A conductivity study was then carried out using differing concentrations of salt in the PEDOT-PEG co-block polymer. Both salts showed an overall decrease in diffusion coefficient, stabilising at a value of around $1\times10^{-12}\mathrm{m}^2/\mathrm{s}$. The overall decrease of lithium conductivity in the PEDOT-PEG system could be related to the degree of ion pairing, as previously observed for the RDF plots. With an increase in the salt, it becomes more difficult for Li cations to avoid the I/Cl anions. With increased ion pairing, lithium coordination, and thus conductivity becomes more inhibited.

Despite PEG being considered a model material with regards to ionic conductivity, it is of interest to see that PEDOT actually gave a higher diffusion coefficient, conductivity and coordination number than both PEG and PEDOT-PEG in the case of a single lithium salt. While this result is inconclusive due to only a single lithium ion being present, it could be that the way in which oxygen atoms are distributed in the PEDOT chains may be preferable for hosting lithium cations. With

two oxygen atoms per monomer unit, it is possible that lithium may coordinate in a way that involves both of the oxygen atoms in a unit, or perhaps coordinating between two oxygen atoms from neighbouring PEDOT units. Furthermore, it is also possible that due to a bulkier structure overall, the arrangement of the PEDOT chains may even inhibit ion pairing to a certain degree.

8.3 Antenna simulations and measurements

Simulations were performed in order to design a suitable antenna to be integrated with a battery. The simulations demonstrated the possibility of creating a fully integrated system which could function in the Microwave band using potential battery material properties from published literature. A coplanar waveguide slot dipole antenna was designed, since slot antennas can function with much thinner substrates compared to microstrip patch antennas. Despite relatively lossy substrates, which would be more closely associated with a solid state battery, reasonable gains and efficiencies could be obtained, along with wide bandwidth.

A study was undertaken to assess antenna performance at lower ground plane conductivities, which would be more closely associated with polymer electrolytes. The study showed that antenna performance could be maintained down to ground plane conductivities of 5.8×10^2 S/m. This result is promising in the case of designing a non-metallic battery.

Since current collectors in a solid state battery would be present both on the top and bottom of the structure, as demonstrated in Nagatomo's polyacetylene battery, a second ground plane was added underneath the antenna structure and simulated. With slots also cut into the bottom current collector/ground plane, good bandwidth values could be obtained. As stated previously, an ultra low-profile integrated system is highly desirable. The substrate thickness for the designed antenna was reduced to a value of 0.3mm. Additional parameters of ionic conductivity and relative permittivity were taken from the literature and applied to the model. Once again, a good bandwidth and usable efficiency was obtained.

Farfield studies were also undertaken, investigating what effect the slot width beneath the dipole on the lower ground plane had on the radiation patterns. The effect of the loss tangent of the substrate was also observed. It was shown that the efficiency decreased as the slot beneath the dipole was reduced, while increasing the substrate loss would also lead to a reduction in efficiency, which is expected.

The Bluetooth frequency (2.4GHz) provided one potential application for the antenna. The model was adjusted in order to function at this frequency. Furthermore, permittivity and dielectric loss measurements performed on a sample of PEDOT:PSS were applied to the antenna model, which suggested that the losses may not be as high as expected, with reasonable bandwidths and usable efficiencies

obtained.

The simulations were complimented with measurements performed on a Mylar prototype, consisting of two ground planes. The S_{11} and farfield measurements compared well with the equivalent simulations in this case. In addition to being measured in free space, the antenna was mounted onto a variety of surfaces including MDF, PVC, copper and flesh. The antenna demonstrated a good match between simulation and measurement in terms of the S_{11} patterns in the case of MDF and PVC. Copper, as expected, resulted in significant degradation of the patterns, which relates back to the original problem regarding antenna performance in the presence of a metallic plane. A match was unable to be achieved between simulation and experiment in the case of flesh, which could be due to inaccuracies in the dielectric parameters used in the simulation.

A study of capacitance was carried out with the theory that by having two capacitive plates in very close proximity to each other, the effect of the end caps in the slot dipole would be negligible, and thus could be removed. However, the results of this study showed that removing the end caps, along with ensuring that the upper and lower ground planes had matching overall dimensions, resulted in a slight downshift in the resonant frequency.

Overall, the results demonstrated that a fully functioning antenna with two ground planes very close together and an ultra-thin substrate could be both simulated and synthesised. Therefore, it is feasible for the integrated antenna-battery to be of ultra-thin design without significant degradation with regards to both bandwidth and efficiency.

8.4 Summary of conclusions

Overall, the results of this study show that polymer electrolytes, particularly PEDOT-PEG provide a good potential alternative for use in a non-metallic solid state battery. With conductivity values comparing well with that observed in PEG experimentally, PEDOT-PEG may well be a suitable mixed conducting polymer in a non-metallic battery. A suitable antenna design for integration with a battery has been simulated, with a prototype also measured. These results indicate that an antenna can function using parameters associated with battery materials, while still maintaining usable efficiencies. Furthermore, the antenna can be structured in a way that more closely resembles a solid state battery, such as having two ground planes, and an ultra-thin substrate. Overall, the results suggest that the non-metallic integrated antenna-battery design is feasible, and with further investigation, a more realistic prototype can be fabricated in the near future.

8.5 Future work

With regards to the polymers, larger chains lengths could be investigated in each case. So far, the maximum chain length analysed was 160 units in PEDOT-PEG. With the ability to simulate much larger chains, these results would be more comparable with experimental systems. It is also of interest to see if the same physical characteristics would be observed. Particularly in the case of PEDOT-PEG, it would be of great interest to see if phase separation still occurs for much larger systems.

In the case of lithium insertion, a more extensive study on the PEDOT system could be undertaken. It was observed that for the case of a single lithium ion, PEDOT demonstrated a noticeably higher coordination number and conductivity than PEG. It would be interesting to see if this remained the case with increasing concentrations of the LiI and LiCl salts.

Furthermore, due to the extent of ion pairing seen in the PEDOT-PEG system, a larger salt such as $LiBF_4$ or $LiPF_6$ would be interesting to analyse. Since these anions will not bind as strongly to lithium, compared to individual iodine or chlorine anions, the extent of ion pairing may be significantly reduced. In turn, this may lead to increased Li-O coordination since more lithium ions will likely be coordinating to oxygen as opposed to the counterion. As a result, diffusion would potentially increase, leading to higher conductivities.

With the multi-block geometry of PEDOT-PEG having been investigated, it would be useful to see how the tri-block structure compares. Experimentally, the tri-block structure is known to have higher electrical conductivities. It would be interesting to observe how the ionic conductivity compares, along with physical properties such as phase separation.

In addition to PEDOT-PEG, PEDOT:PSS is also a good potential candidate in a non-metallic battery, having demonstrated good electrical conductivity values in laboratory environments. It would also be useful to investigate this polymer in terms of ionic conductivity, both computationally and experimentally. As well as PEDOT:PSS, other co-block polymers could be analysed.

Ab initio calculations could be undertaken on the polymers. This would allow us to calculate properties such as permittivity, which would be useful in terms of predicting how the antenna may behave. The calculated polymer permittivity could be used in the antenna simulations to observe how the bandwidths and efficiencies may change.

With regards to the antenna, the next stage would be to design a prototype in which the Mylar substrate is replaced with a conducting polymer such as PEDOT-PEG or PEDOT:PSS. It is highly desirable to see if this prototype will give usable results with a design closer to a solid state battery. Since we expect a polymer substrate to be more lossy, a reduction in efficiency should be anticipated. Further tests could also be conducted to obtain a match between simulation and experiment

when the antenna is mounted on flesh. Since there is increasing interest in antennas placed directly onto human skin, even in the form of tattoos, designing an antenna which can function in this environment has potential applications and benefits.

Appendix A

Additional computational procedures

A.1 Zebedde

Zebedde requires several input files of its own to build a polymer chain. Firstly, a CAR file (Obtained from Materials Studio - see Appendix A.2) of the monomer unit needs to be created. This is the seed and will define the atomic structure of the monomer along with a point of attachment, which is where Zebedde is instructed to grow the polymer chain from on the repeat unit.

In the CAR file, the atomic labels and coordinates are displayed, along with the force field, atom type and electron charge. Here, the hydrogen atom types, H_A and H_B, represent the points of attachment from which further monomer units can grow in Zebedde to form a polymer. These H_A/H_B atoms are essentially removed to form a C-C bond between the C atoms of different fragments. As well as the monomer unit, a CAR file is required for the fragment of the repeat unit to be grown from the seed. This has exactly the same format as the seed molecule. A separate file is also necessary to define the periodic boundary conditions to be used in the building process. A force field file is also used in order to assign the force field to the newly built polymer chains.

At each stage of the building process (for each new monomer unit added to the chain), an ARC file is created. This file is important as it defines the atomic structure of the polymer for each chain length, along with the force field parameters, as instructed by Zebedde. ARC files can be opened in the Materials Studio package, which is described below.

A.2 Materials Studio

Materials Studio [160] is a package that creates a complete modelling and simulation environment, allowing researchers to investigate a large range of materials, and

analyse their properties and behaviour. It is suited for many different applications such as pharmaceuticals, catalysts and polymers. Many different simulation tools are available to the user, such as the Discover and Forcite programs. Figure A.1 shows an example of a PEDOT monomer in the Materials Studio interface.

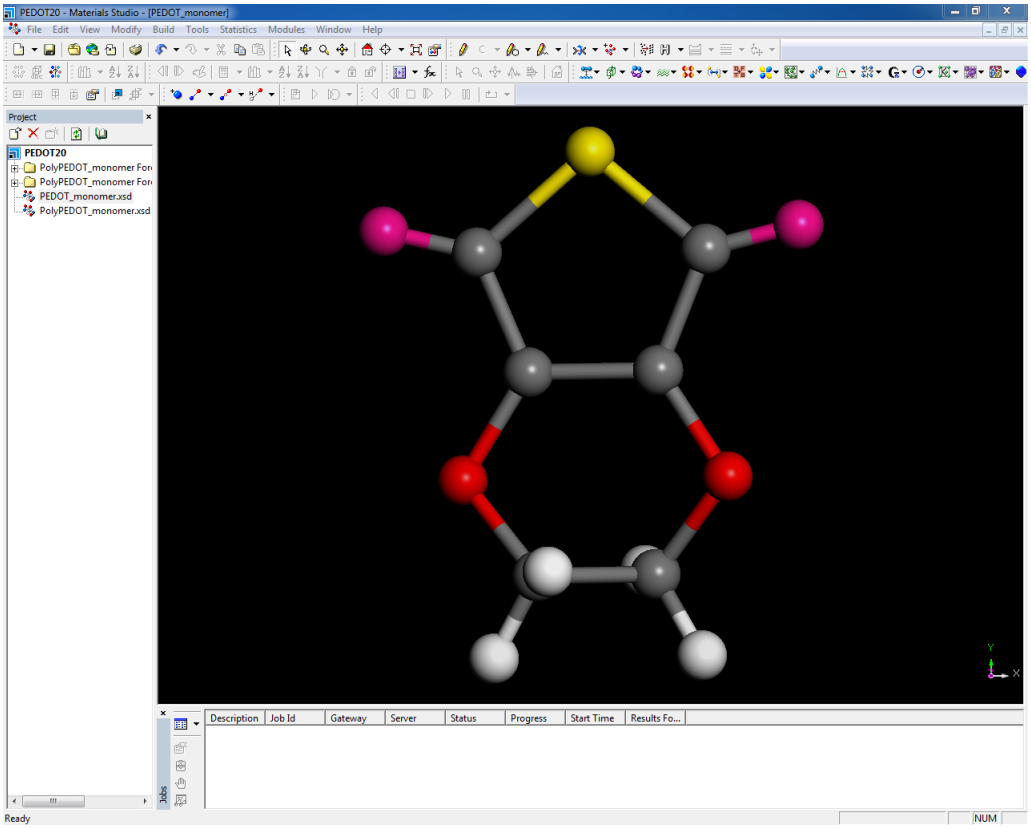

Figure A.1: Example of a PEDOT monomer unit created in Materials Studio

A.3 Discover

Discover is a simulation engine used in Materials Studio [254]. It uses a wide range of molecular mechanics and dynamics methodologies which are applicable to molecular design. It uses a derived force field as its foundation, and is useful for computing minimum energy conformations as well as families of structural and dynamical trajectories of molecular systems. It can support a variety of simulation strategies, for example, simulation of crystalline or amorphous solid state systems with periodic boundary conditions.

In our case, Discover is used in order to assign the PCFF force field to polymers. It is simply activated in the Materials Studio software by selecting the setup menu on the Discover section and choosing the force field to assign. Other options such as CVFF and COMPASS are also available.

After the process is complete, the resulting output structure will have the force field assigned to the model, and can be exported into a variety of file formats for use with other programs.

A.4 Forcite

Forcite plus is used via the Materials Studio interface and from the Forcite menu, the type of calculation can be selected. For example, a geometry optimisation can be used so that the structure is at its minimum energy. A variety of optimisation algorithms can be used. After this is performed, a molecular dynamics simulation can be run on the system of choice, using a range of dynamics ensembles, thermostats and barostats. Run settings can be altered such as the timestep, number of steps and system temperature.

Once the simulation has been run for the specified number of steps, the output files are stored in a Materials Studio project. The Forcite plus analysis tools can be used to obtain a wide range of information and results, such as the mean square displacement (MSD), radial distribution function (RDF) and velocity autocorrelation function (VAF), allowing the user to gain an understanding into what is occurring in the molecular system.

A.5 dl_poly prep

The dl_poly prep code is an in-house utility [255], which can be used to convert CAR files of polymers obtained from Zebedde into DL_POLY input files. A CONFIG and FIELD file are created from the CAR file input, ensuring that the atomic coordinates are correct, with the periodic boundary applied, as well as ensuring that the force field selected by the user is assigned.

This utility requires several files for the conversion to take place. Firstly, the CAR file of the polymer to simulate must be present. As Zebedde creates ARC files, the best procedure is to import these files into Materials Studio first of all. Here, the ARC file can be opened and edited if the user deems it necessary, such as adding atoms to terminate the polymer chain. The Discover module is used to reassign the force field, ensuring that the system is charge neutral. The ARC file can be exported as a CAR file. The code requires the force field file that was used in Zebedde to ensure that it can be assigned to the new FIELD file in DL_POLY.

After running the code, the two output files obtained are the CONFIG and FIELD files, which are then able to be used with DL_POLY to perform MD simulations. dl_poly prep was chosen in this case due to its rapid conversion of these files from Zebedde, as well as its simplicity in terms of usage.

A.6 XCrySDen

The software package XCrySDen [256] was used primarily for ensuring that the CRYSTAL09 input files were correct, by showing the resulting crystal structure. It was also used in order to insert lithium ions into the monomer/polymer structures

used in Chapter 5. XCrySDen allows the user to manipulate the position of the ions, placing them ideally near a coordination centre such as an oxygen atom. Figure A.2 shows an example of lithium inserted into a PEG monomer input structure in the XCrySDen interface.

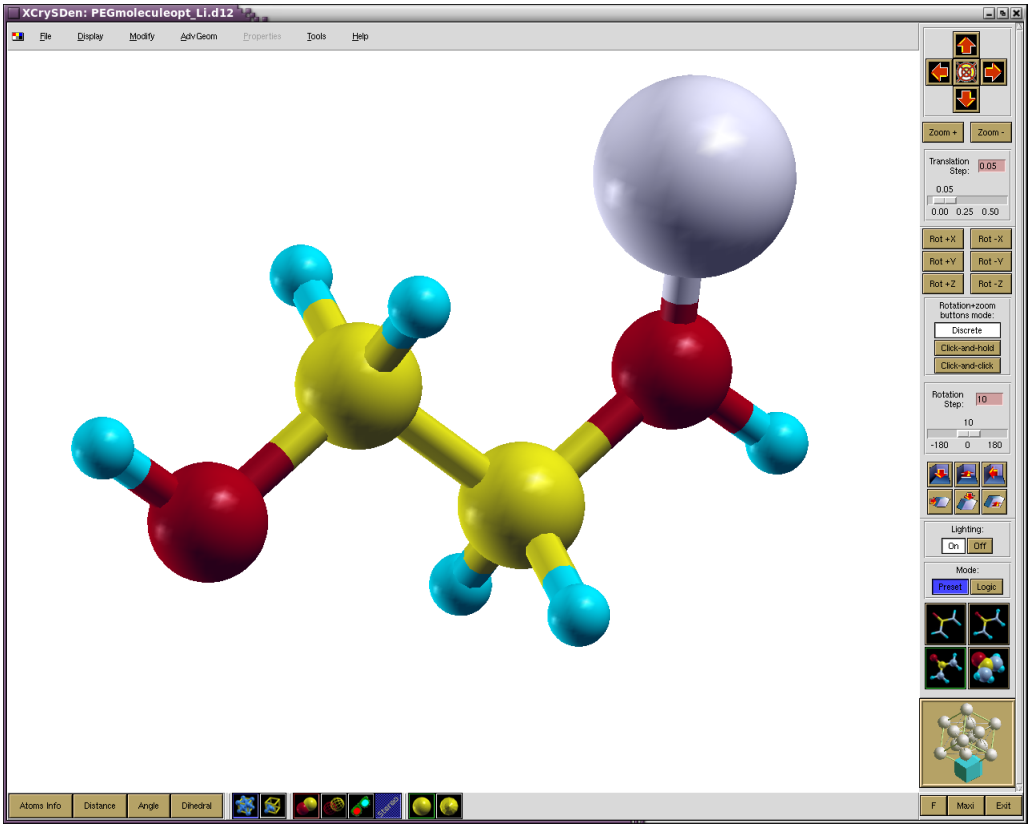

Figure A.2: Example of a lithium ion inserted into a PEG monomer in XCrySDen

A.7 GDIS

In order to insert lithium ions into the polymer structures (See Chapter 5), a package called GDIS (Graphical Display Interface for Structures) [257] was used. The CAR files created in Materials Studio were imported, and for the resulting structure, both lithium ions and either chlorine or iodine anions could be inserted. The program also allowed manipulation of the ion positions which was useful for smaller ion concentrations where it was desirable to place cations closer to oxygen and anions further apart from the cations. Figure A.3 shows an example of PEDOT-PEG with lithium and iodine ions inserted into the structure in GDIS.

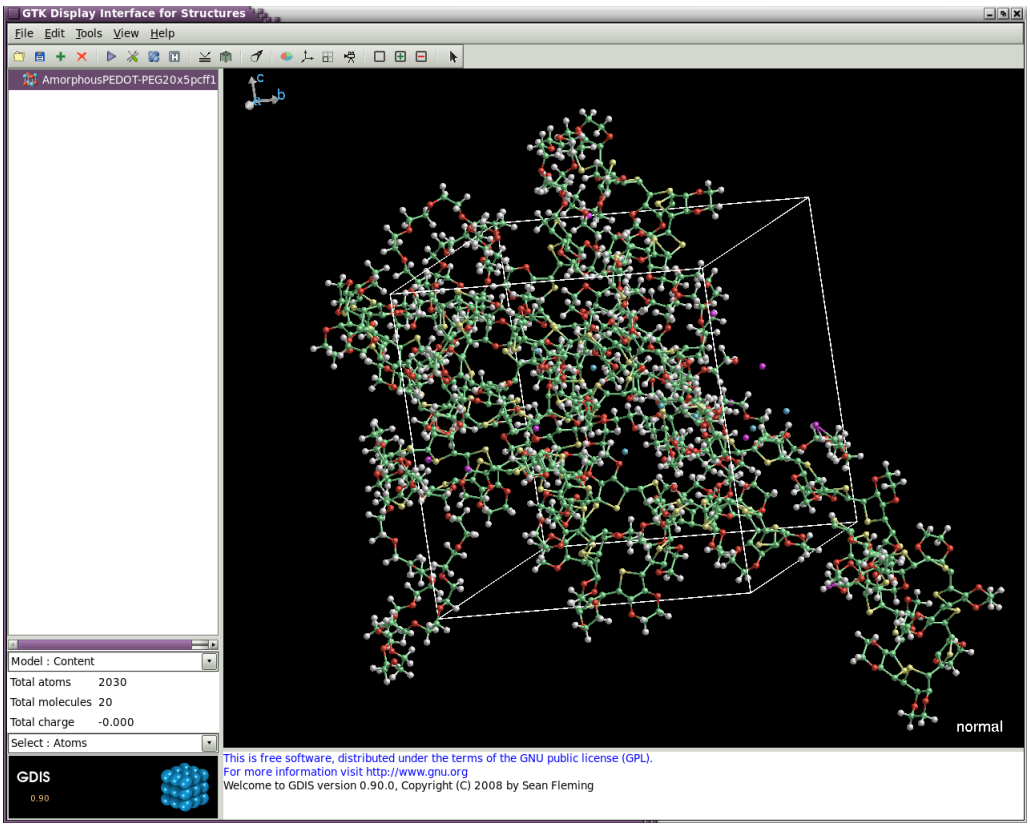

Figure A.3: Example of PEDOT-PEG with ions inserted in GDIS

A.8 Viewing simulation output

A.8.1 MDPREP

In order to visualise MD simulation output ran in DL_POLY, a code known as mdprep [258] could be used. This simply required the HISTORY file from the completed simulation as its input. In this situation, the code was used in order to obtain the ARC files for the simulation, which then allowed the trajectory to be analysed in Materials Studio. This trajectory could be animated so that the structure at each frame of the calculation could be viewed, allowing us in particular to look at the shape and structure of the polymer along with bond lengths. The trajectory could also be analysed using Forcite, which allows us to view statistics such as the bond distribution. Using these ARC files, the resulting structure at the end of the simulation was visualised.

A.8.2 J-ICE

Here, the online resource known as J-ICE [220] was used in order to view CRYSTAL09 output files. J-ICE uses a Java interface, and can load a multitude of different output files such as CRYSTAL09 and XYZ files. Particular uses in this project were to view the geometry optimisation animations, which show how the structure

changes as the simulation progresses. This was particularly useful when analysing the position of lithium in polymers. Also, simulated FTIR frequencies could be viewed for a model, which can then be compared to experimental data. These frequencies could also be animated, showing how the structure moves and conforms at a particular frequency. Figure A.4 shows an example of a lithium ion interacting with a polystyrene sulphonate (PSS) monomer in J-ICE.

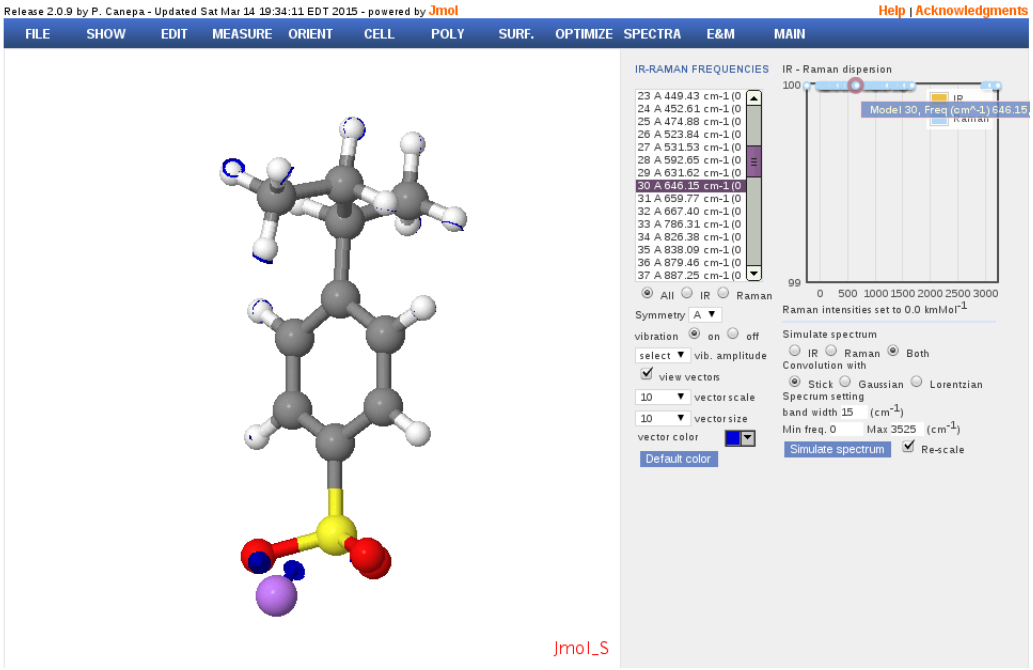

Figure A.4: Lithium ion interacting with PSS monomer in J-ICE

A.8.3 Visual Molecular Dynamics (VMD)

VMD [259] is a tool which allows the user to view a variety of different Molecular Dynamics output. In this case, it was used mainly to view DL_POLY output to assess lithium coordination in polymers. It uses a HISTORY file in order to load the trajectory, with which the frame by frame output could be viewed as an animation. Other useful features included the ability to view atomic distances, which gave an early indication into what potential ion coordination distances may be. Figure A.5 shows an example of a PEDOT-PEG polymer in VMD.

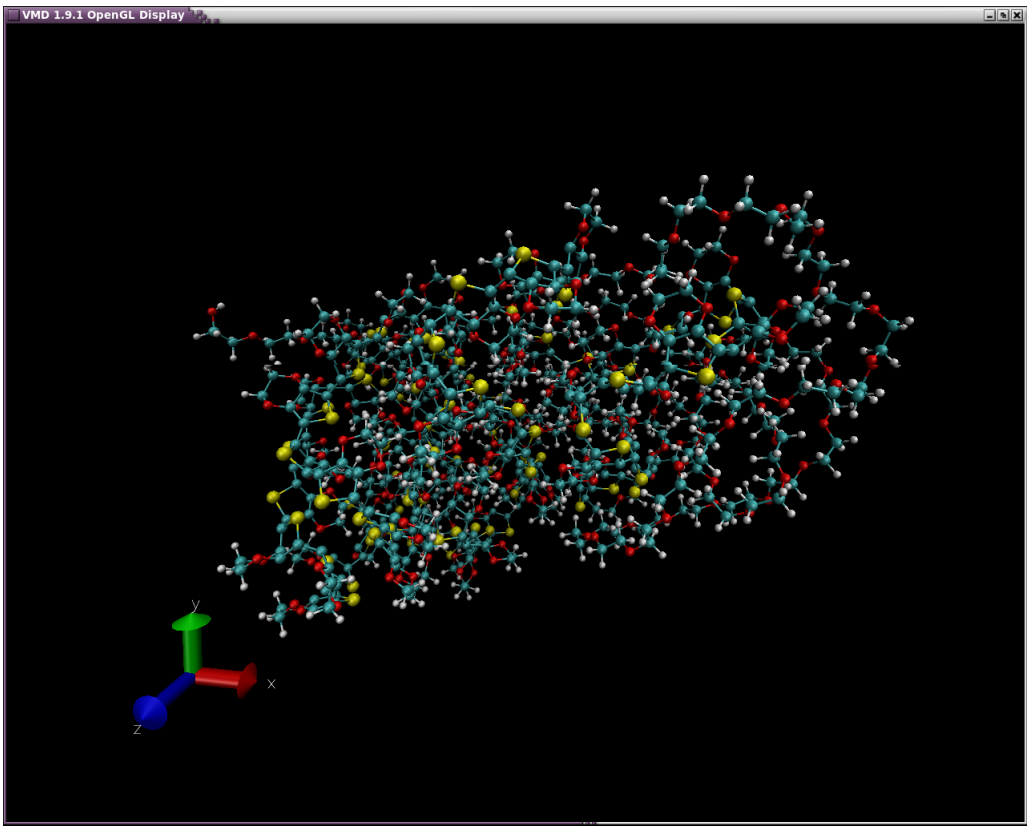

Figure A.5: PEDOT-PEG in VMD

A.8.4 analyse_hist

analyse_hist is a routine which can carry out various forms of analysis on DL_POLY OUTPUT and HISTORY files [260]. In this project, it was used primarily to obtain the mean square displacement (MSD) plots for the polymers. It also requires the FIELD file used for the simulation input in order to determine how the atoms are grouped in the molecules. In order to use analyse_hist, a specific input file is required. In this file, the names of the HISTORY, OUTPUT and FIELD files are defined. In addition, the time frame (referred to as T1) for the simulation needs to be calculated. This is the time in picoseconds between each frame in the HISTORY file, multiplied by the simulation timestep.

For obtaining the MSD plot from the simulation, the plot range must be specified. This generally begins with the time frame value. The final value in the range (defined as T2) is usually around half of the total time of the HISTORY file. This allows for multiple time origins. Finally, the molecule type, as defined in the HISTORY and FIELD files must be chosen. This is the type of molecule with which the MSD analysis is carried out upon. Multiple molecular types can be defined in this case. For example, if Li^+ is defined as molecule 2 in the FIELD file, then a value of 2 is chosen in the analyse_hist input file.

Bibliography

[1] C.-I. Lin and K.-L. Wong, "Printed Monopole Slot Antenna for Internal Multiband Mobile Phone Antenna", *IEEE Trans. Antennas Propag.*, 2007, **55**, 3690–3697.

[2] Q. Guo, R. Mittra, F. Lei, Z. Li, J. Ju and J. Byun, "Interaction Between Internal Antenna and External Antenna of Mobile Phone and Hand Effect", *IEEE Trans. Antennas Propag.*, 2013, **61**, 862–870.

[3] G. Sarre, P. Blanchard and M. Broussely, "Aging of lithium-ion batteries", *J. Power Sources*, 2004, **127**, 65–71.

[4] H. C. Keong, K. Thotahewa and M. R. Yuce, "Transmit-Only Ultra Wide Band Body Sensors and Collision Analysis", *IEEE Sens. J.*, 2013, **13**, 1949–1958.

[5] M. Armand and J.-M. Tarascon, "Building better batteries", *Nature*, 2008, **451**, 652–657.

[6] J.-M. Tarascon and M. Armand, "Issues and challenges facing rechargeable lithium batteries", *Nature*, 2001, **414**, 359–367.

[7] P. Bruce, B. Scrosati and J.-M. Tarascon, "Nanomaterials for Rechargeable Lithium Batteries", *Angew. Chem. Int. Edit.*, 2008, **47**, 2930–2946.

[8] F. Connor, *Introductory Topics in Electronics and Telecommunication: Antennas*, Edward Arnold (Publishers) Ltd., 1972.

[9] J. Griffiths, *Radio Wave Propagation and Antennas, An Introduction*, Prentice-Hall International (UK) Ltd., 1987.

[10] Argonne National Laboratory, *How a lithium-ion battery works*, https://www.flickr.com/photos/argonne/5029455937, Accessed: 01-06-2015.

[11] A. Amigues, *MSc thesis*, Université de Picardie Jules Verne, Amiens, 2012.

[12] S. Bhadra, D. Khastgir, N. Singha and J. Lee, "Progress in preparation, processing and applications of polyaniline", *Prog. Polym. Sci.*, 2009, **34**, 783–810.

[13] J. Kawahara, P. Ersman, I. Engquist and M. Berggren, "Improving the color switch contrast in PEDOT:PSS-based electrochromic displays", *Org. Electron.*, 2012, **13**, 469–474.

[14] Z. Guo, J. Wang, H. Liu and S. Dou, "Study of silicon/polypyrrole composite as anode materials for Li-ion batteries", *J. Power Sources*, 2005, **146**, 448–451.

[15] H. Li, Y.-M. Chen, X.-T. Ma, J.-L. Shi, B.-K. Zhu and L.-P. Zhu, "Gel polymer electrolytes based on active PVDF separator for lithium ion battery. I: Preparation and property of PVDF/poly(dimethylsiloxane) blending membrane", *J. Membrane Sci.*, 2011, **379**, 397–402.

[16] X. Li, Q. Cao, X. Wang, S. Jiang, H. Deng and N. Wu, "Preparation of Poly(vinylidene fluoride)/Poly(methyl methacrylate) Membranes by Novel Electrospinning System for Lithium Ion Batteries", *J. Appl. Polym. Sci.*, 2011, **122**, 2616–2620.

[17] Imperial College, *Conducting Polymers*, http://www.ch.ic.ac.uk/local/organic/tutorial/steinke/4yrPolyConduct2003.pdf, Accessed: 02-06-2015.

[18] P. Novák, K. Müller, K. Santhanam and O. Haas, "Electrochemically Active Polymers for Rechargeable Batteries", *Chem. Rev.*, 1997, **97**, 207–281.

[19] M. Ratner and D. Shriver, "Ion-transport in solvent-free polymers", *Chem. Rev.*, 1988, **88**, 109–124.

[20] H. Shirakawa, E. Louis, A. MacDiarmid, C. Chiang and A. Heeger, "Synthesis of Electrically Conducting Organic Polymers - Halogen Derivatives of Polyacetylene, $(CH)_X$", *J. Chem. Soc. Chem. Comm.*, 1977, 578–580.

[21] J. Ĉaja, R. Kaner and A. MacDiarmid, "A Rechargeable Battery Employing a Reduced Polyacetylene Anode and a Titanium Disulfide Cathode", *J. Electrochem. Soc.*, 1984, **131**, 2744–2750.

[22] Y.-S. Gal, S.-H. Jin, K. T. Lim and J.-W. Park, "Synthesis, Structural and Spectral Properties of an Ionic Polyacetylene: Poly[*N*-(5-nitro-2-furanmethylene)-2-ethynylpyridinium bromide]", *J. Appl. Polym. Sci.*, 2011, **122**, 987–992.

[23] A. Kaiser and V. Skákalová, "Electronic conduction in polymers, carbon nanotubes and graphene", *Chem. Soc. Rev.*, 2011, **40**, 3786–3801.

[24] R. Baughman, S. Hsu, G. Pez and A. Signorelli, "The structures of cis-polyacetylene and highly conducting derivatives", *J. Chem. Phys.*, 1978, **68**, 5405–5409.

[25] Q. Zhu, J. Fischer, R. Zusok and S. Roth, "Crystal Structure of Polyacetylene Revisited: An X-ray Study", *Solid State Commun.*, 1992, **83**, 179–183.

[26] G. Moss, "International Union of Pure and Applied Chemistry-Basic Terminology of Stereochemistry", *Pure Appl. Chem.*, 1996, **68**, 2193–2222.

[27] F. Bates and G. Baker, "Polyacetylene Single-Crystals", *Macromolecules*, 1983, **16**, 1013–1015.

[28] F. Bates and G. Baker, "Soluble Polyacetylene Graft Co-polymers", *Macromolecules*, 1983, **16**, 704–707.

[29] L. Leibler, "Theory of Microphase Separation in Block Co-polymers", *Macromolecules*, 1980, **13**, 1602–1617.

[30] T. Nagatomo, C. Ichikawa and O. Omoto, "All-Plastic Batteries with Polyacetylene Electrodes", *J. Electrochem. Soc.*, 1987, **134**, 305–308.

[31] J. Mike and J. Lutkenhaus, "Recent Advances in Conjugated Polymer Energy Storage", *J. Polym. Sci. Pol. Phys.*, 2013, **51**, 468–480.

[32] A. Moliton and R. Hiorns, "Review of electronic and optical properties of semiconducting π-conjugated polymers: applications in optoelectronics", *Polym. Int.*, 2004, **53**, 1397–1412.

[33] G. Klaerner and R. Miller, "Polyfluorene Derivatives: Effective Conjugation Lengths from Well-Defined Oligomers", *Macromolecules*, 1998, **31**, 2007–2009.

[34] J. Rissler, "Effective conjugation length of π-conjugated systems", *Chem. Phys. Lett.*, 2004, **395**, 92–96.

[35] M. Wohlgenannt, X. Jiang and Z. Vardeny, "Confined and delocalized polarons in π-conjugated oligomers and polymers: A study of the effective conjugation length", *Phys. Rev. B*, 2004, **69**, 241204(1–4).

[36] L. Shao, J.-W. Jeon and J. Lutkenhaus, "Polyaniline/Vanadium Pentoxide Layer-by-Layer Electrodes for Energy Storage", *Chem. Mater.*, 2012, **24**, 181–189.

[37] G. Boara and M. Sparpaglione, "Synthesis of polyanilines with high electrical conductivity", *Synthetic Met.*, 1995, **72**, 135–140.

[38] Y. Cao and T. Mallouk, "Morphology of Template-Grown Polyaniline Nanowires and Its Effect on the Electrochemical Capacitance of Nanowire Arrays", *Chem. Mater.*, 2008, **20**, 5260–5265.

[39] J. Cheung, W. Stockton and M. Rubner, "Molecular-Level Processing of Conjugated Polymers. 3. Layer-by-Layer Manipulation of Polyaniline via Electrostatic Interactions", *Macromolecules*, 1997, **30**, 2712–2716.

[40] B. Somboonsub, S. Srisuwan, M. Invernale, S. Thongyai, P. Praserthdam, D. Scola and G. Sotzing, "Comparison of the thermally stable conducting polymers PEDOT, PANi, and PPy using sulfonated poly(imide) templates", *Polymer*, 2010, **51**, 4472–4476.

[41] C. Arbizzani, M. Mastragostino and M. Rossi, "Preparation and electrochemical characterization of a polymer $Li_{1.03}Mn_{1.97}O_4$/PEDOT composite electrode", *Electrochem. Commun.*, 2002, **4**, 545–549.

[42] C. Arbizzani, A. Balducci, M. Mastragostino, M. Rossi and F. Soavi, "$Li_{1.01}Mn_{1.97}O_4$ surface modification by poly (3,4-ethylenedioxythiophene)", *J. Power Sources*, 2003, **119**, 695–700.

[43] D. de Leeuw, P. Kraakman, P. Bongaerts, C. Mutsaers and D. Klaassen, "Electroplating of conductive polymers for the metallization of insulators", *Synthetic Met.*, 1994, **66**, 263–273.

[44] H. Yamato, M. Ohwa and W. Wernet, "Stability of polypyrrole and poly (3,4-ethylenedioxythiophene) for biosensor application", *J. Electroanal. Chem.*, 1995, **397**, 163–170.

[45] J. Carlberg and O. Inganäs, "Poly(3,4-ethylenedioxythiophene) as Electrode Material in Electrochemical Capacitors", *J. Electrochem. Soc.*, 1997, **144**, L61–L64.

[46] J. Kolafa and M. Ratner, "Oligomers of poly(ethylene oxide): Molecular dynamics with a polarizable force field", *Mol. Simulat.*, 1998, **21**, 1–26.

[47] A. Johansson, *PhD thesis*, Uppsala University, 1995.

[48] Y. Takahashi and H. Tadokoro, "Structural Studies of Polyethers, (-(CH2)m-O-)$_n$. X. Crystal Structure of Poly(ethylene oxide)", *Macromolecules*, 1973, **6**, 672–675.

[49] C. Robitaille and D. Fauteux, "Phase Diagrams and Conductivity Characterization of Some PEO -LiX Electrolytes", *J. Electrochem. Soc.*, 1986, **133**, 315–325.

[50] Å. Wendsjö, J. Lindgren, J. Thomas and G. Farrington, "The Effect of Temperature and Concentration on the Local Environment in the System $M(CF_3SO_3)_2PEO(n)$ for M = Ni, Zn and Pb", *Solid State Ionics*, 1992, **53**, 1077–1082.

[51] M. Winter, J. Besenhard, M. Spahr and P. Novák, "Insertion Electrode Materials for Rechargeable Lithium Batteries", *Adv. Mater.*, 1998, **10**, 725–763.

[52] A. Hektor, M. Klintenberg, A. Aabloo and J. Thomas, "Molecular dynamics simulation of the effect of a side chain on the dynamics of the amorphous $LiPF_6$−PEO system", *J. Mater. Chem.*, 2003, **13**, 214–218.

[53] C. Berthier, W. Gorecki, M. Minier, M. Armand, J. Chabagno and P. Rigaud, "Microscopic investigation of ionic conductivity in alkali metal salts-poly(ethylene oxide) adducts", *Solid State Ionics*, 1983, **11**, 91–95.

[54] A. Lauenstein, A. Johansson and J. Tegenfeldt, "Water-Absorption of the Polymer Electrolyte Systems $Pb(CF_3SO_3)_2$PEOn and $Zn(CF_3SO_3)_2$PEOn", *J. Electromchem. Soc.*, 1994, **141**, 1819–1823.

[55] S. Sapp, S. Luebben, Y. Losovyj, P. Jeppson, D. Schulz and A. Caruso, "Work function and implications of doped poly(3,4-ethylenedioxythiophene)-co-poly(ethylene glycol)", *Appl. Phys. Lett.*, 2006, **88**, 152107:1–3.

[56] I.-S. Song, S.-W. Heo, J.-Y. Lee and D.-K. Moon, "Study on the ClO_4 doped PEDOT-PEG in organic solvent using a hole injection layer for PLEDs", *J. Ind. Eng. Chem.*, 2011, **17**, 651–656.

[57] I. Kang, Y. Lee and D. Kim, "Improved Cycling Stability of Lithium Electrodes in Rechargeable Lithium Batteries", *J. Electrochem. Soc.*, 2014, **161**, A53–A57.

[58] J. Li, J. Liu, C. Gao, J. Zhang and H. Sun, "Influence of MWCNTs Doping on the Structure and Properties of PEDOT:PSS Films", *Int. J. Photoenergy*, 2009, **2009**, 1–5.

[59] G. Snook, P. Kao and A. Best, "Conducting-polymer-based supercapacitor devices and electrodes", *J. Power Sources*, 2011, **196**, 1–12.

[60] S. Ghosh and O. Inganäs, "Self-assembly of a conducting polymer nanostructure by physical crosslinking: applications to conducting blends and modified electrodes", *Synthetic Met.*, 1999, **101**, 413–416.

[61] Y. Xia, K. Sun and J. Ouyang, "Solution-processed metallic conducting polymer films as transparent electrode of optoelectronic devices", *Adv. Mater.*, 2012, **24**, 2436–2440.

[62] Y. Xia, K. Sun and J. Ouyang, "Highly conductive poly(3,4-ethylenedioxythiophene):poly(styrene sulfonate) films treated with an amphiphilic fluoro compound as the transparent electrode of polymer solar cells", *Energy Environ. Sci*, 2012, **5**, 5325–5332.

[63] Y. Kim, C. Sachse, M. Machala, C. May, L. Müller-Meskamp and K. Leo, "Highly Conductive PEDOT:PSS Electrode with Optimized Solvent and Thermal Post-Treatment for ITO-Free Organic Solar Cells", *Adv. Funct. Mater.*, 2011, **21**, 1076–1081.

[64] P. Das, L. Komsiyska, O. Osters and G. Wittstock, "PEDOT:PSS as a Functional Binder for Cathodes in Lithium Ion Batteries", *J. Electrochem. Soc.*, 2015, **162**, A674–A678.

[65] H. Li, M. Sun, T. Zhang, Y. Fang and G. Wang, "Improving the performance of PEDOT-PSS coated sulfur@activated porous graphene composite cathodes for lithium-sulfur batteries", *J. Mater. Chem. A*, 2014, **2**, 18345–18352.

[66] D. Pozar, *Microwave Engineering*, Wiley, 4th edn, 2012.

[67] K.-L. Wong, *Compact and Broadband Microstrip Antennas*, John Wiley and Sons, 2002.

[68] O. Ozgun, S. Mutlu, M. Aksun and L. Alatan, "Design of dual-frequency probe-fed microstrip antennas with genetic optimization algorithm", *IEEE Trans. Antennas Propag.*, 2003, **51**, 1947–1954.

[69] T. Tran and S. Sharma, "Performance of single layer multimode microstrip patch antenna with reconfigurable radiation patterns", *Antennas and Propagation Society International Symposium*, 2009, 1–4.

[70] A. Bhadouria and M. Kumar, "Microstrip patch antenna for radiolocation using DGS with improved gain and bandwidth", *Advances in Engineering and Technology Research International Conference*, 2014, 1–5.

[71] M. Dahiya, R. Goel, S. Kumar and V. Kaushik, "Comparison of Bow shape Microstrip Antenna and Rectangular patch Microstrip Antenna", *International Journal of Soft Computing and Engineering*, 2012, **2**, 499–501.

[72] D. Orban and G. Moernaut, *The Basics Of Patch Antennas, Updated*, Orban microwave inc. technical report, 2009.

[73] N. Herscovici, "A wide-band single-layer patch antenna", *IEEE Trans. Antennas Propag.*, 1998, **46**, 471–474.

[74] J.-F. Zürcher, A. Skrivervik, O. Staub and S. Vaccaro, "A compact dual-port, dual-frequency printed antenna with high decoupling", *Microw. Opt. Techn. Let.*, 1998, **19**, 131–137.

[75] V. Fusco, *Foundations of Antenna Theory and Techniques*, Pearson Education Limited 2005, 2005.

[76] M. Miao, B. Ooi and P. Kooi, "Broadband CPW-fed wide slot antenna", *Microw. Opt. Techn. Let.*, 2000, **25**, 206–211.

[77] A. Eldek, A. Elsherbeni, C. Smith and K.-F. Lee, "Wideband Slot Antennas for Radar Applications", *Radar Conf.*, 2003, 79–84.

[78] K. Nithisopa, J. Nakasuwan, N. Songthanapitak, N. Anantrasirichai and T. Wakabayashi, "Design CPW fed slot antenna for wideband applications", *Piers Online*, 2007, **3**, 1124–1127.

[79] I. Grant and W. Phillips, *Electro-magnetism*, Wiley, 1990.

[80] P. Canepa, *PhD thesis*, University of Kent, 2012.

[81] A. Shah, K. Luo, T. Ralph and F. Walsh, "Recent trends and developments in polymer electrolyte membrane fuel cell modelling", *Electrochim. Acta*, 2011, **56**, 3731–3757.

[82] R. Dovesi, V. Saunders, C. Roetti, R. Orlando, C. Zicovich-Wilson, F. Pascale, B. Civalleri, K. Doll, N. Harrison, I. Bush, P. D'Arco and M. Llunell, *CRYSTAL09 User's Manual*, University of Torino, 2009.

[83] J. Foresman and Æ. Frisch, *Exploring Chemistry with Electronic Structure Methods*, Gaussian, Inc., 2nd edn, 1996.

[84] W. Koch and M. Holthausen, *A Chemist's Guide to Density Functional Theory*, Wiley-VCH, 2nd edn, 2002.

[85] D. Sholl and J. Steckel, *Density Functional Theory - A Practical Introduction*, Wiley, 2009.

[86] M. Alfredsson, *PhD thesis*, Uppsala University, 1999.

[87] W. Kohn and L. Sham, "Self-Consistent Equations Including Exchange and Correlation Effects", *Phys. Rev. A*, 1965, **140**, 1133–1138.

[88] R. Parr and W. Yang, *Density-Functional Theory of Atoms and Molecules*, Oxford University Press: Oxford, 1989.

[89] A. Leach, *Molecular Modelling: Principles and Applications*, Pearson Education, 2001.

[90] P. Hohenberg and W. Kohn, "Inhomogenous Electron Gas", *Phys. Rev. B*, 1964, **136**, 864–871.

[91] J. Slater, *Quantum Theory of Molecules and Solids: The Self-Consistent Field for Molecules and Solids*, New York, McGraw-Hill, vol. 4.

[92] J. Perdew, E. McMullen and A. Zunger, "Density-functional theory of the correlation energy in atoms and ions: A simple analytic model and a challenge", *Phys. Rev. A*, 1981, **23**, 2785–2789.

[93] D. Ceperley and B. Alder, "Ground State of the Electron Gas by a Stochastic Method", *Phys. Rev. Lett.*, 1980, **45**, 566–569.

[94] S. Vosko, L. Wilk and M. Nusair, "Accurate Spin-dependent Electron Liquid Correlation Energies for Local Spin Density Calculations: A Critical Analysis", *Can. J. Phys.*, 1980, **58**, 1200–1211.

[95] J. Perdew and Y. Wang, "Accurate and simple density functional for the electronic exchange energy: Generalized gradient approximation", *Phys. Rev. B*, 1986, **33**, 8800–8802.

[96] J. Perdew and Y. Wang, "Erratum: Accurate and simple density functional for the electronic exchange energy: Generalized gradient approximation", *Phys. Rev. B*, 1989, **40**, 3399.

[97] J. Perdew and Y. Wang, "Accurate and simple analytic representation of the electron-gas correlation energy", *Phys. Rev. B*, 1992, **45**, 13244.

[98] J. Perdew, *Electronic Structure of Solids 1991*, Akademie Verlag, Berlin, 1991.

[99] J. Perdew, K. Burke and M. Ernzerhof, "Generalized Gradient Approximation Made Simple", *Phys. Rev. Lett.*, 1996, **77**, 3865–3868.

[100] A. Becke, "Density-functional exchange-energy approximation with correct asymptotic behavior", *Phys. Rev. A*, 1988, **38**, 3098–3100.

[101] C. Lee, W. Yang and R. Parr, "Development of the Colle-Salvetti correlation-energy formula into a functional of the electron density", *Phys. Rev. B*, 1988, **37**, 785–789.

[102] A. Becke, "Density-functional thermochemistry. III. The role of exact exchange", *J. Chem. Phys.*, 1993, **98**, 5648–5652.

[103] A. Becke, "A new mixing of Hartree-Fock and local density-functional theories", *J. Chem. Phys.*, 1993, **98**, 1372–1377.

[104] S. Boys and F. Bernardi, "The Calculation of Small Molecular Interactions by the Differences of Separate Total Energies. Some Procedures with Reduced Errors", *Mol. Phys.*, 2002, **100**, 65–73.

[105] P. Dirac, "Note on exchange phenomena in the Thomas-Fermi atom", *Proc. Cambridge Phil. Soc.*, 1930, **26**, 376–385.

[106] H. Monkhorst and J. Pack, "Special points for Brillouin-zone integrations", *Phys. Rev. B*, 1976, **13**, 5188.

[107] G. Gilat and L. Raubenheimer, "Accurate Numerical Method for Calculating Frequency-Distribution Functions in Solids", *Phys. Rev.*, 1966, **144**, 390.

[108] G. Gilat, "Analysis of methods for calculating spectral properties in solids", *J. Comp. Phys.*, 1972, **10**, 432–465.

[109] B. Alder and T. Wainwright, "Phase Transition for a Hard-sphere System", *J. Chem. Phys.*, 1957, **27**, 1208–1209.

[110] A. Rahman, "Correlations in the Motion of Atoms in Liquid Argon", *Phys. Rev. A*, 1964, **136**, 405–411.

[111] A. Rahman and F. Stillinger, "Molecular Dynamics Study of Liquid Water", *J. Chem. Phys.*, 1971, **55**, 3336–3359.

[112] L. Verlet, "Computer 'Experiments' on Classical Fluids. I. Thermodynamical Properties of Lennard-Jones Molecules", *Phys. Rev.*, 1967, **159**, 98–103.

[113] R. Hockney, "The Potential Calculation and Some Applications", *Methods Comput. Phys.*, 1970, **9**, 136–211.

[114] W. Swope, H. Anderson, P. Berens and K. Wilson, "A Computer Simulation Method for the Calculation of Equilibrium Constants for the Formation of Physical Clusters of Molecules: Application to Small Water Clusters", *J. Chem. Phys.*, 1982, **76**, 637–649.

[115] F. Jensen, *Introduction to Computational Chemistry*, Wiley, 1999.

[116] A. Rappé and C. Casewit, *Molecular Mechanics across Chemistry*, University Science Books, 1997.

[117] P. Morse, "Diatomic Molecules According to the Wave Mechanics. II. Vibrational Levels", *Phys. Rev.*, 1929, **34**, 57.

[118] F. London, "Theory and Systematics of Molecular Forces", *Z. Physik*, 1930, **63**, 245–279.

[119] J. Lennard-Jones, "On the determination of molecular fields.-II. From the equation of state of a gas", *Proc. R. Soc. London, Ser. A*, 1924, **106**, 463.

[120] T. Hill, *J. Chem. Phys.*, 1948, **16**, 399.

[121] M. Hodges, A. Stone and S. Xantheas, "Contribution of Many-body Terms to the Energy for Small Water Clusters: A Comparison of Ab Initio Calculations and Accurate Model Potentials", *J. Phys. Chem. A*, 1997, **101**, 9163–9168.

[122] H. Thomas, K. Chen and N. Allinger, "Toward a Better Understanding of Covalent Bonds: The Molecular Mechanics Calculation of C-H Bond Lengths and Stretching Frequencies", *J. Am. Chem. Soc.*, 1994, **116**, 5887–5897.

[123] A. Mackerell, J. Wiórkiewicz-Kuczera and M. Karplus, "An All-atom Empirical Energy Function for the Simulation of Nucleic Acids", *J. Am. Chem. Soc.*, 1995, **117**, 11946–11975.

[124] W. Cornell, P. Cieplak, C. Bayly, I. Gould, K. Merz Jr., D. Ferguson, D. Spellmeyer, T. Fox, J. Caldwell and P. Kollman, "A Second Generation Force Field for the Simulation of Proteins, Nucleic Acids, and Organic Molecules", *J. Am. Chem. Soc.*, 1995, **117**, 5179–5197.

[125] W. Cornell, P. Cieplak, C. Bayly, I. Gould, K. Merz Jr., D. Ferguson, D. Spellmeyer, T. Fox, J. Caldwell and P. Kollman, "A Second Generation Force Field for the Simulation of Proteins, Nucleic Acids, and Organic Molecules - Correction/Addition", *J. Am. Chem. Soc.*, 1996, **118**, 2309.

[126] J. Maple, M.-J. Hwang, T. Stockfisch, U. Dinur, M. Waldman, C. Ewig and A. Hagler, "Derivation of class II force fields. I. Methodology and quantum force field for the alkyl functional group and alkane molecules", *J. Comput. Chem.*, 1994, **15**, 162–182.

[127] M.-J. Hwang, T. Stockfisch and A. Hagler, "Derivation of Class II Force Fields. II. Derivation and Characterization of a Class II Force Field, CFF93, for the Alkyl Functional Group and Alkane Molecules", *J. Am. Chem. Soc.*, 1994, **116**, 2515–2525.

[128] J. Maple, M.-J. Hwang, T. Stockfisch and A. Hagler, "Derivation of Class II Force Fields. III. Characterization of a Quantum Force Field for Alkanes", *Isr. J. Chem*, 1994, **34**, 195–231.

[129] Z. Peng, C. Ewig, M.-J. Hwang, M. Waldman and A. Hagler, "Derivation of Class II Force Fields. IV. van der Waals Parameters of Alkali Metal Cations and Halide Anions", *J. Phys. Chem. A*, 1997, **101**, 7243–7252.

[130] T. Halgren, "Merck molecular force field .1. Basis, form, scope, parameterization, and performance of MMFF94", *J. Comput. Chem.*, 1996, **17**, 490–519.

[131] T. Halgren, "Merck molecular force field .2. MMFF94 van der Waals and electrostatic parameters for intermolecular interactions", *J. Comput. Chem.*, 1996, **17**, 520–552.

[132] T. Halgren, "Merck molecular force field .3. Molecular geometries and vibrational frequencies for MMFF94", *J. Comput. Chem.*, 1996, **17**, 553–586.

[133] T. Halgren and R. Nachbar, "Merck molecular force field .4. Conformational energies and geometries for MMFF94", *J. Comput. Chem.*, 1996, **17**, 587–615.

[134] T. Halgren, "Merck molecular force field .5. Extension of MMFF94 using experimental data, additional computational data, and empirical rules", *J. Comput. Chem.*, 1996, **17**, 616–641.

[135] H. Sun, "COMPASS:An ab Initio Force-Field Optimized for Condensed-Phase Applications - Overview with Details on Alkane and Benzene Compounds", *J. Phys. Chem. B*, 1998, **102**, 7338–7364.

[136] J. Maple, U. Dinur and A. Hagler, "Derivation of force fields for molecular mechanics and dynamics from ab initio energy surfaces", *Proc. Natl. Acad. Sci. USA*, 1988, **85**, 5350–5354.

[137] A. Hagler, E. Huler and S. Lifson, "Energy functions for peptides and proteins. I. Derivation of a consistent force field including the hydrogen bond from amide crystals", *J. Am. Chem. Soc.*, 1974, **96**, 5319–5327.

[138] A. Hagler and S. Lifson, "Energy functions for peptides and proteins. II. Amide hydrogen bond and calculation of amide crystal properties", *J. Am. Chem. Soc.*, 1974, **96**, 5327–5335.

[139] S. Lifson, A. Hagler and P. Dauber, "Consistent force field studies of intermolecular forces in hydrogen-bonded crystals. 1. Carboxylic acids, amides, and the CO$\cdots$H hydrogen bonds", *J. Am. Chem. Soc.*, 1979, **101**, 5111–5121.

[140] A. Hagler, S. Lifson and P. Dauber, "Consistent force field studies of intermolecular forces in hydrogen-bonded crystals. 2. A benchmark for the objective comparison of alternative force fields", *J. Am. Chem. Soc.*, 1979, **101**, 5122–5130.

[141] A. Hagler, P. Dauber and S. Lifson, "Consistent force field studies of intermolecular forces in hydrogen-bonded crystals. 3. The CO$\cdots$HO hydrogen bond and the analysis of the energetics and packing of carboxylic acids", *J. Am. Chem. Soc.*, 1979, **101**, 5131–5141.

[142] A. Pertsin and A. Kitaigorodsky, *The Atom-Atom Potential Method: Applications to Organic Molecular Solids*, Springer-Verlag, New York, vol. 43.

[143] D. Williams, "Representation of the Molecular Electrostatic Potential by Atomic Multipole and Bond Dipole Models", *J. Comput. Chem.*, 1988, **9**, 745–763.

[144] D. Williams, "Alanyl Dipeptide Potential-derived Net Atomic Charges and Bond Dipoles, and their Variation with Molecular-conformation", *Biopolymers*, 1990, **29**, 1367–1386.

[145] H. Sun, "Force-field for Computation of Conformational Energies, Structures, and Vibrational Frequencies of Aromatic Polyesters", *J. Comput. Chem.*, 1994, **15**, 752–768.

[146] H. Sun, S. Mumby, J. Maple and A. Hagler, "An ab Initio CFF93 All-Atom Force Field for Polycarbonates", *J. Am. Chem. Soc.*, 1994, **116**, 2978–2987.

[147] H. Sun, "Ab initio calculations and force field development for computer simulation of polysilanes", *Macromolecules*, 1995, **28**, 701–712.

[148] H. Sun, "Ab initio characterizations of molecular structures, conformation energies, and hydrogen-bonding properties for polyurethane hard segments", *Macromolecules*, 1993, **26**, 5924–5936.

[149] H. Sun, S. Mumby, J. Maple and A. Hagler, "Ab Initio Calculations on Small Molecule Analogs of Polycarbonates", *J. Phys. Chem.*, 1995, **99**, 5873–5882.

[150] H. Sun and D. Rigby, "Polysiloxanes: ab initio force field and structural, conformational and thermophysical properties", *Spectrochim. Acta A*, 1997, **53**, 1301–1323.

[151] D. Rigby, H. Sun and B. Eichinger, "Computer simulations of poly(ethylene oxide): Force field, PVT diagram and cyclization behaviour", *Polym. Int.*, 1997, **44**, 311–330.

[152] W. Smith and T. Forester, "DL_POLY_2.0: A general-purpose parallel molecular dynamics simulation package", *J. Mol. Graphics*, 1996, **14**, 136–141.

[153] I. Todorov and W. Smith, *The DL POLY 4 user manual*, STFC Daresbury Laboratory, 2011.

[154] W. Smith, "Molecular dynamics on hypercube parallel computers", *Comput. Phys. Commun.*, 1991, **62**, 229–248.

[155] W. Smith, "Molecular dynamics on distributed memory (MIMD) parallel computers", *Theor. Chim. Acta.*, 1993, **84**, 385–398.

[156] S. Mayo, B. Olafson and W. Goddard, "DREIDING: A Generic Force Field for Molecular Simulations", *J. Phys. Chem.*, 1990, **94**, 8897–8909.

[157] J. Tersoff, "Modeling solid-state chemistry: Interatomic potentials for multicomponent systems", *Phys. Rev. B*, 1989, **39**, 5566.

[158] A. Trewin, D. Willock and A. Cooper, "Atomistic Simulation of Micropore Structure, Surface Area, and Gas Sorption Properties for Amorphous Microporous Polymer Networks", *J. Phys. Chem. C*, 2008, **112**, 20549–20559.

[159] D. Lewis, D. Willock, C. Catlow, J. Thomas and G. Hutchings, "De novo design of structure-directing agents for the synthesis of microporous solids", *Nature*, 1996, **382**, 604–606.

[160] Accelerys Software Inc., *Materials Studio 6.1*, 2011.

[161] Accelerys Software Inc., *Forcite plus*, 2011.

[162] A. Rappe, C. Casewit, K. Colwell, W. Goddard and W. Skiff, "UFF, a full periodic table force field for molecular mechanics and molecular dynamics simulations", *J. Am. Chem. Soc.*, 1992, **114**, 10024–10035.

[163] P. Dauber-Osguthorpe, V. Roberts, D. Osguthorpe, J. Wolff, M. Genest and A. Hagler, "Structure and energetics of ligand binding to proteins: Escherichia coli dihydrofolate reductase-trimethoprim, a drug-receptor system", *Proteins*, 1988, **4**, 31–47.

[164] ChemAxon (http://www.chemaxon.com), *Marvin 5.10.0*, 2012.

[165] Computer Simulation Technology (CST), *CST Studio Suite Help*, 2014.

[166] Pentalogix, *ViewMate*, http://www.pentalogix.com/viewmate.php, Accessed: 21-05-2015.

[167] M. Woods, O. Rakibet, P. Young, R. Luck, M. Alfredsson and J. Batchelor, "Integrated Antenna-Battery for Low-profile Short Range Communications", *8th European Conference on Antennas and Propagation (EuCAP)*, 2014, 1754–1756.

[168] C. Zicovich-Wilson, B. Kirtman, B. Civalleri and A. Ramírez-Solís, "Periodic density functional theory calculations for 3-dimensional polyacetylene with empirical dispersion terms", *Phys. Chem. Chem. Phys.*, 2010, **12**, 3289–3293.

[169] T. Sugawara and E. Kanda, "The Crystal Structure of Acetylene. I", *Sci. Rep. Res. Tohoku A*, 1952, **4**, 607–614.

[170] R. McMullan and Å Kvick, "Structures of cubic and orthorhombic phases of acetylene by single-crystal neutron diffraction", *Acta Cryst. B*, 1992, **B48**, 726–731.

[171] H. Koski and E. Sándor, "Neutron Powder Diffraction Study of the Low-Temperature Phase of Solid Acetylene-d_2", *Acta Cryst. B*, 1975, **31**, B350–353.

[172] S. Grabowski, "Simulation of the Orthorhombic Crystal Structure of Acetylene using Atom-Atom Potential Calculations", *J. Chem. Res. S.*, 1996, 534–535.

[173] H. Koski, "A Study of the Cubic Phase of Solid Acetylene-d_2", *Z. Naturforsch. A*, 1975, **30**, 1028–1031.

[174] G. van Nes and F. van Bolhuis, "Single-Crystal Structures and Electron Density Distributions of Ethane, Ethylene and Acetylene. II.* Single-Crystal X-ray Structure Determination of Acetylene at 141 K", *Acta Cryst. B*, 1979, **B35**, 2580–2593.

[175] H. Koski, "The Structure of Solid Acetylene-d_2, C_2D_2, at 4.2K. A further refinement", *Acta Cryst. B*, 1975, **B31**, 933–935.

[176] H. Koski, *Cryst. Struct. Commum.*, 1975, **4**, 337–341.

[177] H. Koski, *Cryst. Struct. Commum.*, 1975, **4**, 343–347.

[178] P. Hobza, J. Sponer and T. Reschel, "Density-Functional Theory and Molecular Clusters", *J. Comput. Chem.*, 1995, **16**, 1315–1325.

[179] M. Allen and D. Tozer, "Helium dimer dispersion forces and correlation potentials in density functional theory", *J. Chem. Phys.*, 2002, **117**, 11113–11120.

[180] S. Kristyán and P. Pulay, "Can (semi)local density functional theory account for the London dispersion forces?", *Chem. Phys. Lett.*, 1994, **229**, 175–180.

[181] J. Pérez-Jordá and A. Becke, "A density-functional study of van der Waals forces: rare gas diatomics", *Chem. Phys. Lett.*, 1995, **233**, 134–137.

[182] D. Patton and M. Pederson, "Application of the generalized-gradient approximation to rare-gas dimers", *Phys. Rev. A*, 1997, **56**, R2495–R2498.

[183] Y. Zhang, W. Yang and W. Pan, "Describing van der Waals Interaction in diatomic molecules with generalized gradient approximations: The role of the exchange functional", *J. Chem. Phys.*, 1997, **107**, 7921–7925.

[184] X. Wu, M. Vargas, S. Nayak, V. Lotrich and G. Scoles, "Towards extending the applicability of density functional theory to weakly bound systems", *J. Chem. Phys.*, 2001, **115**, 8748–8757.

[185] C. Adamo and V. Barone, "Exchange functionals with improved long-range behavior and adiabatic connection methods without adjustable parameters: The mPW and mPW1PW models", *J. Chem. Phys.*, 1998, **108**, 664–675.

[186] S. Tsuzuki and H. Lüthi, "Interaction energies of van der Waals and hydrogen bonded systems calculated using density functional theory: Assessing the PW91 model", *J. Chem. Phys.*, 2001, **114**, 3949–3957.

[187] O. Couronne and Y. Ellinger, "An ab initio and DFT study of $(N_2)_2$ dimers", *Chem. Phys. Lett.*, 1999, **306**, 71–77.

[188] E. Meijer and M. Sprik, "A density-functional study of the intermolecular interactions of benzene", *J. Chem. Phys.*, 1996, **105**, 8684–8689.

[189] S. Tsuzuki, T. Uchimaru and K. Tanabe, "Intermolecular interaction potentials of methane and ethylene dimers calculated with the Møller-Plesset, coupled cluster and density functional methods", *Chem. Phys. Lett.*, 1998, **287**, 202–208.

[190] S. Grimme, "Semiempirical GGA-Type Density Functional Constructed with a Long-Range Dispersion Correction", *J. Comput. Chem.*, 2006, **27**, 1787–1799.

[191] S. Grimme, "Accurate Description of van der Waals Complexes by Density Functional Theory Including Empirical Corrections", *J. Comput. Chem.*, 2004, **25**, 1463–1473.

[192] M. Piacenza and S. Grimme, "Van der Waals interactions in aromatic systems: structure and energetics of dimers and trimers of pyridine", *Chem. Phys. Chem.*, 2005, **6**, 1554–1558.

[193] M. Piacenza and S. Grimme, "Van der Waals Complexes of Polar Aromatic Molecules: Unexpected Structures for Dimers of Azulene", *J. Am. Chem. Soc.*, 2005, **127**, 14841–14848.

[194] B. Civalleri, C. Zicovich-Wilson, L. Valenzano and P. Ugliengo, "B3LYP augmented with an empirical dispersion term (B3LYP-D*) as applied to molecular crystals", *CrystEngComm*, 2008, **10**, 405–410.

[195] P. Jurečka, J. Černý, P. Hobza and D. Salahub, "Density functional theory augmented with an empirical dispersion term. Interaction energies and geometries of 80 noncovalent complexes compared with ab initio quantum mechanics calculations", *J. Comput. Chem.*, 2007, **28**, 555–569.

[196] C. Gatti, V. Saunders and C. Roetti, "Crystal-field effects on the topological properties of the electron-density in molecular-crystals - the case of urea", *J. Chem. Phys.*, 1994, **101**, 10686–10696.

[197] C. Broyden, "The Convergence of a Class of Double-rank Minimization Algorithms 1. General Considerations", *IMA J. Appl. Math.*, 1970, **6**, 76–90.

[198] C. Broyden, "The Convergence of a Class of Double-rank Minimization Algorithms 2. The New Algorithm", *IMA J. Appl. Math.*, 1970, **6**, 222–231.

[199] R. Fletcher, "A new approach to variable metric algorithms", *Comput. J*, 1970, **13**, 317–322.

[200] D. Goldfarb, "A family of variable-metric methods derived by variational means", *Math. Comput.*, 1970, **24**, 23–26.

[201] D. Shanno, "Conditioning of quasi-Newton methods for function minimization", *Math. Comput.*, 1970, **24**, 647–656.

[202] W. Dulmage and W. Lipscomb, "The Crystal Structure of Hydrogen Cyanide", *Acta. Cryst.*, 1951, **4**, 330–334.

[203] E. Sándor and R. Farrow, "Crystal Structure of Solid Hydrogen Chloride and Deuterium Chloride", *Nature*, 1967, **213**, 171–172.

[204] S. Murad, "The structure of hydrogen chloride: Dimer, liquid and ordered solid", *Mol. Phys.*, 1984, **51**, 525–529.

[205] M. Johnson, E. Sándor and E. Arzi, "The Crystal Structure of Deuterium Fluoride", *Acta. Cryst. B*, 1975, **B31**, 1998–2003.

[206] W. Haynes, *Handbook of Chemistry and Physics*, CRC Press, 94th edn, 2013.

[207] S. Swaminathan, B. Craven and R. McMullan, "The Crystal Structure and Molecular Thermal Motion of Urea at 12, 60 and 123K from Neutron Diffraction", *Acta. Cryst. B*, 1984, **B40**, 300–306.

[208] A. Hewat and C. Riekel, "The Crystal Structure of Deuteroammonia between 2 and 180 K by Neutron Powder Profile Refinement", *Acta. Cryst. A*, 1979, **A35**, 569–571.

[209] A. Jones, "Sublimation Pressure Data for Organic Compounds", *J. Chem. Eng. Data*, 1960, **5**, 196–200.

[210] R. Stephenson and S. Malanowski, *Handbook of the thermodynamics of organic compounds*, New York: Elsevier, 1987.

[211] K. Shuler and C. Dykstra, "A Model Study of Aggregation of Acetylene Molecules", *J. Phys. Chem. A*, 2000, **104**, 11522–11530.

[212] S. Nyburg and C. Faerman, "The role of bonding electrons in intermolecular forces; solid acetylene", *Mol. Phys.*, 1989, **67**, 447–454.

[213] M. Marshall and W. Klemperer, "Deuterium nuclear quadrupole coupling constants in vibrationally excited C_2HD: Evidence for electron reorganization", *J. Chem. Phys.*, 1984, **81**, 2928–2932.

[214] S. Luebben and S. Sapp, "New Conducting and Semiconducting Polymers for Plastic Electronics", *Material Matters*, 2007, **2**, 11.

[215] Accelerys Software Inc., *Amorphous Cell*, 2011.

[216] *Poly(3,4-ethylenedioxythiophene), bis-poly(ethyleneglycol), lauryl terminated*, http://www.sigmaaldrich.com/catalog/product/aldrich/736287?lang=en&region=GB, Accessed: 03-11-2014.

[217] K. Hellwege and A. Hellwege (ed.), *Landolt-Bornstein: Group II: Atomic and Molecular Physics Volume 7: Structure Data of Free Polyatomic Molecules*, Springer-Verlag, 1976.

[218] K. Kuchitsu (ed.), *Landolt-Bornstein: Group II: Atomic and Molecular Physics Volume 21: Structure Data of Free Polyatomic Molecules*, Springer-Verlag, 1992.

[219] S. Abbrent, J. Lindgren, J. Tegenfeldt and Å. Wendsjö, "Gel electrolytes prepared from oligo(ethylene glycol)dimethacrylate: glass transition, conductivity and Li^+-coordination", *Electrochim. Acta*, 1998, **43**, 1185–1191.

[220] P. Canepa, R. Hanson, P. Ugliengo and M. Alfredsson, "J-ICE: a new Jmol interface for handling and visualizing Crystallographic and Electronics properties", *J. Appl. Cryst.*, 2011, **44**, 225–229.

[221] A. Lichanot, E. Aprà and R. Dovesi, "Quantum mechanical Hartree-Fock study of the elastic properties of Li_2S and Na_2S", *Phys. Stat. Sol. (b)*, 1993, **177**, 157–163.

[222] L. Valenzano, F. Torres, K. Doll, F. Pascale, C. Zicovich-Wilson and R. Dovesi, "Ab Initio study of the vibrational spectrum and related properties of crystalline compounds; the case of $CaCO_3$ calcite", *Z. Phys. Chem.*, 2006, **220**, 893–912.

[223] R. Dovesi, C. Ermondi, E. Ferrero, C. Pisani and C. Roetti, "Hartree-Fock study of lithium hydride with the use of a polarizable basis set", *Phys. Rev. B*, 1984, **29**, 3591–3600.

[224] G. Socrates, *Infrared and Raman Characteristic Group Frequencies, Tables and Charts*, Wiley, 3rd edn, 2001.

[225] M. Waldman and A. Hagler, "New Combining Rules for Rare-gas van-der-Waals Parameters", *J. Comput. Chem.*, 1993, **14**, 1077–1084.

[226] A. Warshel and S. Lifson, "Consistent Force Field Calculations. II. Crystal Structures, Sublimation Energies, Molecular and Lattice Vibrations, Molecular Conformations, and Enthalpies of Alkanes", *J. Chem. Phys.*, 1970, **53**, 582.

[227] A. Hagler, E. Huler and S. Lifson, "Energy functions for peptides and proteins. I. Derivation of a consistent force field including the hydrogen bond from amide crystals", *J. Am. Chem. Soc.*, 1974, **96**, 5319–5327.

[228] J. Chandrasekhar, D. Spellmeyer and W. Jorgensen, "Energy component analysis for dilute aqueous solutions of lithium(1^+), sodium(1^+), fluoride(1^-), and chloride(1^-) ions", *J. Am. Chem. Soc.*, 1984, **106**, 903–910.

[229] K. Heinzinger, "The structure of aqueous electrolyte solutions as derived from MD (molecular dynamics) simulations", *Pure Appl. Chem.*, 1985, **57**, 1031–1042.

[230] J. Åqvist, "Ion-water interaction potentials derived from free energy perturbation simulations", *J. Phys. Chem.*, 1990, **94**, 8021–8024.

[231] H. Kistenmacher, H. Popkie and E. Clementi, "Study of the structure of molecular complexes. III. Energy surface of a water molecule in the field of a fluorine or chlorine anion", *J. Chem. Phys.*, 1973, **58**, 5627–5638.

[232] C. Ewig, T. Thacher and A. Hagler, "Derivation of Class II Force Fields. 7. Nonbonded Force Field Parameters for Organic Compounds", *J. Phys. Chem. B*, 1999, **103**, 6998–7014.

[233] H. Werner and W. Meyer, "Finite perturbation calculations for the static dipole polarizabilities of the first-row atoms", *Phys. Rev. A*, 1976, **13**, 13–16.

[234] E.-A. Reinsch and W. Meyer, "Finite perturbation calculation for the static dipole polarizabilities of the atoms Na through Ca", *Phys. Rev. A*, 1976, **14**, 915–918.

[235] J. Deltour, "Electronic polarizability and magnetic susceptibility of alkali-halide crystals: A phenomenological discussion in terms of interacting ions", *Physica*, 1971, **51**, 292–298.

[236] O. Borodin and G. Smith, "Molecular Dynamics Simulations of Poly(ethylene oxide)/LiI Melts. 1. Structural and Conformational Properties", *Macromolecules*, 1998, **31**, 8396–8406.

[237] Y. Maréchal, "The molecular structure of liquid water delivered by absorption spectroscopy in the whole IR region completed with thermodynamics data", *J. Mol. Struct.*, 2011, **1004**, 146–155.

[238] A. Bernson, J. Lindgren, W. Huang and R. Frech, "Coordination and conformation in PEO, PEGM and PEG systems containing lithium or lanthanum triflate", *Polymer*, 1995, **36**, 4471–4478.

[239] J. Londono, B. Annis, A. Habenschuss, O. Borodin, G. Smith, J. Turner and A. Soper, "Cation Environment in Molten Lithium Iodide Doped Poly(ethylene oxide)", *Macromolecules*, 1997, **30**, 7151–7157.

[240] G. Mao, M.-L. Saboungi, D. Price, M. Armand and W. Howells, "Structure of Liquid PEO-LiTFSI Electrolyte", *Phys. Rev. Lett.*, 2000, **84**, 5536–5539.

[241] D. Brandell, A. Liivat, A. Aabloo and J. Thomas, "Molecular dynamics simulation of the crystalline short-chain polymer system $LiPF_6 \cdot PEO_6$ (Mw $\sim$ 1000)", *J. Mater. Chem.*, 2005, **15**, 4338–4345.

[242] O. Borodin, G. Smith and R. Douglas, "Force Field Development and MD Simulations of Poly(ethylene oxide)/$LiBF_4$ Polymer Electrolytes", *J. Phys. Chem. B*, 2003, **107**, 6824–6837.

[243] A. Johansson, A. Gogoll and J. Tegenfeldt, "Diffusion and ionic conductivity in $Li(CF_3SO_3)PEG_{10}$ and $LiN(CF_3SO_2)_2PEG_{10}$", *Polymer*, 1996, **37**, 1387–1393.

[244] A. Johansson, A. Lauenstein and J. Tegenfeldt, "The Effect of Water on Diffusion and Ionic Conductivity in PEG and $LiCF_3SO_3PEG_{10}$", *J. Phys. Chem.*, 1995, **99**, 6163–6166.

[245] M. Rani, R. Babu and S. Rajendran, "Conductivity study on PVDF-HFP/PMMA electrolytes for lithium battery applications", *Int. J. ChemTech Res.*, 2013, **5**, 1724–1732.

[246] V. Yadav, D. Sahu, Y. Singh and D. Dhubkarya, "The effect of frequency and temperature on dielectric properties of pure Poly Vinylidene Fluoride (PVDF) thin films", *Proc. IMECS 2010, Hong Kong*, 2010, **III**, year.

[247] *Tile*, http://www.thetileapp.com/, Accessed: 26-11-2014.

[248] M. Woods and J. Batchelor, "Low-profile Slot Antenna integrated with a thin polymer non-metallic battery", *IEEE Loughborough Antenna and Propagation Conference*, 2013.

[249] X. Zhang, D. Chang, J. Liu and Y. Luo, "Conducting polymer aerogels from supercritical CO_2 drying PEDOT-PSS hydrogels", *J. Mater. Chem.*, 2010, **20**, 5080–5085.

[250] W. Westphal and A. Sils, *Dielectric Constant and Loss Data*, Massachusetts institute of technology technical report, 1972.

[251] Y. Mobarak, M. Bassyouni and M. Almutawa, "Materials Selection, Synthesis, and Dielectrical Properties of PVC Nanocomposites", *Advances in Materials Science and Engineering*, 2013, **2013**, 1–6.

[252] M. Ziai and J. Batchelor, "Temporary On-Skin Passive UHF RFID Transfer Tag", *IEEE Trans. Antennas Propag.*, 2011, **59**, 3565–3571.

[253] D.Andreuccetti, R.Fossi and C.Petrucci, *An Internet resource for the calculation of the dielectric properties of body tissues in the frequency range 10 Hz - 100 GHz*, http://niremf.ifac.cnr.it/tissprop/, IFAC-CNR, Florence (Italy), 1997. Based on data published by C.Gabriel et al. in 1996. Accessed: 26-02-2015.

[254] Accelerys Software Inc., *Discover*, 2011.

[255] G. Meleshko, J. Kulhavy, A. Paul, D. Willock and J. Platts, "All-atom molecular dynamics simulation of HPMA polymers", *RSC Adv.*, 2014, **4**, 7003–7012.

[256] A. Kokalj, "Computer graphics and graphical user interfaces as tools in simulations of matter at the atomic scale", *Comp. Mater. Sci.*, 2003, **28**, 155–168.

[257] S. Fleming, *GDIS*, http://gdis.sourceforge.net/, Accessed: 22-05-2015.

[258] G. Watson, *mdprep 4.62*.

[259] W. Humphrey, A. Dalke and K. Schulten, "VMD – Visual Molecular Dynamics", *J. Molec. Graphics*, 1996, **14**, 33–38.

[260] *analyse_hist routine, Cardiff University*, http://blogs.cardiff.ac.uk/willock/analyse$_$hist/, Accessed: 05-05-2015.